ABSTRACT

MODELING DEWETTING, DEMIXING, AND THERMAL EFFECTS IN NANOSCALE METAL FILMS

by
Ryan Howard Allaire

Thin film dynamics, particularly on the nanoscale, is a topic of extensive interest. The process by which thin liquids evolve is far from trivial and can lead to dewetting and drop formation. Understanding this process involves not only resolving the fluid mechanical aspects of the problem, but also requires the coupling of other physical processes, including liquid-solid interactions, thermal transport, and dependence of material parameters on temperature and material composition. The focus of this dissertation is on the mathematical modeling and simulation of nanoscale liquid metal films, which are deposited on thermally conductive substrates, liquefied by laser heating, and subsequently dewet into nanoparticles, before cooling and resolidifying. Both single- and multi-metal configurations are considered.

In the former case, continuum theory is used to describe the thermohydrodynamics. Separation of length scales (in-plane length scales are larger than those in the out-of-plane direction) allows for formulation of asymptotic theory that reduces the fluid dynamics problem, involving Navier-Stokes equations in evolving domains, to a fourth order nonlinear partial differential equation for the fluid thickness. Similarly, a leading order thermal model is developed that is novel, computationally efficient, and accurate. The resulting coupled fluid dynamics and thermal transport model is then used to simulate metal film evolution in both two and three dimensional domains, and to investigate the role of various material parameters. Thermal effects are found to play an important role; in particular it is found that the inclusion of temperature dependence in the metal viscosity modifies the time scale of the evolution significantly. On the other hand, in the considered setup the Marangoni (thermocapillary) effect

turns out to be insignificant. The rate of heat lost in the substrate, measured by a Biot number (Bi) is found to influence peak metal film temperatures and liquid lifetimes (time from film melting to resolidification) more strongly than substrate thickness (H_s). Nevertheless, changes in both Bi and H_s can lead to films that freeze in place prior to full dewetting due to the strong dependence of viscosity on temperature.

In the case of multi-metal configurations, molecular dynamics simulations are used to investigate the competition between chemical instabilities and Rayleigh-Plateau type dewetting behavior in NiAg alloys of various geometries. Phase separation occurs for decreasing temperatures and results in Ag@Ni core-shell particles. During the breakup, phase separation and the Rayleigh-Plateau instability either compete or cooperate depending on the relative positioning of Ag and Ni. When the phase separation length scale is sufficiently large, axial migration of Ag onto Ni can result in both Ag@Ni core-shell and pure Ag nanoparticles. Chemical instabilities, therefore, can strongly affect the dewetting mechanism.

MODELING DEWETTING, DEMIXING, AND THERMAL EFFECTS IN NANOSCALE METAL FILMS

by
Ryan Howard Allaire

A Dissertation
Submitted to the Faculty of
New Jersey Institute of Technology and
Rutgers, The State University of New Jersey – Newark
in Partial Fulfillment of the Requirements for the Degree of
Doctor of Philosophy in Mathematical Sciences

Department of Mathematical Sciences
Department of Mathematics and Computer Science, Rutgers-Newark

August 2021

APPROVAL PAGE

MODELING DEWETTING, DEMIXING, AND THERMAL EFFECTS IN NANOSCALE METAL FILMS

Ryan Howard Allaire

Dr. Lou Kondic, Dissertation Co-Advisor   Date
Distinguished Professor, Department of Mathematical Sciences,
New Jersey Institute of Technology

Dr. Linda J. Cummings, Dissertation Co-Advisor   Date
Professor, Department of Mathematical Sciences,
New Jersey Institute of Technology

Dr. Shahriar Afkhami, Committee Member   Date
Professor, Department of Mathematical Sciences,
New Jersey Institute of Technology

Dr. Richard O. Moore, Committee Member   Date
Director of Programs and Services,
Society for Industrial and Applied Mathematics

Dr. Miguel Fuentes-Cabrera, Committee Member   Date
Research Staff, Center for Nanophase Materials Sciences,
Oak Ridge National Laboratory.

<center>**BIOGRAPHICAL SKETCH**</center>

Author: Ryan Howard Allaire

Degree: Doctor of Philosophy

Date: August 2021

Undergraduate and Graduate Education:

- Doctor of Philosophy in Mathematical Sciences,
  New Jersey Institute of Technology, Newark, New Jersey, 2021

- Master of Science in Pure and Applied Mathematics,
  Montclair State University, Montclair, New Jersey, 2015

- Bachelor of Arts in Mathematics
  Rutgers, The State University of New Jersey, New Brunswick, New Jersey, 2012

Major: Mathematical Sciences

Publications:

R. H. Allaire, L. Kondic, L. J. Cummings, P. D. Rack, and M. Fuentes-Cabrera, "The role of phase separation on Rayleigh-plateau type instabilities in alloys," *J. Phys. Chem. C*, 125:5723-5731, 2021.

R. H. Allaire, L. J. Cummings, and L. Kondic, "On efficient asymptotic modelling of thin films on thermally conductive substrates," *J. Fluid Mech.*, 915:A133, 2021.

R. H. Allaire, A. Dhakane, R. Emery, P. Ganesh, P. D. Rack, L. Kondic, L. J. Cummings, and M. Fuentes-Cabrera, "Surface, interface, and temperature effects on the phase separation and nanoparticle self assembly of bi-metallic $Ni0.5Ag0.5$: A molecular dynamics study," *Nanomaterials*, 9, 2019.

B. G. Nita and R. Allaire, "On the three dimensional interaction between flexible fibers and fluid flow," *Fluids*, 2, 2017.

R. Allaire, P. Guerron, B. Nita, P. Nolan, and A. Vaidya, "On the equilibrium configurations of flexible fibers in a flow," *Int. J. Non Linear Mech.*, 69:157-165, 2015.

Presentations:

R. H. Allaire, L. J. Cummings, and L. Kondic "Detailed thermal modelling of droplet assembly in nanoscale molten metal films," *Conference Presentation*, The 7th International Conference on Micro and Nano Flows (MNF 2021), Imperial College London, London, UK, May 25, 2021

R. H. Allaire, "Thin Film Dynamics of Nanoscale Liquid Metals," *Invited Talk*, Complex Fluids and Soft Matter Group Workshop, NJIT, Newark, NJ, February 17, 2021

R. H. Allaire, "GPU Computing of Thermal Effects in Thin Films on Thermally Conductive Substrates," *Invited Talk*, Complex Fluids and Soft Matter Group Workshop, NJIT, Newark, NJ, November 18, 2020

R. H. Allaire, L. Kondic, and L. J. Cummings "Simulating instabilities of liquid metal alloys on nanoscale using molecular dynamics simulations," *Conference Presentation*, 72nd Annual Meeting of the American Physical Society Division of Fluid Dynamics, Seattle, Washington, 2019.

R. H. Allaire, "Molecular Dynamics Simulations of Pulse-Laser Induced Self and Directed Assembly of Nanoscale Thin Liquid Metal Films," *Invited Talk*, Complex Fluids and Soft Matter Group Workshop, NJIT, Newark, NJ, September 26, 2018

R. H. Allaire, L. Kondic, and L. J. Cummings "Including thermal effects in computing dynamics of thin films on thermally conductive substrates," *Conference Presentation*, 71st Annual Meeting of the American Physical Society Division of Fluid Dynamics, Atlanta, Georgia, November 18, 2018.

R. H. Allaire, "On Temperature Effects in Reacting Porous Media Applications," *Workshop Presentation*, Graduate Student Math Modeling Camp, Rensselaer Polytechnic Institute, Troy, NY 2018.

Posters:

R. H. Allaire, "Thermal effects in Nanoscale Liquid Metal Assembly," Dana Knox Student Research Showcase, New Jersey Institute of Technology, Newark, NJ, April 17, 2019.

R. H. Allaire, "Molecular Dynamics Simulations of Liquid Metal Assembly at the Nanoscale," Center for Nanophase Materials Sciences User Meeting, Oak Ridge National Laboratory, Oak Ridge, TN, August 15, 2018.

When life gets complex,

multiply by its complex conjugate.

-Anonymous

ACKNOWLEDGMENT

TABLE OF CONTENTS

LIST OF TABLES

Figure   **Page**

Figure   **Page**

Figure   **Page**

Figure   **Page**

CHAPTER 1

INTRODUCTION

1.1 Motivation from Nanoscale Metallic Films

Metal films on the nanoscale are relevant for a number of applications. Recently, there has been great interest in using pulsed laser-induced dewetting (PLiD) to turn these thin metallic films into ensembles of nanoparticles. During PLiD, the nanoscale liquid metals and other patterned nanostructures are irradiated by a nanosecond laser pulse, break up (dewet) into nanoparticles, and subsequently freeze in place on underlying substrates. These arrangements of metallic nanoparticles have a number of applications due to the optical and magnetic properties [18, 77, 111], and have been used, for example, as a catalyst for the growth of nanowires [25, 54, 72, 114, 145], to enhance solar cell devices by trapping light [8], and as waveguides to transport electromagnetic energy [88]. Numerous other examples ranging from advanced sensing to photonics leverage metallic nanoparticles [9, 38, 87, 94, 130]. The initial deposited films could either be made out of a single metal, or multiple metals. The motivation for considering multiple metals is that, when molten, the film may destabilize, leading to particles with a specific composition, which may inherit properties from each of the constituent metals. Harnessing these effects to direct the assembly of nanostructures is a grand challenge in materials synthesis [6, 36, 70].

The dynamics of thin liquid films has been a topic of interest for a number of years, with a range of applications such as paint drying and tear films, as well as many others (see [27] for a review). Understanding the thin film dynamics becomes increasingly difficult in the context of liquid metals deposited on thermally conductive substrates because, in addition to the fluid dynamics, one must account for thermal effects, including the external heating, dependence of material properties

on temperature, heat losses, and phase changes. One must also account for the heat flow within the substrate as well as the interaction between the liquid and the substrate. Numerous models have been developed to address these complications using continuum theory, which in general describes both the thermodynamics and fluid dynamics in terms of partial differential equations (PDEs), derived from first principles. Since the films are typically thin relative to their width (small aspect ratio) long-wave theory (LWT) can be used to simplify the fluid dynamics problem into a 4th order PDE for film thickness.

A number of authors have used the LWT approach and have developed models that include a number of the thermal effects listed above [7, 33, 118, 119, 124, 127, 135]. Notably, many models assume that heat is lost primarily at the surface of the film rather than through the metal-substrate interface [7, 102, 119], which alters the model significantly compared with those that neglect such free-surface heat loss. Others consider heat loss through the substrate to be the primary cooling mechanism, but use a simplified thermal model, which omits in-plane diffusion [33, 124, 135]. The best model depends on the situation of interest, and on which effects are determined to be dominate or be negligible.

Due to the short length scales, an alternate approach to LWT is to use Molecular Dynamics (MD) simulations. These simulations use inter-atomic potentials, which are well-documented for metals, to describe the forces that one metallic particle has on another. A number of authors have taken this approach to model dewetting in liquid metals. Previous work by Nguyen *et al.* [97] presents MD simulations of liquid metal rings and shows that the behavior is consistent with LWT. The work by Fowlkes *et al.* [40], for example, shows simulations of liquid filaments deposited on graphite substrates. There, the filaments were exposed to instabilities on the surface and dispersion relations were obtained via Fourier analysis. MD simulations have also been used to extract various information, such as diffusion coefficients [20] and

wettability [48], which may be useful to those that use continuum modeling. MD simulations are computationally expensive, however: experimental size geometries may contain millions of atoms; and furthermore, in order to generate data, averages must be taken over many simulations. Nonetheless, with appropriate resources, MD can potentially provide some important details that continuum theory cannot.

The approach that we take here in this dissertation is twofold. We focus first on single metal configurations using continuum theory. In particular, we utilize LWT to derive an asymptotically consistent thermal model, and investigate various thermal effects on the evolution of the liquid metal films. The second component of the thesis deals with multi-metal configurations. In particular, we consider the NiAg alloy, which is immiscible at sufficiently low temperatures. For this topic, we focus on the competition between chemical instabilities that occur due to phase separation and the classical Rayleigh-Plateau (RP) instability that arises due to surface tension in free-standing liquid jets. This work on alloys was done in part at Oak Ridge National Laboratory, initiated by a Summer internship funded by the Department of Energy (DOE) Office of Science Graduate Student Research Program (SCGSR), which is administered by the Oak Ridge Institute for Science and Education, for the DOE, under contract number DE-SC0014664.

1.2 Overview and Structure

The rest of the dissertation is organized as follows. In Chapter 2, we focus on films deposited on thin substrates. In Section 2.3, we formulate a general mathematical model by introducing appropriate scales, the corresponding dimensionless system, and relevant dimensionless parameter groups. We present three different models of heat conduction: a full diffusion model (F), a 1D diffusion model (1D), and an asymptotic model (A); and we summarize the derivation of the thin film evolution equation (the fluid mechanical model used throughout our continuum modeling work

for the single-metal configurations), accomplished using LWT and accounting for the possibility of temperature dependence of material parameters. Section 2.4 contains our main results. In Section 2.4.1, we perform linear stability analysis (LSA) on the film evolution equation to understand the circumstances under which disturbances to the liquid film lead to instabilities, and to predict the manner of film breakup. In Section 2.4.2, we summarize the conditions under which our simulations are carried out, and in Section 2.4.3, we display results comparing the three models for heat conduction. In Section 2.4.4, we restrict attention to the asymptotic model for heat conduction and study how temperature dependence of both viscosity and surface tension influence the results. We find that temperature dependence of the viscosity has the most significant effect on the instability development, while temperature-induced variation of surface tension plays only a minor role. Furthermore, in the physically-relevant regime, allowing viscosity to vary with temperature produces films that dewet fully in the liquid phase, while if viscosity is fixed at its melting temperature value the dewetting occurs much closer to the solidification time, which may result in only partial drop formation. We conclude in Section 2.5 with a brief summary and discussion. The material presented in Chapter 2 is published in the *Journal of Fluid Mechanics* [3].

In Chapter 3, we focus on films deposited on thick substrates and investigate the role that the substrate has on the heating and evolution of the film, in both two and three spatial dimensions. In Section 3.3, we extend the thermal model developed in Chapter 2 to include substrates that are thick and whose thermal conductivity may vary with temperature. The main results for this chapter are given in Section 3.4. In Section 3.4.2, we investigate the role of substrate thickness, substrate heat loss, and nonlinear thermal conductivity effects in the heating of non-deformable flat films. Section 3.4.3 then considers the evolution of 2D films and the dependence on substrate thickness and heat loss. 3D evolving films are studied in Section 3.4.4 and conclusions

are drawn in Section 3.5. The material presented in Chapter 3 is being prepared for publication and the 3D numerical codes therein can be found online at Github [2].

In Chapter 4, we turn our focus to $Ni_{0.5}Ag_{0.5}$ alloys and use molecular dynamics simulations to investigate the demixing process. We give a brief introduction in Section 4.2. In Section 4.3, we outline the methodology used for the discrete molecular dynamics simulations. Results are then presented in Section 4.4. Phase-separated bulk and droplets (exposed to vacuum) are presented and analyzed in Sections 4.4.1 and 4.4.2, respectively. The droplets are then placed on graphite substrates and the role of wettability is explained in Section 4.4.3. Conclusions are drawn in Section 4.5. The work presented in Chapter 4 is based on a paper, which is published in the journal *Nanomaterials* [4].

In Chapter 5, we examine the competition between demixing and dewetting with $Ni_{0.5}Ag_{0.5}$ alloys and the classical Rayleigh-Plateau instability. We begin with a brief introduction in Section 5.2. In Section 5.3, we present the methodology used for constructing metallic bulk and templated nanostructures. Rayleigh-Plateau theory is applied to the templated nanostructures and used to make predictions about the dewetting procedure in Section 5.4. Section 5.5 contains results that show the process by which these alloys evolve into droplets and how the procedure is affected by phase separation. In Section 5.6, we conclude by outlining the importance of phase separation on the dewetting process. The work of Chapter 5 is based on a paper, which is published in the *Journal of Physical Chemistry, C* [5].

In Chapter 6, we revisit the initial goals of the dissertation and explain the overarching conclusions that may be drawn. We then discuss possible future directions of research for which the results presented in this thesis could provide a basis.

CHAPTER 2

ON EFFICIENT ASYMPTOTIC MODELLING OF THIN FILMS ON THERMALLY CONDUCTIVE SUBSTRATES

2.1 Overview

We consider a free surface thin film placed on a thermally conductive substrate and exposed to an external heat source in a setup where the heat absorption depends on the local film thickness. Our focus is on modeling film evolution while the film is molten. The evolution of the film modifies local heat flow, which in turn may influence the film surface evolution through thermal variation of the film's material properties. Thermal conductivity of the substrate plays an important role in determining the heat flow and the temperature field in the evolving film and in the substrate itself. In order to reach a tractable formulation, we use asymptotic analysis to develop a novel thermal model that is accurate, computationally efficient, and that accounts for the heat flow in both the in-plane and out-of plane directions. We apply this model to metal films of nanoscale thickness exposed to heating and melting by laser pulses, a setup commonly used for self and directed assembly of various metal geometries via dewetting while the films are in the liquid phase. We find that thermal effects play an important role, and in particular that the inclusion of temperature dependence in the metal viscosity modifies the time scale of the evolution significantly. On the other hand, in the considered setup the Marangoni (thermocapillary) effect turns out to be insignificant.

2.2 Introduction

The dynamics of thin liquid films is a topic of extensive interest with a number of applications ranging from biomedical [24, 83] to electronic coatings and nanotechnology [147]. The inclusion of thermal effects in thin film dynamics, relevant for

many applications, is a mathematically challenging problem. To develop a realistic model one must consider multiple factors, such as the heat supply mechanism(s), possible dependence of material parameters on temperature, heat loss mechanisms, and phase changes. When the liquid of interest is placed upon a thermally conductive substrate, one must also account for the heat flow within the substrate as well as the interaction between the liquid and the substrate. Numerous models have been developed to address these complications using continuum theory, which in general describes both the thermodynamics and fluid dynamics in terms of partial differential equations (PDEs), derived from first principles. In situations where there is a small aspect ratio (ratio of typical film thickness to typical lateral length scale of interest), long-wave theory (LWT) may be used, which effectively enables the fluid dynamics problem to be reduced to a 4th order PDE for film thickness. LWT has already proved very valuable in a variety of settings such as liquid crystals, paint coatings, tear-films, nanotechnology and many others (see [27] for a comprehensive review). Due to the variety of length and time scales present, the applicability of LWT to the problem of heat conduction in a thin liquid film is not always clear-cut. Of the issues outlined above, we highlight the following in this work: (i) the influence of temperature on film evolution; (ii) heating/cooling mechanisms; and (iii) the application of LWT to heat conduction.

Various thermal effects that may influence the evolution of the film thickness have been considered in prior work. For an isothermal nanoscale film the primary dewetting mechanism is liquid-solid interaction, often modeled by a disjoining pressure (see [66] for an extended review). For non-isothermal films, gradients in temperature may give rise to surface tension gradients (thermocapillary or Marangoni effects), which develop when heating from below [123] and can destabilize the film. The work of Shklyaev *et al.* [126] finds novel stability thresholds between monotonic and oscillatory instabilities (in both cases, in the linear regime the instability grows

as $e^{\omega t}$ with $\Re(\omega) > 0$, but $\Im(\omega)$ is zero in the former case and nonzero in the latter) that also account for heat losses from the free surface of the film (referred to here as radiative heat losses). In that work, the film is heated from below via a constant heat flux from a substrate of much lower thermal conductivity. Batson *et al.* [10] perform a stability analysis similar to that in [126], but model the substrate explicitly rather than as a simple boundary condition. They solve a full heat equation for the substrate temperature, and find that oscillatory instabilities arise primarily due to thermal coupling between the film and the substrate. A number of other works have considered the coupling between the evolution of film and substrate temperatures. Saeki *et al.* [118], for example, consider a film/substrate system heated by a laser and find that the rate of change of film reflectivity R with thickness h, dR/dh, may promote either stability or instability of the film depending on the sign of dR/dh. The magnitude of the incident laser energy was earlier shown to influence film thickness evolution by Oron [101], who showed in particular that increasing the laser energy can partially inhibit film instability.

Another important effect that may influence film evolution is the dependence of material parameters, such as density, thermal conductivity, surface tension, heat capacity and viscosity, on temperature. These relationships are often assumed to be linear, although a strongly nonlinear Arrhenius-type dependence of viscosity on temperature may exist. Oron *et al.* [103] formulated a thin film model in which viscosity variation is included, and in the later work of Seric *et al.* [124], it was found that film evolution is strongly affected by the inclusion of temperature-dependent viscosity. If temperature variations are sufficiently large, the film may undergo a phase change (liquefaction or solidification). This has been considered using a variety of approaches; for example, Trice *et al.* [135] use a latent heat model to describe such phase change whereas others, such as Seric *et al.* [124], assume phase change to be instantaneous.

Modelling of heat losses in a liquid film often focuses on the boundary effects, since viscous dissipation can usually be ignored. Radiative heat losses from the liquid to the surrounding medium are typically modelled by a Robin type boundary condition [7,101,118,119,126] whereas the heat loss/gain from the film to the substrate has been modelled variously by (i) a constant temperature [101,104,118], (ii) constant flux [7, 126], or (iii) continuity of temperatures and fluxes, known as perfect thermal contact [33,118,124,135]. The choice of boundary conditions plays an important role when formulating and solving equations to describe the heat flow.

In many cases an asymptotic approach may be adopted, giving rise to simplified leading order temperature equation(s). The work of Saeki *et al.* [118], for example, includes both radiative heat losses and heat transfer at the liquid-solid interface, and gives rise to a depth-averaged (z-direction) equation for film temperature, which retains parametric z-dependence even when radiative heat losses are ignored. In later work, Saeki *et al.* [119] developed similar leading order equations for film temperature when the film is optically transparent. In this case, the film temperature dependence on z is slaved to the inclusion of radiative heat losses. Trice *et al.* [135], on the other hand, conclude that using a z-independent film temperature model is sufficient when radiative heat losses can be neglected and film-to-substrate heat losses are dominant (*e.g.*, when there is a high thermal conductivity ratio between the film and substrate). These previous works demonstrate that boundary conditions play an integral role in the asymptotic formulation of a model and may facilitate simple models that eliminate z-dependence (*e.g.*, [126]).

Due to the small aspect ratio of the film, a commonly used "reduced" model for heat conduction is one that neglects in-plane diffusion altogether [33, 124, 135]. This model, which we refer to here as (1D), is much simpler than a model that includes full heat diffusion and is typically justified by arguing that in-plane diffusion occurs on a much longer time scale than that of out-of-plane diffusion. Alternative simplified

models have also been proposed. The work of Shklyaev *et al.* [126], for example, uses LWT to derive evolution equations for heat conduction that differ significantly from the 1D model of Dong & Kondic [33] (and from the asymptotic model considered in this dissertation). Atena & Khenner [7] also derive leading order temperature equations that do not rely on the 1D approximation. More recent work by Seric *et al.* [124] briefly compares predictions from (1D) with those using a full thermal diffusion model, and suggests that (1D) performs poorly by comparison, though the analysis is far from complete. Despite the extensive literature, the scenarios for which thermal diffusion model (1D) is valid remain unclear. *A key objective of this dissertation is to present a thermal model for thin film flow that includes in-plane heat conduction at reasonable computational complexity* and to compare with both (1D) and with the full heat diffusion model (which serves as a benchmark).

In this chapter, we consider films placed upon a thermally conductive substrate and heated by a laser. Heat generation by a laser source is complicated to model and requires in general that one accounts for the optical properties of the film, such as reflectivity, transmittance, and absorption. These properties may depend on refractive indices of the air, film and substrate, as well as the respective extinction coefficients. Again, various modeling approaches have been taken in the literature: we note for example that Saeki *et al.* [118, 119] present a detailed model for laser energy that involves complicated expressions for the optical properties; whereas Trice *et al.* [135] propose a simpler approach (to be discussed later) in which these properties are approximated. An important application of laser heating is pulsed laser induced dewetting (PLiD) of metal films. The mechanism by which liquid metals evolve into assemblies of droplets has been explored via experiments [59], simulations [33, 124], and theory [135] with applications ranging from nanowire growth [72, 114, 125], to plasmonics [55] and photovoltaics [8]; see also [64] and [89] for recent application-centered reviews, and [115] and [76] for reviews focusing on

molten metal film instabilities. Of late, PLiD has been used to organize nanoparticles into patterns of droplets via Rayleigh-Plateau type instabilities [34, 92, 116], induced by exposing metal films/filaments upon (typically) Si/SiO$_2$ substrates to laser irradiation, effectively liquefying the film for tens of nanoseconds. The liquefied film breaks up into droplet patterns, which then resolidify, freezing the patterns in place. Thermal effects are found to be highly relevant, influencing the stability, evolution, and final (solidified) configurations of molten metal films (see for example, [135]). A number of experimental studies have considered metallic systems such as Co [34,35,37,135], Ag [78], Au [144], Ni [42], as well as multi-metal systems [44]. The large variety of experimental work that has been done on nanoscale metal films calls for a firm theoretical foundation, which can both explain existing results and suggest new approaches.

The focus of the present chapter is development of a consistent, asymptotically valid, mathematical model that accounts for (i) heat absorption that is influenced by the local value of (time-dependent) film thickness; (ii) in-plane and out-of-plane heat diffusion in a tractable manner; (iii) self-consistent coupling of the heat flow and film evolution, and (iv) thermal variation of material properties, in particular of surface tension and viscosity. Long-wave theory (LWT) is used to reduce modeling of the film evolution to a 4th order PDE for the film thickness and to develop an asymptotic model for heat conduction. We consider a setup where the primary heat loss mechanism is through the substrate rather than the liquid-air interface, and the thermal conductivity of the film is much higher than of the substrate, as appropriate for metal films on SiO$_2$ substrates. We will show that the proposed model (called asymptotic model (A) in what follows) produces accurate results, while avoiding the shortcomings of models that ignore coupling of fluid dynamics and thermal transport and producing results with a reasonable computational effort. It should be emphasized that the use of a more complex model (called full (F)

model below) is orders of magnitude more computationally expensive (even for small computational domains, the computing time is measured in days on a modern computational workstation (in a serial mode)). Our asymptotic model provides essentially indistinguishable results at a fraction of the computational cost.

The rest of the chapter is organized as follows. In Section 2.3, we formulate a general mathematical model by introducing appropriate scales, the corresponding dimensionless system, and relevant dimensionless parameter groups. We present three different models of heat conduction: a full diffusion model (F), a 1D diffusion model (1D), and an asymptotic model (A); and we summarize the derivation of the thin film evolution equation (the fluid mechanical model always used), accomplished using LWT and accounting for the possibility of temperature dependence of material parameters. Section 2.4 contains our main results. In Section 2.4.1, we perform linear stability analysis (LSA) on the film evolution equation to understand the circumstances under which disturbances to the liquid film lead to instabilities, and to predict the manner of film breakup. In Section 2.4.2 we summarize the conditions under which our simulations are carried out, and in Section 2.4.3 we display results comparing the three models for heat conduction. In Section 2.4.4, we restrict attention to the asymptotic model for heat conduction and study how temperature dependence of both viscosity and surface tension influence the results. We find that temperature dependence of the viscosity has the most significant effect on the instability development, while temperature-induced variation of surface tension plays only a minor role. Furthermore, in the physically-relevant regime, allowing viscosity to vary with temperature produces films that dewet fully in the liquid phase, while if viscosity is fixed at its melting temperature value the dewetting occurs much closer to the solidification time, which may result in only partial drop formation. We conclude in Section 2.5 with a brief summary and discussion.

Figure 2.1 3D schematic of the film, substrate and laser system. In dimensionless units the mean film thickness is equal to 1, the substrate thickness is given by H_s and the domain width is $2N\pi$ (both $N = 1$ and $N = 20$ will be used in simulations). The model is presented in 3D but for simplicity simulations will be performed only in 2D.

2.3   Model Formulation

Consider a molten metal film (assumed initially solid) of characteristic lateral length-scale L, and (nanoscale) thickness H, heated by a laser, and in contact with a thermally conductive solid substrate of finite thickness, which itself rests upon a much thicker Si slab. The basic setup is sketched in Figure 2.1. Here we consider the substrate to be thin, and comparable in size to the film thickness, H. We define the aspect ratio of the film to be $\epsilon = H/L \ll 1$.

In this chapter, we refer to the in-plane coordinates as x, y and the out-of-plane coordinate as z. For completeness, we present the governing equations for a 3D system, though the results presented in this chapter will be for the 2D case in which

all quantities are independent of y. We define L, H, U, ϵU, t_s, T_melt, $\mu_\mathrm{f} U/(\epsilon^2 L)$ and γ_f (where μ_f and γ_f are the viscosity and surface tension of the film at melting temperature, T_melt) to be the in-plane length scale, out-of-plane length scale, in-plane velocity scale, out-of plane velocity scale, time scale, temperature scale, pressure scale, and surface tension scale, respectively (the values of the material parameters used are given in Table A.1 in Appendix A.1.1). Similar to [52], we set $t_\mathrm{s} = 3\mu_\mathrm{f} L/(\epsilon^3 \gamma_\mathrm{f})$, which can be interpreted as a viscous time scale. The in-plane velocity scale is fixed as $U = \epsilon^3 \gamma_\mathrm{f}/(3\mu_\mathrm{f})$ so that $t_s = L/U$. The length scale is fixed as $L = \lambda_\mathrm{m}/(2\pi)$, where λ_m is the most unstable wavelength obtained from linear stability analysis (LSA) with surface tension and viscosity fixed as γ_f and μ_f, respectively (see Appendix A.1.2 for details). We treat the film as an incompressible Newtonian fluid and assume that viscosity is independent of z. The resultant dimensionless system then comprises the following fluid equations, which hold on $0 < z < h$,

$$\epsilon^2 \mathrm{Re}\left(\partial_t u + \boldsymbol{u} \cdot \boldsymbol{\nabla} u\right) = -\partial_x p + \epsilon^2 \boldsymbol{\nabla}_2 \cdot (\mathcal{M}\boldsymbol{\nabla}_2 u) + \mathcal{M}\partial_z^2 u + \epsilon^2 \partial_y \mathcal{M}\partial_x v, \tag{2.1}$$

$$\epsilon^2 \mathrm{Re}\left(\partial_t v + \boldsymbol{u} \cdot \boldsymbol{\nabla} v\right) = -\partial_y p + \epsilon^2 \boldsymbol{\nabla}_2 \cdot (\mathcal{M}\boldsymbol{\nabla}_2 v) + \mathcal{M}\partial_z^2 v + \epsilon^2 \partial_x \mathcal{M}\partial_y u, \tag{2.2}$$

$$\epsilon^4 \mathrm{Re}\left(\partial_t w + \boldsymbol{u} \cdot \boldsymbol{\nabla} w\right) = -\partial_z p + \epsilon^4 \boldsymbol{\nabla}_2 \cdot (\mathcal{M}\boldsymbol{\nabla}_2 w) + \epsilon^2 \mathcal{M}\partial_z^2 w + \epsilon^2 \boldsymbol{\nabla}_2 \mathcal{M} \cdot \partial_z(u, v), \tag{2.3}$$

$$\boldsymbol{\nabla} \cdot \boldsymbol{u} = 0, \tag{2.4}$$

the following equations of heat conduction,

$$\epsilon^2 \mathrm{Pe}_\mathrm{f} \partial_t T_\mathrm{f} = \epsilon^2 \nabla_2^2 T_\mathrm{f} + \partial_z^2 T_\mathrm{f} + \epsilon^2 Q, \qquad \text{for} \quad z \in (0, h), \tag{2.5}$$

$$\mathrm{Pe}_\mathrm{s} \partial_t T_\mathrm{s} = \epsilon^2 \nabla_2^2 T_\mathrm{s} + \partial_z^2 T_\mathrm{s}, \qquad \text{for} \quad z \in (-H_\mathrm{s}, 0), \tag{2.6}$$

and boundary conditions,

$$w = \partial_t h + u\partial_x h + v\partial_y h, \qquad \text{on} \quad z = h, \qquad (2.7)$$

$$[\boldsymbol{n} \cdot \boldsymbol{T} \cdot \boldsymbol{n}] = 3\gamma \left(\boldsymbol{\nabla} \cdot \boldsymbol{n}\right) - 3\Pi(h), \qquad \text{on} \quad z = h, \qquad (2.8)$$

$$\epsilon \left[\boldsymbol{n} \cdot \boldsymbol{T} \cdot \boldsymbol{t}_1\right] = -3\partial_x\gamma, \qquad \text{on} \quad z = h, \qquad (2.9)$$

$$\epsilon \left[\boldsymbol{n} \cdot \boldsymbol{T} \cdot \boldsymbol{t}_2\right] = -3\partial_y\gamma, \qquad \text{on} \quad z = h, \qquad (2.10)$$

$$\boldsymbol{n} \cdot \boldsymbol{\nabla} T_{\text{f}} = 0, \qquad \text{on} \quad z = h, \qquad (2.11)$$

$$\partial_z T_{\text{f}} = \mathcal{K}\epsilon^2 \partial_z T_{\text{s}}, \quad T_{\text{f}} = T_{\text{s}}, \qquad \text{on} \quad z = 0, \qquad (2.12)$$

$$\boldsymbol{u} = \boldsymbol{0}, \qquad \text{on} \quad z = 0, \qquad (2.13)$$

$$\partial_z T_{\text{s}} = \text{Bi}\left(T_{\text{s}} - T_{\text{a}}\right), \qquad \text{on} \quad z = -H_{\text{s}}, \qquad (2.14)$$

$$\partial_x T_{\text{f}} = \partial_x T_{\text{s}} = 0, \qquad \text{on} \quad x = \pm N\pi, \qquad (2.15)$$

$$\partial_y T_{\text{f}} = \partial_y T_{\text{s}} = 0, \qquad \text{on} \quad y = \pm N\pi. \qquad (2.16)$$

Here, the fluid velocity is given by $\boldsymbol{u} = (u, v, w)$, pressure by p, and film and substrate temperatures by T_{f} and T_{s}, respectively. Subscripts f and s stand for film and substrate, respectively, unless otherwise stated and $\boldsymbol{0} = (0,0,0)$. We refer to the gradient operator as $\boldsymbol{\nabla} = (\partial_x, \partial_y, \partial_z)$, its in-plane counterpart as $\boldsymbol{\nabla}_2 = (\partial_x, \partial_y, 0)$, and the in-plane Laplacian operator as ∇_2^2 (defined by $\nabla_2^2 u = \partial_x^2 u + \partial_y^2 u$ for a given scalar function u). Equations (2.1)–(2.6) are the Navier-Stokes (NS) equations representing conservation of mass and momentum for the film, together with thermal energy conservation in both film $(0 < z < h)$ and substrate $(-H_{\text{s}} < z < 0)$ domains, both of lateral extent $2N\pi$, $-N\pi < x, y < N\pi$ (for simulations we use either $N = 1$ or $N = 20$, but N can be any positive integer). The unit vector $\boldsymbol{n}$ denotes the outward normal to the film's free surface, $z = h$. The equations above introduce the following dimensionless parameters:

$$\mathrm{Re} = \frac{\rho_{\mathrm{f}} U L}{\mu_{\mathrm{f}}}, \qquad \mathcal{M} = \frac{\mu}{\mu_{\mathrm{f}}}, \qquad \mathcal{K} = \frac{k_{\mathrm{s}}}{k_{\mathrm{f}}} \epsilon^{-2}, \qquad (2.17)$$

$$\mathrm{Pe_f} = \frac{(\rho c)_{\mathrm{f}} U L}{k_{\mathrm{f}}}, \qquad \mathrm{Pe_s} = \frac{(\rho c)_{\mathrm{s}} U \epsilon H}{k_{\mathrm{s}}}, \qquad \mathrm{Bi} = \frac{\alpha H}{k_{\mathrm{s}}},$$

which are the Reynolds number, dimensionless viscosity, (scaled) thermal conductivity ratio, Peclet numbers, and Biot number, respectively. We assume $\epsilon^2 \mathrm{Re} \ll 1$; the remaining quantities in Equation (2.17) are assumed $O(1)$. For further discussion of the choice of scales and parameter values see Appendix A.1.1, in particular Table A.1, and Section 2.3.1.3 later. The definitions of the laser source term Q and the disjoining pressure $\Pi(h)$ are given in the discussion below. The material parameters $(\rho, c, k)_{\mathrm{f,s}}$ represent the density, specific heat capacity, and thermal conductivity of the film and substrate, respectively. We assume that the substrate is optically transparent and does not absorb laser energy.

In experiments, a Si substrate is often used [59, 141, 144] on top of which a native layer of oxide, usually SiO_2, 3-4 nm in thickness, typically exists (though an additional oxide layer, typically about 100 nm thick, may also be deposited). Below the oxide in either case is Si, which has a much higher thermal conductivity, and can therefore be assumed isothermal relative to the SiO_2. Consistently, we consider the (SiO_2) substrate to be positioned on top of a thick layer of much higher conductivity, assumed to be at constant ambient temperature, T_{a}. We model the heat loss from the top (SiO_2) substrate to the thick Si layer below via a Newton law of cooling at $z = -H_{\mathrm{s}}$ (Equation (2.14)) with Biot number, Bi (related to the dimensional heat transfer coefficient, α). The value of Bi was chosen so that the film melts and solidifies on a time scale comparable to the film evolution (although the value $\mathrm{Bi} = 2 \times 10^{-3}$ is presented, the range 7×10^{-4}-7×10^{-3} was considered). We assume the following form of the heat source, Q in Equation (2.5), representing the external volumetric

heating due to the laser at normal incidence (see [124, 135]),

$$Q = F(t) \left[1 - R(h) \right] \exp \left[-\alpha_{\mathrm{f}} \left(h - z \right) \right], \qquad (2.18)$$

$$F(t) = C \exp \left[- \left(t - t_{\mathrm{p}} \right)^2 / (2\sigma^2) \right],$$

$$C = \frac{E_0 \alpha_{\mathrm{f}} L^2}{\sqrt{2\pi} \sigma t_{\mathrm{s}} H k_{\mathrm{f}} T_{\mathrm{melt}}},$$

where C is a constant (assumed $O(1)$) proportional to the amount of incident energy, E_0, applied from the laser onto the film, α_{f}^{-1} is the (scaled) absorption length for laser radiation in the film, and $F(t)$ captures the temporal power variation of the laser, taken to be a Gaussian pulse centred at t_{p} and of width defined by $\sigma = t_{\mathrm{p}}/(2\sqrt{2\ln 2})$. Similar to prior work by a number of authors [33, 101, 118, 119, 124, 135] the transmittance of laser-source heating is modeled via the Bouguer-Beer-Lambert Law (see, *e.g.*, [63]), which in Equation (2.18) is presented as a spatially-dependent source term, $\exp(-\alpha_{\mathrm{f}}(h - z))$. In general, the reflectivity of the film, $R(h)$, on a transparent substrate, can be determined by solving Maxwell's equations with the appropriate boundary conditions [58]. The resultant form is quite cumbersome to work with, however, and instead we approximate $R(h)$ by the simple functional form [124]

$$R(h) = r_0 \left(1 - \exp \left(-\alpha_{\mathrm{r}} h \right) \right),$$

where r_0 and α_{r} are dimensionless fitting parameters, determined by a least-squares fit of the approximate $R(h)$ to the full expression for reflectivity.

Equations (2.7)–(2.11) are boundary conditions on the free surface, $z = h(x, y, t)$, with unit normal $\boldsymbol{n} = \boldsymbol{\nabla} \left(z - \epsilon h \right) / |\boldsymbol{\nabla} \left(z - \epsilon h \right)|$ and tangent vectors $\boldsymbol{t}_1$ and $\boldsymbol{t}_2$ given by $\boldsymbol{t}_1 = (1, 0, \epsilon \partial_x h)/\sqrt{1 + \epsilon^2 (\partial_x h)^2}$ and $\boldsymbol{t}_2 = (0, 1, \epsilon \partial_y h)/\sqrt{1 + \epsilon^2 (\partial_y h)^2}$. The kinematic boundary condition (KBC) is given by Equation (2.7); Equations (2.8), (2.9) and (2.10) are the dynamic boundary conditions, representing a balance of stress between the liquid and air phases, where $\boldsymbol{T}$ is the Newtonian stress tensor, γ

is the surface tension, and $\Pi(h)$ is the disjoining pressure representing liquid-solid interaction. Many forms of $\Pi(h)$ are used in the literature[1]; we take

$$\Pi(h) = K \left[\left(\frac{h_*}{h} \right)^n - \left(\frac{h_*}{h} \right)^m \right], \qquad K = \frac{A_H L}{6\pi\epsilon\gamma_f h_*^3 H^3}, \qquad (2.19)$$

with equilibrium thickness h_*, exponents $n > m > 1$ (we use $(n, m) = (3, 2)$ since these values were shown by [52] to be appropriate for liquid metals), and Hamaker constant A_H. We assume that the radiative heat loss from the film to the air is small compared to the heat conduction from the film to the substrate. As a consequence, we neglect heat loss through the liquid-air interface and apply Equation (2.11), an insulating boundary condition. Furthermore, we model the (assumed) primary heat loss mechanism through the interface between the film and the substrate at $z = 0$ by perfect thermal contact via Equation (2.12). At $z = 0$ we also assume no-slip and no-penetration of fluid via Equation (2.13). Finally, we assume that the film and substrate are thermally insulated at the lateral ends, $x = \pm N\pi$ and $y = \pm N\pi$.

We will now proceed to simplify the full model as outlined above. We begin in Section 2.3.1 with a discussion of the various models for heat conduction, and derive a leading order asymptotic model that (we will show) compares well with the full heat conduction model. In Section 2.3.2, we discuss the long-wave approximation for thin films and the inclusion of thermal effects in the resultant thin film equation.

2.3.1 Thermal Modeling

In what follows, we present three different models for the inclusion of thermal effects (the fluid dynamics in all cases will be described by the long-wave model, see Section 2.3.2). In Section 2.3.1.1 we give a "Full" model for heat conduction, denoted (F), which includes both in-plane and out-of-plane heat diffusion, but omits both

---

[1]For more information regarding the microscopic nature of the disjoining pressure, we refer the reader to [66].

viscous dissipation and thermal advection. As discussed in Chapter 1, a number of previous works have utilized a much simpler model that neglects lateral heat diffusion (*e.g.*, [33, 124, 135]). Although the exact relevance of such lateral (in-plane) heat transfer has not yet been carefully analyzed, prior work by [124] suggests that it may be important. To study and quantify the possible significance, in Section 2.3.1.2 we describe such a "one dimensional" model for heat conduction, denoted (1D). Finally, in Section 2.3.1.3 we apply long-wave theory to (F) to develop an "Asymptotic" model for heat conduction, (A). This model utilizes key assumptions on the non-dimensional parameters introduced in Equation (2.17) to arrive at a system that is simpler than (F), but unlike (1D) retains lateral heat diffusion. These three models will be compared in Section 2.4.3.

2.3.1.1 Full model. In order to compare models of heat conduction, we must first declare a model that serves as a benchmark. We refer to Equations (2.5)–(2.6), (2.11)–(2.12), and (2.14)–(2.16) (despite the presence of terms that may appear asymptotically small with respect to ϵ in comparison to other terms), as the **Full Model (F)** for heat conduction.

2.3.1.2 1D model. Here we display the model obtained by neglecting in-plane heat conduction in (F), assuming that the term $\epsilon^2 \nabla_2^2 T_{\mathrm{f}}$ may be neglected compared with $\partial_z^2 T_{\mathrm{f}}$ in Equation (2.5) but retaining all other terms. Equation (2.11) is replaced by $\partial_z T_{\mathrm{f}} = 0$ since $\boldsymbol{n} = (0, 0, 1) + O(\epsilon^2)$. This yields the following **1D Model (1D)**

for heat conduction:

$$\epsilon^2 \mathrm{Pe_f} \partial_t T_f = \partial_z^2 T_f + \epsilon^2 Q, \qquad \text{for} \quad z \in (0, h), \qquad (2.20)$$

$$\mathrm{Pe_s} \partial_t T_s = \partial_z^2 T_s, \qquad \text{for} \quad z \in (-H_s, 0), \qquad (2.21)$$

$$\partial_z T_f = 0, \qquad \text{on} \quad z = h, \qquad (2.22)$$

$$\partial_z T_f = \mathcal{K} \epsilon^2 \partial_z T_s, \qquad \text{on} \quad z = 0, \qquad (2.23)$$

$$T_f = T_s, \qquad \text{on} \quad z = 0, \qquad (2.24)$$

$$\partial_z T_s = \mathrm{Bi}\,(T_s - T_a), \qquad \text{on} \quad z = -H_s, \qquad (2.25)$$

$$\partial_x T_f = 0, \qquad \text{on} \quad x = \pm N\pi, \qquad (2.26)$$

$$\partial_y T_f = 0, \qquad \text{on} \quad y = \pm N\pi, \qquad (2.27)$$

where Q is given by Equation (2.18). We note that although the substrate temperature T_s only diffuses in the out-of-plane direction, z, it is still functionally dependent on the in-plane coordinates x, y, due to Equation (2.24) and the dependence of film temperature T_f on x, y (via dependence on film height h). It follows from (2.24), (2.26) and (2.27) that $\partial_x T_s = 0$ at $x = \pm N\pi$, and $\partial_y T_s = 0$ at $y = \pm N\pi$ automatically. For the rest of the dissertation, we refer to Equations (2.20)–(2.27) as the (1D) model.

2.3.1.3 Asymptotic model. Next, we formulate a model of intermediate complexity by carrying out further asymptotic analysis. To do so, we first make a number of assumptions about the non-dimensional parameters defined in Equation (2.17) and provide estimates of time scales based on the parameters given in Table A.1:

(**i**) $\mathrm{Pe_f} = O(1)$. The term $\epsilon^2 \mathrm{Pe_f} = \left[(\rho c)_f \, H^2 / k_f \right] / t_s = t_{\mathrm{D_f}} / t_s$ appearing in Equation (2.5) is a ratio of two time scales: $t_{\mathrm{D_f}}$, the time scale of diffusion of heat in the film, and t_s, the time scale of film evolution. Thus, we assume $t_{\mathrm{D_f}} \ll t_s$; heat diffuses rapidly through the film, before any significant film evolution can occur. In our setup, $t_{\mathrm{D_f}} \approx 1.17$ ps, whereas $t_s \approx 26.86$ ns.

(ii) $\mathrm{Pe_s} = O(1)$. Similar to (i) the Peclet number for the solid layer can be written as a ratio of time scales, $\mathrm{Pe_s} = [(\rho c)_\mathrm{s}\, H^2/k_\mathrm{s}]/t_\mathrm{s} = t_{D_\mathrm{s}}/t_\mathrm{s}$, where t_{D_s} is the time scale of out-of-plane thermal diffusion in the substrate. We assume that this diffusion occurs on a time scale comparable to that of film evolution. Here, $t_{D_\mathrm{s}} \approx 0.147$ ns. Although this is small relative to t_s, this assumption ensures that the time-derivative is retained in Equation (2.21), which is numerically convenient and has a negligible effect on results.

(iii) $\mathrm{Bi} = O(1)$. The Biot number $\mathrm{Bi} = (H/k_\mathrm{s})/(1/\alpha)$ can be interpreted as the ratio of internal thermal resistance due to diffusion, H/k_s, and external thermal resistance, $1/\alpha$, due to convection away from the boundary $z = -H_\mathrm{s}$. We assume these internal and external thermal resistances are comparable.

(iv) $\mathcal{K} = k_\mathrm{s}/(\epsilon^2 k_\mathrm{f}) = O(1)$; the film has much higher thermal conductivity than the substrate.

(v) $H_\mathrm{s} = O(1)$, indicating that the substrate thickness is comparable in size to the film thickness. Hence the substrate is also thin.

The difference in length scales in the problem motivates the idea that in-plane and out-of-plane diffusion can occur on different time scales. As a consequence of the thin substrate assumption, (v), the in-plane diffusion is much slower than that of out-of-plane diffusion. The ratio of the film evolution time scale to that of diffusion is therefore much smaller for in-plane diffusion than out-of-plane. Consequently, in-plane diffusion can be neglected in the substrate (cf. [124]).

To obtain an asymptotically valid model, we assume the following expansions:

$$T_\mathrm{f} = T_\mathrm{f}^{(0)} + \epsilon^2 T_\mathrm{f}^{(1)} + \cdots, \qquad T_\mathrm{s} = T_\mathrm{s}^{(0)} + \epsilon^2 T_\mathrm{s}^{(1)} + \cdots,$$

so that, on substituting in Equations (2.5)–(2.6), (2.11)–(2.12), (2.14)–(2.15) and using assumptions (i)–(v) listed above, the leading order model is given by

$$\partial_z^2 T_f^{(0)} = 0, \qquad \text{for} \quad z \in (0, h), \qquad (2.28)$$

$$\text{Pe}_s \partial_t T_s^{(0)} = \partial_z^2 T_s^{(0)}, \qquad \text{for} \quad z \in (-H_s, 0),$$

$$\partial_z T_f^{(0)} = 0, \qquad \text{on} \quad z = h, \qquad (2.29)$$

$$\partial_z T_f^{(0)} = 0, \qquad \text{on} \quad z = 0, \qquad (2.30)$$

$$T_f^{(0)} = T_s^{(0)}, \qquad \text{on} \quad z = 0,$$

$$\partial_z T_s^{(0)} = \text{Bi}\left(T_s^{(0)} - T_a\right), \qquad \text{on} \quad z = -H_s,$$

$$\partial_x T_f^{(0)} = 0, \qquad \text{on} \quad x = \pm N\pi,$$

$$\partial_y T_f^{(0)} = 0, \qquad \text{on} \quad y = \pm N\pi.$$

Equations (2.28)–(2.30) result in a leading order film temperature that is independent of z but still unknown, $T_f^{(0)} = T_f^{(0)}(x, y, t)$. We must therefore proceed to next order in the asymptotic expansion to obtain a closed model for the leading order film temperature. Collecting terms at next order in Equation (2.5) yields:

$$\text{Pe}_f \partial_t T_f^{(0)} = \nabla_2^2 T_f^{(0)} + \partial_z^2 T_f^{(1)} + F(t)\left[1 - R(h)\right]\exp\left[-\alpha_f\left(h - z\right)\right], \qquad (2.31)$$

while the boundary conditions (2.11) and (2.12) at the same order are:

$$\partial_z T_f^{(1)} = \boldsymbol{\nabla}_2 h \cdot \boldsymbol{\nabla}_2 T_f^{(0)}, \qquad \text{on} \quad z = h, \qquad (2.32)$$

$$\partial_z T_f^{(1)} = \mathcal{K} \partial_z T_s^{(0)}, \qquad \text{on} \quad z = 0. \qquad (2.33)$$

Since $T_f^{(0)}$ is independent of z we can integrate Equation (2.31) from $z = 0$ to $z = h$. Doing so, and applying the boundary conditions (2.32) and (2.33), gives the following evolution equation for leading order film temperature:

$$h\text{Pe}_f \partial_t T_f = \boldsymbol{\nabla}_2 \cdot (h\boldsymbol{\nabla}_2 T_f) - \mathcal{K}\left(\partial_z T_s\right)|_{z=0} + h\overline{Q}, \qquad (2.34)$$

for $x, y \in (-N\pi, N\pi)$, where $\overline{Q} = h^{-1} \int_0^h F(t) \left[1 - R(h)\right] \exp\left[-\alpha_f (h - z)\right] dz$ is the averaged heat source and the superscripts on T_f, T_s are dropped for convenience, since now only leading order quantities are considered. Here, $\boldsymbol{\nabla}_2 \cdot (h \boldsymbol{\nabla}_2 T_f)$ in Equation (2.34) describes the lateral heat diffusion, while the terms $\mathcal{K} \partial_z T_s$ and $h\overline{Q}$ represent the heat lost from the film due to contact with the substrate and the generation of heat in the film due to the laser source, respectively. The final asymptotic model for heat conduction is Equation (2.34) in the film, together with:

$$\text{Pe}_s \partial_t T_s = \partial_z^2 T_s, \qquad\qquad \text{for} \quad z \in (-H_s, 0), \qquad (2.35)$$

$$T_f = T_s, \qquad\qquad \text{on} \quad z = 0, \qquad (2.36)$$

$$\partial_z T_s = \text{Bi}\,(T_s - T_a), \qquad\qquad \text{on} \quad z = -H_s, \qquad (2.37)$$

$$\partial_x T_f = 0, \qquad\qquad \text{on} \quad x = \pm N\pi, \qquad (2.38)$$

$$\partial_y T_f = 0, \qquad\qquad \text{on} \quad y = \pm N\pi. \qquad (2.39)$$

We note that, even though lateral diffusion is neglected in equation (2.35), the substrate temperature T_s remains a function of x, y and z, the in-plane variation entering through the boundary condition (2.36). By the same reasoning as in the previous section, the lateral end insulating conditions on T_s, Equations (2.15)–(2.16), are satisfied vacuously.

In summary, we have formulated an asymptotic model for heat conduction that exploits the natural geometry of the problem as well as the relative sizes of material parameters (assumptions (i)–(v)). This model, denoted (A), has advantages over both (F) and (1D). By integrating over the z-direction, a closed model is obtained for a leading order temperature profile that is independent of z, simplifying the problem significantly. As a consequence, (A) is considerably less computationally demanding than (F). Solving (F) for the temperature profile throughout the evolving film is cumbersome since the domain is deformable (see the appendix for details): model (A) eliminates this complication since film temperature depends only on the in-plane

direction(s) and time. Model (A) is also (as we will see) substantially more accurate and faster to compute than (1D).

A number of other authors have developed reduced models for heat transfer within films, which we now briefly highlight and contrast with our model (A). The models presented in [33, 124, 135] ignore in-plane diffusion in the substrate, similar to Equation (2.35). Furthermore, all use a Dirichlet boundary condition at the bottom of the substrate rather than the Newton law of cooling used here (Equation (2.37)). [126] arrive at a leading order temperature equation through arguments similar to ours above. Their model also retains the in-plane diffusion term, $\boldsymbol{\nabla}_2 \cdot (h\boldsymbol{\nabla}_2 T_{\mathrm{f}})$ in Equation (2.34), but considers radiative heat losses through the liquid-air interface to be dominant rather than the heat loss through the substrate. One important difference between our model (A) and that of [126] is that in (A) volumetric heating is considered, which depends on the local value of the film thickness. This fully couples the fluid and thermal problems, whereas the heating mode considered by Shklyaev *et al.* [126] (heating from the substrate below) does not depend directly on the film thickness. Atena & Khenner [7] also assume such volumetric heating but consider the case where the internal heat generation is promoted to leading order so that z-dependence is retained in the film temperature, leading to a more computationally demanding formulation.

2.3.2 Free Surface Evolution

Each of our heat conduction models couples to the film evolution problem, which must be solved simultaneously. Here we briefly summarize the long-wave approximation that we utilize in all our simulations, which effectively reduces the NS equations to a 4th order PDE for film thickness, h. To retain maximum generality and reasonable tractability, we allow both viscosity and surface tension (which appears in boundary conditions (2.8)–(2.10)) to vary with temperature but treat material

density, specific heat, and thermal conductivity as fixed at their respective values at melting temperature. We present forms for both surface tension and viscosity that utilize the average free-surface temperature, defined for our purposes by

$$\overline{T} = \frac{1}{(2N\pi)^2} \int_{-N\pi}^{N\pi} \int_{-N\pi}^{N\pi} (T_{\mathrm{f}}|_{z=h}) \, \mathrm{d}x\mathrm{d}y. \tag{2.40}$$

We assume that surface tension depends linearly on temperature in the following sense:

$$\gamma = 1 + \frac{2\mathrm{Ma}}{3}(\overline{T} - 1) + \epsilon^2 \frac{2\mathrm{Ma}}{3}\Delta T + O(\epsilon^4) = \Gamma + \epsilon^2 \frac{2\mathrm{Ma}}{3}\Delta T + O(\epsilon^4), \tag{2.41}$$

where Ma is the Marangoni number, given by $\mathrm{Ma} = (3\gamma_{\mathrm{T}} T_{\mathrm{melt}})/(2\gamma_{\mathrm{f}})$, where $\gamma_T = (\gamma_{\mathrm{f}}/T_{\mathrm{melt}})\mathrm{d}\gamma/\mathrm{d}\overline{T}|_{\overline{T}=1}$ is the change in surface tension with temperature when the film (on average) is at melting temperature, $\overline{T} = 1$ (the factors of $2/3$ are used for later convenience); and ΔT is given by

$$\Delta T = T_{\mathrm{f}}|_{z=h} - \overline{T}. \tag{2.42}$$

Since $\overline{T}$ depends only on time, Equation (2.41) can be interpreted as defining a surface tension that varies in time (at leading order) due to variations in the average temperature, and in space (at higher order), due to spatial variations in temperature. This asymptotic form of γ proposed in Equation (2.41) provides a consistent balance in the normal and tangential stress balances presented below. The temperature dependence of the dimensionless viscosity, $\mathcal{M} = \mu/\mu_{\mathrm{f}}$, is modeled by an Arrhenius-type relationship, which we take as

$$\mathcal{M}(t) = \exp\left(\frac{E}{RT_{\mathrm{melt}}}\left(\frac{1}{\overline{T}} - 1\right)\right), \tag{2.43}$$

where $R = 8.314 \mathrm{JK^{-1}mol^{-1}}$ is the universal gas constant and E is the activation energy [49].

To leading order in ϵ^2 the normal and tangential stress balances (Equations (2.8)–(2.10)) are:

$$p = -3\Gamma\nabla_2^2 h - 3\Pi(h), \qquad\qquad \text{on} \quad z = h, \qquad (2.44)$$

$$\mathcal{M}\partial_z(u, v) = 2\mathrm{Ma}\nabla_2\left(\Delta T\right), \qquad\qquad \text{on} \quad z = h. \qquad (2.45)$$

To obtain an evolution equation for film thickness, we express conservation of mass in the form

$$\partial_t h + \nabla_2 \cdot (h\overline{u}) = 0, \qquad (2.46)$$

where $\overline{u}$ is the film-averaged (in-plane) velocity, $\overline{u} = h^{-1}\int_0^h (u, v)\,\mathrm{d}z$. To determine u and v, we expand pressure and velocity fields in Equations (2.1)–(2.3) to leading order in ϵ, assume Γ is $O(1)$, and apply the boundary conditions (2.44) and (2.45), together with the kinematic condition (2.7), to obtain the leading order velocity profile,

$$(u, v) = \frac{1}{\mathcal{M}}\left[\left(\frac{z^2}{2} - zh\right)\nabla_2 p + 2z\mathrm{Ma}\nabla_2\left(\Delta T\right)\right], \qquad (2.47)$$

and z-independent pressure, p. Equation (2.44), therefore, gives the pressure throughout the layer and $\nabla_2 p$ is found by taking the gradient of (2.44). After plugging (2.47) into (2.46) we then arrive at the thin film equation,

$$\partial_t h + \nabla_2 \cdot \left[\frac{1}{\mathcal{M}}\left(h^3\nabla_2\left(\Gamma\nabla_2^2 h + \Pi(h)\right) + h^2\mathrm{Ma}\nabla_2\left(\Delta T\right)\right)\right] = 0. \qquad (2.48)$$

Following the time derivative term in Equation (2.48), the terms (from left to right) represent the capillary, disjoining pressure, and Marangoni terms, respectively. In general, Equation (2.48) describes the evolution of a nanoscale thin film and is applicable for any of our three thermal models (A), (F), or (1D) by using ΔT (Equation (2.42)) and $\overline{T}$ (Equation (2.40)) from the appropriate model.

Equation (2.48) is already sufficiently general to incorporate in-plane variation of viscosity. For model (A), this may be accomplished by using $T_\mathrm{f}^{(0)}$ in place of $\overline{T}$

in equation (2.43). This is an additional advantage of (A) that is not immediately shared by (F) or (1D) (including spatial dependence of viscosity is more complex with these models due to the dependence of temperature on z, as discussed further in the next section).

Although the choice of scales made at the start of Section 2.3 is standard in the long-wave approximation (*e.g.*, [103]), the introduction of heat conduction adds significant complications, and it is important to check for consistency. For example, to retain surface tension to leading order in Equation (2.48), the velocity scale must be such that $\Gamma = O(1)$. This leads to the specific choice of time scale t_s, which may be slower than the (nanoseconds) duration of the Gaussian pulse. Further discussion of the choice of scales is provided in Appendix A.1.1. We note that as a consequence of our chosen scalings, it would be asymptotically consistent to replace Equations (2.34) and (2.35) by their quasi-steady analogues; however, solving the resulting boundary value problems is numerically more complicated (and does not affect results), hence we retain these time derivatives in the formulation.

2.4   Results

For simplicity, we limit our considerations to two spatial dimensions, eliminating y-dependence, so that the film's free surface is at $z = h(x, t)$. In Section 2.4.1, we perform linear stability analysis (LSA), which provides a framework for describing instability growth and motivates our choice of initial film profile(s). Section 2.4.2 outlines the setup of the simulations, including the initial conditions and numerical procedures. Sections 2.4.3 and 2.4.4 show simulation results for both film and thermal evolution. In Section 2.4.3 we compare the thermal models. In Section 2.4.4, we (almost) exclusively use (A) to solve for heat conduction and allow the surface tension and viscosity to vary with temperature. For what follows, we define the spatially-

averaged film temperature,

$$T_{\mathrm{avg}} = \frac{1}{2N\pi} \int_{-N\pi}^{N\pi} \frac{1}{h} \int_0^h T_{\mathrm{f}} \, \mathrm{d}z\mathrm{d}x, \qquad (2.49)$$

where the film temperature T_{f} is found using model (1D), (F) or (A) (leading-order temperature for (A)).[2] The parameters used are as given in Table A.1, except where specified otherwise.

2.4.1 Linear Stability Analysis (LSA)

To provide insight into the mechanism by which films dewet, we carry out linear stability analysis (LSA). Consider a uniform film of height h_0, perturbed as follows

$$h(x,t) = h_0 \left(1 + \delta e^{ikx+\beta t}\right),$$

where k is the wavenumber, β is the growth rate, and $\delta \ll 1$ is the amplitude. A more complete analysis could also incorporate independent perturbations to temperature profiles, as was done by [126]; for simplicity we do not take this approach. We also neglect, for now, the influence of thermal gradients on film instability by setting $\mathrm{Ma} = 0$ in Equation (2.48). LSA then provides the following dispersion relation,

$$\beta(k) = \frac{1}{\mathcal{M}} h_0^3 k^2 \left(2 - \Gamma k^2\right). \qquad (2.50)$$

From Equation (2.50), it is immediately apparent that viscosity sets the timescale of the perturbation growth/decay. The stability of the film, on the other hand, is controlled by the surface tension. For our purposes we only consider perturbations that grow ($\beta > 0$ when $k^2 < 2/\Gamma$). The wavenumber k_{m} corresponding to maximum growth is found from Equation (2.50) by setting $\partial\beta/\partial k = 0$. The wavelength of maximum growth Λ_{m} and the maximum growth rate $\beta_{\mathrm{m}} = \beta(k_{\mathrm{m}})$ can then be written

---

[2]For model (A) this is exactly the 2D free-surface average given by (2.40). For models (F) and (1D) it is the average temperature of the entire film.

in the simple form:

$$\Lambda_{\mathrm{m}} = 2\pi\sqrt{\Gamma}, \qquad \beta_{\mathrm{m}} \equiv \frac{h_0^3}{\Gamma\mathcal{M}}. \tag{2.51}$$

Since increasing temperature decreases Γ and $\mathcal{M}$ (see Equations (2.41) and (2.43)), higher temperatures will lead to smaller Λ_{m} and larger β_{m}. In what follows next, Λ_{m} will be used to define simulation geometries. We note that Λ_{m} and L are related when $\Gamma = 1$ via $\Lambda_{\mathrm{m}} = \lambda_{\mathrm{m}}/L = 2\pi$, where the expression for λ_{m} is given in Appendix A.1.2.

2.4.2 Simulation Setup

Here we describe the details of the simulations. The numerical solution of (2.48) is obtained using an approach adapted from [31] with uniform grid size, $\Delta x = h_*$ (h_* is defined in Equation (2.19) and is fixed for all simulations as $h_* = 0.1$), which is sufficient to ensure accuracy. Models (F), (1D), and (A) are all solved using central difference spatial discretisation. Model (F) utilizes a mapping onto a rectangle to account for the moving boundary (this is not needed for models (1D) and (A) due to lack of in-plane diffusion and lack of z-dependence, respectively); see Appendix A.3.1 for details. For (1D) temporal discretisation is performed using the Crank-Nicolson scheme, while for (A) an implicit-explicit (IMEX) scheme is used (see Appendix A.3.2). Model (F) is solved using an alternating direction implicit (ADI) method, treating mixed derivative terms explicitly. Adaptive time stepping is used to ensure a tolerance of 10^{-3} maximum allowable relative error in temperature and film thickness. Note that the time-stepping tolerance criteria must be satisfied for both film and heat evolution equations in order to proceed with a successful iteration (a point to which we return later). No-flux boundary conditions $\partial_x h = \partial_x^3 h = 0$ are imposed at $x = \pm N\pi$ ($h\overline{\boldsymbol{u}} = 0$ from Equation (2.46)). The domain length, $2N\pi = N\Lambda_{\mathrm{m}}(\Gamma = 1)$, is now set by fixing $N = 1$ or $N = 20$. For $N = 1$, the initial

film profile is set to represent a small perturbation to a uniform film thickness,

$$h(x, 0) = h_0 \left(1 - \delta \cos \left(\frac{2\pi x}{\Lambda_{\mathrm{m}}} \right) \right), \tag{2.52}$$

where $\delta = 0.01$. We refer to the corresponding simulations as those with domain length Λ_{m}. For $N = 20$ the following initial film profile is imposed:

$$h(x, 0) = h_0 \left[1 + \delta \sum_{i=1}^{40} A_i \Big(\cos \left(2\pi x / \lambda_i \right) + \sin \left(2\pi x / \lambda_i \right) \Big) \right], \tag{2.53}$$

where the amplitudes A_i are randomly chosen in $[-1, 1]$ and $\lambda_i = 2\Lambda_{\mathrm{m}}/i$. Similarly, we refer to simulations that use Equation (2.53) as those with domain length $20\Lambda_{\mathrm{m}}$. For both values of N, the film and substrate are each initially set to the ambient temperature,

$$T_{\mathrm{f}}^{(0)}(x, 0) = T_{\mathrm{f}}(x, z, 0) = T_{\mathrm{s}}(x, z, 0) = T_{\mathrm{a}}.$$

The numerical solutions for T_{f} and T_{s} are found first, with the film static, since the film is initially solid ($T_{\mathrm{a}} < 1$). Once the film is melted (we define this shortly) the solutions for h, T_{f}, T_{s} are then iterated successively. The flow of the numerical algorithm is as follows:

- **Film solid and static.**
  - Update T_{f}.
  - Update T_{s}.
  - Repeat the previous 2 steps until melted.

- **Film melted.**
  - Set $\Gamma, \mathcal{M}, \Delta T$. Update $h(x, t)$.
  - Update T_{f}.
  - Update T_{s}.
  - Repeat the previous 3 steps until re-solidification.

- **End**.

Once the film is melted, both film evolution and heat conduction are solved at every time step (although the numerical algorithm allows for a less frequent numerical solution of the temperature equation relative to that of h). The film evolution is coupled to the temperature profile through the material parameters Γ (surface tension) and $\mathcal{M}$ (viscosity), and the Marangoni term ΔT in Equation (2.48). The film is allowed to evolve (flow) only when the temperature is everywhere greater than the melting temperature: it then evolves according to Equation (2.48). Subsequently, as the laser heat source decays, the film temperature eventually drops below the melting point and the film re-solidifies. All simulations shown in this chapter are ended when the average temperature decreases to solidification temperature, $T_{\mathrm{avg}} = 1$. In what follows, we will be using the liquid lifetime (LL), defined as the time interval during which the average film temperature is above melting ($T_{\mathrm{avg}} > 1$).

2.4.3 Model Comparison with Fixed Parameters

We now compare models (F), (1D), and (A) holding the material parameters fixed. As a basic check, we first consider a stationary flat film ($h = h_0$), with material parameters fixed at the values corresponding to the melting temperature ($\Gamma = 1, \mathcal{M} = 1$). For such a film there is no in-plane heat conduction: the temperature T_{f} is a function of time t only; and models (F), (1D), and (A) all agree.

Figure 2.2a plots average film temperature against h_0 and time, showing that temperature depends on film thickness in a non-monotonous manner. Figure 2.2b plots the change of temperature with film thickness, $\partial T_{\mathrm{f}}/\partial h$, evaluated at $h = 1$ (this value of h will be used in later simulations), as a function of time. For early times ($t < 2.95$), $\partial T_{\mathrm{f}}/\partial h < 0$, so that a decrease in film thickness corresponds to an increase in temperature (thinner film is hotter). For later times $\partial T_{\mathrm{f}}/\partial h > 0$, so that a decrease in film thickness leads to a decrease in temperature (thinner film
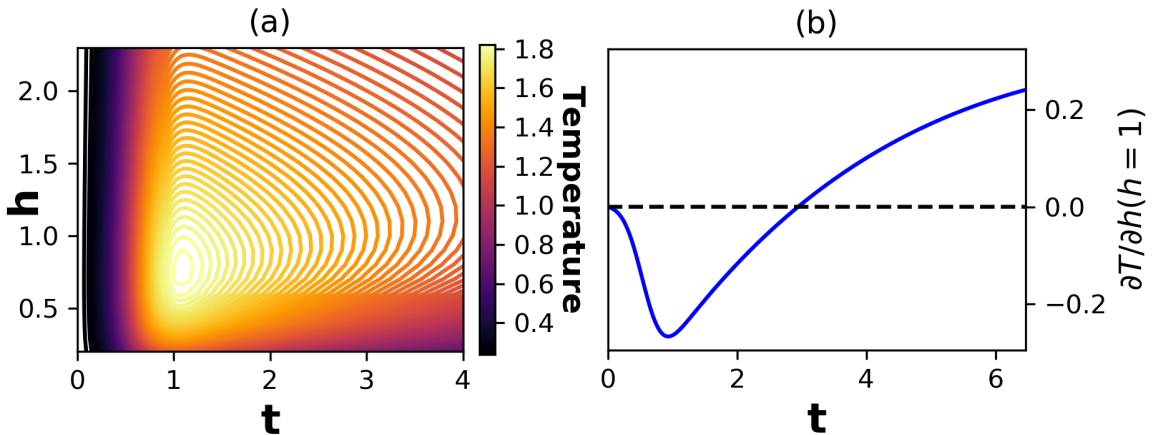
Figure 2.2 (a) Contour plots of average film temperature for a static flat film. (b) Rate of change of temperature with film thickness, $\partial T_{\mathrm{f}}/\partial h$ as a function of time for $h = 1$. At early times ($t < 2.95$) $\partial T_{\mathrm{f}}/\partial h < 0$ and later ($t > 2.95$) $\partial T_{\mathrm{f}}/\partial h > 0$.

is colder). This non-monotonic behavior of $\partial T_{\mathrm{f}}/\partial h$ in time is due to the changing balance between the heating from the source and the heat loss through the substrate (see Appendix A.4 for more details).

We next consider evolving films, with the initial film profile given by Equation (2.52). Figure 2.3a shows the evolution using model (F), though the behaviour is also representative of (A) and (1D). Melting temperature is reached at $t \approx 0.54$; by time $t = 3.32$ the liquid film begins to evolve appreciably; at $t = 4.52$ significant film evolution has occurred and the film first reaches the equilibrium film thickness; and at $t = 6.50$ the film has fully dewetted. Figure 2.3b shows average film temperatures using models (F), (1D) and (A), as well as the film height at the midpoint $x = 0$. The average film temperatures are in good agreement before dewetting, but afterwards model (1D) begins to deviate significantly from models (F) and (A), which show excellent agreement for the entirety of the simulation. The cooling rate, $\mathrm{d}T_{\mathrm{avg}}/\mathrm{d}t$, is faster for (1D) than for (F) and (A) since heat cannot diffuse laterally through the film in (1D). This, in turn, produces a film that solidifies sooner (this will be discussed further in Section 2.4.4). Despite this difference, the midpoint film height $h(x = 0)$, shown here for (F), is similar for all models (see also Figure 2.3a).
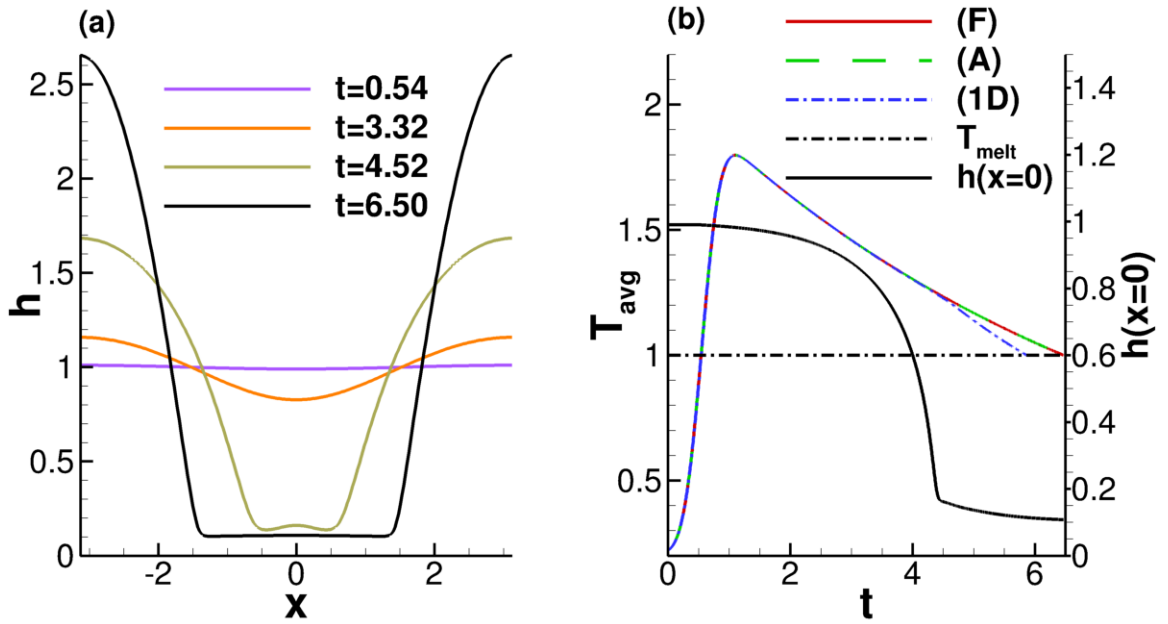
Figure 2.3 (a) Evolution of film thickness when material parameters are fixed and $h(x, 0)$ is given by Equation (2.52), at a few representative time points. (b) Average film temperature (see Equation (2.49)) and midpoint film thickness $h(0, t)$ for the film profiles given in (a). Deviation between the models appears after the the film dewets. The material parameters are set to their melting temperature values, $\Gamma = 1$ and $\mathcal{M} = 1$.
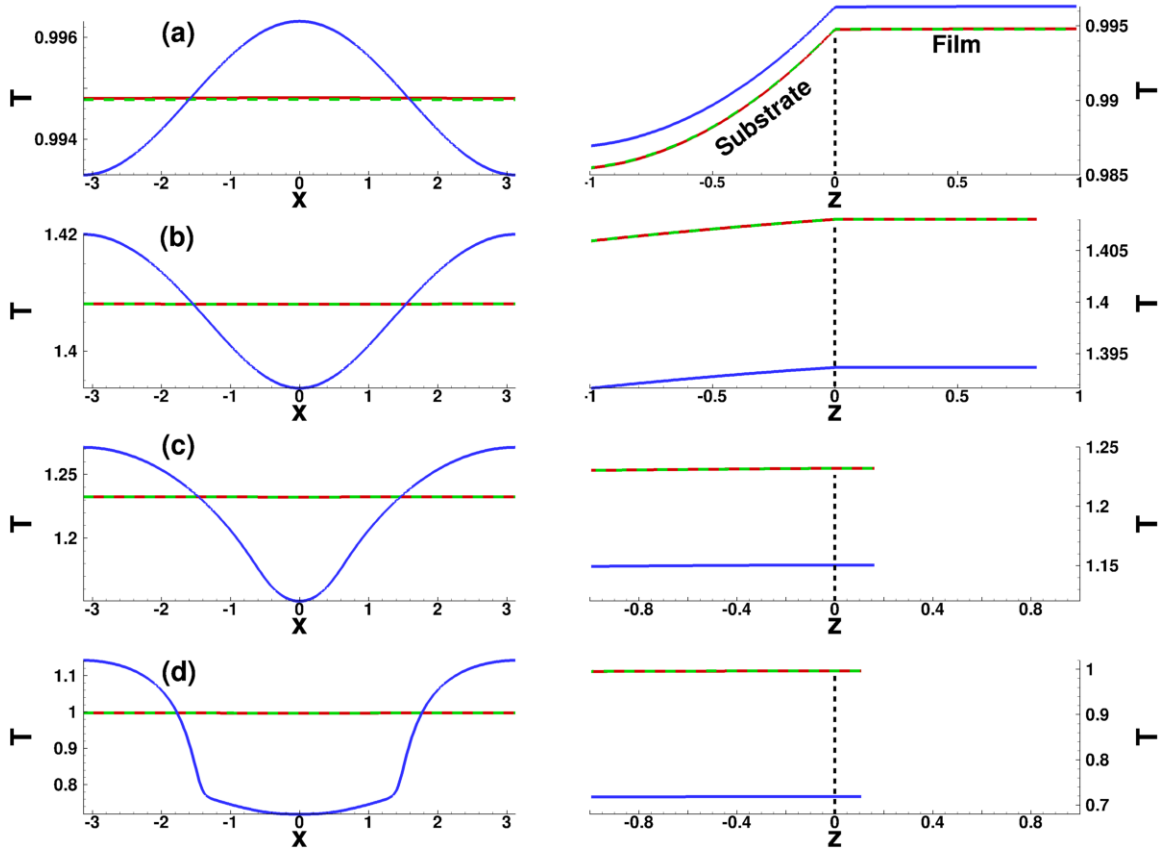
Figure 2.4 Left: Free surface ($z = h$) temperature profiles, $T_f|_{z=h}$ and Right: Midpoint ($x = 0$) temperature corresponding to times (a) $t = 0.54$, (b) $t = 3.32$, (c) $t = 4.52$, and (d) $t = 6.50$. Here $\Gamma = 1$, $\mathcal{M} = 1$ and the overlapping curves correspond to models (F) and (A). Note the difference in vertical axis scales between parts (a)-(d). Color code: (F) (red), (A) (green dashed), (1D) (blue).

We next discuss the spatial variation of temperature. Figure 2.4 shows free surface temperatures (left column) and film midpoint temperatures (at $x = 0$; right column) at the times displayed in Figure 2.3a. Since the film thins at its midpoint as t increases (see Figure 2.3b), the film domain ($z > 0$) shrinks from (a)-(d) in the right column. The lateral spatial variation of temperature is seen to be much weaker for models (F) and (A) than for model (1D) (left column), due to the inclusion of lateral heat diffusion in (F) and (A); and the substrate/film midpoint temperatures are lower for (1D) than for (F)/(A) in frames (b)-(d) (right column). In particular we find that the temperature predictions of models (F) and (A) differ by at most 0.01%, whereas (F) and (1D) differ by as much as 30%. For model (1D) the temperature is initially higher at the film midpoint ($x = 0$) than at the edges, a situation that is reversed at later times (*e.g.*, Figure 2.4b). Using model (1D), therefore, may lead to overestimated temperature gradients, such as in [135], which may significantly alter the evolution of the film.

To emphasize the lateral temperature variation for all models, Figure 2.5 plots the difference between the free surface temperatures at the thinnest ($x = 0$) and thickest ($x = \pm\pi$) parts of the film. Consistent with Figure 2.4a this temperature difference for model (1D) is much larger than for models (F) and (A). All models show the same trend: initially the thinnest part of the film is hottest, but ultimately the thickest parts are hottest. We attribute this change of behaviour, which occurs relatively early in the film evolution, to the combination of lateral diffusion and the heat loss through the substrate (see Equation (2.30)).

To conclude this section, we summarize our main findings. We have compared models (F), (1D), and (A) and found that (A) provides a much better approximation to (F) than does (1D). After dewetting, the film cools more rapidly with model (1D) than with (A) and (F) due to the neglect of in-plane thermal diffusion. Consequently, the average film temperatures in model (1D) vary significantly from those predicted by
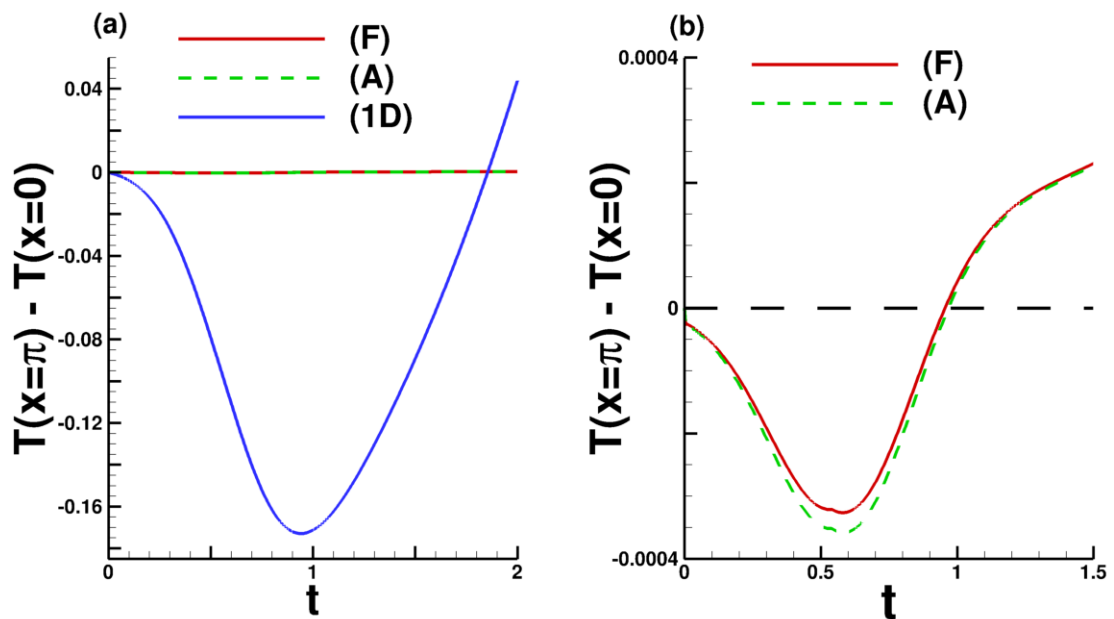
Figure 2.5 (a) Difference between free surface temperatures at the thickest part of the film ($x = \pm\pi$) and the thinnest part ($x = 0$) for models (F) (red), (A) (green), and (1D) (blue). (b) Zoom-in of results for models (F) and (A) from (a) to illustrate behaviour more clearly. The black dashed line represents the horizontal axis where $T(x = \pi) = T(x = 0)$.

models (F) and (A). From a computational point of view, since the film temperature is independent of z in model (A), it is significantly more computationally efficient than (F), and even more efficient than (1D). For illustration, we note that for a 255×200 computational grid in x and z, the simulation times for a typical run reported in this section are 73.4, 1.3, 4.8 hours for models (F), (A), and (1D), respectively, on a reasonably fast workstation.

2.4.4 Variation of Material Parameters

In this section, we consider the effect of varying surface tension and viscosity with temperature (see Equations (2.41) and (2.43)) and consider the influence of the Marangoni effect, by comparing film evolution with $\text{Ma} = 0$ and $\text{Ma} \neq 0$. In the previous section (as well as in additional tests, not reported here for brevity), we have demonstrated that model (A) provides a good approximation to the full model (F) with considerably less computational effort, and so henceforth, we will focus on exploring the differences between models (A) and (1D). In this section, domain lengths of Λ_{m} and $20\Lambda_{\text{m}}$ are simulated, beginning with the former (domain length of Λ_{m} may be assumed until otherwise stated).

We focus first on the case where both surface tension and viscosity depend on average temperature and are therefore time-dependent, $\Gamma(t), \mathcal{M}(t)$, but we ignore the Marangoni effect (set $\text{Ma} = 0$ in Equation (2.48)). In the subsequent text, any reference to time-dependent surface tension or viscosity, $\Gamma(t), \mathcal{M}(t)$, refers solely to time-dependence through the average temperature. Figure 2.6a shows the film thickness profiles and Figure 2.6b shows the free-surface temperature profiles, $T_{\text{f}}|_{z=h}$, at the thin ($\bigstar$) and thicker ($\blacksquare$) parts of the film. We observe that model predictions differ only after dewetting ($\mathbf{B}$) and therefore the film thickness profiles in (1D) and (A) remain nearly identical. After dewetting, the two models exhibit marked differences in the temperature profiles. The large difference in cooling rates between (A) and
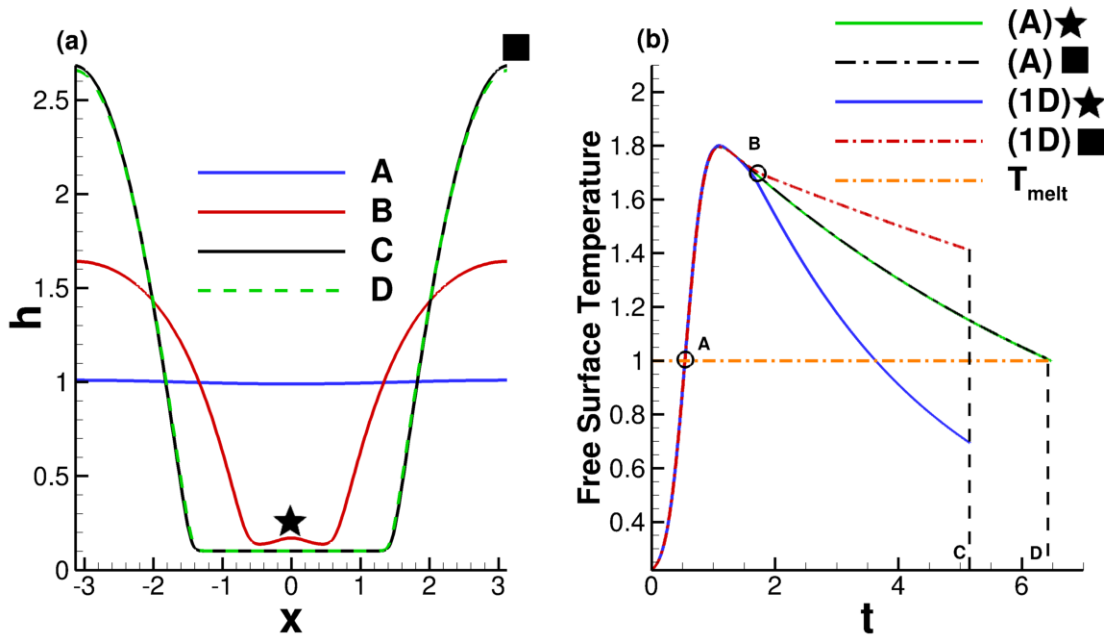
Figure 2.6 (a) Film thickness profiles (simulated with (F), but representative of (A) and (1D) also) for times **A** (melting), **B** (dewetting), **C** (1D) re-solidification and **D** (A) re-solidification. The markers in (a) represent $x = 0$ (★) and $x = \pi$ (■). (b) Free surface temperature at ★ and ■ for (A) and (1D). The temperature profiles agree until the film dewets (**B**). Then, (1D) temperatures vary significantly at ★ and ■, whereas (A) produces similar temperatures at both locations. Surface tension and viscosity vary in time, but Marangoni effect is not included (Ma $= 0$).
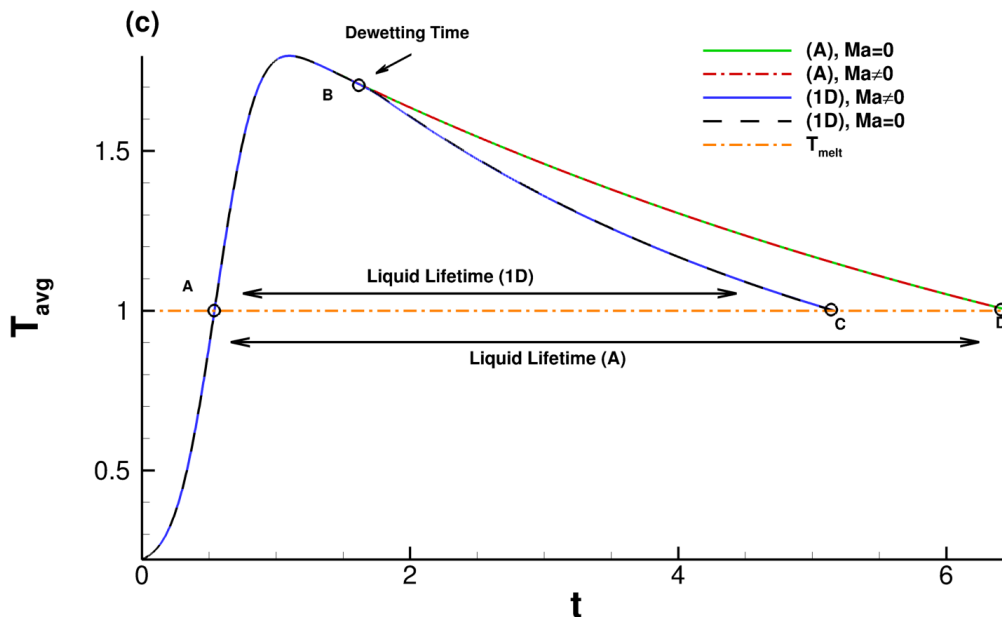
Figure 2.7 Average film temperatures using models (A) and (1D) for Ma $= 0$ and Ma $\neq 0$, and using $\Gamma(t)$ and $\mathcal{M}(t)$. Points **A-D** correspond to those of Figure 2.6(a). Near $t = 0.54$ (**A**), the film melts in both models. The models begin to deviate around $t = 1.72$ (**B**) when dewetting occurs; from this point until solidification (which for Ma $= 0$ occurs at **C** for (1D), **D** for (A); the times for the Ma $\neq 0$ cases are similar) the temperature in model (1D) is lower than that in (A). The liquid lifetimes (LL) are LL ≈ 4.73 (1D) and LL ≈ 5.94 (A).

(1D) is consistent with Figure 2.3b. For (1D), this leads to the thin part of the film ★ being significantly colder than the thicker parts ■ and the difference is exacerbated by the retention of heat in the thick part of the film.

Figure 2.7 shows the average film temperatures for models (A) and (1D) with $\Gamma(t), \mathcal{M}(t)$ as considered in Figure 2.6, for both Ma $= 0$ and Ma $\neq 0$. The Marangoni effect seems to have only a very minor influence on T_{avg} for both models. Furthermore, the rapid cooling seen in model (1D) leads to a significantly shorter liquid lifetime (LL $= 4.73$) than that predicted by model (A) (LL $= 5.94$).

Figure 2.8 compares the results obtained with(out) temperature variation of material properties. From Figure 2.8a, we immediately conclude that the Marangoni effect is very weak, and will be ignored henceforth (Ma $= 0$ for the remaining results).
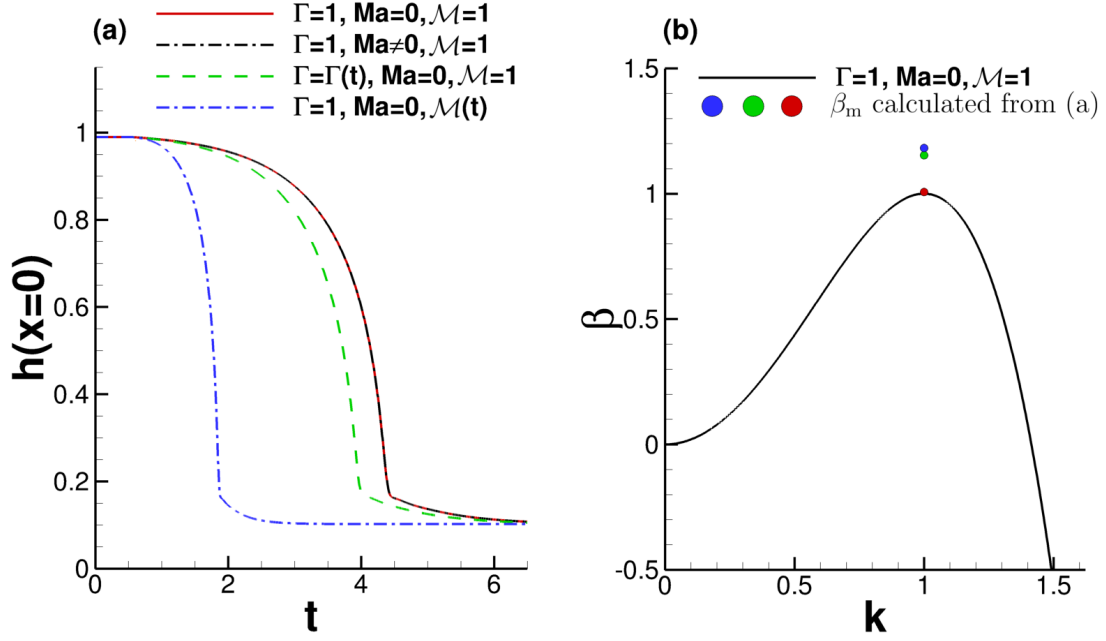
Figure 2.8 (a) Midpoint film thickness, $h(0, t)$, for the cases: surface tension and viscosity fixed, $\Gamma = 1, \mathcal{M} = 1$, with no Marangoni effect, Ma $= 0$ (red, solid line); surface tension and viscosity fixed with Marangoni effect, Ma $\neq 0$ (**black**, dash-dotted line); surface tension varies in time, $\Gamma(t)$, with viscosity fixed and no Marangoni (green, dashed line); viscosity varies in time, $\mathcal{M}(t)$, surface tension fixed and no Marangoni (blue, dot-dashed line). In all cases model (A) was used to calculate temperature. (b) Growth rate, β as a function of wavenumber, k, using Equation (2.50) with $\Gamma = 1$ and $\mathcal{M} = 1$ and no Marangoni effect, Ma $= 0$. The blue, green, and red dots represent maximum growth rate extracted from the corresponding simulations in (a).

The weak Marangoni effect is, at least in part, due to the high thermal conductivity of the film, which sets the thermal timescale and gives rise to the very weak spatial variations in interfacial temperatures seen in Figure 2.4. The second observation is that allowing surface tension to depend on time, $\Gamma = \Gamma(t)$, has a small but measurable effect on the results. With this dependence included, the film instability appears to develop faster than in the constant-Γ case (compare the green dashed curve with the red solid curve in Figure 2.8a). The third observation is that the time-dependence of viscosity has by far the largest effect on the film instability development, leading to much faster dewetting.

We now revisit the predictions of LSA and compare them to simulation results. Figure 2.8b plots the dispersion curve according to Equation (2.50), for the constant parameter case $\Gamma = 1$ and $\mathcal{M} = 1$ (with Ma $= 0$). To estimate the maximum growth rate, β_{m}, in our numerical simulations, we assume the film perturbation grows exponentially at early times, consistent with LSA: $h = h_0(1 + \delta \exp(ik_{\mathrm{m}}x + \beta_{\mathrm{m}}t))$, where k_{m} is the corresponding wavenumber.[3] We then perform a best linear fit of $\ln((h(0,t) - h_0)/(\delta h_0))$ versus t for early times. The red, green and blue dots correspond to growth rates β_{m} extracted from the corresponding colour-coded simulations in Figure 2.8a. The film with parameters fixed (red) grows at the rate predicted by LSA, whereas the film with time-dependent surface tension (green) grows at a slightly faster rate. The growth rate in the time-dependent viscosity case (blue) is similar to the time-dependent surface tension case, despite the much faster instability development in Figure 2.8a. This indicates the relevance of the nonlinear part of instability growth.

To highlight further the significance of time-dependent viscosity, Figure 2.9 compares film evolution for the constant (a) and variable (b) viscosity cases. The

---

[3]Though in practice perturbations of many different wavenumbers exist, the one usually most apparent in the unstable regime is k_{m}.
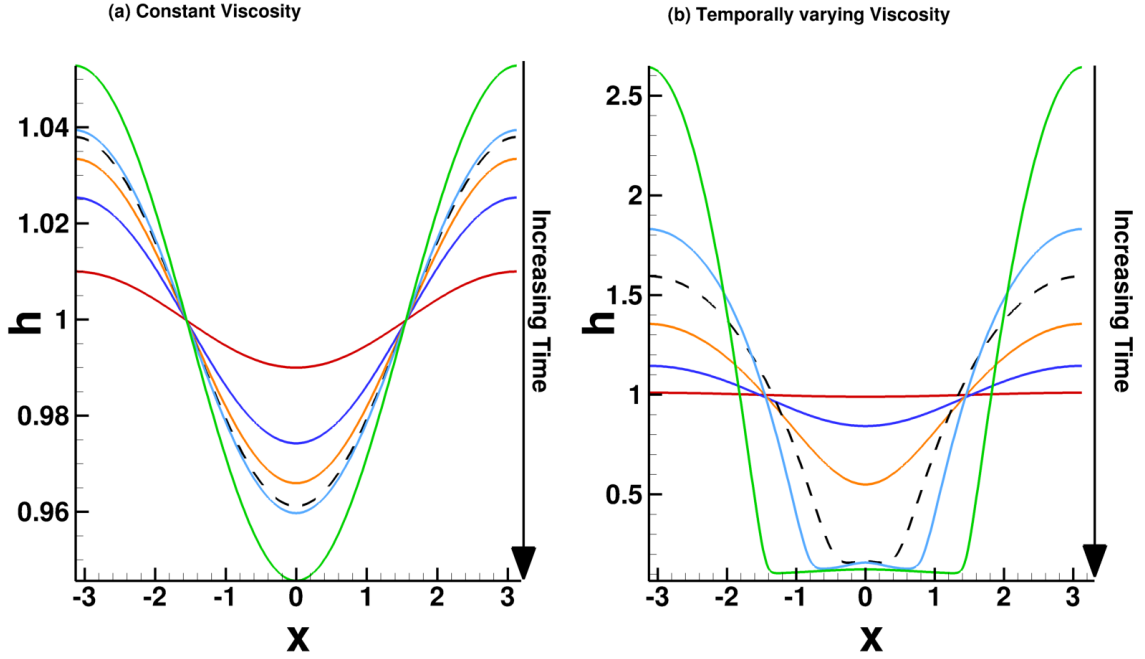
Figure 2.9 Comparison of free surface evolution $h(x,t)$ when (a) viscosity is fixed at the melting value, $\mathcal{M} = 1$, and (b) viscosity varies in time according to average temperature, $\mathcal{M}(t)$ (see Equation (2.43)). In both cases surface tension is fixed at the melting value $\Gamma = 1$, and all times plotted are prior to film re-solidification. In this and in the figures that follow, Ma $= 0$. In (a) we find that re-solidification happens before dewetting (note the vertical axis scale), while the converse is true for (b), indicating the importance of variable viscosity. The times are as follows: $t = 0$ (red), $t = 1.47$ (blue), $t = 1.75$ (orange), $t = 1.88$ (black dashed), $t = 1.92$ (light blue), $t = 2.21$ (green).

difference in film evolution is significant, with much larger instability growth rate for time-dependent viscosity.

To summarize, we have simulated and compared the results with and without the Marangoni effect, with and without time-varying surface tension, and with and without time-varying viscosity. We have found that allowing either surface tension or viscosity to depend on time through the average temperature speeds up the dewetting mechanism. In particular, varying viscosity has the strongest impact on film dynamics.

For completeness, we also consider the possible variation of viscosity with x. For model (A), since $T_{\mathrm{f}}^{(0)}(x,t)$ is a function only of the in-plane spatial variable x (and time t), we may replace $\overline{T}$ in the definition of $\mathcal{M}$ (Equation (2.43)) by $T_{\mathrm{f}}^{(0)}$, so that viscosity, which we denote in this case by $\mathcal{M}(x,t)$, depends on both space and time, namely:

$$\mathcal{M}(x,t) = \exp\left(\frac{E}{RT_{\mathrm{melt}}}\left(\frac{1}{T_{\mathrm{f}}^{(0)}(x,t)} - 1\right)\right). \tag{2.54}$$

For model (1D) on the other hand, the calculated film temperature $T_{\mathrm{f}}(x,z,t)$ depends on both spatial coordinates x and z, so obtaining an analogous model for $\mathcal{M}(x,t)$ requires some additional assumptions. We use the free-surface temperature $T_{\mathrm{f}}|_{z=h}$, so that viscosity takes the form

$$\mathcal{M}(x,t) = \exp\left(\frac{E}{RT_{\mathrm{melt}}}\left(\frac{1}{(T_{\mathrm{f}}|_{z=h})} - 1\right)\right). \tag{2.55}$$

The film thickness profiles produced in these $\mathcal{M}(x,t)$ cases (both (1D) and (A)) are similar to the $\mathcal{M}(t)$ cases shown above and are thus omitted from the main text for brevity (an example is shown in Appendix A.2). Figure 2.10 plots the average film temperature profiles for each of the models; we observe that the temperatures agree up until point **A**, at which the film dewets for variable viscosity. The inset shows that, with model (A), the variable viscosity cases ($\mathcal{M}(t), \mathcal{M}(x,t)$) lead to a
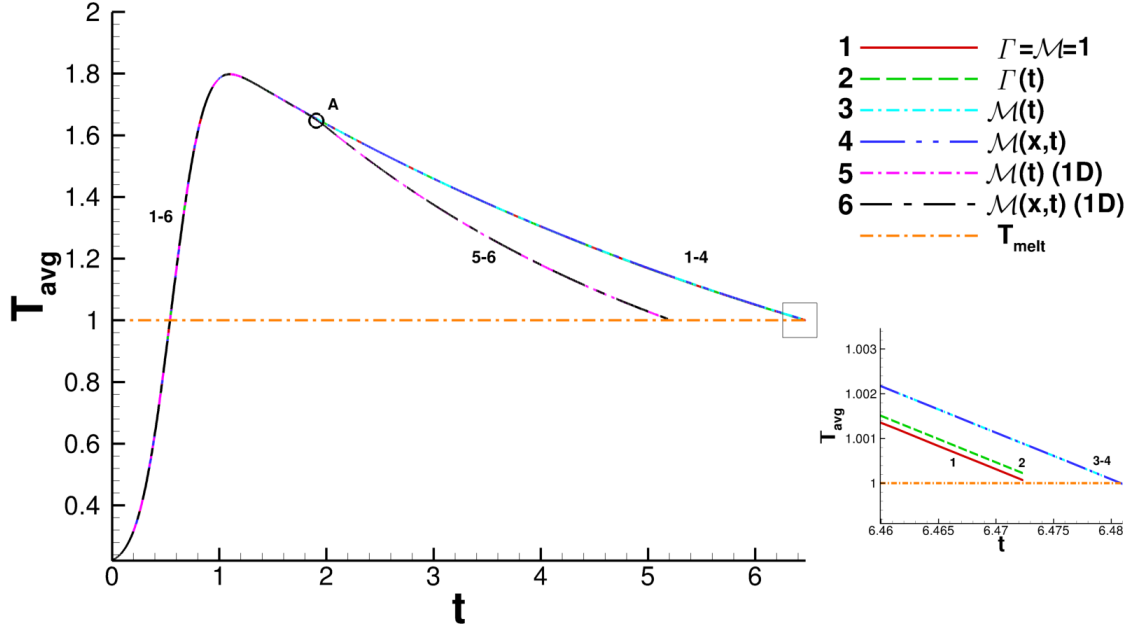
Figure 2.10 Average film temperatures with model (A): $\Gamma = 1, \mathcal{M} = 1$ (red solid line); $\Gamma(t), \mathcal{M} = 1$ (green dashed line); $\Gamma = 1, \mathcal{M}(t)$ (cyan dash-dotted line); $\Gamma = 1$, spatiotemporally-varying viscosity $\mathcal{M}(x,t)$ (blue dashed double-dotted line). Average film temperatures with model (1D): $\Gamma = 1, \mathcal{M}(t)$, (magenta dash-dotted line) and $\Gamma = 1, \mathcal{M}(x,t)$, (black dash-dotted line). In all cases the domain length is Λ_{m} from LSA. Point **A** marks the film dewetting time for the time-varying viscosity $\mathcal{M}(t)$ case. Inset: zoomed-in image of solidification point for the model (A) cases. Here, including $\mathcal{M}(t)$ or $\mathcal{M}(x,t)$ leads to a slightly longer LL than the constant viscosity ($\mathcal{M} = 1$) cases. Contrast with model (1D) where variable viscosity produces a LL that differs significantly from the rest. Simulations are marked 1-6 and placed near the curves as a guide. 1-4 were simulated with (A) and 5-6 with (1D).

slightly longer LL than if viscosity is constant, $\mathcal{M} = 1$. This may be important considering that the films dewet much nearer the resolidification time when $\mathcal{M} = 1$. This difference, however, is always small relative to that between models (A) and (1D). When viscosity varies with time and/or space, model (1D) predicts LLs that are far shorter. Furthermore, for both models the results for $\mathcal{M}(x, t)$ and $\mathcal{M}(t)$ are identical. This is, we believe, due to the film temperatures not deviating far from the respective average temperatures (even for model (1D) where x-variation of temperature is much larger than for (A), the temperature deviates from the average by at most 30%, which appears to be insufficient to cause significant differences between results for $\mathcal{M}(t)$ and $\mathcal{M}(x, t)$). We conclude, therefore, that to simulate cases where film dewetting occurs much faster than resolidification, the dependence of viscosity on average temperature is the most important effect to include.

To emphasize the importance of accurately modeling the film viscosity, we present simulation results for domains of length $20\Lambda_{\mathrm{m}}$, with films subjected to initial random perturbations according to Equation (2.53). Figure 2.11 plots film thickness for (a) $\mathcal{M} = 1$ and (b) $\mathcal{M}(t)$, both using model (A) with $\Gamma = 1$ and $\mathrm{Ma} = 0$. We again see that films with time-dependent viscosity (Figure 2.11b) dewet much faster than those with constant viscosity (Figure 2.11a). The black curve represents the solidification time of (a) (nearly the same as that for (b)), and hence represents the final configurations of both simulations. The main finding is that the $\mathcal{M} = 1$ case does not fully dewet, whereas the $\mathcal{M}(t)$ case does. This difference in dewetting time scales is consistent with the earlier results for domains of length Λ_{m}, except that there the film was completely dewetted at solidification for both cases. We note slight coarsening in Figure 2.11a,b with some droplets merging, leading to fewer than 20 resultant (primary) droplets. The film height evolution for model (1D), cases $\mathcal{M}(t), \mathcal{M}(x, t)$, and model (A) case $\mathcal{M}(x, t)$ is identical to Figure 2.11b. In the Appendix A.2, we show a case where models (1D) and (A) lead to diverging results
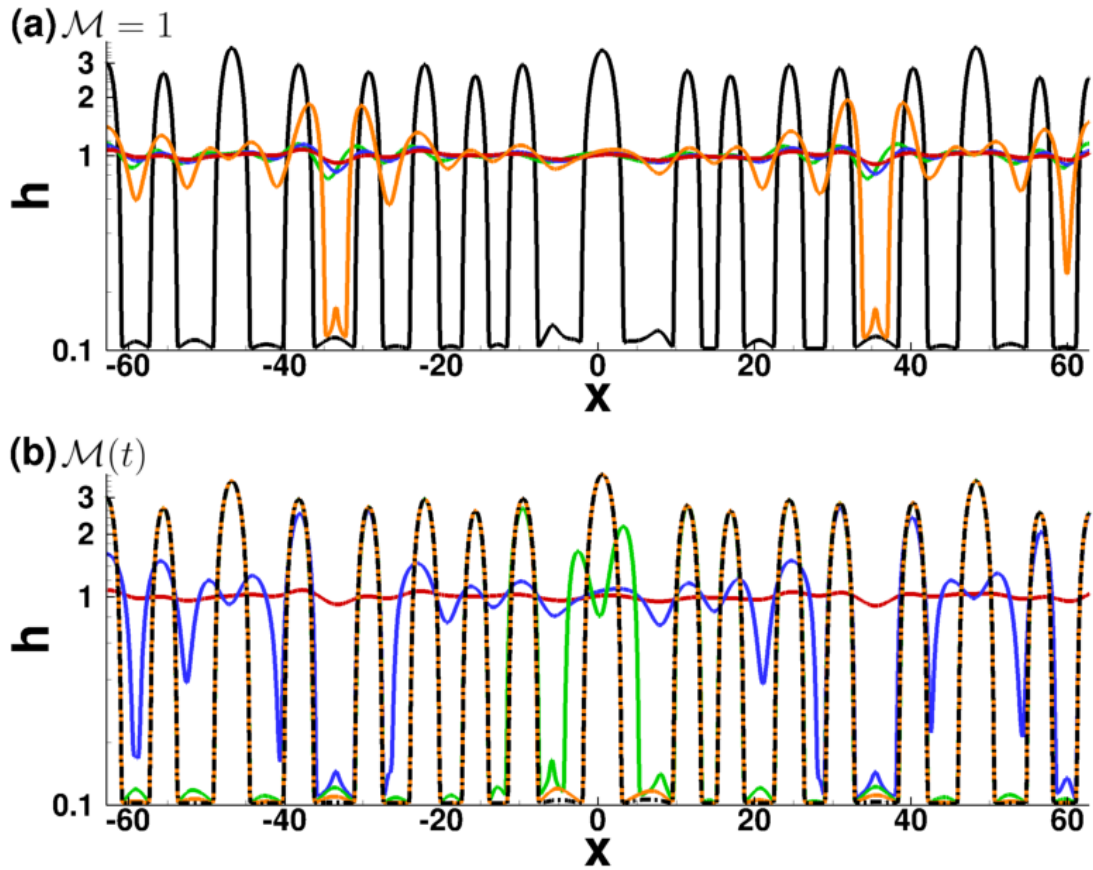
Figure 2.11 Evolution of films subject to initial random perturbations for (a) constant viscosity, $\mathcal{M} = 1$, and (b) time-dependent viscosity, $\mathcal{M}(t)$. Color code: red $t = 0$; blue $t = 1.66$; green $t = 2.30$; orange $t = 3.31$; black $t = 6.47$ (re-solidification time for (a)). The domain length was taken to be $20\Lambda_\mathrm{m}$ and all simulations were done using model (A) with $\Gamma = 1$. The h-axis is plotted on a log scale to emphasize satellite droplet formation.

46

(for a different choice of parameters). We omit the temperature profiles here as the short LL for (1D) and identical $\mathcal{M}(t)$ and $\mathcal{M}(x,t)$ results are consistent with the results on domain length Λ_m.

To summarize the results on long domains of length $20\Lambda_m$, we have found that including the time-dependence of viscosity permits the films to fully dewet in the span of the liquid lifetime whereas keeping viscosity fixed at the melting temperature value ($\mathcal{M} = 1$) produces films that dewet only partially during the liquid phase. Any effects due to spatial variation of viscosity appear to be irrelevant here. Finally, the liquid lifetime is much shorter for model (1D) than model (A), as expected.

2.5   Conclusions

To conclude this chapter, we have formulated three models for heat conduction in nanoscale thin films on thermally conductive substrates: a full model (F) that accounts for heat conduction in all directions in both film and substrate; an asymptotically-reduced model (A) that exploits a disparity in length scales in both film and substrate to derive an equation governing in-plane diffusion of heat within the film coupled to out-of-plane heat diffusion in the substrate; and a one-dimensional model (1D) model that simply neglects any in-plane diffusion in both film and substrate. In all cases a thin film model is used to describe the associated fluid dynamics. The main finding is that including in-plane diffusion in the thermal modeling influences strongly the film evolution. In particular, neglecting in-plane diffusion is found to amplify (artificially) in-plane thermal gradients and expedite film cooling. We have found that model (A) is significantly more accurate than (1D) while being considerably more computationally efficient than (F). We have also found that when material parameters are allowed to vary in time through the average film temperature, model (A) produces liquid lifetimes significantly longer than those of

model (1D), due to the absence of lateral heat conduction in (1D). Therefore model (A) combines both accuracy and efficiency.

With regard to the individual (dimensionless) material parameters that arise in our models, Ma (Marangoni number), Γ (surface tension parameter) and $\mathcal{M}$ (film viscosity), we find that the variation of viscosity with time has the greatest effect on model outcomes. By including time-dependent viscosity, films exposed to laser heating (on both small and large domains) fully dewet while in the molten state. In contrast, when viscosity is held constant, dewetting occurs much later in the cooling process, which may result in partial droplet formation only. This suggests strongly that time-dependent viscosity is needed to represent accurately experiment-like behavior. Using a spatiotemporally varying viscosity, $\mathcal{M}(x,t)$, produces essentially identical results to the case where viscosity depends only on time. Introducing time dependence of the surface tension ($\Gamma(t)$) has a larger effect on the film instability growth rate (increasing it) than does the Marangoni effect (Ma $\neq 0$), though the effect is always small, and insignificant when compared to the variation of viscosity with time. The Marangoni effect was found to be negligible in all cases considered.

Although model (A) is found to be useful in the current setting, its validity relies on a number of underlying assumptions. Therefore, its applicability to other problems must be carefully verified prior to use. In this chapter, we have considered the time and space variation of only selected physical parameters (surface tension and viscosity) through temperature, and have not considered how temperature dependence of other material parameters, such as thermal conductivity and density, may influence the results. Furthermore, all simulations presented here are restricted to the two-dimensional geometry: much more significant computational benefit of model (A) is expected in three spatial dimensions (3D). In Chapter 3, we will extend model (A) to include thicker substrates and temperature-varying thermal conductivity, as well as present simulations in 3D.

CHAPTER 3

MODELING SUBSTRATE THERMAL EFFECTS IN THE DEWETTING OF NANOSCALE THIN FILMS

3.1 Overview

We consider metal films of nanoscale thickness, deposited on a much thicker substrate and melted by an external laser heat source. Our primary focus is on the influence of the underlying substrate on the temperature and the evolution of the film. We consider the influence of substrate thickness, H_s, the rate of heat loss in the substrate (characterized by a Biot number, Bi), and nonlinear effects due to temperature-dependent thermal conductivity. We show that a balance between absorption and heat loss in the substrate separates the $(H_\mathrm{s}, \mathrm{Bi})$ parameter space into two regions, where the maximum (spatially-averaged) film temperature, T_peak, is either positively or negatively correlated to substrate thickness depending on the size of Bi. Using an in-house 3D GPU code that solves the governing partial differential equations, we simulate both film evolution and heat conduction on large domains. We find that including the temperature dependence of substrate thermal conductivity in the model decreases T_peak, modulating film viscosity and hence the dewetting speed, leading to (in some cases) partial drop formation only. The rate of heat lost in the substrate is found to influence peak temperatures and liquid lifetimes more strongly than substrate thickness (H_s). Nevertheless, changes in both Bi and H_s can lead to films that solidify in place prior to full dewetting due to the strong dependence of film viscosity on temperature.

3.2 Introduction

This work explores the role of thermal effects in the dynamics of thin films on the nanoscale, which has become increasingly important in nanotechnology [54], electronic

coatings [147], and photovoltaics [8], as well as numerous other applications. Thin film dynamics is well-studied, with a diverse range of applications including liquid crystals, paint drying, and the flow of lava (see the review by Craster & Matar [27]). A particular challenge can be to model external effects that couple to the fluid dynamics of the film. For example, certain studies have investigated the influence of an electric field on the dynamics of thin liquid films [23, 93, 137], the competition between chemical instabilities in multi-mixture liquids and their dewetting [5, 32, 46, 96, 133], and even the effect of permeable underlying substrates [28, 146]. The modeling of thermal effects in nanoscale thin films has received an increasing share of attention, in particular in the context of the pulsed laser irradiation of liquid metal films deposited on thermally conductive substrates [7, 39, 118, 119, 124, 135], inspired by a number of potential applications (*e.g.*, arrangements of liquid metal droplets may be used as a catalyist for growing carbon nanowires [54]). Numerous experimental works have investigated the assembly mechanism of droplets that result from liquified metal films [78, 79, 144]. From a mathematical perspective, accurate modeling and simulation of such effects is challenging since one must account for phase changes, temperature dependence of material parameters, and substrate effects.

Recently, we developed a novel thermal model for a thin molten metal film evolving on a thin substrate that accounts for many of these effects and their influence on film evolution [3]. We used long wave theory (LWT) to develop a consistent model for the coupled fluid/thermal dynamics. A key finding was that to leading order, film temperature is uniform across the film thickness, with spatial and temporal evolution governed by an in-plane diffusion equation with additional terms accounting for the laser heating and heat loss to the substrate. Neglecting in-plane diffusion in the film [33, 124, 135] leads to inaccurate results for heat transport and may shorten liquid lifetimes. A second focus of the work by Allaire *et al.* [3] was on the influence of temperature-dependent surface tension and viscosity on the dewetting of the films.

It was found that including temperature-varying viscosity is crucial for accurately simulating films that dewet during the liquid phase. Although the dynamics of the film were coupled to the thermal transport in the substrate, the study was limited to asymptotically thin substrates, and the influence of substrate physical characteristics on film temperature and fluid dynamics remains to be addressed, especially since in practice, substrates may be much thicker than the metal film.

Many other authors have developed thermal models in the present context. Shklyaev *et al.* [126], for example, used LWT to derive a model similar to that provided in our previous work [3], but omitting laser heating. There, the underlying substrate, due to the assumed difference in thermal conductivities of substrate and film, is modeled simply by a constant temperature gradient rather than solving for the temperature self-consistently. Batson *et al.* [10] found that self-consistently solving for substrate temperature is crucial for the development of oscillatory free surface film instabilities, which have been previously observed, for example, when thermocapillary effects are present in multi-layer film configurations [11] and when the film is heated from below by a sufficiently low conductivity substrate [126]. Atena & Khenner [7] developed a model for liquid metals that accounts for heat transport in the substrate as well as laser heating, but considers heat loss at the film surface to be relevant (see also work by Oron [102] and Saeki *et al.* [118, 119] in this context), leading to differences with the model of Allaire *et al.* [3]. In contrast, other works assume heat loss to the substrate to dominate over any free surface losses [33, 135]. Many authors have investigated the significance of temperature-dependent material parameters. Viscosity, for example, is often modeled by an Arrhenius dependence [102, 124, 135] on temperature. Allaire *et al.* [3] showed that it is sufficient to use the spatially-averaged film temperature in the Arrhenius definition of viscosity. Trice *et al.* [135] explicitly modeled temperature dependence of a number of other material parameters for the film, but did not consider the variation of substrate parameters, such as thermal

conductivity, with temperature. Regarding substrate thermal conductivity, little is known about its value at high temperatures, but a cubic dependence on temperature is found to provide a good fit to experimental data at low temperatures [73]. Following Combis *et al.* [26], the approach used in the present work is to define a thermal conductivity that utilizes this cubic relationship at low temperatures, supplemented with manufacturer data [60] at higher temperatures.

Our focus in this work is to investigate the role that the underlying substrate has on both the heating of the film and its free surface evolution. In particular, we focus on the role of substrate thickness, heat loss through the lower substrate boundary, and nonlinear effects due to temperature varying thermal conductivity. The thermal model developed in our earlier work (asymptotically thin substrates, constant thermal properties) [3] is extended to account for thick substrates that have temperature-dependent thermal conductivity. Similarly, temperature variation of surface tension and viscosity are also included, but Marangoni effects are neglected since these were demonstrated to be very weak [3].

The remainder of the chapter is organized as follows. In Section 3.3, we present the thin film equation governing the fluid dynamics and the extension of the thermal model developed previously [3]. The main results are presented in Section 3.4. In Section 3.4.1 we outline the numerical scheme used to solve our models. In Section 3.4.2, we present results that highlight effects due to thermal transport only, in the absence of film evolution (the film surface is held flat and static even when above melting temperature); in particular the correlation between peak film temperatures and substrate thickness, as the heat loss from the substrate varies (via tuning the Biot number, Bi). In Section 3.4.3 we consider evolving 2D films and investigate the influence of thermal effects on the film dynamics. In Section 3.4.4, we present large-scale 3D numerical results for both film evolution and heat conduction. The main finding is that in both 2D and 3D the substrate heat loss, thickness, and

thermal conductivity temperature dependence may influence the final solidified film configuration, and depending on their values, films may either dewet fully or only partially by the time they resolidify. In Section 3.5, we present the conclusions and directions for future work.

3.3   The Model

Consider a metal film of nanoscale thickness, H, and characteristic lateral length-scale L, which is initially solid and in contact (at $z = 0$) with a thermally conductive solid SiO_2 substrate, with thickness H_s that may be much larger than that of the film (for our setup we consider substrates at least 5 times thicker than the film). The whole assembly is placed upon another, thicker, slab of Si. The metal film is heated by a laser and may change phase (solid to liquid and vice-versa). The basic setup is sketched in Figure 3.1. We define the aspect ratio of the film to be $\epsilon = H/L \ll 1$. For clarity we list a number of underlying assumptions:

- the film has free surface, $z = h(x, y, t)$ and is thin, $\epsilon \ll 1$;

- inertial effects are negligible;

- liquid-solid interactions are relevant and can be modeled by a disjoining pressure;

- the laser energy is absorbed volumetrically in the film, but the substrate is optically transparent;

- the film is in perfect thermal contact with the SiO_2 substrate at $z = 0$;

- heat loss in the film is only through the substrate and not through radiative losses;

- the underlying SiO_2 substrate is thick relative to the film, $H/H_s \ll 1$;

- the Si slab underneath the SiO_2 is a perfect conductor so that it remains at ambient temperature (this is reasonable since its thermal conductivity is much larger than that of SiO_2) but there is contact resistance at the interface $z = -H_s$;

- the surface tension and viscosity of the film as well as the thermal conductivity of the substrate may vary with temperature; and

- the film does not evaporate.
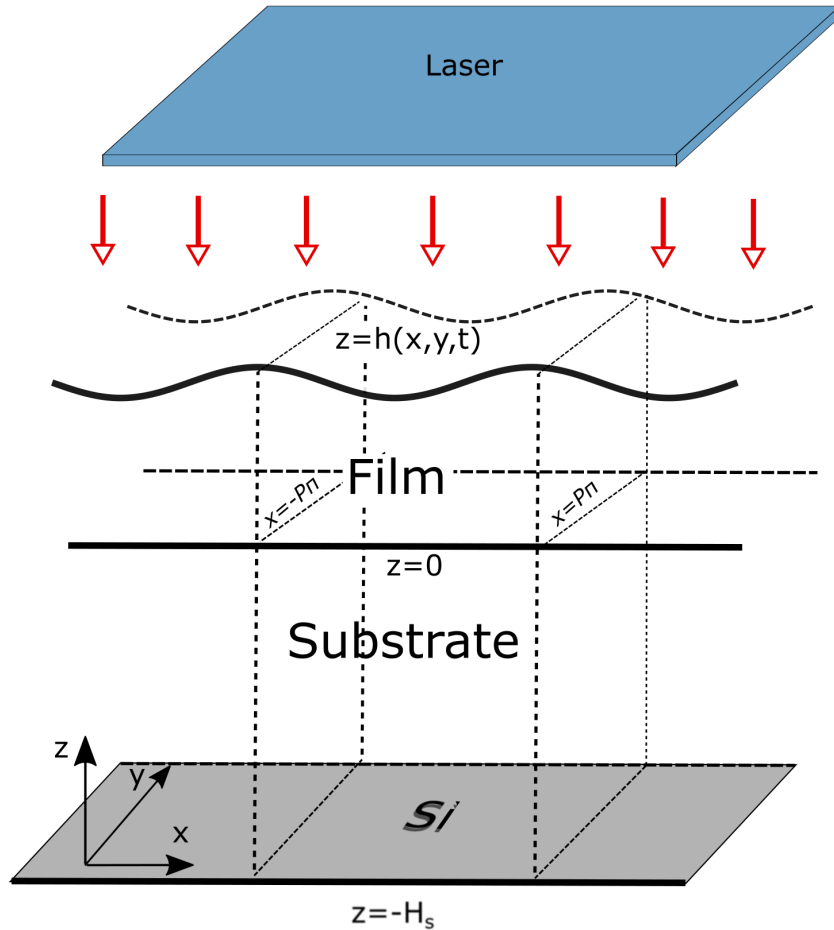
Figure 3.1 Schematic of a three-dimensional (3D) film with free surface $z = h(x, t)$, deposited on a substrate that may be much thicker than the film and is in contact with an even thicker Si slab underneath.

We refer to the in-plane coordinates as x, y and the out-of-plane coordinate as z and define the in-plane and out-of-plane length scales as L and H, respectively. Following our earlier work [3], we choose the in-plane velocity scale $U = \epsilon^3 \gamma_{\mathrm{f}}/(3\mu_{\mathrm{f}})$ (where γ_{f} and μ_{f} are surface tension and viscosity at melting temperature, T_{melt}) so that the time scale, L/U, is comparable to the duration of the laser pulse, but the model also retains surface tension effects to leading order in ϵ. Subsequently,

we choose ϵU, T_{melt}, $\mu_{\text{f}} U/(\epsilon^2 L)$ and γ_{f} as the out-of-plane velocity, temperature, pressure, and surface tension scales, respectively. We take the domain length/width to be $2P\pi$, where P is a positive integer. In what follows, the words two-dimensional and three-dimensional, are referred to as 2D and 3D, respectively.

We treat the film as an incompressible Newtonian fluid, assume that the viscosity and surface tension may vary in time through the average film temperature (details to be specified below; in Appendix A.11 we consider spatial dependence as well), but fix material density and heat capacity at their melting temperature values. Since our focus is on substrate effects we also assume the film thermal conductivity is fixed at the melting temperature value. However, for thick substrates, large temperature gradients could lead to significant differences in thermal conductivity across the depth. Therefore, we allow thermal conductivity of the substrate to vary with temperature and use its value at ambient temperature, k_{s}, as the thermal conductivity scale. For what follows we use T_{f} and T_{s} to denote the temperatures of the film and substrate, respectively. We assume that surface tension depends linearly on average temperature, to leading order, and is given by:

$$\Gamma = 1 + \frac{2\text{Ma}}{3}(T_{\text{avg}} - 1), \tag{3.1}$$

where the Marangoni number Ma and time-dependent average free surface temperature, $T_{\text{avg}}(t)$, are given by

$$\text{Ma} = \frac{3\gamma_{\text{T}} T_{\text{melt}}}{2\gamma_{\text{f}}}, \qquad T_{\text{avg}}(t) = \frac{1}{(2N\pi)^2} \int_{-N\pi}^{N\pi} \int_{-N\pi}^{N\pi} T_{\text{f}} \, \mathrm{d}x \mathrm{d}y. \tag{3.2}$$

Here, $\gamma_T = (\gamma_{\text{f}}/T_{\text{melt}})\mathrm{d}\gamma/\mathrm{d}T_{\text{avg}}|_{T_{\text{avg}}=1}$ is the change in surface tension with temperature when the film (on average) is at melting temperature, $T_{\text{avg}} = 1$. For the remainder of the text we omit the argument of $T_{\text{avg}}(t)$ with the understanding that it is dependent on time. It should be noted that more general expressions for surface tension exist that account for spatial variation of temperature (Marangoni effect). It has been

shown, however, that the Marangoni effect has little influence on film evolution in the present context and thus we omit spatial dependence of Γ [3].

We follow the long-wave theory approach [27] adopted in our earlier work [3], which reduces conservation of mass and momentum to a 4th order nonlinear PDE for film thickness, h, written in the general form $\partial_t h + \boldsymbol{\nabla}_2 \cdot (h\bar{\mathbf{u}}) = 0$, where $\boldsymbol{\nabla}_2 = (\partial_x, \partial_y)$ is the in-plane gradient, and $\bar{\mathbf{u}} = (u, v)$ is the depth-averaged in-plane fluid velocity, related to the pressure gradient. For the remaining text, vector quantities are in bold and scalar quantities are not. We assume that the pressure at the interface, $z = h$, is given by a modified Laplace-Young type boundary condition, which includes both free surface curvature and also liquid-solid interactions, modeled by a disjoining pressure $\Pi(h)$. Although various forms of $\Pi(h)$ have been proposed [85], we use

$$\Pi(h) = \mathrm{K} \left[\left(\frac{h_*}{h} \right)^n - \left(\frac{h_*}{h} \right)^m \right], \qquad \mathrm{K} = \frac{A_\mathrm{H} L}{6\pi\epsilon\gamma_\mathrm{f} h_*^3 H^3}. \qquad (3.3)$$

In Equation (3.3) the terms on the right-hand side represent the repulsive and attractive components; h_* is the equilibrium film thickness, where the attraction and repulsion balance; A_H is the Hamaker constant [52]; and $n > m$ are positive exponents. In this manuscript, we use $(n, m) = (3, 2)$ following Gonzalez $et\ al.$ [52], who showed that this exponent pair is appropriate for liquid metals. The thin film equation can then be written as

$$\partial_t h + \boldsymbol{\nabla}_2 \cdot \left[\frac{1}{\mathcal{M}} \left(h^3 \boldsymbol{\nabla}_2 \left(\Gamma \boldsymbol{\nabla}_2^2 h + \Pi(h) \right) \right) \right] = 0, \qquad (3.4)$$

where $\mathcal{M} = \mu/\mu_\mathrm{f}$ is the dimensionless viscosity, assumed to vary exponentially with average temperature via an Arrhenius law,

$$\mathcal{M}(t) = \exp \left(\frac{E}{RT_\mathrm{melt}} \left(\frac{1}{T_\mathrm{avg}} - 1 \right) \right), \qquad (3.5)$$

where $R = 8.314 \mathrm{JK}^{-1}\mathrm{mol}^{-1}$ is the universal gas constant, and E is the activation energy [49]. Other approaches have been used to implement temperature dependence

of viscosity; see for example, the work of Craster & Matar [27] for an alternate form in the context of thin films, or that of Kaptay [69] for a comparison of Arrhenius and statistical mechanics approaches, or Oron [103], who derives an analog of Equation (3.4) that includes z-dependence of viscosity. We follow the approach of Seric *et al.* [124] in utilizing the Arrhenius expression Equation (3.5), but we use average film temperature and thus omit spatial dependence of viscosity (which has been shown to lead to essentially identical results to those obtained using spatially dependent viscosity [3]). Following the time derivative term in Equation (3.4), the terms (from left to right) represent the capillary and disjoining pressure terms, respectively.

Equation (3.4) describes the evolution of the nanoscale thin film, which is coupled to its temperature. The temperature is determined using a similar approach to that of our previous work [3], where a thin substrate was assumed to allow for an asymptotic reduction of the heat flow problem in both film and substrate regions. We assume (i) the film is heated volumetrically by a laser, but the SiO_2 substrate is transparent, (ii) heat conduction in the film is much faster than the evolution of the film, (iii) substrate heat conduction and film evolution occur on similar timescales, and (iv) film heat loss is only through the SiO_2 substrate, which is in perfect thermal contact with the film, and itself loses heat to an underlying Si substrate of much higher thermal conductivity. To extend our previous work we present a formulation that includes temperature-varying thermal conductivity in the substrate, $k(T_s)$ ($k(T_a) = 1$ represents dimensionless thermal conductivity at ambient temperature). Furthermore, we now consider the substrate to be thick, but with negligible in-plane diffusion (in Appendix A.6, we show this assumption to be valid). The leading order film temperature is found to be independent of z and the model

describing the transport of heat in the film/substrate system is then [3]

$$h\mathrm{Pe}_\mathrm{f}\partial_t T_\mathrm{f} = \nabla_2 \cdot (h\nabla_2 T_\mathrm{f}) - \mathcal{K}\left(k(T_\mathrm{s})\partial_z T_\mathrm{s}\right)|_{z=0} + h\overline{Q}, \qquad \text{for} \quad z \in (0, h), \qquad (3.6)$$

$$\mathrm{Pe}_\mathrm{s}\partial_t T_\mathrm{s} = \partial_z \left(k(T_\mathrm{s})\partial_z T_\mathrm{s}\right), \qquad \text{for} \quad z \in (-H_\mathrm{s}, 0), \quad (3.7)$$

$$T_\mathrm{f} = T_\mathrm{s}, \qquad \text{on} \quad z = 0, \qquad (3.8)$$

$$k(T_\mathrm{s})\partial_z T_\mathrm{s} = \mathrm{Bi}\left(T_\mathrm{s} - T_\mathrm{a}\right), \qquad \text{on} \quad z = -H_s, \qquad (3.9)$$

$$\partial_x T_\mathrm{f} = 0, \qquad \text{on} \quad x = \pm P\pi, \qquad (3.10)$$

$$\partial_y T_\mathrm{f} = 0, \qquad \text{on} \quad y = \pm P\pi, \qquad (3.11)$$

where the dimensionless parameters defined by

$$\mathrm{Pe}_\mathrm{f} = \frac{(\rho c)_\mathrm{f} \, UL}{k_\mathrm{f}}, \qquad \mathrm{Pe}_\mathrm{s} = \frac{(\rho c)_\mathrm{s} \, U\epsilon H}{k_\mathrm{s}}, \qquad \mathcal{K} = \frac{k_\mathrm{s}}{k_\mathrm{f}}\epsilon^{-2}, \qquad \mathrm{Bi} = \frac{\alpha_\mathrm{s} H}{k_\mathrm{s}},$$

are the film and substrate Peclet numbers, thermal conductivity ratio, and Biot number, respectively. Following the time derivative in Equation (3.6), the terms from left to right represent lateral diffusion, film heat loss due to contact with the substrate, and the laser heat source, respectively. Equation (3.7) reflects the assumption that heat flow in the substrate is affected by out-of-plane diffusion only. Since the substrate thickness may actually be comparable in size to the domain length, dropping lateral substrate diffusion is not necessarily a consequence of the leading order approximation of heat conduction in ϵ, but rather an assumption, justified later in Appendix A.6 by showing that in-plane derivatives of substrate temperature are orders of magnitude smaller than those in the out-of-plane direction. Equation (3.8) represents continuity of film/substrate temperatures and the nonlinear boundary condition in Equation (3.9) represents heat loss from the $\mathrm{SiO_2}$ substrate to the underlying Si slab, assumed to be at ambient temperature, T_a. Values of the heat transfer coefficient, α_s, in the definition of Bi are difficult to find in the literature so in this work we consider Bi to be a variable parameter within the range given in

Table 3.1. The lateral boundaries are thermally insulated (see Equation (3.10) and (3.11)). The above model assumes that radiative losses are negligible relative to heat loss to the substrate. By a simple energy argument, we find that the time scale on which radiative losses are relevant is on the order of milliseconds, orders of magnitude longer than the time scales considered here; see Appendix A.8 for more details.

We assume the film-averaged heat source, $\overline{Q}$ in Equation (3.6), representing external volumetric heating due to the laser at normal incidence, is given by [124, 135],

$$\overline{Q} = \frac{1}{h} \int_0^h F(t) \left[1 - R(h)\right] \exp\left[-\alpha_{\mathrm{f}} \left(h - z\right)\right] dz, \tag{3.12}$$

$$F(t) = C \exp\left[-\left(t - t_{\mathrm{p}}\right)^2 / (2\sigma^2)\right], \quad C = \frac{E_0 \alpha_{\mathrm{f}} L^2}{\sqrt{2\pi}\sigma t_{\mathrm{s}} H k_{\mathrm{f}} T_{\mathrm{melt}}},$$

where C is a constant proportional to the laser fluence, E_0, the (scaled) absorption length for laser radiation in the film is given by α_{f}^{-1}, and the temporal shape of the laser, $F(t)$, is taken to be Gaussian centered at t_{p} and of width $\sigma = t_{\mathrm{p}}/(2\sqrt{2\ln 2})$. For the reflectivity of the film, $R(h)$, we follow Trice *et al.* [135] and assume

$$R(h) = r_0 \left(1 - \exp\left(-\alpha_{\mathrm{r}} h\right)\right),$$

where r_0 and α_{r} are dimensionless fitting parameters, specified in Table A.3.

Table 3.1 Dimensionless Parameters Based on Material parameters in Table A.3

Dimensionless Numbers	Notation	Value	Expression
Aspect Ratio	ϵ	0.347	H/L
Film Peclet Number	$\mathrm{Pe_f}$	1.42×10^{-3}	$(\rho c)_\mathrm{f} U L / k_\mathrm{f}$
Substrate Peclet Number	$\mathrm{Pe_s}$	2.17×10^{-2}	$(\rho c)_\mathrm{s} U \epsilon H / k_\mathrm{s}$
Biot Number	Bi	$10^{-3} - 10^{3}$	$\alpha H / k_\mathrm{s}$
Thermal Conductivity Ratio	$\mathcal{K}$	0.034	$k_\mathrm{s}/(\epsilon^2 k_\mathrm{f})$
Range of Dimensionless Viscosity	$\mathcal{M}$	$0.028 - 1$	μ/μ_f

3.4 Results

After outlining our numerical approach in Section 3.4.1, we consider 2D films with free surface $z = h(x,t)$ in Section 3.4.2 and Section 3.4.3, focusing on the influence of substrate thickness, Biot number, and variable substrate thermal conductivity. In Section 3.4.4 we expand our consideration to 3D films with free surface $z = h(x,y,t)$.

3.4.1 Numerical Schemes

In the 2D case, Equation (3.4) for $h(x,t)$ is solved using the approach of our earlier work [3], with spatial discretization commensurate with the precursor thickness, $\Delta x = h_* = 0.1$. Equation (3.4) can be rewritten as $\partial_t h + \partial_x J = 0$ for some flux J, and a Crank-Nicolson scheme is used for the time-stepping, turning Equation (3.4) into a nonlinear system of algebraic equations

$$\frac{h_i(t + \Delta t) - h_i(t)}{\Delta t} = \frac{1}{2} D_i(t + \Delta t) + \frac{1}{2} D_i(t), \quad i = 1, 2, \ldots, N, \tag{3.13}$$

where $h_i(t) \approx h(x_i, t)$, $\{x_i\}$ is a N-point spatial discretization, and D_i is a discretization of $\partial_x J$, at x_i. Although any iterative method for solving nonlinear

equations would suffice to solve Equation (3.13), we use Newton's method; since Equation (3.13) must be solved at each time-step, the rapid quadratic convergence ensures faster computing times. The initial condition takes the form of a small perturbation to a flat film $h = h_0$,

$$h(x, 0) = h_0 \left(1 + \delta \cos\left(x\right)\right), \tag{3.14}$$

where $h_0 \delta$ is the perturbation amplitude ($|\delta| \ll 1$), and the wavelength of the perturbation is equal to the domain length, 2π (see Table A.3 for the physical sizes).

A similar approach is used to solve Equation (3.7) for the substrate temperature T_s, while for the film temperature, T_f in Equation (3.6), an implicit-explicit methodology is used (see the appendix of Allaire *et al.* [3] for more details). The film and substrate are initially fixed at room temperature,

$$T_f(x, 0) = T_s(x, z, 0) = 0. \tag{3.15}$$

During the initial laser heating both film and substrate temperatures are found by solving Equations (3.6)–(3.7) with the film flat and static until it melts, which we take to be the time at which the minimum film temperature (over space) surpasses T_{melt}. Film evolution, film temperature, and substrate temperature are then sequentially found at each time step (see Appendix A.12 for more details on the procedure). Once the minimum film temperature decreases past T_{melt} the film is considered solid. After this time, only film and substrate temperatures are solved for; we no longer evolve the free surface, which is frozen in what we refer to as its final configuration.

A successful time iteration requires that two criteria are met for both film evolution and heat conduction: (i) the iterative method should converge to a relative error tolerance of 10^{-9} in fewer than 10 iterations; and (ii) the relative truncation error should be less than 10^{-3}. If either (i) or (ii) are not satisfied, the time step

is decreased and the equations are integrated again for that time. For more details regarding the 2D numerical scheme see Appendix A.12.

For the 3D simulations, one needs to be careful with the choice of the initial condition, so as to produce a surface $h(x, y, 0)$ with perturbations that are uncorrelated (between the x and y directions) and that excite a significant number of Fourier modes (note that using simply a sum or a product of sines and cosines with random amplitudes produces noise that is not random). Here we follow in spirit the approach of Lam *et al.* [81] [1]. The approach described in Appendix A.14 defines the perturbation $\eta(x, y)$, which is then used to define the initial condition by

$$h(x, y, 0) = h_0 \left(1 + \delta \eta(x, y)\right) \tag{3.16}$$

where, as in the 2D case, $\delta = 0.01$.

Equation (3.4) is written as $\partial_t h + \boldsymbol{\nabla}_2 \cdot \mathbf{J} = 0$, with flux $\mathbf{J}$, and solved for $h(x, y, t)$ using the methodology of Lam *et al.* [81], in which an alternating-direction implicit (ADI) method is combined with the Newton iterative method described above (D_i, h_i in Equation (3.13) are now replaced by $D_{i,j}, h_{i,j}$). Equation (3.6) is now solved using an implicit-explicit ADI approach, which consists of a predictor and corrector step. Equation (3.7) is solved similarly to the 2D case, except now $T_s = T_s(x, y, z, t)$. Due to the dependence on three spatial variables, this equation alone amounts to a system of a significant number of discrete nonlinear equations to be solved at each time-step. Similarly, Equations (3.4) and (3.6) lead to large discrete systems, which present a daunting computational challenge. To enhance computational performance the equations are solved in parallel using the Compute Unified Device Architecture (CUDA) programming framework [99] developed by NVIDIA®, which utilizes graphics processing units (GPUs). Lam *et al.* [81] showed that GPUs offer significant computational advantages over traditional (CPU) computing, especially

---

[1]Note that the formulation of Lam *et al.* [81] includes a few typos, which are fixed in the current formulation of the initial condition.

when large domains are considered. The parallel numerical schemes used for heat conduction are described in Appendix A.13.

3.4.2 Flat Film Results - Influence of Substrate Thickness, Biot Number, and Thermal Conductivity

In this section, we suppress dewetting in the molten film and consider the static flat film $h = h_0$, focusing on the influence of substrate properties on film temperature. In particular, we analyze the influence of (i) the substrate thickness, (ii) the substrate heat loss, and (iii) nonlinear effects due to temperature-dependent thermal conductivity in the substrate (compared with constant thermal conductivity, $k = 1$). For more details on the model used for temperature dependent thermal conductivity, see Appendix A.7. In the following discussion we focus on two quantities: peak film temperature, T_{peak} (the maximum spatially-averaged film temperature attained by the film over the duration of the simulation), and the liquid lifetime (LL) of the film, defined as the time interval during which the average film temperature remains above melting ($T_{\text{avg}} > 1$).
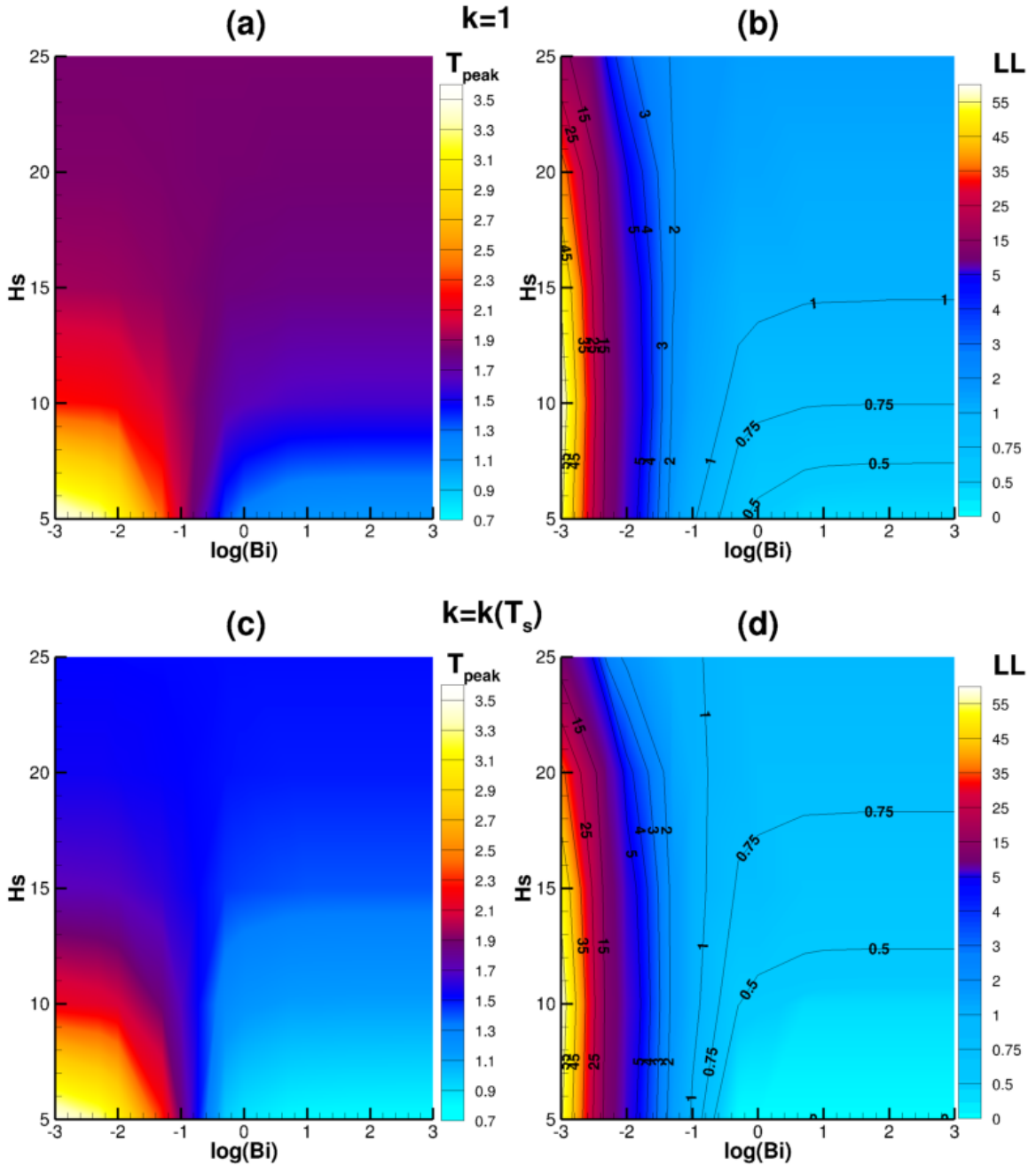
Figure 3.2 Phase plane plots for the film peak temperature, T_{peak} and liquid lifetime (LL). Here surface tension and viscosity are fixed at the melting temperature values, $\Gamma = \mathcal{M} = 1$. (a,c) T_{peak} for thermal conductivity fixed at room temperature ($k = 1$), or temperature dependent, $k = k(T_{\text{s}})$. (b,d): corresponding results for LL. Log base 10 is used on the horizontal axes and the color bars for (b,d) are nonuniform.

Figure 3.2(a) and (b) show contour plots of T_{peak} and LL, respectively, for various values of substrate thickness H_{s} and Biot numbers, Bi; see Equation (3.9).

A zero Biot number corresponds to a perfectly insulated substrate that loses no heat to the underlying Si slab, while $Bi \to \infty$ corresponds to a poorly insulated substrate in contact with a Si slab at ambient temperature, T_a (in Equation (3.9) this corresponds to a Dirichlet boundary condition, $T_f = T_a$). In Figure 3.2(a) we see that films on well-insulated substrates ($Bi \ll 1$) retain more heat and reach higher peak temperatures than those on their poorly-insulated counterparts ($Bi \gg 1$). In Figure 3.2(b) this corresponds to longer LLs for $Bi \ll 1$. Furthermore, we see little variation in T_{peak} in the range $Bi \in [1, 10^3]$, which manifests in Figure 3.2(b) as near-horizontal constant LL contour lines in this range, compared to those in the remaining range of Bi where LL varies significantly. Between $Bi = 10^{-1}$ and $Bi = 1$ there is a sharp transition in peak temperature and LL. This is primarily due to the changing balance between the heating of the substrate and the heat loss from the substrate (there is perfect thermal contact at the film–substrate interface, and since radiative losses are neglected no heat is lost at the film's free surface). For perfectly insulating substrates, heat is retained in the substrate (and thus the film, due to the perfect thermal contact) more so than in the poorly insulating case, where the film rapidly loses heat to a near-room-temperature substrate.

The influence of substrate thickness is also significant, and depends strongly on the value of Bi. For well-insulated substrates ($Bi \ll 1$), peak average film temperature decreases with increasing H_s, while for poorly-insulated substrates ($Bi \gg 1$) peak temperature increases with H_s. This is again due to the competition between the absorption of heat in the substrate and the heat loss at the lower boundary, $z = -H_s$. For $Bi \ll 1$, thicker substrates absorb more energy per unit volume and transfer less heat back to the film, as more heat can be distributed throughout (see Appendix C, movie1). For $Bi \gg 1$, substrate heat loss is rapid and the farther the $z = -H_s$ interface is from the film, the less heat is lost in the film (see Appendix C, movie2). Therefore, in this case thicker substrates yield higher film peak temperatures. Note

that in Figure 3.2(b) the LL scale is nonuniform and the LL varies with substrate thickness even for $\text{Bi} < 10^{-1}$. Liquid lifetime is, in general, positively correlated with peak temperature, despite differences in cooling. Furthermore, peak temperatures are similar for substrates thicker than $H_\text{s} = 20$ (beyond this value the substrate effectively behaves as one of infinite depth). The analytical solution for $H_\text{s} \to \infty$ is given in Trice *et al.* [135] and Seric *et al.* [124]; in Appendix A.9 we demonstrate the convergence of our results to theirs as H_s increases.

Figure 3.2(c) and (d) show peak average film temperatures and LL, respectively, for the substrate whose thermal conductivity varies with temperature according to Equation (A.6). The trend of peak temperature and LL is similar to the $k = 1$ results shown in Figure 3.2(a) and (b), although the temperatures are much lower and thus the LL is shortened for given (Bi, H_s) pairs. For the entire simulation $k(T_\text{s}) \geq 1$, so that substrate diffusion occurs more rapidly, and heat is then transferred faster away from the film, compared with the $k = 1$ case. This becomes increasingly important when considering films that evolve, since viscosity may depend strongly on temperature [3]. Finally, it should be noted that some temperatures in Figure 3.2 surpass the boiling point of the film ($T_\text{boil} \approx 2.088$), while our model neglects possible evaporation. Although models that account for evaporation exist (*e.g.*, see [103] for a classical review), in practice the laser fluence is often adjusted to the system of interest so that no significant mass is lost to evaporation. These results, therefore, can serve as a guideline for such fluence adjustments.

3.4.3   2D Evolving Films

In this section the film surface is initially prescribed by Equation (3.14), with $\delta = 0.01$, on the spatial domain $x \in [-\pi, \pi]$, and we investigate the influence of Bi and H_s on the film evolution. The initially solid film is static until it melts, at which point it evolves according to Equation (3.4). Once the film re-solidifies, its evolution stops. To maintain generality, we allow the material parameters governing surface tension,

viscosity and thermal conductivity to vary with average film temperature, so that $\Gamma = \Gamma(t)$ via Equation (3.1) and $\mathcal{M} = \mathcal{M}(t)$ via Equation (3.5). Similarly, the thermal conductivity of the substrate is allowed to depend on substrate temperature, $k = k(T_s)$ (see Equation (A.6) in Section A.7 for the form used).
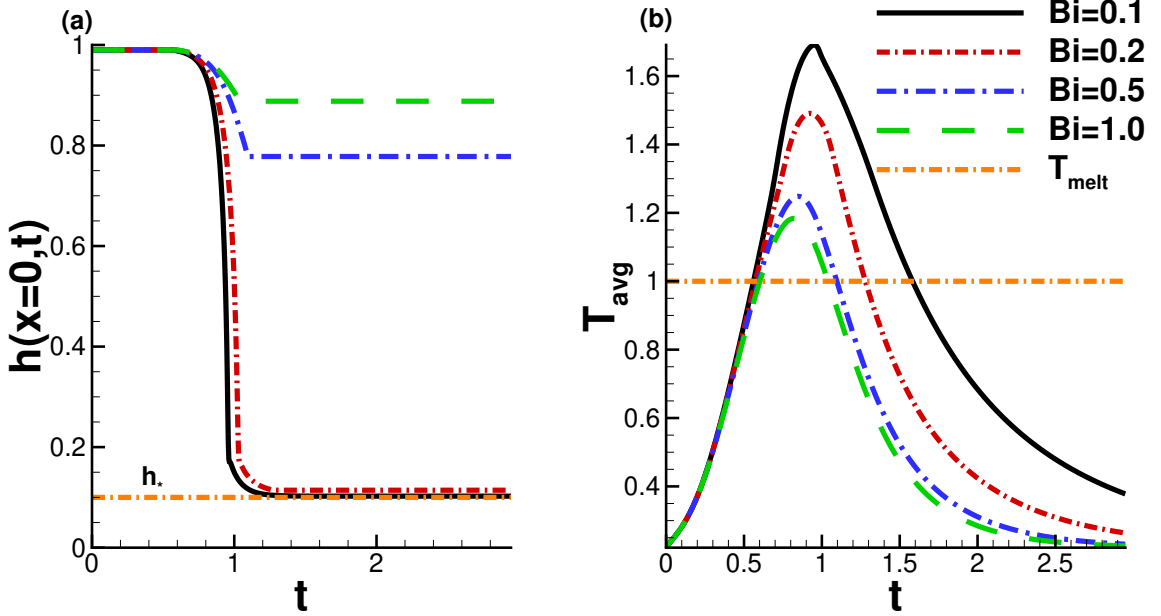
Figure 3.3 (a) Evolution of film thickness at $x = 0$ for Bi $= 0.1$ (black), 0.2 (red, dash-dotted), 0.5 (blue dash-dotted), 1.0 (green dashed); and precursor thickness $h = h_*$ (orange dot-dashed). (b) Average film temperature corresponding to the cases in (a). The material parameters are variable, $\Gamma = \Gamma(t), \mathcal{M} = \mathcal{M}(t), k = k(T_s)$, substrate thickness is fixed, $H_s = 10$, and melting temperature, T_{melt} (orange dot-dashed).

Figure 3.3(a) and (b) show the evolution of the film midpoint ($x = 0$) and the average film temperature, respectively, for various values of Bi and for fixed substrate thickness, $H_s = 10$. The trend of shorter LL in Figure 3.3 as Bi increases is consistent with Figure 3.2(d). Consequently, the films for Bi $= 0.5$ and Bi $= 1.0$ solidify prior to any significant evolution, whereas for Bi $= 0.1$ the film dewets fully. For Bi $= 0.2$ the film mostly dewets, but solidifies just before its surface reaches the equilibrium film thickness, $h = h_*$. This intricate balance between solidification and dewetting

highlights the importance of the value of Bi in determining whether full or partial dewetting occurs.
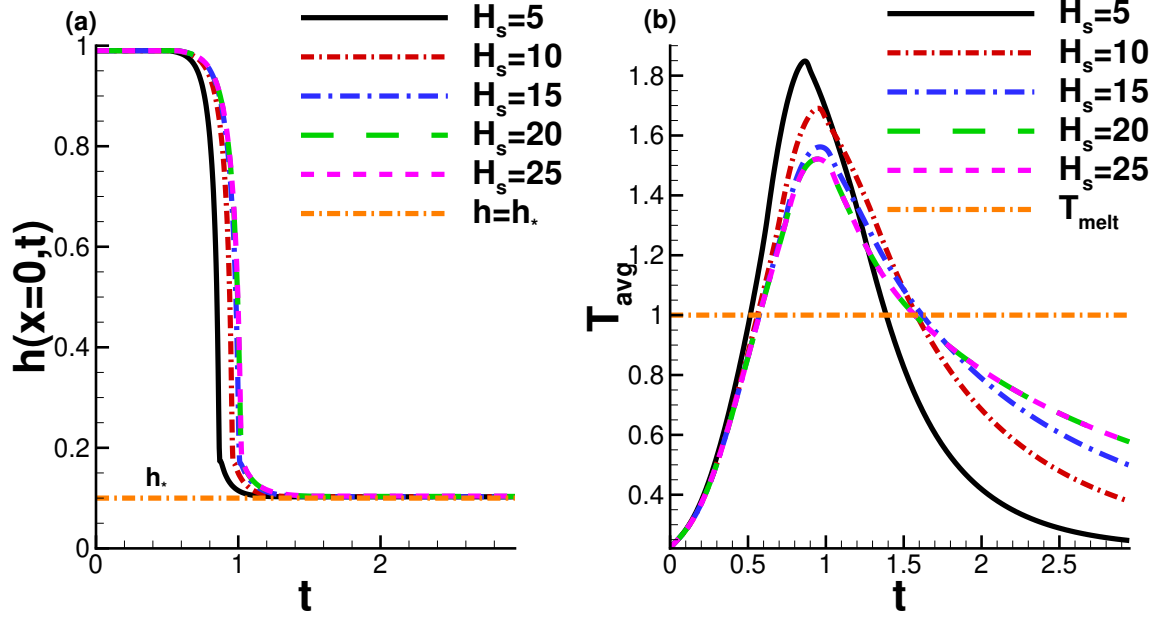
Figure 3.4 (a) Evolution of film thickness at $x = 0$ for $H_{\text{s}} = 5$ (black), 10 (red, dash-dotted), 15 (blue dash-dotted), 20 (green dashed), 25 (magenta dashed), and the precursor thickness $h = h_*$ (orange dot-dashed). (b) Average film temperature corresponding to the H_{s} cases in (a) and melting temperature, T_{melt} (orange dot-dashed). The material parameters are variable, $\Gamma = \Gamma(t), \mathcal{M} = \mathcal{M}(t), k = k(T_{\text{s}})$, and $\text{Bi} = 0.1$.

Next, we consider the influence of substrate thickness. Similarly to Figure 3.3, Figure 3.4(a) and (b) show the midpoint film thickness and average film temperature, but for varying H_{s}. Here the Biot number is fixed at $\text{Bi} = 0.1$. The main finding is that varying H_{s} does not alter the dewetting speed of the film as much as Bi, see Figure 3.4(a). From Figure 3.4(a), we see that increasing substrate thickness increases the dewetting speed by only a small amount. Since in Figure 3.4(b) films on thinner substrates achieve higher temperatures, the film on the thinnest substrate, $H_{\text{s}} = 5$, has lowest viscosity and dewets fastest in (a). The observed increase in peak temperature with substrate thickness, and the similar LLs for $\text{Bi} = 0.1$, are consistent

with Figure 3.2(c) and (d). For completeness, we include the analog of Figure 3.4 for the case Bi = 0.2 in Appendix A.10 and show that the findings are again consistent.

To summarize, varying substrate thickness (H_s) and heat loss from the lower surface (via Bi) may result in films that solidify prior to full dewetting. We will see in Section 3.4.4 that the substrate thickness plays a significant role in determining the final configurations of the 3D films.

3.4.4 3D Evolving Films

Next, we consider the role of the temperature-dependent material parameters, the substrate thickness, H_s, and the Biot number, Bi, in the pattern formation for 3D films, with free surface $z = h(x, y, t)$. For this section, we consider randomly perturbed films with the initial free surface disturbance specified by Equation (3.16) (shown in Figure 3.5), and follow the same melting/solidification procedure described in Section 3.4.3. In all cases, the domain is a square of linear dimension 16π, surface tension is a function of average film temperature via Equation (3.1) and, except where otherwise specified, the Biot number is fixed at Bi = 0.1. We consider both constant viscosity $\mathcal{M} = 1$ and (average) temperature-dependent viscosity $\mathcal{M}(t)$ (see Equation (3.5)), and $k = 1, k(T_s)$ for substrate thermal conductivity.

In earlier work [3, 124], 2D simulations reveal that temperature-dependent viscosity is crucial for modeling the correct dewetting speed of the films. We now confirm the importance of accounting for temperature-dependent viscosity in 3D simulations.
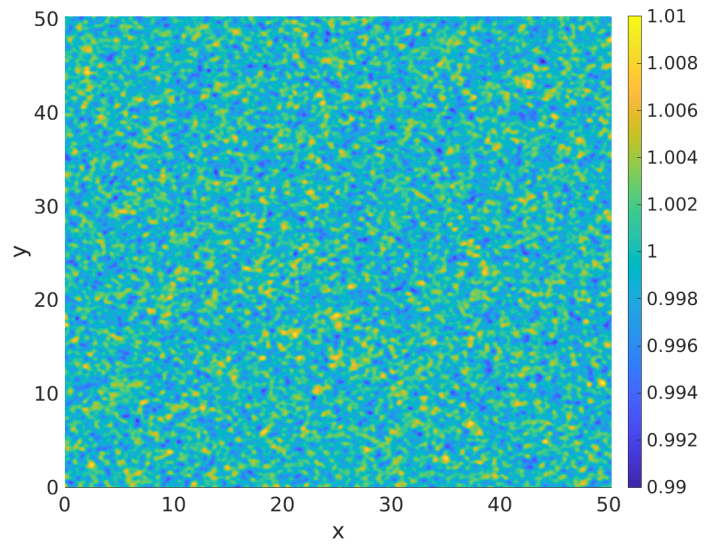
Figure 3.5 Initial film thickness $h(x, y, 0)$ for 3D simulations, described by random noise perturbations to the flat film $h = 1$, and given by Equation (3.16).
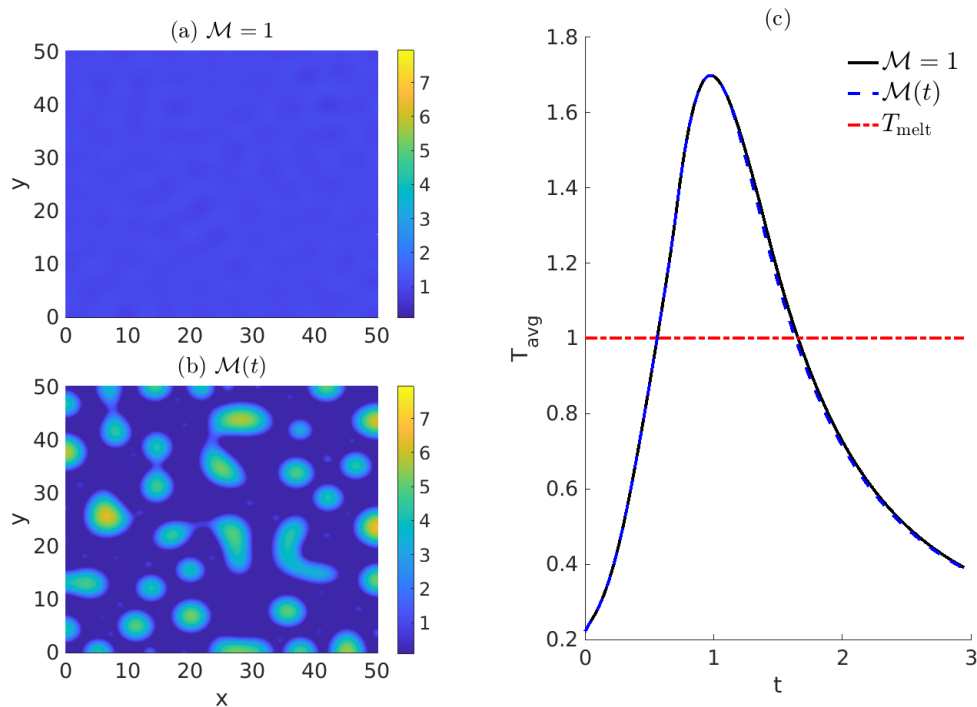
Figure 3.6 Local film thickness, $h(x, y, t)$ for (a) $\mathcal{M} = 1$ and (b) $\mathcal{M}(t)$. Average film temperatures are shown in (c), with melting temperature, T_{melt}. In (a) the film freezes before significant evolution occurs, whereas in (b) further dewetting occurs with some droplet formation. Both films are initialized with the random noise (Equation (3.16), shown in Figure 3.5). The LLs are approximately 1.10 and 1.05 for (a) and (b), respectively. For full animation, see Appendix C, movie3.

3.4.4.1 Influence of viscosity. Figure 3.6(a) and (b) both show the final solidified film for $k = k(T_{\mathrm{s}})$ but (a) corresponds to $\mathcal{M} = 1$ (viscosity fixed at melting value) and (b) to $\mathcal{M} = \mathcal{M}(t)$ (viscosity depends on average temperature as given by Equation (3.5)). The main finding is that the variable-viscosity film in Figure 3.6(b) has mostly dewetted and formed droplets prior to resolidification, whereas the constant-viscosity film in Figure 3.6(a) has barely evolved. Figure 3.6(c) shows the average film temperature T_{avg} in both cases, along with the melting temperature, T_{melt}; we see that T_{avg} is nearly identical for the two cases, despite the very different fluid dynamics. Since the final film structures are very different but the LLs are nearly identical, we conclude that the variable viscosity is crucial for accurate

modeling of dewetting within the liquid phase. Note that the spatially-varying form of viscosity, $\mathcal{M}(x,t)$, given by Allaire *et al.* [3], which replaces T_{avg} by T_{f} in Equation (3.5), produces essentially identical results to Figure 3.6(b), due to the weak in-plane spatial variation of film temperature (result shown in Appendix A.11 for completeness).
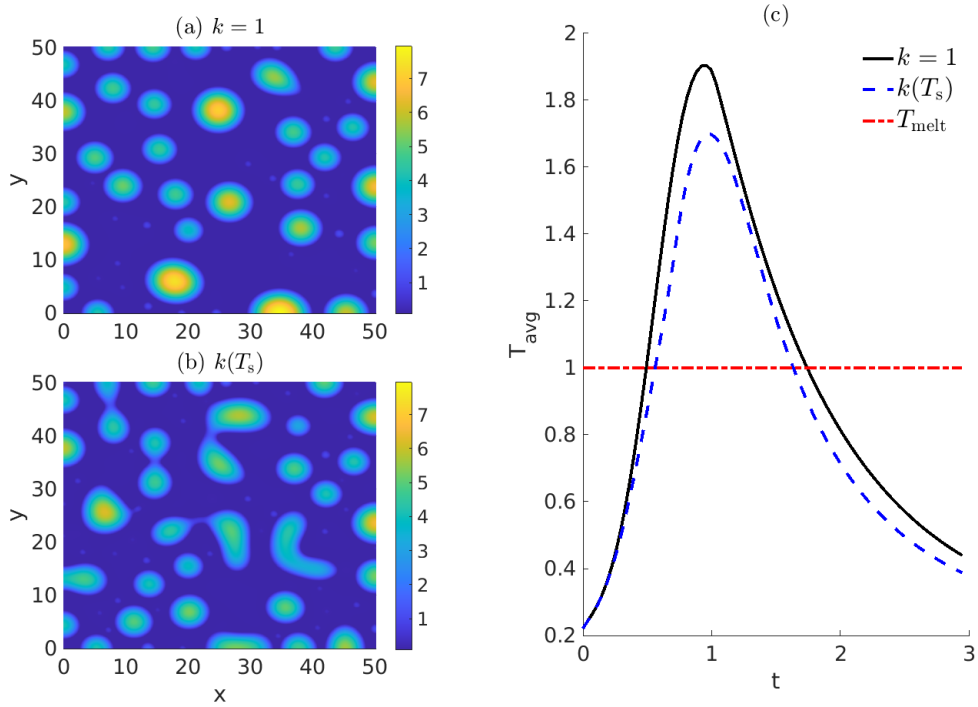
Figure 3.7 Local film thickness, $h(x,y,t)$ for (a) $k = 1$ and (b) $k(T_{\mathrm{s}})$ cases in their final solidified configuration. Average film temperatures are shown in (c), with melting temperature, T_{melt}. Here, $\mathcal{M} = \mathcal{M}(t)$, (b) is identical to Figure 3.6(b) and the LL for (a) is approximately 1.22. For full animation, see Appendix C, movie4.

3.4.4.2 Influence of thermal conductivity. Next, we consider the influence that temperature varying thermal conductivity in the substrate has on the dewetting behavior of the films. Figure 3.7 shows final solidified film thickness for (a) constant, and (b) temperature-varying, substrate thermal conductivity, both with temperature-dependent viscosity $\mathcal{M} = \mathcal{M}(t)$. Figure 3.7(c) shows the average film temperature over time for both cases. The decreased LL and lower peak temperature for $k(T_{\mathrm{s}})$ is

consistent with the flat film results in Figure 3.2(c) and (d), although the difference is not dramatic. Despite this, dewetting has clearly proceeded further in (a) than in (b), as evidenced by the differences in film heights, with thicker droplets in (a) than in (b). This is due to merging of droplets in (a) that did not occur in (b) due to both premature solidification (in (b)) and different values of the surface tension parameter Γ, which is known to alter instability wavelengths [3]. Dewetting in case (b) is also slower, due to the higher film viscosity resulting from lower temperatures.
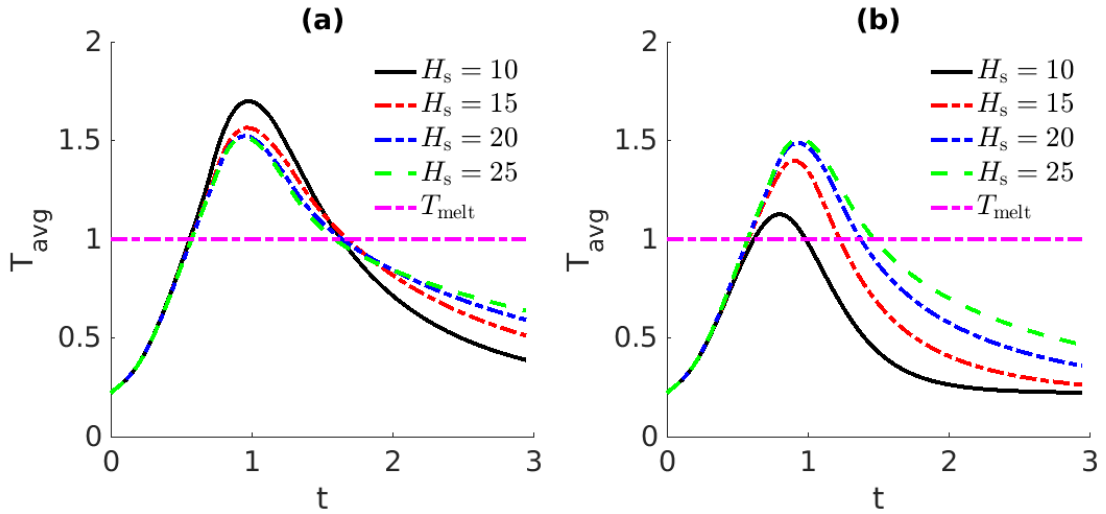
Figure 3.8 Average film temperatures, T_{avg}, in cases (a) Bi $= 0.1$ and (b) Bi $= 10^3$, when deposited on substrates of thickness $H_s = 10$ (black solid line), $H_s = 15$ (red dot dashed line), $H_s = 20$ (blue dot dashed line), and $H_s = 25$ (green dashed line). The melting temperature is given by the magenta dot dashed line.

3.4.4.3 Influence of substrate thickness. In Figures 3.8, 3.9, and 3.10 we investigate the role of H_s on the dewetting process for Bi $= 0.1$ and Bi $= 10^3$. Figure 3.8(a) shows average film temperatures for Bi $= 0.1$ and $H_s = 10$, 15, 20, and 25 where both film viscosity and substrate thermal conductivity are temperature-dependent, $\mathcal{M} = \mathcal{M}(t)$ and $k = k(T_s)$. The similar LLs and small variations in peak temperature observed are nearly identical to those for the 2D film in Figure 3.4(b). Nevertheless, the small deviations in peak temperature as H_s

varies are important because of the strong temperature dependence of viscosity, which changes the dewetting speed.

Figure 3.8(b) similarly shows average film temperature for the same substrate thicknesses as in (a) but for a poorly insulated substrate, $Bi = 10^3$. The significantly decreased temperatures and shorter LLs for thinner substrates are consistent with Figure 3.2(c). Note in particular the reversal of the trend between Figure 3.8(a) and (b), with peak temperature decreasing with H_s in (a), and increasing with H_s in (b). In Figure 3.8(b), the peak temperatures are generally lower and the LLs much shorter, which (we now show) may lead to different final solidified film configurations.
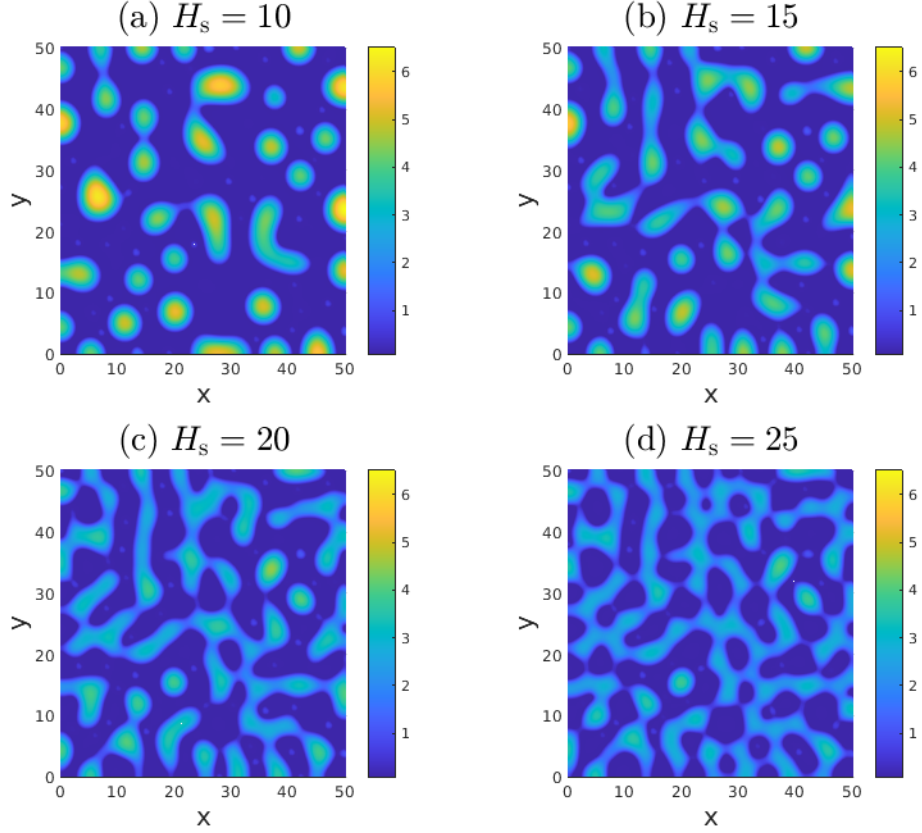
Figure 3.9 Final solidified film heights, $h(x, y, t)$, for Bi $= 0.1$, and on substrates of thickness (a) $H_s = 10$, (b) $H_s = 15$, (c) $H_s = 20$, and (d) $H_s = 25$, with temperature-dependent material parameters, $\Gamma(t)$, $\mathcal{M}(t)$, and $k(T_s)$. Films on thicker substrates dewet more slowly due to the lower temperatures (and higher viscosity) in Figure 3.8(a). Here, (a) is the same as Figure 3.6(b) and the LLs are (a) $t = 1.05$, (b) $t = 1.09$, (c) $t = 1.06$, and (d) $t = 1.00$. For full animation, see Appendix C, movie5.

Figure 3.9 shows the final solid film configurations for (a) $H_s = 10$, (b) $H_s = 15$, (c) $H_s = 20$ and (d) $H_s = 25$, for Bi $= 0.1$ (corresponding to Figure 3.8(a)). Since average peak temperature T_{peak} decreases with H_s, the dewetting speed decreases from (a)-(d) due to the viscosity increase. This is to some degree surprising, since the influence of H_s was not readily apparent in the 2D case. The proposed explanation is that, in our 3D simulations, we prescribe a random initial condition, and therefore it takes time for the fastest growing mode of instability to develop. This surplus time

slows the dewetting sufficiently for the thicker substrates that it is still incomplete at resolidification.
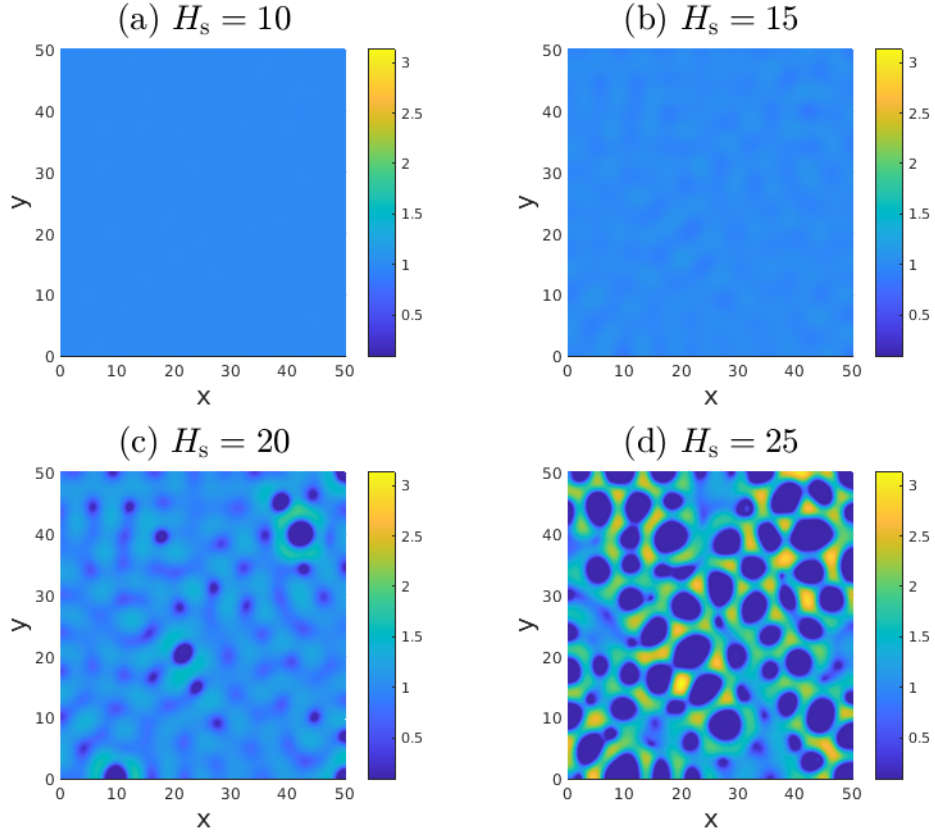
Figure 3.10 Final solidified film heights, $h(x, y, t)$, on poorly insulated substrates, Bi $= 10^3$, of thickness (a) $H_s = 10$, (b) $H_s = 15$, (c) $H_s = 20$, and (d) $H_s = 25$, with temperature-dependent material parameters, $\Gamma(t)$, $\mathcal{M}(t)$, and $k(T_s)$. Films on thicker substrates dewet faster due to the higher temperatures (and lower viscosity) in Figure 3.8(b). The LLs are (a) $t = 0.37$, (b) $t = 0.65$, (c) $t = 0.80$, and (d) $t = 0.89$. For full animation, see Appendix C, movie6.

Figure 3.10 shows the final solid film configurations for (a) $H_s = 10$, (b) $H_s = 15$, (c) $H_s = 20$ and (d) $H_s = 25$ for the poorly insulating substrate, Bi $= 10^3$, corresponding to Figure 3.8(b). Since T_{peak} now increases with substrate thickness, viscosity decreases and dewetting speed increases from (a)-(d). In this case, none of the simulations (a)-(d) fully dewet (recall the lower peak temperatures in Figure 3.8(b)

compared with Figure 3.8(a) leading to earlier resolidification in Figure 3.10 compared with Figure 3.9). The films in Figure 3.10(c) and (d) begin to form holes, but those in (a) and (b) barely evolve. Collectively, Figure 3.9 and 3.10 indicate that the final configuration of the resolidified film depends on both $H_{\rm s}$ and Bi in a nontrivial way.

3.5 Conclusions

We have modeled and simulated the evolution of pulsed laser irradiated nanoscale metallic films that are deposited on thick substrates. In particular, we have focused on the role that the underlying substrate plays in determining both the temperature of the film and its corresponding evolution. With regards to material parameters, our model accounts for temperature dependence of both surface tension and viscosity of the film. Our 3D simulations indicate that if temperature dependence of viscosity is not included, the films may not fully dewet.

The film liquid lifetime (LL) and spatially-averaged peak temperature ($T_{\rm peak}$) are found to depend on the substrate heat loss (as characterized by a Biot number, Bi, governing heat loss at the lower surface), substrate thickness $H_{\rm s}$, and the thermal conductivity model used (specifically, whether it is taken to be constant, or varying with temperature). $T_{\rm peak}$ is found to vary strongly with Bi, but less so with $H_{\rm s}$. In particular, we found that the correlation between $H_{\rm s}$ and $T_{\rm peak}$ changes from negative to positive according to whether the substrate is well-insulated (Bi $\ll$ 1) or poorly-insulated (Bi $\gg$ 1). The choice of well- or poorly-insulated substrates can lead to significantly different final solidified film configurations. Including temperature-varying thermal conductivity, in general, increases the heat loss from the film to the substrate, decreasing $T_{\rm peak}$ and therefore liquid lifetimes. The decreased film temperatures observed with temperature-varying thermal conductivity lead to a much smaller film viscosity, which reduces the speed of dewetting. Our 3D simulations showed that this can lead to films that solidify prematurely, although the effect is not

as dramatic as that of changing H_s. Interestingly, we found that varying H_s does not appear to alter significantly the the LL of the films; however, a small but significant change in T_{peak} results, which again alters viscosity and thus the final configuration of the film.

Our model omits a number of effects, the possible relevance of which we briefly discuss. First, we neglected temperature-dependent thermal conductivity of the metal film. Although this could be added to the model, with notable added complexity to the numerical schemes described in Appendices A.12 and A.13, the modest changes to thermal conductivity [108] would be inconsequential on the fast time scale of heat transfer across the film. Second, our simulations assume that phase change occurs instantaneously. In practice, partial melting and solidification may occur, in different parts of the film. The current model could be altered to include such effects, most readily by modifying the form of Equation (3.5) to account for spatial variations in film temperature, and viscosities that increase dramatically when the film temperature drops below T_{melt}. Radiative heat losses and evaporation are also neglected in the modeling; both effects may become important for certain choices of film materials. Finally, in-plane diffusion is neglected in the substrate. Such modifications will be considered in future work.

SURFACE, INTERFACE, AND TEMPERATURE EFFECTS ON THE PHASE SEPARATION OF BI-METALLIC $NI_{0.5}AG_{0.5}$: A MOLECULAR DYNAMICS STUDY

4.1   Overview

Classical molecular dynamics (MD) simulations were used to investigate how free surfaces, as well as supporting substrates, affect phase separation in a NiAg alloy. Bulk samples, droplets, and droplets deposited on a graphene substrate were investigated at temperatures that spanned regions of interest in the bulk NiAg phase diagram, i.e., miscible and immiscible liquid, liquid-crystal, and crystal-crystal regions. Using MD simulations to cool down a bulk sample from 3000 K to 800 K, it was found that phase separation below 2400 K takes place in agreement with the phase diagram. When free surface effects were introduced, phase separation was accompanied by a core-shell transformation: spherical droplets created from the bulk samples became core-shell nanoparticles with a shell made mostly of Ag atoms and a core made of Ni atoms. When such droplets were deposited on a graphene substrate, the phase separation was accompanied by Ni layering at the graphene interface and Ag at the vacuum interface. Thus, it should be possible to create NiAg core-shell and layer-like nanostructures by quenching liquid NiAg samples on tailored substrates. Furthermore, interesting bimetallic nanoparticle morphologies might be tuned via control of the surface and interface energies and chemical instabilities of the system.

4.2   Introduction

Recently, pulsed-laser-induced dewetting (PLiD) has been used to organize nanoparticles on surfaces with a correlated length scale. The PLiD exposes an $\sim$ 10ns pulsed laser to a metal thin film (single digits to tens of nm thick), which liquefies the film for up to tens of nanoseconds. During the liquid lifetime of the

PLiD procedure, the film [34, 61, 92, 116] or lithographically pattered nanostructure [41, 43, 54, 56, 57, 75, 110, 140, 141] experiences instabilities. The balance of viscous, capillary, and inertial forces induces liquid phase transport at the nanoscale. Natural two-dimensional thin film (spinodal and nucleation) instabilities and one-dimensional Rayleigh–Plateau instabilities have been studied. Since the rapid solidification of the features locks in even metastable morphologies, the sequence of low laser fluence/low liquid lifetime pulse has revealed a transient behavior. While much of the work has been dedicated to elemental metals, multifunctional nanoparticles can be realized by exploiting competing chemical instabilities. For instance, metallic alloys with liquid and solid phase miscibility [141, 142] /immiscibility [67, 117] gap can lead to tunable/multifunctional nanoparticles, respectively. Beyond experimental studies, complementary continuum modeling [7, 52, 75, 135] and molecular dynamics simulations [40, 48, 97, 98] have been used to elucidate the various liquid phase instabilities and transport behavior operative in nanoscale metallic liquids. While historically mainly elemental films have been studied, we are turning our attention to alloys where competing chemical instabilities may also be operative during fluid mechanical evolution.

In order to study the evolution of a liquid alloy to create nanoparticles, one must consider three effects. First, the chemical composition of the alloy, which might lead to phase separation in certain temperature ranges. Second, the surface energies of the metals involved, as one expects that the metal with a smaller surface energy would migrate to the free surface. And third, the interaction of the alloy with the substrate that supports the liquid, which determines the wetting/dewetting angle and also can induce preferential migration of the lower interfacial energy liquid. Cumulatively, various nanoparticle morphologies can emerge depending on the chemical and surface/interface energies.

In this study, in order to understand these three effects, we investigate the $Ni_{0.5}Ag_{0.5}$ alloy. At the $Ni_{0.5}Ag_{0.5}$ atomic composition, the NiAg phase diagram contains four distinct regions: (i) Above $\sim$ 2700 K, a liquid region phase where both Ni and Ag are miscible; (ii) between $\sim$ 2700–1800 K, a liquid-liquid phase where Ni and Ag have limited solubility and two liquid phases emerge; (iii) between $\sim$ 1700–1200 K, a liquid-solid phase where the Ag-rich phase is liquid, the Ni-rich phase is crystalline and both have limited solubility; and finally (iv) below $\sim$ 1200 K, a solid-solid phase where both Ni-rich and Ag-rich phases are crystalline and again have limited solid solubility. The phase fraction and specific phase compositions, of course, vary with temperature.

Here, we use classical molecular dynamics (MD) simulations to study the $Ni_{0.5}Ag_{0.5}$ chemical composition, and we focus on how surface and liquid-substrate interfacial interactions affect phase separation at the aforementioned regions of interest in the phase diagram. The results obtained provide a road map for future studies, which will investigate competing chemical and hydrodynamic instabilities that occur during the bimetallic liquid phase assembly of nanoparticles.

4.3 Materials and Methods

The simulations started from a 256 atom structure of $Ni_{0.5}Ag_{0.5}$, created from a face-centered cubic (FCC) lattice, where Ni and Ag were randomly mixed and the lattice parameter of Ni (3.524 Å) was assumed in the original structure. Subsequent to generating the $Ni_{0.5}Ag_{0.5}$ lattice, its total energy was minimized. An illustration of this structure is shown in Figure 4.1.

81
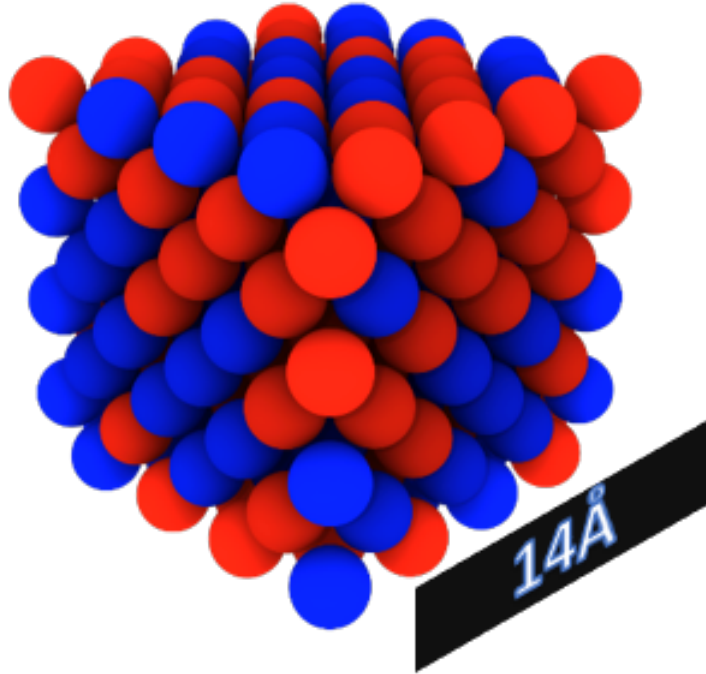
Figure 4.1 FCC structure of NiAg with 256 atoms and a 50/50 composition.

The 256 atom NiAg structure was then expanded in the x, y, and z directions to generate a sample that contained 55,296 atoms. We refer to this sample as the bulk sample, as we employed periodic boundary conditions at each +/- x, y, and z boundary. Then, the bulk sample was studied, first assuming the isothermal-isobaric (NPT) ensemble for 300 ps, followed by a canonical (NVT) ensemble for 600 ps, followed by the microcanonical ensemble (NVE) for 300 ps, all using a time step of 1 fs. These simulation times were found to be sufficient to converge the values of pressure, temperature, and energy in NPT, NVT, and NVE, respectively. The highest temperature considered was 3000 K, and once the sample was equilibrated with NVE at this temperature, it was quenched by reducing the temperature in 200 K increments until reaching 800 K. The corresponding atomic densities for the equilibrated 3000

K and 800 K structures were 54 and 65.8 atoms/nm^3, respectively. Because at every temperature the sample was equilibrated for 1.2 ns (300 ps NPT, 600 ps NVT and 300 ps NVE), the cooling rate in our simulations was 200 K every 1.2 ns, i.e., 1.67×10^{11} K/s. The melting points of Ni and Ag were 1726 and 1235 K, respectively, and by creating a Ni$_{0.5}$Ag$_{0.5}$ sample at different temperatures we aimed to study the different regions that appeared in the phase diagram.

The embedded-atom method (EAM) potential derived by Zhou *et al.* [149] was used to describe the Ni-Ni, Ag-Ag, and Ni-Ag interactions. This potential was developed for studying a NiAg alloy and it is the only NiAg potential we know of that is capable of capturing the relevant Ni-Ag phase separation. Indeed, we used the universal form of the EAM potential for Ni and Ag, and the NiAg Finnis–Sinclair potential of Pan *et al.* [105]. With the former, no phase separation was observed when the system was similarly quenched; with the latter, we obtained a similar radial distribution function to that shown by Pan *et al.* Figure 7 of [105] for a Ag$_{80}$Ni$_{20}$ alloy. However, when we used this potential to quench Ni$_{0.5}$Ag$_{0.5}$ from 3000 K to 800 K with a cooling rate 1.67×10^{11} K/s, phase separation was not observed.

To ensure that the Zhou *et al.* [149] EAM potential for Ni$_{0.5}$Ag$_{0.5}$ was accurate for the individual elements, we melted and cooled down a sample of 2048 atoms of Ni and Ag using NPT with melting and cooling rates of 2×10^{13} K/s (in 100 K increments for 500 ps each). Figure 4.2 shows the change in volume with temperature for the samples containing only Ni and only Ag, respectively. A sudden increase/decrease in the volume indicates melting/freezing has taken place and the hysteretic behavior is consistent with what is commonly observed [86]. In the case of Ni (Ag), the volume increases suddenly between 1800 K and 1900 K (1300 and 1400 K), which is close to the experimental melting point of 1726 K (1235 K). Upon cooling, the Ni (Ag) volume decreases dramatically at a temperature between 1000 and 900 K (800 and 700 K). Table 4.1 shows the slopes of the plots during the heating and cooling. Ag has a higher

dV/dT relative to Ni, which is consistent with the fact that Ag ($\sim 19 \times 10^{-6}$ /K) has a higher coefficient of thermal expansion than Ni ($\sim 13 \times 10^{-6}$ /K). As expected, both liquids have higher dV/dT than their respective solids. For comparison, we also heated and cooled a sample of 2048 atoms of $Ni_{0.5}Ag_{0.5}$ atomic composition; the results are also shown in Figure 4.2.

Table 4.1 Slope of Melting and Cooling Curves Given in Figure 4.2 for Ni, Ag, and NiAg

Element	Solid Phase Slope(Å/K)	Liquid Phase Slope (Å/K)
Ni	2.047	2.072
Ag	2.855	3.549
NiAg	1.962	2.815
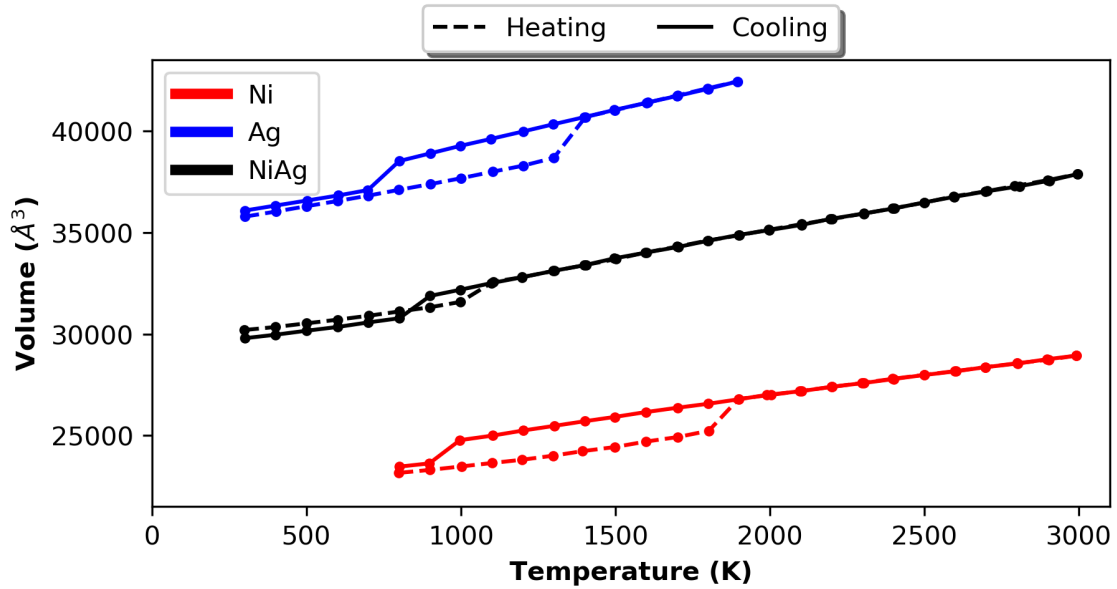
Figure 4.2 Melting and cooling of a 2048 atom sample of Ni (red), Ag (blue), and NiAg (black).

In this case, upon heating (cooling), only one abrupt volume change was observed between 1000 and 1100 K (900 and 800 K). This abrupt change was due

to the Ag phase transformation, where both the heating and cooling were shifted to slightly lower temperatures, which could have been due to the smaller cluster size of the Ag. The slope of the cooling curve of the $Ni_{0.5}Ag_{0.5}$ is approximately the average between the Ag and Ni cooling curve slopes. Notably, the Ni phase transformation is not observed, which is likely due to the sluggish phase separation and perhaps supersaturation of the Ni phase. Interestingly, the $Ni_{0.5}Ag_{0.5}$ slope is also close to the average of the solid Ni and liquid Ag (2.8 Å/K). Interestingly, the slope of the $Ni_{0.5}Ag_{0.5}$ heating curve is close to that of pure Ni and lower than the average. From the bulk sample created at each temperature, we generated droplets by simply adding a vacuum interface. It was found, then, that running 1800 ps of NVT and 300 ps of NVE was enough to equilibrate the resultant droplets. An example of an equilibrated NiAg droplet at 2000 K is shown in Figure 4.3a. Finally, a droplet at 2000 K was deposited on a single layer graphene substrate at an initial distance of 3 Å, see Figure 4.3b. The droplet was subsequently equilibrated using 1500 ps of NVT, while the substrate, as in previous studies [80], was kept frozen.

(a) (b)
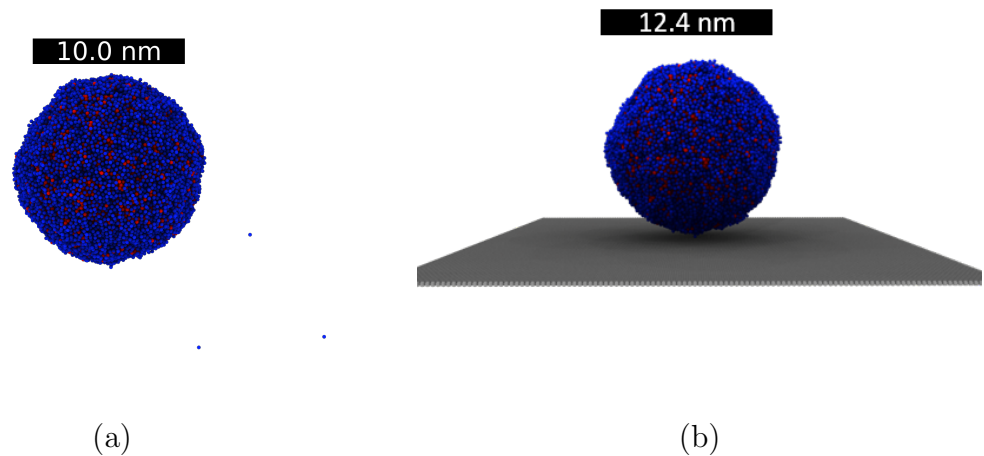
Figure 4.3 (a) Droplet of NiAg at 2000 K. (b) Droplet of NiAg at 2000 K deposited on 1-layer of graphite. The scale bar on (b) corresponds to the diameter of the droplet. Color code: Ni, red and Ag, blue.

Table 4.2 Lennard-Jones Parameters for Ni-C and Ag-C Interactions

Interaction	ε(eV)	σ (Å)	r_c (Å)
Ni-C	0.071	2.8	11.0
Ag-C	0.01	3.006	11.0

When the droplet was deposited on the graphitic substrate, the metal-C interactions were described with a 12-6 Lennard-Jones potential given by

$$V(r) = 4\varepsilon \left[\left(\frac{\sigma}{r} \right)^{12} - \left(\frac{\sigma}{r} \right)^{6} \right], \quad r < r_\text{c}, \tag{4.1}$$

where ε is the depth of the potential well, r is the inter-particle distance, σ is the distance at which the potential is zero, and r_c is the truncation radius. Previous studies [1, 53, 80, 121, 132] have provided values for ε, σ, and r_c but, as explained in Appendix B, Figure B.1, we found that none of these sets of values were able to reproduce the contact angle of pure Ni and Ag liquid droplets deposited on graphite. Here, we find that using the values in Table 4.2 for ε, σ, and r_c, respectively, we obtain a contact angle of 59° for Ni on graphite, and 145° for Ag on graphite; these theoretical contact angles are very close to the values found experimentally (Ag-C = 135° and Ni-C = 60°) [19, 62, 82, 95, 112, 139]. All the simulations were done with the software LAMMPS [107].

4.4 Results

In what follows, we show how temperature and environment (bulk, suspended droplet, or droplet on graphite), affect the phase separation and nanostructure morphology.

4.4.1 Bulk Samples

Crystallization and phase separation are realized in MD simulations by calculating the radial pair distribution function (RDF). Figure 4.4 shows the RDF (computed

with OVITO [129]) for the $Ni_{0.5}Ag_{0.5}$ system at all the temperatures considered. Each panel in the figure shows the RDF of Ni-Ni, Ag-Ag, and Ni-Ag. At 3000 K, the RDF shows that there is a slight preference to form homogeneous pairs, i.e., Ni-Ni and Ag-Ag, rather than heterogeneous Ni-Ag pairs. The difference is slight, and it can be said that at this temperature the system is a miscible liquid of Ni and Ag. According to the phase diagram, the onset of phase separation starts below 2700 K. In the simulations, phase separation starts clearly at 2400 K. As seen in Figure 4.4, at 2400 K, the first Ni-Ni and Ag-Ag peaks increase while the first peak for Ni-Ag decreases, a sign that Ni and Ag are forming homogeneous clusters and that heterogeneous clusters containing Ni-Ag are becoming smaller and less numerous. This trend continues down to 2000 K, and the fact that between 2400 and 2000 K there are no clear second and third peaks in the RDFs indicates that the system is still liquid, albeit immiscible. At 1800 K, Ni is close to its melting point and the first peak of the RDF has increased considerably, while a second peak has emerged. Ag, on the other hand, still remains liquid at 1800 K. Between 1600 and 1400 K, the crystallization of Ni is obvious, Ag still remains liquid, and the number of Ni-Ag pairs has decreased even further. The system is now phase separated into a Ni-rich crystal and an Ag-rich liquid. At 1200 K and below, the Ag-rich phase has already started to crystallize, and the system consists of a mixture of Ag-rich and Ni-rich crystalline phases, where both phases have very low solubility of the other constituent. The amplitudes of the first peaks are plotted in Figure 4.4d, showing an increase in pure metal pairs (Ni-Ni, Ag-Ag) and a decrease in mixed pairs (Ni-Ag) with decreasing temperature.

Phase separation is also observed with the coordination number, CN. The CN of the bulk samples at different temperatures is shown in Figure 4.5. Here, the CN was computed using the Visual Molecular Dynamics (VMD) software [65], by prescribing the radius at which the RDF attains the first minimum, corresponding to the first coordination number, and was performed for each pure and mixed pair.

At 3000 K, the number of Ag (Ni) neighbors around Ag (Ni) is 8 (6.2), whereas the number of Ag (Ni) neighbors around Ni (Ag) is 5.8. Upon cooling from 3000 K, the CN remains constant until about 2400 K, when the number of Ag (Ni) neighbors around Ag (Ni) starts to increase slightly, while the number of Ag neighbors around Ni starts to decrease, also slightly. Below 2000 K, the rate of change of the CN increases and there is a sharp increase and decrease in the number of homogeneous and heterogeneous pairs, respectively. At 800 K, there are very few heterogeneous pairs while the homogeneous ones have reached a value of 12 in the CN, which is consistent with the FCC crystal structure.
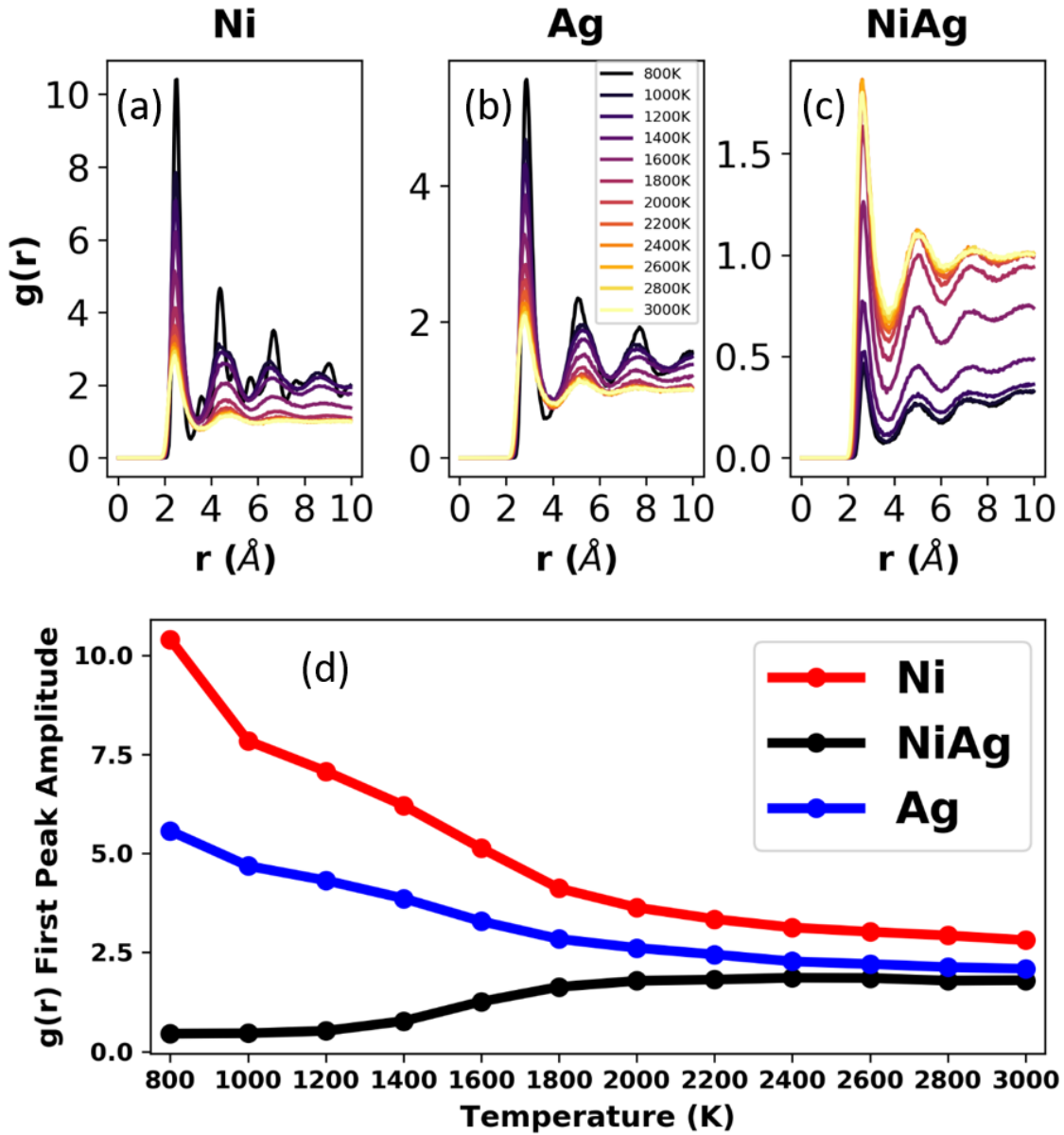
Figure 4.4 Radial distribution functions (RDFs) for the bulk samples at all the temperatures studied for Ni (a), Ag (b), and NiAg (c). (d) Plot of the the amplitude of the first peak (located between radii of 2 and 3 Å), as a function of temperature for Ni, Ag, and NiAg.

Despite the fact that the cooling rate used here is much greater than the rates used in typical PLiD experiments, the MD simulations with the atomic potential are still capable of capturing phase separation in $Ni_{0.5}Ag_{0.5}$, in accordance with the

experimental phase diagram. This encouraged us to explore the effect of a free surface
and a supporting graphene substrate on phase separation.
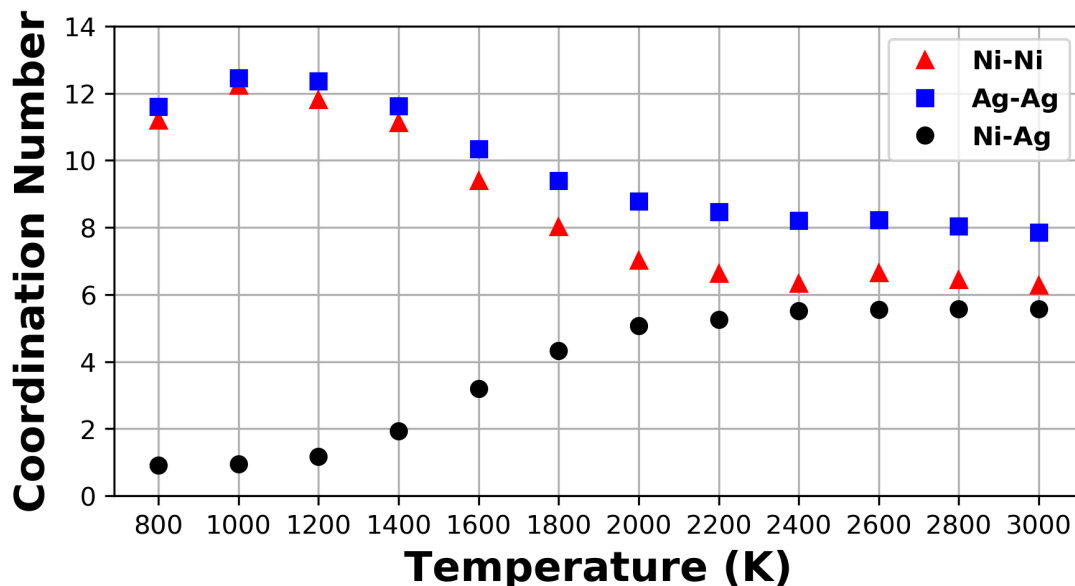
Figure 4.5 Coordination numbers for the bulk samples at different temperatures.

4.4.2 Droplets

To investigate the free surface effects on phase separation, we added a vacuum
interface to each of the already extant bulk samples and equilibrated each resultant
droplet. Equilibration was achieved with 1800 ps of NVT. This approach, as compared
to directly quenching a single droplet from 3000 to 800 K (which was avoided due
to surface evaporation of Ag atoms), reduces the effect of Ag surface migration, as
each bulk sample starts from a more nanogranular initial condition. Nonetheless, we
expect that the results obtained in this way approximately represent the effect of
Ag surface migration in the phase separation of a $Ni_{0.5}Ag_{0.5}$ droplet. As it will be
seen, even at low temperature, where diffusion is slower, we observe the expected Ag
diffusion towards the surface of the droplet.

    The RDFs for the droplets, along with their peak amplitudes, at all temper-
atures studied are shown in Figure 4.6. These RDFs are similar to those of the

corresponding bulk samples (see Figure 4.4) and thus at first one might conclude that phase separation is not significantly affected by the presence of a free surface. However, as Figure 4.7a and 4.7b illustrate, at 2200 K the NiAg droplet's surface is preferentially Ag-rich due to its lower surface energy; for instance, the surface energies of Ni and Ag at their respective melting temperatures are approximately 1.78 N/m and 0.93 N/m. To demonstrate the morphology evolution, Figure 4.7c shows the plots of the relative Ag and Ni concentration in 5 Å concentric annuli slices as a function of the inner radius of the slice. We did not consider spheres beyond an inner radius of 60 Å, as any atoms at locations beyond this radius are either due to small perturbations in the spherical shape or due to evaporated particles.
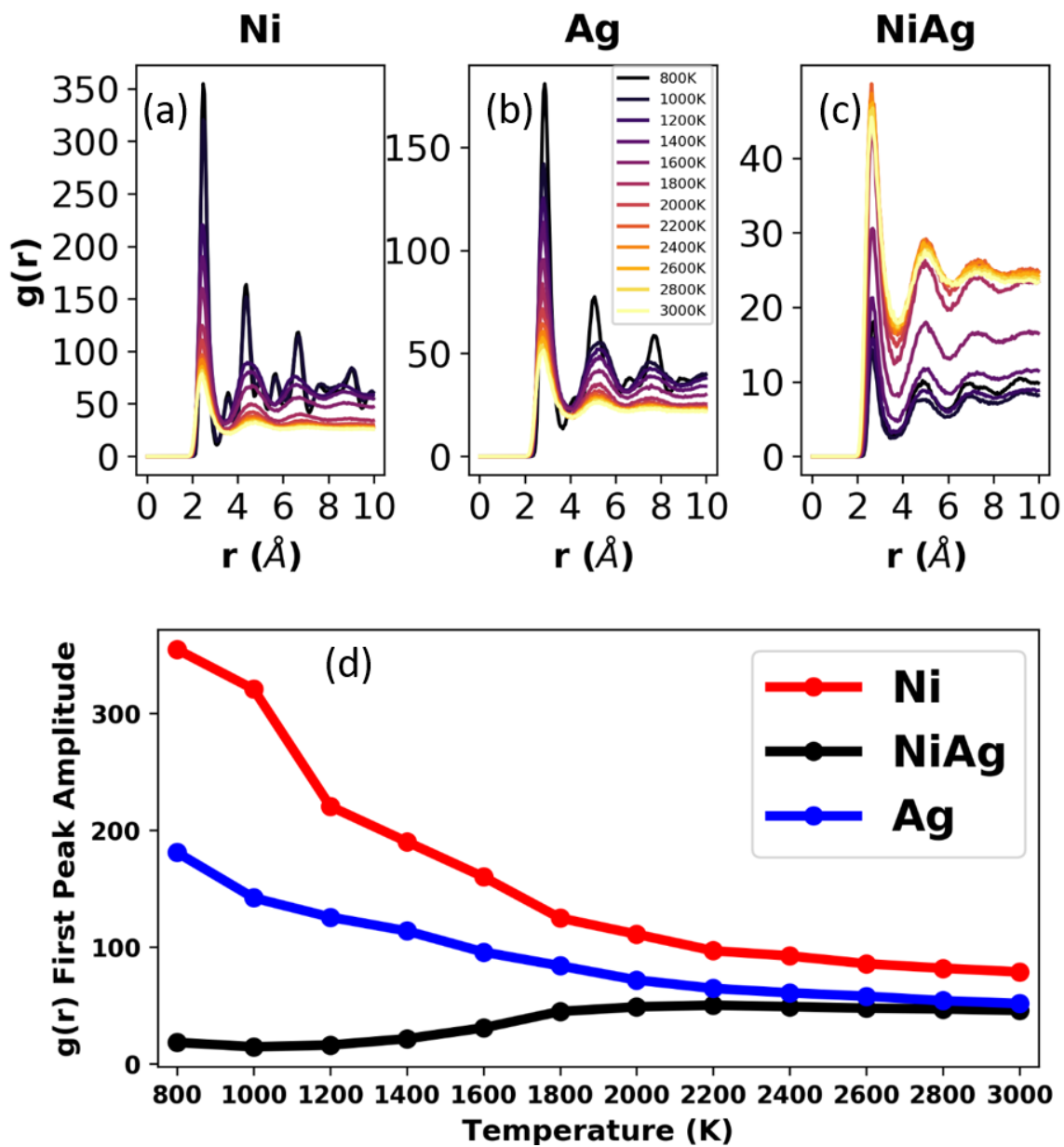
Figure 4.6 RDFs for the droplets at all temperatures for Ni (a), Ag (b), and NiAg (c). (d) Plot of the amplitude of the first peak (located between radii of 2 and 3 Å), as a function of temperature for Ni, Ag, and NiAg.

(a)   (b)

(c)
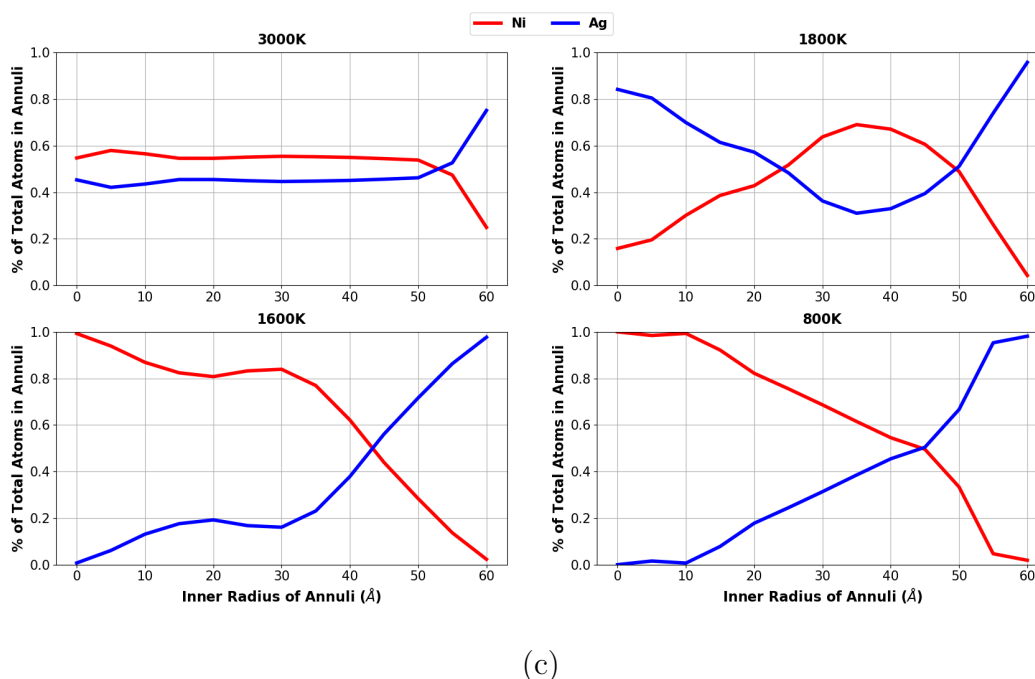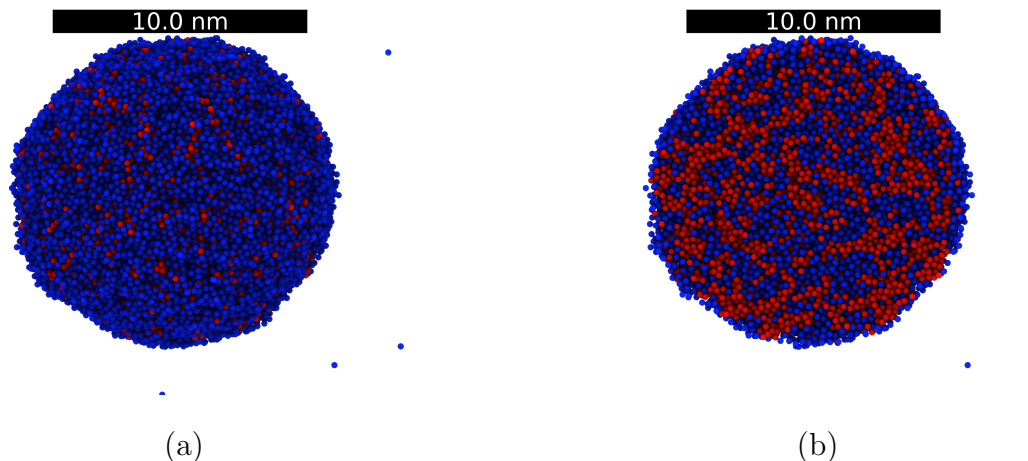
Figure 4.7 (a) NiAg droplet at 2200 K showing preferential movement of Ag to the surface, (b) slice of NiAg droplet at 2200 K, and (c) atomic concentration distribution analysis for the droplets at 3000 K, 1800 K, 1600 K, and 800 K. Color code: Ni, red and Ag, blue.

At 3000 K, the local distributions of Ni and Ag are nearly equal, with a slightly higher concentration of Ag at the surface as well as preferential Ag evaporation, see Figure 4.7c. Except for the surface, the amounts of Ni and Ag are practically the same everywhere in the droplet. This, together with the corresponding RDFs, indicates that the system is not phase separated, i.e., is a miscible liquid. As the

temperature decreases, the concentration of Ag atoms in the surface increases steadily, and similarly to the bulk simulation RDFs, phase separation is initiated at ~ 2400 K (the atomic local distribution analysis for all the temperatures in this study is shown in the Appendix B, Figure B.2). At 1800 K, close to the Ni melting point, the following significant change is observed: the concentration of Ni (Ag) increases (decreases) significantly in the middle of the droplet (i.e., the region between the surface and the center of the droplet), whereas, the opposite effect is seen in the center. To understand this behavior, Figure 4.8a-4.8c shows a cross section of the droplet at 2000, 1800, and 1600 K.

(a)

(b)

(c)

(d)
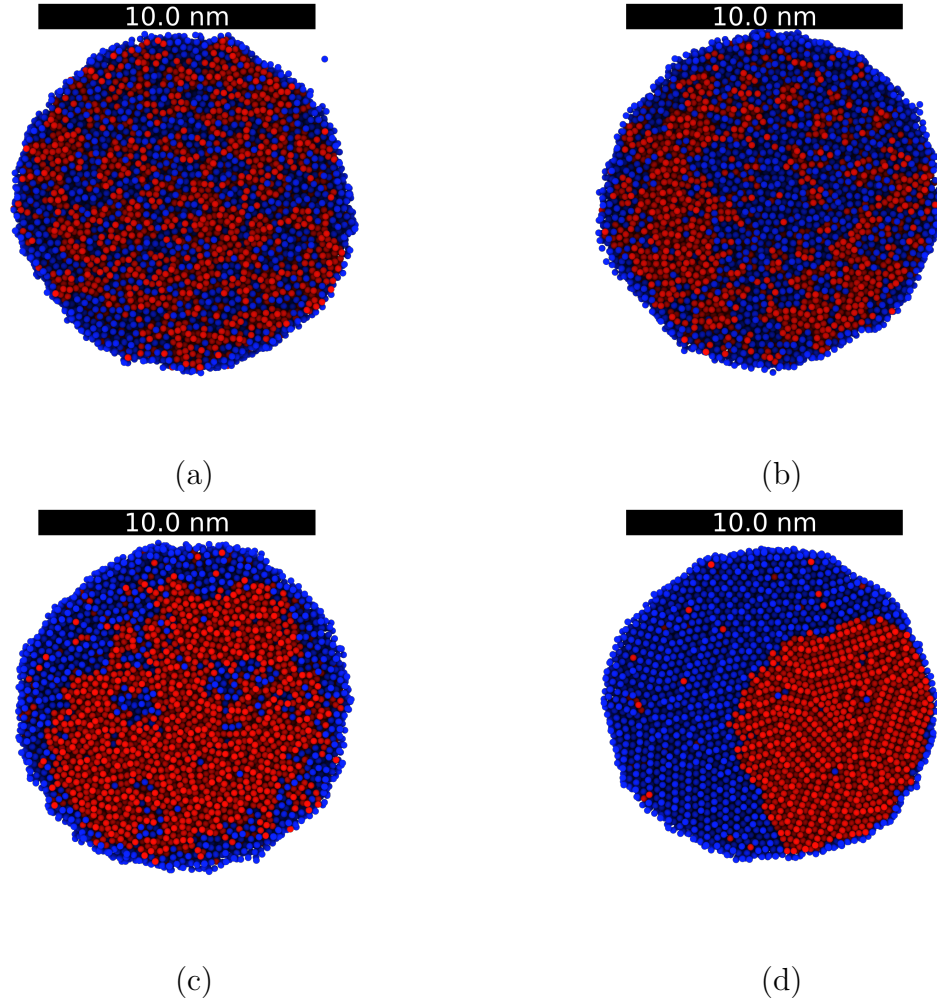
Figure 4.8 Cross sections of the droplets at 2000 K (a), 1800 K (b), 1600 K (c), and 800 K (d). Color code: Ni, red and Ag, blue.

As shown in Figure 4.8, it is observed that Ni clustering is clearly occurring at 2000 K, and that at 1800 K the Ni grains coarsen and occupy the middle section of the droplet; at 1600 K, the Ni solidifies, as evidenced by the RDF peak increase, and coarsens nearly to a single large cluster with a few Ag cluster inclusions. At the liquid-to-solid phase transformation, the solubility of Ag in Ni also drops. Finally, at 1600 K the Ni cluster occupies most of the interior of the droplet, whereas, the Ag atoms migrate to the surface and form a shell around the Ni core. As seen in Figure 4.8d, the core-shell morphology continues down to 800 K; at this temperature, the Ni cluster is displaced from the sphere centroid, but the surface layer of Ag is still present. Notably the solubilities at 800 K, at which both metals are in a solid state, is very low as evidenced by the few solute atoms in each solvent matrix.

4.4.3 Droplets on Graphite

An equilibrated droplet at a temperature of 2000 K was deposited on a one-layer graphene substrate and subsequently re-equilibrated. Next, the droplet was quenched to 1600 K with a cooling rate of 1.33×10^{11} K/s. Figure 4.9 shows snapshots of a cross section of the droplet on graphite at 2000, 1800, and 1600 K. As explained in the Methodology section, the Ni-C and Ag-C interactions were described with a Lennard–Jones potential adjusted to reproduce the wetting angles of liquid droplet Ni and Ag on graphite. This produces a Ni-C interaction ($\varepsilon = 0.072$ eV) that is stronger than that for Ag-C ($\varepsilon = 0.01$ eV). Consequently, when a droplet of $Ni_{0.5}Ag_{0.5}$ at 2000 K is deposited on graphite, Ni atoms migrate towards the C atoms, whereas, Ag atoms migrate to the surface of the droplet. This creates a layered-like structure in the $Ni_{0.5}Ag_{0.5}$ droplet, with Ni (Ag) occupying most of the graphite-metal (vacuum) interface, see Figure 4.9a. Lowering the temperature to 1800 K and then 1600 K (Figure 4.9b and 4.9c) does not change this migration of Ni and Ag. When the temperature decreases, the solubility decreases, and the coarsening of Ag and Ni takes

place. However, because of the presence of a graphite substrate, Ni agglomeration is located mostly near the droplet-substrate interface. This is consistent with the fact that Ni has a lower surface energy than Ag on graphite, and thus the contact angle resembles that of Ni.
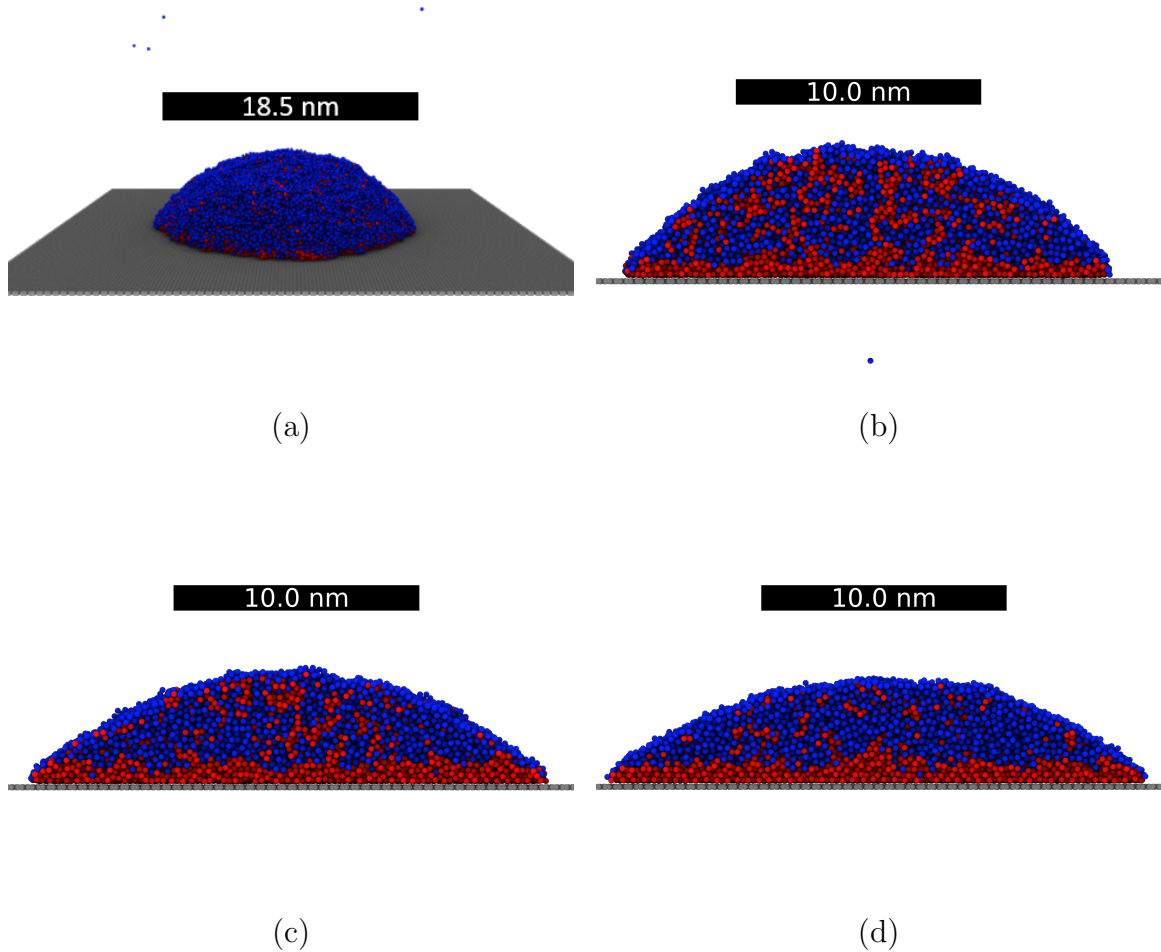
Figure 4.9 (a) 2000 K droplet deposited on one-layer of graphite. (b), (c), and (d) a cross-section snapshot at 2000, 1800, and 1600 K, respectively. The scale bar in (a) corresponds to the length of the droplet. Color code: Ni, red; Ag, blue; and C, grey.

To make clear the layering effect seen in Figure 4.9, atomic compositions of Ni and Ag are plotted in Figure 4.10 as a function of the distance from the substrate. These slices were taken in 5 Å increments from the droplet-substrate interface to the

top of the droplet. In each slice, the Ni and Ag compositions were both measured. Figure 4.10 reveals that the crossover point where the slice compositions are equal are all at approximately 8 Å from the substrate. Below this point, the composition of Ni is higher due to the lower surface energy of Ni-C relative to Ag-C. Interestingly, the wetting angle decreases with decreasing temperature, as evidenced by the change in height for the composition profiles. The larger Ni-C interface at a lower temperature causes the total nickel content to be higher in this ~ 8 Å layer. Thus, as is illustrated in the graphs, the Ni composition increases above the crossover point with increasing temperature.
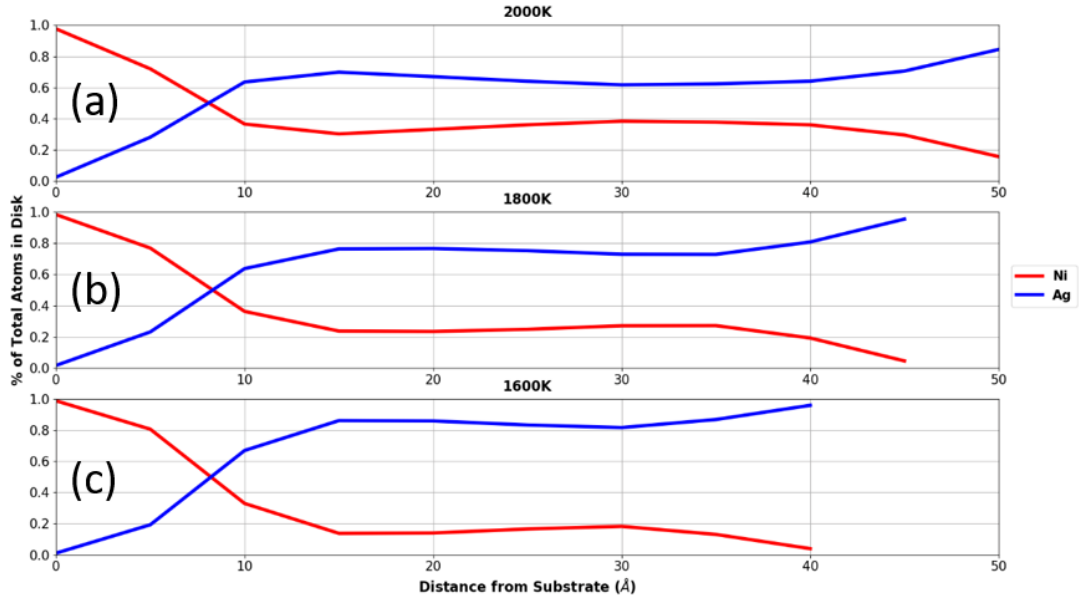
Figure 4.10 Atomic concentration distribution analysis of the droplets at (a) 2000 K, (b) 1800 K, and (c) 1600 K on substrates as a function of the distance from the substrate.

4.5 Conclusions

Molecular dynamics simulations were used to investigate the effects of free surface and substrate in the phase separation process of a NiAg alloy. It was found that the atomic potential employed in the simulations was capable of reproducing the phase separation observed in the experimental phase diagram. Subsequently, droplets were

created, and it was found that while phase separation still occurred, surface effects drove Ag towards the surface of the droplet substrate while Ni moved towards the interior. This led to the creation of Ni-Ag core-shell nanodroplets, with Ni in the interior and Ag in the surface. On the other hand, when these droplets were deposited on a graphitic substrate, phase separation led to a layered-type structure in which Ni agglomerated close to the substrate, while Ag still migrated to the surface of the droplet. In Chapter 5, we use the information gathered here to combine both phase separation and fluid mechanical instabilities.

THE ROLE OF PHASE SEPARATION ON RAYLEIGH-PLATEAU TYPE INSTABILITIES IN ALLOYS

5.1   Overview

Classical molecular dynamics (MD) simulations are used to investigate the role of phase separation (PS) on the Rayleigh-Plateau (RP) instability. Ni-Ag bulk structures are created at temperatures (2000 K and 1400 K) that generate different PS length scales, λ_{PS}, relative to the RP instability length scale, λ_{RP}. Rectanguloids are then cut from the bulk structures and patterned with a perturbation of certain amplitude and wavelength, λ_{RP}. It is found that when $\lambda_{PS} \ll \lambda_{RP}$ (2000 K), the patterned rectanguloids break up into nanoparticles in a manner consistent with classical RP theory, whereas when $\lambda_{PS} \approx \lambda_{RP}$ (1400 K), soluto-capillarity affects the RP instability significantly. Specifically, since Ag has a lower surface energy than Ni, Ag migrates to cover neighboring Ni regions, therefore modifying the RP instability. Thus, we demonstrate that the phase separation length scale of an immiscible alloy can be exploited to direct the assembly of functional bimetallic alloys.

5.2   Introduction

This work extends recent studies that explore how hydrodynamic instabilities in two dimensional single-component thin metal films [16,34,37] and nanostructures [75,140] can be used to create different arrays of organized and correlated nanoparticles. The Rayleigh-Plateau (RP) instability, for instance, is a phenomenon that emerges in a liquid jet: as different modes of surface-tension-driven instabilities evolve on the surface of the liquid, the fastest-growing mode dominates and pinches the liquid jet at regular points along its length, breaking it into droplets. The spinodal and nucleation types of instability for a thin film deposited on a substrate are other examples; in

such a configuration, thin films break up and may generate nanoparticles with a correlated size and length scale; see recent reviews [76, 115] for more details. Other effects can compete with (or enhance) these types of instabilities. For example, thermal gradients can lead to gradients in surface energy (the thermo-capillary effect, also known as thermal Marangoni effect), which may influence the dewetting mechanism [7, 136]. Similarly, differences in chemical concentration may lead to gradients in surface energy [57], known as the soluto-capillary effect (or concentration Marangoni effect). In this work, we focus on how RP hydrodynamic instabilities compete with soluto-capillarity. We leverage so-called synthetic perturbations, which are lithographically patterned rectanguloids with varicose edge perturbations, to control the competition/cooperation of the RP and soluto-capillarity. Synthetic perturbations in elemental liquid metals have been demonstrated experimentally and verified via detailed simulations to direct the precise assembly of nanoparticle arrays via unstable RP instabilities [41, 43].

Similar to Chapter 4, we use here classical MD simulations to study the Ni-Ag system at $Ni_{0.5}Ag_{0.5}$ chemical composition but now focus on the influence of phase separation (PS) on RP-type hydrodynamic instabilities. Several previous MD studies have investigated the spinodal [97, 98] and RP [40, 71, 97] instabilities, as well as other dewetting phenomena [1, 14, 15, 17, 29, 30, 47, 48, 80] in single-component films. Additionally, several groups have studied liquid-state PS in metallic systems, such as Al-Pb [84] and Al-Ge-Mn [131]; see also our recent work exploring the role that a liquid-vacuum and liquid-substrate interface has on the phase separation in Ag-Ni single drops [4]. The Ag-Ni system is interesting in that Ag is an efficient plasmonic material and Ni is ferromagnetic, thus in principle bi-functional magnetoplasmonic nanoparticles can be generated [50]. Recent experimental pulsed laser induced dewetting studies of various alloys for plasmonic [12, 22, 100, 142, 143], magnetic [77], and magnetoplasmonic [67, 117, 128] systems have been performed. For instance,

control of the thin film thickness of gold and silver affects the resultant nanoparticle size distribution, which subsequently affects the surface plasmon resonance energy.

5.3   Materials and Methods

Bulk structures of $Ni_{0.5}Ag_{0.5}$ were equilibrated at 3000 K using a small initial sample of 256 atoms with the isothermal-isobaric (NPT), canonical (NVT), and micro-canonical (NVE) ensembles, respectively. We employed both the Nose-Hoover thermostat and barostat [45] with a temperature damping parameter of 100 fs and pressure damping parameter of 0.5 fs. The embedded-atom method (EAM) potential derived by Zhou *et al.* [149] was used to describe the Ni-Ni, Ag-Ag, and Ni-Ag interactions (see the work done by Allaire *et al.* for details [4]). Subsequently, the small samples were expanded to a large bulk of 829440 atoms and equilibrated (using the same ensembles) from 3000 K to 1400 K in 200 K increments similar to our previous work [4]. For temperatures 1800K-3000K the bulk structure was sequentially equilibrated using 400 ps of NPT, 600 ps of NVT, and 200 ps of NVE (total of 1.2 ns). Thus, the cooling rate from 3000 K to 1800 K was 1.67×10^{11} K/s. At 1600K, the bulk is equilibrated for 4.8 ns (400 ps NPT, 2400 ps NVT, 2000 ps NVE) so the cooling rate from 1800 K to 1600 K was 0.42×10^{11} K/s. We cooled the bulk to 1400 K from 1600 K in 6.6 ns (400 ps NPT, 1800 ps NVT, and 4400 ps NVE), so the cooling rate was 0.30×10^{11} K/s. Note that lower temperatures required more time to equilibrate temperature and energy.

In our previous work, we found that phase separation of Ni and Ag phases in a $Ni_{0.5}Ag_{0.5}$ bulk started at temperatures below 2400 K, consistent with the equilibrium phase diagram, and that larger phase separation length scales emerged as the temperature was lowered [4]. When the bulk $Ni_{0.5}Ag_{0.5}$ was suspended in vacuum, such that a free surface existed, a Ag@Ni core-shell morphology emerged due to Ag's lower surface energy. Based on our previous work, here we consider temperature as a proxy to control the PS length scale, which we call λ_{PS}. We focus on two

temperatures: 2000 K, which is in the immiscible Ag-Ni liquid-liquid phase region of the phase diagram; and 1400 K, which for a bulk material is in the Ag-Ni liquid-solid phase. In materials at the nanoscale, however, it is well-known that the melting point is suppressed. Recently, Ridings *et al.* [113] showed that for the effective radii investigated below (~ 18 Å), that the (100) and (110) planes have surface melting temperatures $\sim$1300 K and 1200 K, respectively. Furthermore, the "bulk" cylinder core has a melting temperature close to 1400 K. Thus, in the dewetting studies below, the suppressed nickel melting point leads to a Ag-Ni (liquid-liquid) system where some nanogranular solid Ni could exist in the cylinder core. It should be noted, however, that the RP-like instabilities, while derived for liquid filaments, are operative in both solid [68, 134] and granular materials [109, 138].

To emulate pulsed laser induced dewetting experiments, where metal nano structures are lithographically patterned onto substrates, we cut thin rectanguloids (referred to as lines for simplicity) from the bulk structures with lengthwise (x) perturbations of a prescribed wavelength and amplitude. We denote the length of the respective bulk and associated line by L and impose periodic boundary conditions at $x = 0, L$. Figure 5.1 shows bulk structures created at 2000 K (a), and at 1400 K, (b). Note that both the lengths of the bulks in Figure 5.1a, 5.1b and the width of the respective lines are not constructed exactly equal (see Appendix B.4 for more details).
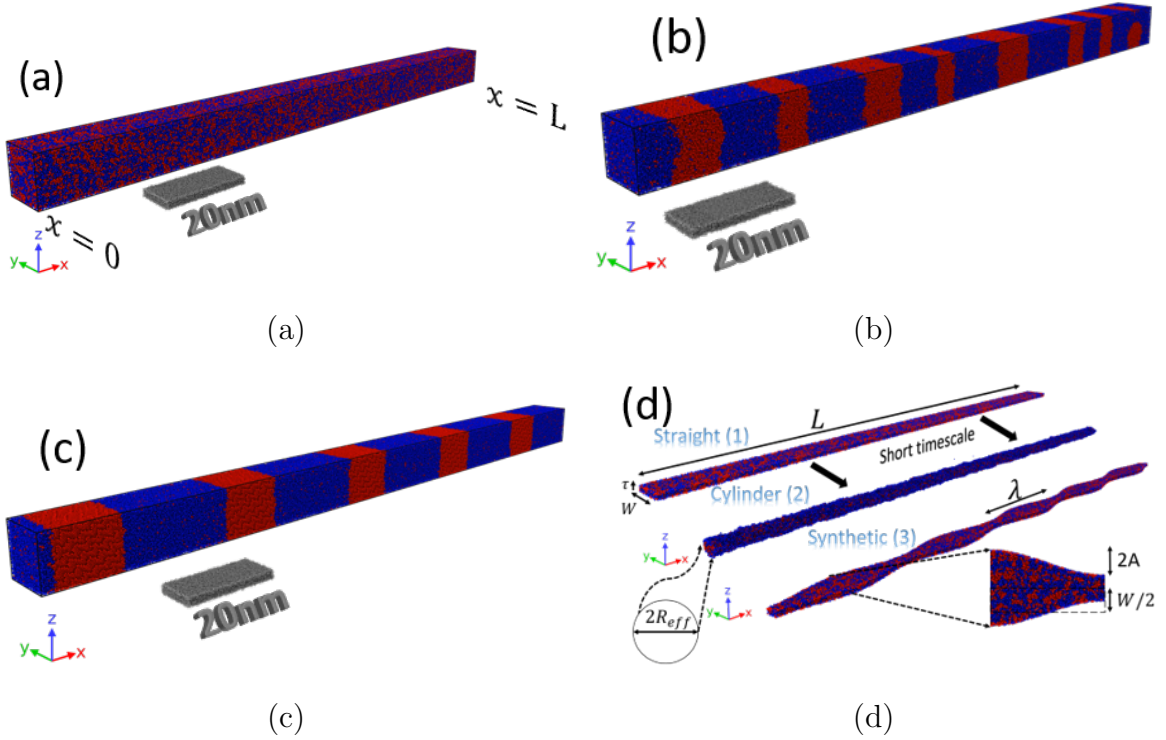
Figure 5.1 Equilibrated $Ni_{0.5}Ag_{0.5}$ bulk structures at (a) 2000 K and (b), (c) 1400 K. In (a) phase separation leads to the formation of small clusters of Ni and Ag, whereas in (b) PS results in the formation of unequally sized stripes along the x-axis. In (c) PS stripes were created to have a fixed length (the difference in size is due to the unequal atomic volumes of the two phases). (d) Straight lines (1) and lines with perturbations (referred to as synthetic lines) (3) are cut from bulks (a)-(c) (here the lines from (a) are shown). In vacuum, the lines quickly deform into cylinders (2). The cross-sections of (1) and (3) are both rectangles of thickness, τ but (1) has a fixed width, W, whereas the width in (3) varies with x. The cross-sections of (2) are circles of radius R_{eff}. For (3) the perturbations have wavelength λ and amplitude A (half the distance of peak to trough). Color code: Ni (red), Ag (blue).

As seen in Figure 5.1a, at 2000 K small clusters of Ni and Ag form. Using the cluster analysis tool in Ovito [129], the average sizes of Ni and Ag clusters (assuming clusters are all densely [13] filled spheres) are found to be 6.2 and 6.7 Å, respectively, and $\lambda_{PS} = 12.9$ Å is defined to be the sum of the Ni and Ag average cluster sizes. In Figure 5.1b, at 1400 K, Ni (red) and Ag (blue) stripes form along the longitudinal axis, x. There is some variation in the lengths of each of the stripes as the line was

equilibrated from high temperature. The PS length scale is defined as a sum of the average lengths of both Ni and Ag stripes, $\lambda_{PS} = 170.7$ Å.

To emphasize and better interrogate the competing effects that phase separation has on the dewetting dynamics, we equilibrated so-called "forced" periodic structures with regions of equal number of Ag and Ni regions at length scales similar to those observed in Figure 5.1b. The bulk (Figure 5.1c) was first created with 5120 atoms, equal parts Ni and Ag. The energy was minimized and both NPT/NVT ensembles were used to equilibrate pressure, volume, and temperature at 300K, 1000K, and then finally 1400 K. The small bulk structure was then replicated (expanded) into one containing 921,600 atoms (this is where the stripe patterns emerge) and subsequently equilibrated with 1.2ns of NVT and 9ns of NVE, which we found to be sufficient for convergence. Note that controlled bimetal patterns can be achieved via lithography [57] (albeit at larger length scales) and chemical synthesis routes [91].

Similar to Figure 5.1b, Ni and Ag stripes form but now, by design, each Ag-Ni stripe pair has a fixed length; note also that each Ag and Ni stripe has approximately the same number of atoms, but the atoms are closer to each other for Ni (the atomic volume for Ag is roughly 1.66 times larger than that for Ni at 1400 K). The PS length scale, defined in the same manner as in Figure 5.1b, is $\lambda_{PS} = 315.6$ Å.

Figure 5.1d shows an example of lines cut from the bulk structure at 2000 K (Figure 5.1a). Here, image (1) shows a straight line of length L and width W, and image (3) is a line of the same length L with applied perturbations of amplitude A and wavelength λ (referred to as a synthetic line). Note that, when suspended in vacuum, both straight and synthetic lines quickly form a cylinder, so as to minimize surface energy (such a cylinder is shown in Figure 5.1d, image (2)); even in the case of the synthetic lines cylinders form faster than line breakup, as discussed in what follows.

5.4   The Rayleigh-Plateau Theory for Liquid Metals

Consider a perturbed liquid cylinder of radius $R(x,t)$ with axis, x and surface given by:

$$R(x,t) = R_0 + A \exp\left(ikx + \omega t\right), \tag{5.1}$$

where R_0 is the average radius and A, k, and ω are the perturbation amplitude, wavenumber, and growth rate, respectively, with $A \ll R_0$. Classical RP theory predicts that such small perturbations to liquid cylinders in vacuum, neglecting viscosity, will grow at the rate given by

$$\omega^2 = \frac{\gamma}{\rho R_0^3} k R_0 \frac{I_1\left(kR_0\right)}{I_0\left(kR_0\right)} \left(1 - k^2 R_0^2\right), \tag{5.2}$$

where γ, ρ are the liquid surface tension and density, and I_0, I_1 are Bessel functions of the first kind of the zeroth and first order, respectively. In this chapter, we focus on the (unstable) modes that grow ($\omega > 0$, only possible when $kR_0 < 1$). Of the unstable modes, the one that grows the fastest is that with wavenumber k_{m}, found by maximizing $\omega(k)$ in Equation (5.2) with given values of γ, ρ (see Table 5.1) and R_0 (see Table 5.2), given by

$$k_{\mathrm{m}} R_0 \approx 0.697. \tag{5.3}$$

The corresponding wavelength, $\lambda_{\mathrm{m}} = 2\pi/k_{\mathrm{m}}$, of this mode depends only on the initial radius of the cylinder, and is given by $\lambda_{\mathrm{m}} = 9.01 R_0$.

Table 5.1 Material Parameters for Ni, Ag, and $Ni_{0.5}Ag_{0.5}$ Alloy at Both 2000 K and 1400 K, Obtained by Linearly Extrapolating Properties from the Melting Temperature, where Properties for the Alloy are Found by Averaging

Element	$\rho_{2000K}(kg/m^3)$	$\gamma_{2000K}(N/m)$	$\rho_{1400K}(kg/m^3)$	$\gamma_{1400K}(N/m)$
Ni	7587.2	1.7	8283.2	1.9
Ag	8652.4	0.8	9196.4	0.9
$Ni_{0.5}Ag_{0.5}$	8119.8	1.2	8739.8	1.4

Previously, we have shown that synthetic perturbations characterized by an unstable RP wavelength can be used to control the breakup of nanoscale metallic liquid lines into droplets of desired size and spacing [41, 43]. Here we investigate whether the RP instability can be used to describe the breakup of $Ni_{0.5}Ag_{0.5}$ lines (rather than pure element cylinders) in vacuum. Although the RP theory technically only applies to single-element liquids, we apply it to the $Ni_{0.5}Ag_{0.5}$ alloy by averaging densities and surface liquid tensions for the single elements (Vegard's law) as given in Table 5.1. As mentioned earlier, when suspended in vacuum, the lines transform into cylinders of effective radius R_{eff} perturbed along the long axis with effective amplitude A_{eff} (in the case of straight lines, $A_{eff} = 0$). For simplicity, we define the effective radius to be the radius of the cylinder that results from the straight lines, found by equating cross-sectional areas, and is given by:

$$R_{eff} = \sqrt{\frac{W\tau}{\pi}},$$

where τ is the line thickness, which we fix in all cases as $\tau = W/5$. For the synthetic perturbation cases, the effective amplitude can be found by equating the cross-sectional area of the perturbation troughs to that of the thinnest part of the perturbed cylinder. Since the width of the line at troughs is $(W - 2A)$ and the radius of the thinnest parts of the cylinder is $R_{eff} - A_{eff}$, equating cross-sectional areas,

106

$(W - 2A)\tau = \pi(R_{\text{eff}} - A_{\text{eff}})^2$, we find the effective amplitude,

$$A_{\text{eff}} = \sqrt{\frac{W\tau}{\pi}} - \sqrt{\frac{(W - 2A)\tau}{\pi}}$$

For each of Figure 5.1a, 5.1b, and 5.1c, the wavelength is chosen so that $L = 5\lambda$, where L is the (fixed) length of the respective bulk. With the values of the widths W given in Table 5.2, the chosen wavelengths correspond to unstable perturbations (stability curves will be shown shortly). By removing atoms from the bulk structures, $Ni_{0.5}Ag_{0.5}$ lines of certain width, wavelength, amplitude and thickness (values are given in Table 5.2) are extracted at 2000 K and 1400 K. We use A, B and C to denote the straight and synthetic lines cut from Figure 5.1a, 5.1b, and 5.1c, respectively.
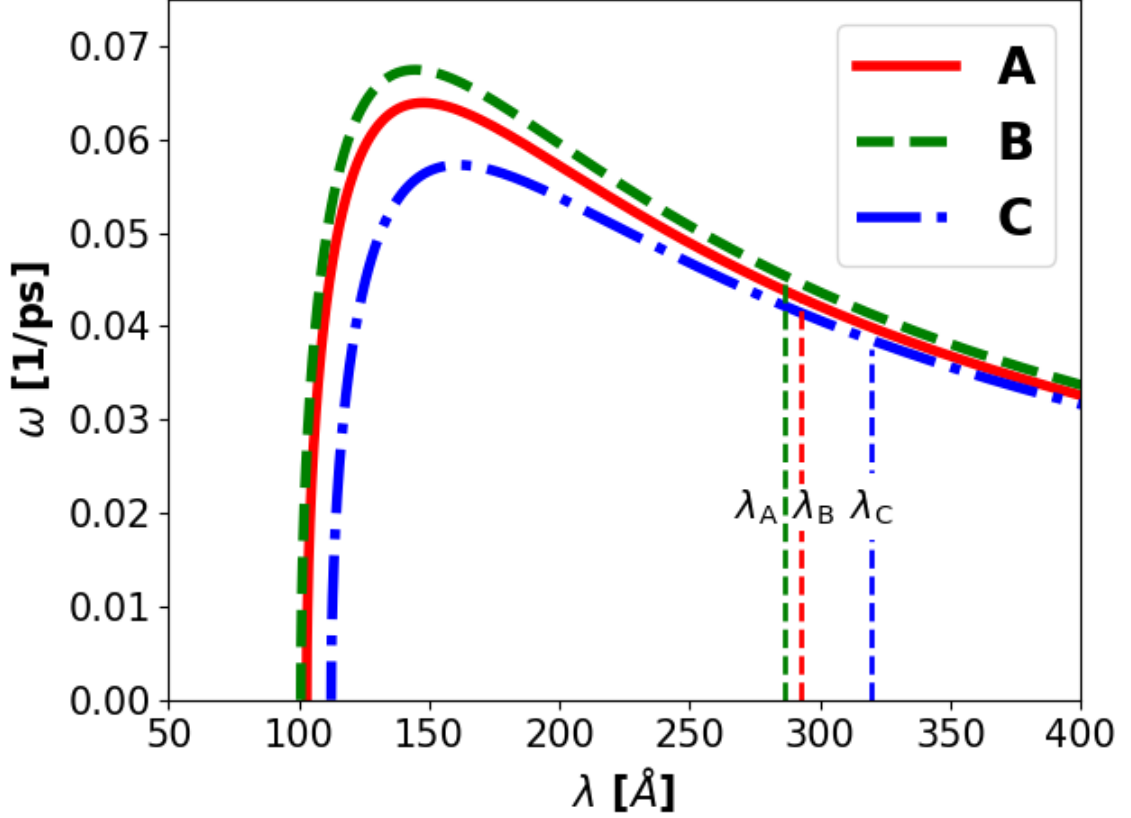
Figure 5.2 RP dispersion curves, using Equation (5.2) with effective cylinder radius R_{eff}, where the growth rate is calculated using the geometric parameters from lines **A** (red solid line), **B** (green dashed line) and **C** (blue dot-dashed line) (Table 5.2), and the material parameters given in Table 5.1. The vertical dashed lines correspond to the wavelengths used in the corresponding simulations.

Figure 5.2 displays the theoretical dispersion curves for the material parameters given in Table 5.1 and using $R_0 = R_{\text{eff}}$ in Equation (5.2) for **A**, **B** and **C**. The values of the chosen wavelengths for **A**, **B** and **C** are given by vertical dashed lines and are denoted here by λ_A, λ_B and λ_C, respectively. Except for the differences in maximum growth rate, ω_m at $\lambda_m = 9.01 R_{\text{eff}}$, these curves are very similar. Note that we have used a non-maximum wavelength, $\lambda > \lambda_m$, in each case so that the RP dynamics occur on a longer timescale (see Appendix B.6, Figure B.3, for a case where λ_m is used). The numerical values of λ and $\omega(\lambda)$ are given in Table 5.2 along with the widths, effective radii, lengths, temperatures and PS length scales. The values of

A_{eff} will be discussed further at the end of Section 5.5. The question now is, how do the values for ω and λ obtained from the RP analysis differ from those obtained via MD simulations? Specifically, we are interested in studying how phase separation interacts with the RP instability and affects the breakup of the lines.

Table 5.2 Temperature, Width W, Wavelength λ, Phase Separation Length Scale λ_{PS}, and Length L, for Lines **A**, **B** and **C**, as well as Transformed Cylinder Effective Radius R_{eff}, and Associated RP Growth-Rate Prediction ω, via Equation (5.2)

Line	Temp. (K)	W (Å)	R_{eff} (Å)	λ (Å)	λ_{PS} (Å)	L (Å)	ω (1/ps)
A	2000	65.0	16.4	292.6	13.0	1463.2	4.3×10^{-2}
B	1400	63.6	16.1	286.7	170.7	1433.7	4.5×10^{-2}
C	1400	71.0	17.9	319.8	315.6	1598.9	3.8×10^{-2}

5.5   Results

In what follows we show how temperature and the phase separation length scale affect the breakup of straight and synthetic lines into nanoparticles, producing results that differ from those predicted by the RP theory. Unless otherwise stated we set the RP length scales to the wavelengths provided in Table 5.2 and denote them λ_{RP} to differentiate from λ_{PS}.
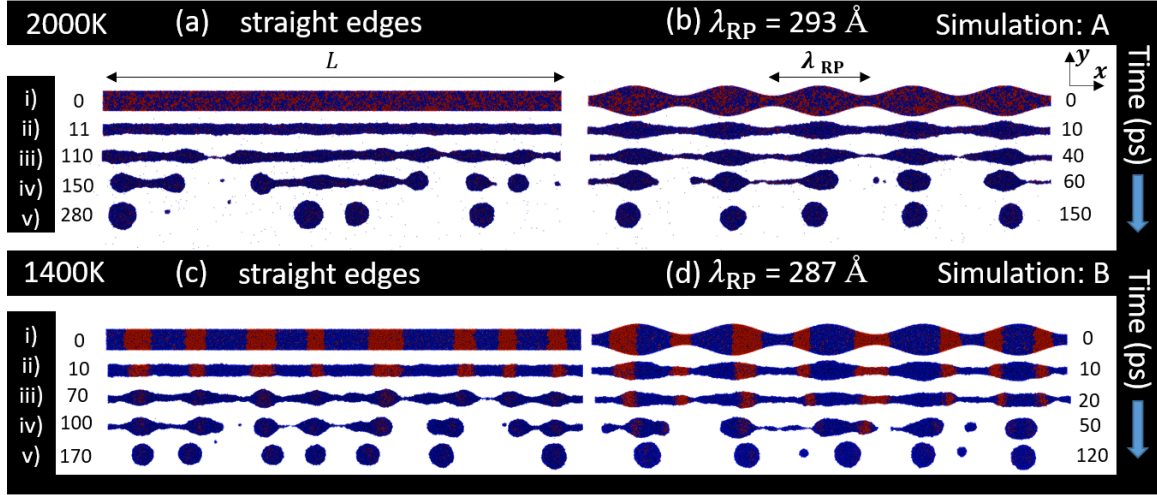
Figure 5.3 Time evolution of straight (left) and synthetic (right) lines at 2000 K ((a) and (b)) and 1400 K ((c) and (d)). The parameters for 2000 K and 1400 K are given in Table 5.2 under **A** and **B**, respectively. Time labels in ps (see text below) are placed next to the corresponding lines. Color code: Ni (red), Ag (blue).

Figure 5.3 shows the temporal evolution of $Ni_{0.5}Ag_{0.5}$ lines in vacuum. Note that the lines are evolved using the NVE ensemble. Straight and synthetic lines are shown in the left and right columns of Figure 5.3, respectively. Labels i)-v) indicate the time stamps at which the lines undergo significant changes during the simulation: i) indicates the initial configuration; ii) the time at which surface perturbations develop; iii) the time immediately prior to the breakup of the line; iv) the intermediate time between the breakup and the formation of nanoparticles; and v) the time of nanoparticle formation. On panel (b), the wavelength of the imposed perturbation is also indicated. In Figure 5.3 a key difference between the initial structures (row i)) is in the relative sizes of the PS and RP length scales. At 2000 K, the PS length scale is a stable RP wavelength (surface perturbations due to PS would decay: $\omega(\lambda_{PS}) < 0$ in Figure 5.2), whereas at 1400 K surface perturbations of wavelength λ_{PS} are RP-unstable ($\omega(\lambda_{PS}) > 0$). For what follows we refer to a small PS length scale as one where PS-induced perturbations decay, and a large PS length scale as one where they grow.

At 2000 K, the PS length scale is small and the straight line (Figure 5.3(a)) develops surface perturbations at 11ps (row ii)) due to small fluctuations in the initial configuration rather than perturbations induced by PS. By comparison, in the synthetic lines (Figure 5.3(b)), at 10 ps (row ii)) the perturbation is already well developed, as expected since the perturbation of wavelength λ_{RP} was already prescribed in the initial configuration. Nanoparticles are formed in the synthetic lines 90 ps faster than in the straight lines. Five nanoparticles are formed in the synthetic lines, which corresponds well to the five patterned wavelengths, whereas in the straight lines the asymmetry of line breakup results in shortening of the resulting line parts via material transport, leading to (in this case) four nanoparticles only. For instance, note that, following line breakup the central part of Figure 5.3(a), row iv) at 150 ps has 3 varicose perturbations (and thus one would expect 4 droplets), but the breakup only occurs near the middle of this region (the surrounding instabilities are suppressed) resulting in just two particles. The two droplets in the rightmost region of Figure 5.3(a), row iv), on the other hand, coalesce into one droplet by row v). The locations of the nanoparticles differ in the straight and synthetic lines. For the latter, as expected, nanoparticles form at the peaks of the perturbation and are well spaced; for the straight lines, the nanoparticles are not equidistant/periodic. For both types of lines, the resultant nanoparticles are homogeneous and contain Ni and Ag in a liquid-like configuration with a small phase separation length scale.

At 1400 K (Figure 5.3(c) and (d)), the PS length scale is large. As the simulations proceed, the troughs of the perturbation develop primarily in Ag-rich regions or at the interface between adjacent Ag-rich/Ni-rich regions. Both lines break up faster than their 2000 K counterparts, 110ps and 30ps faster for the straight and synthetic lines, respectively. This is somewhat counterintuitive: 1400 K is below the melting point of Ni (1728 K) and less than 200 K above the melting point of Ag (1235 K). Therefore, at 1400 K one would expect the atom mobility to be less than at 2000

K and thus breakup to take longer. The reason behind a faster breakup at 1400 K is due to the thinning of the line in Ag-rich locations (Ag "migrates" to neighboring regions faster than does Ni due to the lower melting temperature). The straight line, for instance, forms seven nanoparticles, whereas the synthetic line forms five. Interestingly, these nanoparticles are not uniform but have a core-shell like structure, with Ag in the shell and Ni in the core (see particle slices in Appendix B.6).

For reference, pure Ni and Ag straight lines with comparable $R_{\text{eff}} = 16.1$ Å were simulated at 1400 K (and equilibrated similar to the alloys as described above). The evolution of the pure metals (see Appendix B.7), confirms that the dewetting instability is RP-like even in the Ni metal. In fact, the initial breakup time for Ni (~ 120 ps) is faster than for Ag (140 ps), which confirms that the Ni is largely, if not fully, liquefied as a solid phase filament would dewet much more slowly, even if still RP-like. The faster Ni dewetting time is consistent with Ni having a higher surface energy than Ag. Finally, we also compared the radial distribution functions for Ni-Ni in the bulk and in the filament at 1400 K (from Figure 5.1b and 5.3(c)ii, respectively; see Appendix B.7). As expected, the peak in the Ni-Ni radial distribution function for the ~ 16 Å cylinder is smaller than the bulk, suggestive of a reduced order and at least partial melting.

From the results above, it appears that at 1400 K for lines where the PS length scale is on the order of the RP instability length scale, the soluto-capillary Ag migration induces unstable perturbations that modify the existing RP instability and affect breakup. To investigate this effect more carefully, we created synthetic lines and prescribed perturbations (cut from bulk Figure 5.1c) where troughs are located in the Ag-rich or Ni-rich regions, or close to the interface between these two regions, see Figure 5.4(a), (b), and (c), respectively. In all these lines, the lengths of Ni and neighboring Ag regions sum to the RP wavelength, λ_{RP}. As stated earlier, the length of the Ag phase-separated regions (average length of blue regions in Figure 5.3(c))

is slightly larger than that of the Ni regions. This difference is small, however, thus the structures seen for the lines in Figure 5.4 correspond to the regime where the PS length scales of Ni and Ag are approximately half the RP length scale. Two different perturbation amplitudes were considered, 3.2 Å and 16 Å, which we refer to as small and large amplitudes.
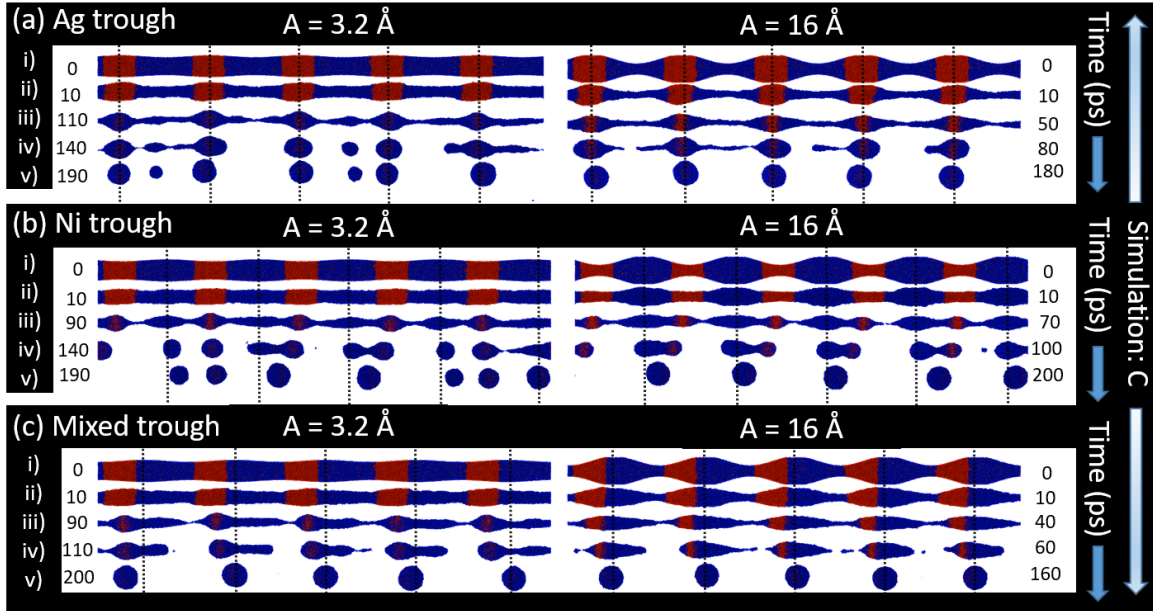
Figure 5.4 Time evolution of synthetic lines for Ag-rich troughs (a), Ni-rich troughs (b), and mixed Ni and Ag troughs (c) for perturbations of amplitudes A=3.2 Å (left) and A=16.0 Å (right). The labels i)-v) correspond to different time intervals in ps with description as in Figure 5.3. Guides (dotted lines) are placed at the location of the original synthetic peak position in i). The geometric details for the lines are given in Table 5.2 under simulation **C**. Color code: Ni (red), Ag (blue).

Figure 5.4 shows the temporal evolution of $Ni_{0.5}Ag_{0.5}$ lines at 1400 K. The troughs of the perturbations are either located at (a) Ag-rich regions (referred to as Ag trough), (b) Ni-rich regions (Ni trough) or (c) mixed Ni/Ag regions (Mixed trough). The main finding is that the location of the resultant nanoparticles differs between (a), (b) and (c).

The primary difference between the small (Figure 5.4, left column) and large amplitude (Figure 5.4, right column) is the time it takes the lines to reach the first

pinch. In general, the large amplitude lines pinch faster than their small amplitude counterparts since there is less material in the trough of the perturbation. The large amplitude case can be thought of as further along in the destabilization process that is inherited from the RP instability. The largest difference in the pinch time (60ps) occurs in case (a). Further, the small amplitude case generates small secondary or satellite particles near two of the perturbation peak regions in Figure 5.4(b), left column.

Figure 5.4(a), (b), and (c) collectively highlight the importance of the initial trough composition. Consider, in the large amplitude cases (right panel of Figure 5.4), the position of the resultant nanoparticles in v) relative to the trough guides (the dashed vertical lines). In (a), the nanoparticles are primarily located at the peak of the perturbation (the dashed lines), which is consistent with the typical RP instability where the material thins at the troughs and accumulates at the peaks. In comparison, the resultant nanoparticles in (b) are slightly misaligned relative to the prescribed peaks. This difference can be explained as follows. The RP instability tends to thin and pinch the lines at the trough of the perturbation. If the trough is Ag-rich, the Ag migration and the RP instability cooperate in breaking the line. However, if the trough is Ni-rich, Ag migration and the RP instability compete. Cooperation and competition should be more apparent in the small amplitude case, since in this case breakup occurs later. Indeed, the left panel of Figure 5.4 shows that for the Ag-rich trough (a), the primary particle positions are aligned with the peak regions. For the Ni-rich trough (b), the trough coarsens slightly as the Ag soluto-capillary effect opposes the RP instability. The initially Ag-rich regions eventually act as the pinch points and the primary particles end slightly off-center from the original synthetic perturbation peak; secondary particles also emerge due to the inter-Ag filament thinning. Notably, all secondary satellite particles are nearly pure Ag and

thus, while most of the core-shell nanoparticles are approximately $Ni_{0.5}Ag_{0.5}$, primary particles that neighbor a secondary satellite are Ag-deficient.
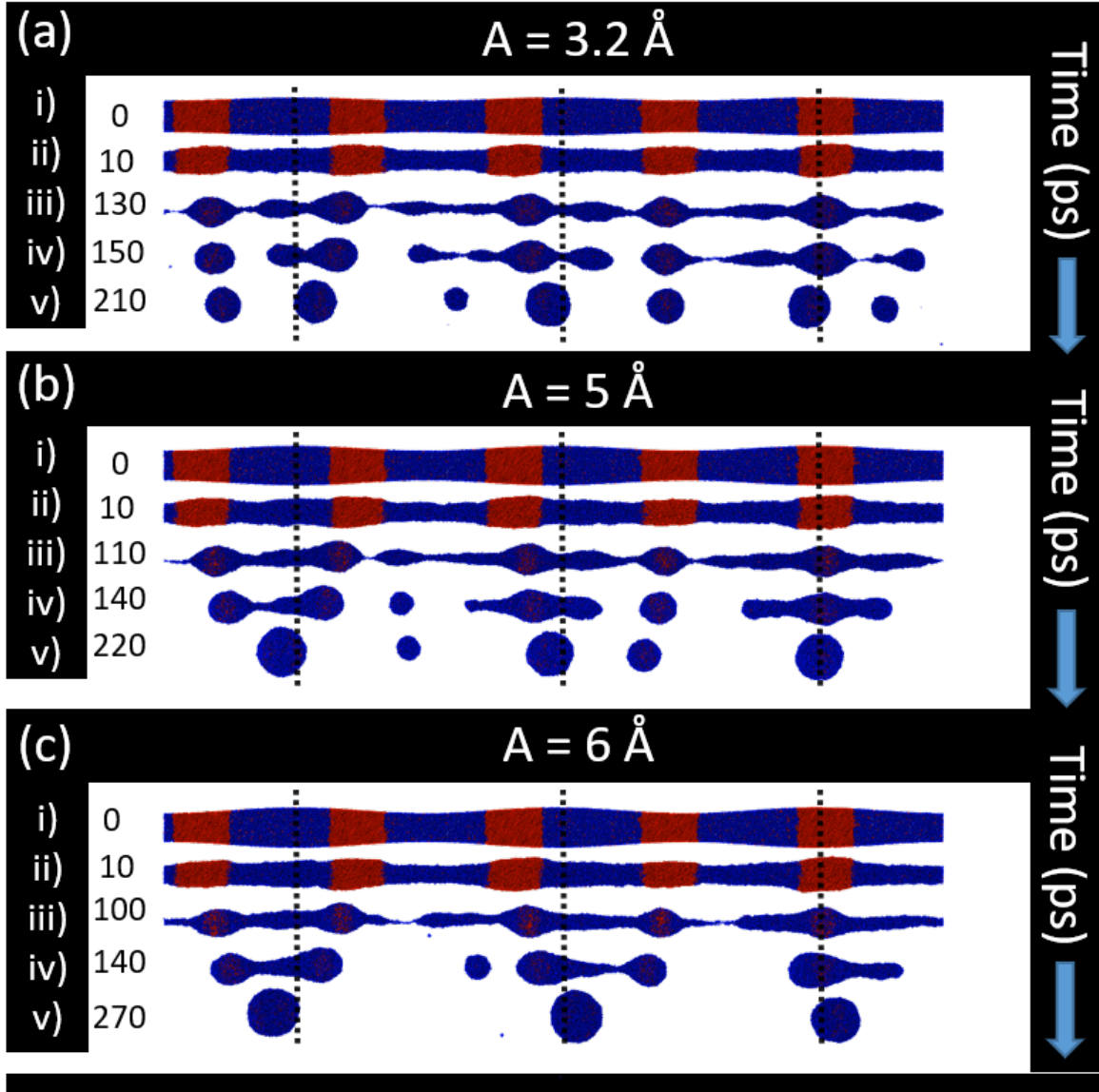
Figure 5.5 Time evolution of synthetic lines patterned with wavelength $\lambda_{RP} = 533.0$ Å and amplitudes $A = 3.2$ Å (a), $A = 5$ Å (b), and $A = 6$ Å (c). Time labels (in ps) are placed next to the corresponding lines. The labels i)-v) correspond to those of in Figure 5.4. Guides (dotted lines) are placed at the location of the original peak in i). Except for the wavelength, the geometric details for the lines are as given in Table 5.2 under simulation **C**. Color code: Ni (red), Ag (blue)

To test the competition between the soluto-capillary effect and the RP, we use the PS length scale, λ_{PS} , from Figure 5.4 (see **C** from Table 5.2 for the parameters);

and in addition we pattern the synthetic perturbations at longer (slower growth rate) unstable wavelengths ($\lambda_{RP} = 533.0$ Å; see Figure 5.2, simulation **C**) and variable amplitudes. Figure 5.5 illustrates the time evolution of these structures with the following initial amplitudes in i): (a) 3.2 Å, (b) 5 Å, and (c) 6 Å (larger amplitudes were also simulated, and the outcomes are similar to (c)). The times i)-iv) are similar to those described for Figure 5.3 and 5.4. Time v) represents the earliest time stamp of full droplet coalescence. The main finding is that the number of resultant primary droplets depends on the amplitude of the prescribed perturbation. At low amplitude ($A < 5$Å; (a)), the soluto-capillary driven instability clearly dominates as 5 primary nanoparticles (droplets roughly comparable in size) result and are positioned near the original Ni-rich regions (the Ag migration offsets the resultant droplet positioning slightly and leads to formation of 2 smaller satellite droplets). At intermediate amplitudes (5Å $< A < 6$Å; (b)), there is a transition: 4 primary nanoparticles result (also one satellite droplet), and the coalescence of two Ni regions occurs adjacent to the peak located in the Ag region (left-most droplet). Finally, at higher amplitudes ($A > 6$Å; (c)), the RP driven instability dominates as 3 primary nanoparticles result and are located at the peaks of the synthetic perturbations.

Table 5.3 Comparison of Simulated Breakup (Pinch) Times and Predicted Pinch Times According to RP Theory for the Simulations **A**, **B**, and **C**, where Label (3) Refers to Figure 5.3 and (4) Refers to Figure 5.4

Temp. (K)	Reference	Amplitude (Å)	Effective Amplitude (Å)	MD Pinch Time (ps)	RP Pinch Time (ps)
2000	(3) (2000 K)	16	4.7	40	29
1400	(3) (1400 K)	16	4.7	30	27
1400	(4) (Ni Trough)	3.2	0.8	100	80
1400	(4) (Ni Trough)	16	4.6	70	35
1400	(4) (Ag Trough)	3.2	0.8	120	80
1400	(4) (Ag Trough)	16	4.6	60	35
1400	(4) (Mixed Trough)	3.2	0.8	100	80
1400	(4) (Mixed Trough)	16	4.6	50	35

Finally, we compare MD pinch times of the nanoscale alloys to RP theory pinch times. Table 5.3 lists the MD simulated breakup times for the simulations reported here (where data was recorded every 10 ps), and the prediction made via RP theory. The theoretical breakup times are based on the linear growth rate ω, amplitude, A,

and effective radius, R_{eff}, via:

$$t_{\text{pinch}} = \frac{-\ln\left(A_{\text{eff}}/R_{\text{eff}}\right)}{\omega}. \tag{5.4}$$

Though detailed statistics and higher time resolution output would enhance the accuracy of the MD pinch time, the simulated breakup times agree well with the theoretical predictions even though, in some instances, PS competes with or enhances RP. Thus, it appears that the soluto-capillary dynamics occur on timescales similar[1] to those of traditional RP.

5.6   Conclusions

Molecular dynamics (MD) simulations are used to investigate the effect of phase separation on the breakup mechanism of thin liquid lines of $Ni_{0.5}Ag_{0.5}$ alloy in vacuum. At 2000 K, the NiAg structures are mostly homogeneous and the defining phase separation (PS) length scale, λ_{PS}, is much smaller than the Rayleigh-Plateau (RP) length scale, λ_{RP}. Here, breakup occurs in the classical manner, as if the structure were homogeneous with material parameters averaged over those of the constituents, and resultant nanoparticles are aligned with the peak of the underlying synthetic perturbations. At 1400 K, the PS length scale is comparable to the RP length scale and the long axis migration of Ag onto Ni influences the resultant droplet location relative to the initial perturbation. The positioning of the final droplets is found to be influenced by the composition of the trough of the undulations and the strength of the RP instability (controlled by the amplitude). For small amplitudes, PS competes with RP when lines contain Ni-rich troughs, resulting in some primary nanoparticles of Ag@Ni core-shell morphology aligned with the initially Ni-rich regions as well as some pure Ag satellite drops. When the troughs contain either Ag-rich or mixed

---

[1]Although the MD pinch times are comparable in size to the RP predictions, they are consistently longer, possibly due to nonlinear effects which slow down the exponential growth predicted by linear stability analysis.

NiAg troughs the RP instability is complemented by the PS structure resulting in primary nanoparticles aligned with the peaks of the initial perturbation. In general, these resultant nanoparticles are of Ag@Ni core-shell morphology, but for the low amplitude, Ag-rich trough, some pure Ag satellite droplets form.

The soluto-capillary/RP competition is further interrogated by simulating lines with PS length scales shorter than λ_{RP}, so that growth of the RP instability is slow relative to PS-induced perturbations. We demonstrate that tuning the synthetic perturbation amplitude dictates whether soluto-capillarity or RP drives the instability. Keeping in mind the average line radius of 35.5 Å, when the amplitude is sufficiently small (here, $A < 5$ Å), soluto-capillarity dominates. Increasing the amplitude increases the "strength" of the RP instability and for $A > 6$Å the RP mechanism dominates. The MD breakup times of the nanoscale alloys are found to be in good agreement with the predictions of RP theory.

CHAPTER 6

CONCLUSIONS AND FUTURE WORK

To conclude, we used both continuum modeling and molecular dynamics simulations to understand the dewetting dynamics of liquid metals with thermal transport. First, in Chapter 2, we focused on pure element metals and formulated an asymptotically-reduced continuum model for heat conduction, model (A), which couples in-plane diffusion within the film to out-of-plane diffusion in the substrate, which is assumed thin. This validity of this model is verified by simulating both a full heat conduction model (F), and a model that neglects in-plane diffusion, model (1D). We found that model (A) is more accurate than (1D), and agrees very well with model (F), while being much more computationally efficient.

Regarding the dimensionless parameters that arise in our continuum model, Ma (Marangoni number), Γ (leading order surface tension), and $\mathcal{M}$ (film viscosity), we find that films that account for time-dependent viscosity fully dewet during the liquid phase, whereas films with constant (melting temperature) viscosity barely evolve, for the same external heating. The time-dependent viscosity arises via an Arrhenius law that specifies viscosity as a function of the spatially-averaged film temperature. The variation of surface tension in time (again via dependence on film-averaged temperature) is found to increase the dewetting speed, but the effect is weaker than that of the time-dependent viscosity. The Marangoni effect was found to be weak in comparison to both, and does not significantly alter the evolution of the film, due to the weak spatial gradients of film temperature.

By empirical arguments, this asymptotic model (A) was then extended, in Chapter 3, to substrates of arbitrary thickness and the influence of the substrate on the temperatures and evolution of the film were investigated. The influence of

the thickness of the substrate, H_s, the heat loss measured by the Biot number, Bi, and temperature-varying thermal conductivity in the substrate, $k(T_\mathrm{s})$, were all investigated. Due to the fast computations afforded by model (A), we were able to simulate a large parameter sweep in Bi, H_s (the parameter Bi characterizes how well insulated the substrate is, with the limit Bi $\rightarrow$ 0 corresponding to a perfectly insulated substrate). The influence of Bi was found to be significant, in that the peak film temperatures and liquid lifetime (LL) of the molten film significantly decrease from small to large Bi. Consequently, the dewetting speeds varied across the range of Bi through time-varying viscosity, and as a result, the films with relatively large Bi solidified prior to fully dewetting. Substrate thickness H_s also alters the peak film temperatures and LLs, in a way that depends strongly on the value of Bi: films on perfectly and poorly insulated substrates behave very differently.

By developing a 3D GPU code that solves the underlying model, (A), we were able to investigate these effects on larger domains, with computational ease. Our 3D simulations revealed clearly the influence of H_s on the film evolution for different substrate Biot numbers. For substrates that are perfectly insulated below (Bi $\rightarrow$ 0), dewetting speed decreases with increased H_s, whereas if the substrate is only poorly-insulated below (Bi $\rightarrow \infty$), dewetting speed increases with substrate thickness. This can result in different final solidified film configurations for different H_s and Bi pairs. Inclusion of temperature-dependent substrate thermal conductivity in our model as well, we found a decrease in the peak film temperatures and LL, resulting in films that solidified close to, but before, the final stages of dewetting.

We next turned our attention to alloys, in Chapters 4 and 5, with a focus on the competition between chemical instabilities and dewetting in $Ni_{0.5}Ag_{0.5}$ alloy nanostructures. Due to the computational complexity of the problem, we used molecular dynamics simulations with the software LAMMPS [107] on both Titan and Summit supercomputers at Oak Ridge National Laboratory. We considered two

structures: a bulk, which contains no free surface, and a sphere, whose surface is freely exposed to vacuum. The latter is used to gather qualitative behavior about the droplets that emerge from the dewetting process. We found that phase separation increases with decreasing temperature. In the spheres the phase separation becomes apparent around 1800 K. By depositing the spheres on graphene substrates, the wettability is used to tune the Lennard-Jones potential governing the liquid-solid interactions.

We then used those potentials to model the competition between phase separation and Rayleigh-Plateau (RP) type instabilities in the alloy free-standing rectanguloid alloys that are patterned with a wave of a given wavelength guided by RP theory. In particular, we looked at two different temperatures (2000 K and 1400 K), which generate different phase separation length scales, λ_{PS}, relative to the RP instability length scale λ_{RP}. We found that when the phase separation length scale is short, $\lambda_{PS} \ll \lambda_{RP}$ (2000 K), the breakup of the rectanguloids is consistent with classical RP theory, whereas when the phase separation length scale is comparable in size to RP, $\lambda_{PS} \approx \lambda_{RP}$, the soluto-capillarity driven instability (concentration gradients) affects the RP instability. Due to the decreased surface energy of Ag relative to Ni, the Ag-rich regions move along the long axis of the rectanguloid early in the dewetting. This induces surface perturbations consistent with λ_{PS} and modifies the RP instability mechanism, resulting in shifted placement of nanoparticles that are either Ag@Ni core-shell or pure Ag.

We conclude by highlighting model limitations and directions for future work. First, the validity of the asymptotic thermal model (A) relies on a number of simplifying assumptions. For example, the time scale of heat conduction in the film is assumed fast relative to film evolution. In this dissertation we used material parameters from copper. Before utilizing this model for other metals the consistency of these assumptions should be checked. Secondly, in all of our continuum modeling

we have neglected in-plane diffusion in the substrate. Although this can be asymptotically justified for thin substrates considered in Chapter 2, this is not the case for the thick substrate simulations presented in Chapter 3. We were able to justify the validity of model (A) in that setting empirically in Appendix A.6, but in other cases the effect of the in-plane derivatives may become important. Utilizing our 3D GPU code to simulate different film configurations where such thermal effects are relevant is one possible future direction of this work. To this point, the in-house numerical code is scalable. So, simulating larger domains than those presented here is possible and should be done so as to better compare to experiments.

When simulating films on thick substrates, some of our simulations revealed very high metal temperatures. However, evaporation of the liquefied metal was neglected in all of our continuum modeling. The inclusion of evaporative losses is another possible future direction of this work, which would make some of the simulations more realistic, and would complement the existing melting/solidification phase changes implemented.

When considering metal alloys we restricted our investigations to molecular dynamics simulations, and did not use any continuum modeling. To develop a consistent continuum model one must couple concentration dynamics (for each metal species present) into the existing thin film dynamics, which would present a significant numerical challenge. Extending the existing 3D GPU code to include such dynamics is one possible direction of future work, and would help bridge the scale between molecular dynamics and experiments. Besides the brief consideration of wettability of droplets, all the molecular dynamics metal alloy simulations presented were performed in vacuum. Performing these simulations on substrates would certainly be relevant and interesting, and should be done so as to compare to both continuum modeling and experiments. Furthermore, future studies warrant the simulation of other geometries considered in experiments such as films [32, 67] and rings [141].

APPENDIX A

IMPLEMENTATION DETAILS AND ADDITIONAL RESULTS FOR THE CONTINUUM SIMULATIONS OF PURE METAL FILMS

In this appendix, we provide additional results and discuss details of the simulations performed in Chapters 2 and 3. This includes, but is not limited to, a discussion on the choice of scalings made, the values of parameters used, and the numerical algorithms used.

A.1 Scalings and Parameter Values for Simulations of Films on Thin Substrates

A.1.1 Discussion of the Choice of Scales and Table of Parameters

The choice of scales has important implications for the derivation of both the thin film equation (Equation (2.48)) and the thermal model (A) (Equations (2.34)-(2.39)). The choice of timescale is typically based on the fluid flow, L/U. From the perspective of the thermal model, however, the pulsed laser heating duration is on the order of nanoseconds. With the timescale choice L/U, L and U should be chosen consistent with such a thermal time scale, while still retaining surface tension effects in the fluid flow model, known to be important. Therefore, we choose $U = \epsilon^3 \gamma_f/(3\mu_f)$ and scale L on the (inverse) wavenumber of maximum growth $k_m = 2\pi/\lambda_m$ as $L = k_m^{-1}$ (from Section 2.4.1) so that surface tension effects and disjoining pressure are retained to leading order. The tradeoff is that the aspect ratio ϵ consistent with the data (Table A.1) is rather large, 0.246. However, the time scale is then on the order of nanoseconds, as desired, and we consider this acceptable in order to develop a consistent model.

For the materials in question, the values of $Pe_f, Pe_s, \mathcal{K}$, and Bi are small despite the $O(1)$ assumption (Table A.1). This is primarily a consequence of the size of ϵ, which is directly related to the dependence of L on λ_m. Given this observation,

124

Table A.1 Parameters used for Liquid Cu Film and Thin SiO$_2$ Substrate

Parameter	Notation	Value	Unit
Base Viscosity	μ_{f} [33]	4.3×10^{-3}	Pa $\cdot$ s
Base Surface tension	γ_{f} [33]	1.303	J $\cdot$ m^{-2}
Vertical length scale	H	10	nm
Horizontal length scale	$L = \lambda_{\mathrm{m}}/(2\pi)$	40.58	nm
Time scale	$t_{\mathrm{s}} = 3L\mu_{\mathrm{f}}/(\epsilon^3\gamma_{\mathrm{f}})$	26.86	ns
Melting Temperature	T_{melt}	1358	K
Film density	ρ_{f} [33]	8000	kg $\cdot$ m^{-3}
SiO$_2$ density	ρ_{s} [33]	2200	kg $\cdot$ m^{-3}
Film specific heat capacity	c_{f} [33]	495	J $\cdot$ kg^{-1} $\cdot$ K^{-1}
SiO$_2$ specific heat capacity	c_{s} [33]	937	J $\cdot$ kg^{-1} $\cdot$ K^{-1}
Film heat conductivity	k_{f} [33]	340	W $\cdot$ m^{-1} $\cdot$ K^{-1}
SiO$_2$ heat conductivity	k_{s} [33]	1.4	W $\cdot$ m^{-1} $\cdot$ K^{-1}
Film absorption length	$\alpha_{\mathrm{f}}^{-1}H$ [33]	11.09	nm
Temp. Coeff. of Surf. Tens.	γ_{T} [33]	-0.23×10^{-3}	J $\cdot$ m^{-2} $\cdot$ K^{-1}
Hamaker constant	A_{H} [52]	1.75×10^{-17}	J
Reflective coefficient	r_0 [33]	0.3655	1
Film reflective length	$\alpha_{\mathrm{r}}^{-1}H$ [33]	12.0	nm
Laser energy density	E_0 [92]	300	J $\cdot$ m^{-2}
Gaussian pulse peak time	$t_{\mathrm{p}}t_{\mathrm{s}}$ [92]	15	ns
Equilibrium film thickness	h_*H	1	nm
Mean Film thickness	h_0H	10	nm
SiO$_2$ thickness	$H_{\mathrm{s}}H$	10	nm
Room temperature	$T_{\mathrm{a}}T_{\mathrm{melt}}$	300	K
SiO$_2$ Heat Transfer Coefficient	α	3.0×10^5	W $\cdot$ m^{-2} $\cdot$ K^{-1}
Characteristic Velocity	U	1.504	m $\cdot$ s^{-1}
Activation Energy	E	30.5	kJ $\cdot$ mol^{-1}

Table A.2 Dimensionless Parameters used for Liquid Cu Film and SiO$_2$ Substrate

Dimensionless Numbers	Notation	Value	Expression
Aspect Ratio	ϵ	0.246	H/L
Reynolds Number	Re	0.114	$\rho_{\mathrm{f}} U L / \mu_{\mathrm{f}}$
Film Peclet Number	Pe$_{\mathrm{f}}$	7.14×10^{-4}	$(\rho c)_{\mathrm{f}} U L / k_{\mathrm{f}}$
Substrate Peclet Number	Pe$_{\mathrm{s}}$	5.46×10^{-3}	$(\rho c)_{\mathrm{s}} U \epsilon H / k_{\mathrm{s}}$
Biot Number	Bi	2.14×10^{-3}	$\alpha H / k_{\mathrm{s}}$
Marangoni Number	Ma	0.360	$3\gamma_{\mathrm{T}} T_{\mathrm{melt}} / (2\gamma_{\mathrm{f}})$
Thermal Conductivity Ratio	$\mathcal{K}$	0.068	$k_{\mathrm{s}} / (\epsilon^2 k_{\mathrm{f}})$
Range of Dimensionless Viscosity	$\mathcal{M}$	$0.028 - 1$	μ / μ_{f}

we briefly consider the limit of small Pe$_{\mathrm{f}}$, Pe$_{\mathrm{s}}$, $\mathcal{K}$, and Bi. Firstly, in the limit Pe$_{\mathrm{f}} \to 0$, Equation (2.34) would reduce to a quasi-steady (no time-derivative) equation governing temperature $T_{\mathrm{f}}(x, y, t)$ in the film. The resultant equation is computationally more difficult to solve (and leads to only negligible differences), so we do not adopt this approach. Secondly, in the limit Pe$_{\mathrm{s}} \to 0$, the solution to Equation (2.35) would be linear in z. The numerical solutions given in Figure 2.4 display substrate temperatures that deviate from linear behavior in z. We consider this the motivation for retaining Pe$_{\mathrm{s}}$ in Equation (2.35) (which leads to better agreement between models (A) and (F)). In the limit $\mathcal{K} \to 0$, film temperature no longer depends directly on substrate temperature (although the substrate temperature still depends on the film temperature). Since the primary heat loss mechanism is considered to be through the film-substrate interface, we retain $\mathcal{K}$ in Equation (2.34). If the primary heat loss mechanism is elsewhere, it may be possible to drop the term containing $\mathcal{K}$ in Equation (2.34). Finally, in the limit Bi $\to 0$, Equation (2.37) becomes an insulating boundary condition, which in turn leads to much higher substrate/film temperatures. In the case where SiO$_2$ sits on a native layer of Si it is expected that there is some heat transfer. Therefore, we retain Bi in Equation (2.37).

A.1.2 Wavelength of Maximum Growth

When the material parameters are fixed at melting temperature, $\Gamma, \mathcal{M} = 1$, the dimensional dispersion relation can be written as:

$$\beta(k) = \frac{h_0^2 H^2 k^2}{3\mu_{\mathrm{f}}} \left(P_0 - \gamma_{\mathrm{f}} H h_0 k^2 \right), \tag{A.1}$$

$$P_0 = \frac{A_{\mathrm{H}}}{6\pi h_*^3 H^3} \left[m \left(\frac{h_*}{h_0} \right)^m - n \left(\frac{h_*}{h_0} \right)^n \right], \tag{A.2}$$

where (in this section only) $\beta(k)$ is the dimensional growth rate and k the dimensional wavenumber. The remaining parameters are given in Table A.1. The wavelength of maximum growth, λ_{m}, can then be found by setting $\partial\beta/\partial k = 0$ and written as

$$\lambda_{\mathrm{m}} = 2\pi \left/ \sqrt{\frac{A_{\mathrm{H}}}{12\pi\gamma_{\mathrm{f}} h_*^3 H^3 h_0} \left[m \left(\frac{h_*}{h_0} \right)^m - n \left(\frac{h_*}{h_0} \right)^n \right]}\right. .$$

For the parameters used in Chapter 2, $\lambda_{\mathrm{m}} = 255$nm. For the entirety of Chapter 2, this value is used to define a base length scale $L = \lambda_{\mathrm{m}}/(2\pi)$.

A.2 Effect of Spatially Varying Viscosity with a Larger Biot Number

Here we increase the Biot number to $\mathrm{Bi} = 5.71 \times 10^{-3}$ (more than twice the value used in the main text; see Table A.1). This leads to much earlier resolidification of the film (for (A) resolidification occurs at $t \approx 2.8$ whereas for (1D) $t \approx 2.7$). We specifically focus on the influence of model choice when the spatiotemporally-varying viscosity is used, $\mathcal{M}(x, t)$.
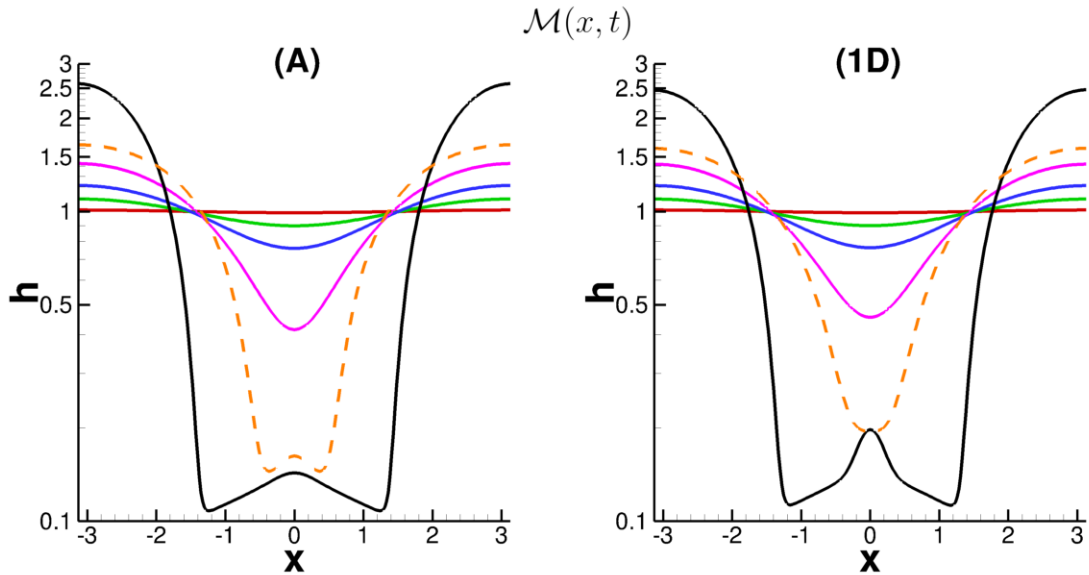
Figure A.1 Film thickness evolution for both the asymptotic model (left) and the 1D model (right) for the spatiotemporal varying viscosity case $\mathcal{M}(x,t)$. The y-axis is plotted on a log scale to emphasize satellite droplet formation which is more prominent with (1D) than with (A). Here the Biot number is $\text{Bi} = 5.71 \times 10^{-3}$. The times are: $t = 0$ (red), $t = 1.47$ (green), $t = 1.84$ (blue), $t = 2.21$ (magenta), $t = 2.40$ (orange dashed), resolidification of (1D), $t = 2.69$ (black).

Figure A.1 shows the film evolution for both models (A) (left) and (1D) (right). The black solid line represents the film profiles at the (1D) solidification time (model (A) predicts a larger solidification time but the final solidified film configuration is nearly identical to the black solid line in Figure A.1a). The times are given in the caption. The main finding is that for sufficiently large α the decay of the satellite droplet that forms for both (A) and (1D) is slower in (1D). Essentially, for (1D) the satellite droplet is cold relative to the thicker parts of the film (recall the much more significant x-variation of temperature observed for (1D)). Since the viscosity varies with space the centre ($x = 0$) of the satellite droplet approaches the precursor thickness more slowly than the surrounding area. In (A), the temperature variation with x is less pronounced and so the satellite droplet has drained more than its (1D) counterpart before reaching the final solidified configuration. In summary, these

results demonstrate that the choice of thermal model can influence the final resulting film profiles.

A.3 Numerical Schemes for Films on Thin Substrates with Constant Substrate Thermal Conductivity

A.3.1 Numerical Solution of Model (F)

To solve Equation (2.5) numerically, along with corresponding boundary conditions in model (F), we define the new variables (u, v, τ) as:

$$u = x, \qquad v = \frac{z h_0}{h}, \qquad \tau = t,$$

which is a time-dependent mapping transforming the deformable domain, describing the film, into a fixed rectangle (see Figure A.2 below).
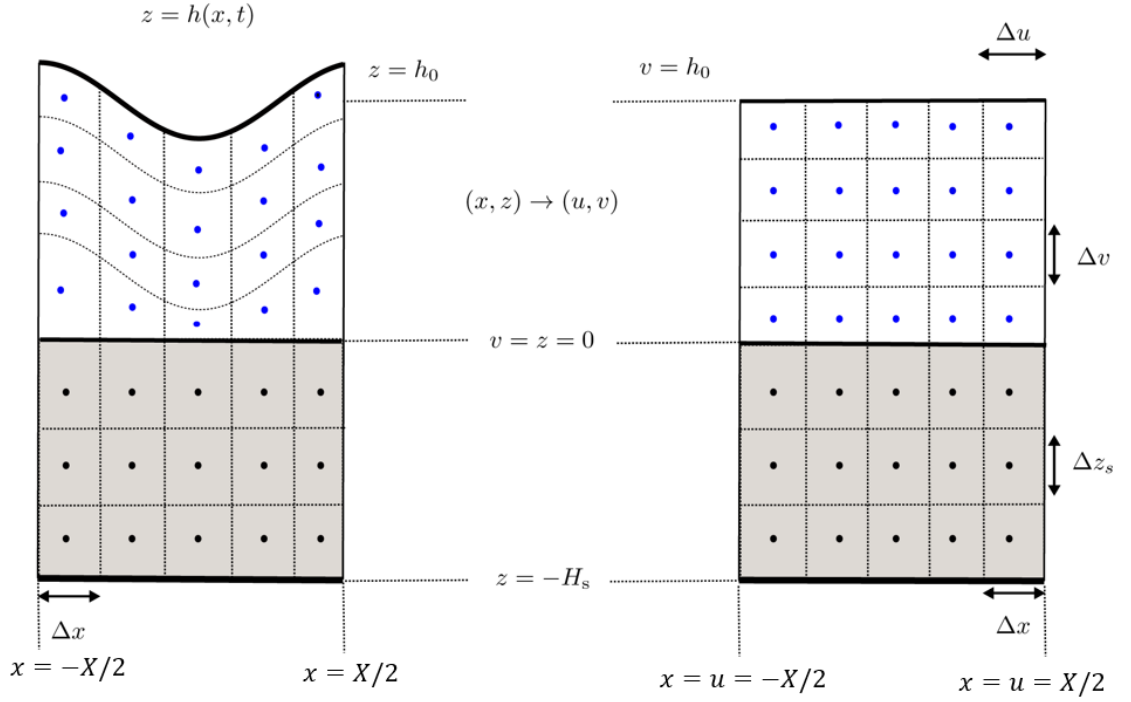
Figure A.2 Schematic of mapping used to transform the computational domain for (F). Here the domain width shown is $X = 2\pi$. Blue points represent the film domain and black points represent the substrate domain.

This approach trades a simplified domain for an increase in complexity of the thermal equation in the film. Equation (2.5) is transformed into the following differential equation:

$$\partial_\tau T_\mathrm{f} = \frac{1}{\mathrm{Pe_f}} \partial_u^2 T_\mathrm{f} + B(u,v)\partial_{uv} T_\mathrm{f} + A(u,v)\partial_v^2 T_\mathrm{f} + F(u,v)\partial_v T_\mathrm{f} + Q(h(u),v,\tau), \quad \text{(A.3)}$$

where

$$B(u, v) = -\frac{1}{\text{Pe}_\text{f}} \left(\frac{2v\partial_u h}{h} \right),$$

$$A(u, v) = \frac{1}{\text{Pe}_\text{f}} \left[\left(\frac{v\partial_u h}{h} \right)^2 + \frac{1}{\epsilon^2} \left(\frac{h_0}{h} \right)^2 \right],$$

$$F(u, v) = \frac{1}{\text{Pe}_\text{f}} \left(\frac{vh\partial_u^2 h}{h^2} - \frac{v(\partial_u h)^2}{h^2} \right) + \frac{v\partial_\tau h}{h},$$

$$Q(h(u), v, \tau) = \frac{F(t)}{\text{Pe}_\text{f}} \left[1 - R(h) \right] \exp\left[-\alpha_\text{f} \left(h - hv/h_0 \right) \right],$$

are the coefficients, and subscripts u, v, τ denote partial derivatives. To solve Equation (A.3) numerically the ADI method is used, with the term containing $B(u, v)$ treated explicitly. A Crank-Nicolson scheme is used to solve Equation (2.6), the heat equation in the substrate. We use a cell-centered grid system:

$$u_i = x_i = x_0 + \Delta x \left(i - 1/2 \right), \quad i = 1, \ldots, n, \qquad \Delta u = \Delta x = \frac{(x_\text{max} - x_0)}{n},$$

$$z_j = -\left(j - 1/2 \right) \Delta z_s, \quad j = 1, \ldots, n_\text{s}, \qquad \Delta z_s = \frac{H_\text{s}}{n_\text{s}},$$

$$v_j = h_0 - \left(j - 1 \right) \Delta v, \quad j = 1, \ldots, n_\text{f}, \qquad \Delta v = \frac{h_0}{n_\text{f}},$$

$$T_{i,j}^k \approx \begin{cases} T_\text{f}(u_i, v_j, t_k), & 1 < j < n_\text{f}, \\ \\ T_\text{s}(x_i, z_j, t_k), & n_\text{f} + 1 < j < n_\text{f} + n_\text{s}, \end{cases}$$

$$h_i^k \approx h(u_i, t_k), \quad Q_{i,j}^k \approx Q(u_i, v_j, t_k).$$

The numerical system can be then written as:

$$\frac{T^*_{i,j} - T^k_{i,j}}{\Delta t} = D^*_{i,j} + G^k_{i,j} + M^k_{i,j} + \frac{1}{2}Q^{k+1/2}_{i,j},$$

$$\frac{T^{k+1}_{i,j} - T^*_{i,j}}{\Delta t} = D^*_{i,j} + G^{k+1}_{i,j} + \frac{1}{2}Q^{k+1/2}_{i,j},$$

$$D^*_{i,j} = \begin{cases} \frac{1}{2}\mathrm{Pe}_\mathrm{f}^{-1}\delta^2_u T^*_{i,j}, & j \le n_\mathrm{f}, \\[2mm] \frac{1}{2}\epsilon^2\mathrm{Pe}_\mathrm{s}^{-1}\delta^2_x T^*_{i,j}, & j \ge n_\mathrm{f}+1, \end{cases}$$

$$G^k_{i,j} = \begin{cases} \frac{1}{2}A^k_{i,j}\delta^2_v T^k_{i,j} + \frac{1}{2}F^k_{i,j}\delta_v T^k_{i,j}, & j \le n_\mathrm{f}, \\[2mm] \frac{1}{2}\mathrm{Pe}_\mathrm{s}^{-1}\delta^2_z T^k_{i,j}, & j \ge n_\mathrm{f}+1, \end{cases}$$

$$M^k_{i,j} = \begin{cases} B^k_{i,j}\delta_{uv} T^k_{i,j}, & j \le n_\mathrm{f}, \\[2mm] 0, & j > n_\mathrm{f}, \end{cases}$$

where $T_\mathrm{f}(x_i, z_j, t_k) \approx T^k_{i,j}$ is a discretisation of the film temperature, and $T^*_{i,j}$ represents the solution at an intermediate time-step. In the interior grid the spatial derivatives are given by:

$$\delta_u T_{i,j} = \frac{T_{i+1,j} - T_{i-1,j}}{2\Delta u}, \qquad \delta_v T_{i,j} = \frac{T_{i,j-1} - T_{i,j+1}}{2\Delta v},$$

$$\delta^2_x T_{i,j} = \delta^2_u T_{i,j} = \frac{T_{i+1,j} - 2T_{i,j} + T_{i-1,j}}{\Delta u^2},$$

$$\delta_{uv} T_{i,j} = \frac{T_{i+1,j-1} - T_{i-1,j-1} - T_{i+1,j+1} + T_{i-1,j+1}}{4\Delta u \Delta v},$$

$$\delta^2_z T_{i,j} = \frac{T_{i,j-1} - 2T_{i,j} + T_{i,j+1}}{\Delta z_\mathrm{s}^2}, \qquad \delta^2_v T_{i,j} = \frac{T_{i,j+1} - 2T_{i,j} + T_{i,j-1}}{\Delta v^2},$$

which are second-order central difference approximations and the source, Q, is approximated by an average at times t_k, and t_{k+1},

$$Q^{k+1/2}_{i,j} = \frac{1}{2}\left(Q^{k+1}_{i,j} + Q^k_{i,j}\right).$$

A.3.2 Numerical Solution of Model (A)

We use the same cell-centered grid as §A.3.1 except for z_j:

$$z_j = -(j-1)\Delta z_{\mathrm{s}}, \quad j = 1, \ldots, n_{\mathrm{s}}, \qquad \Delta z_{\mathrm{s}} = \frac{H_{\mathrm{s}}}{n_{\mathrm{s}} - 1/2},$$

so that a grid point exists on the liquid-solid interface (a Dirichlet boundary condition is prescribed there). For simplicity we let $T_i^k \approx T_{\mathrm{f}}(x_i, t_k)$, $S_{i,j}^k \approx T_{\mathrm{s}}(x_i, z_j, t_k)$ and

$$F_i^k = \frac{1}{\mathrm{Pe_f}} \left[\delta_x^2 T_i^k + \left(\frac{\partial_x h}{h} \right)_i^k \delta_x T_i^k \right],$$

$$G_i^k = -\frac{\mathcal{K}}{\mathrm{Pe_f} h_i^k} \partial_z (S)_I^k,$$

where $\partial_z (S)_I^k = \partial T_{\mathrm{s}}/\partial z|_{z=0}(t = t_k)$. To solve Equation (2.34) and (2.35) we use a predictor-corrector Runge-Kutta/Crank-Nicolson scheme. In the prediction phase we use a forward-Euler scheme to deal with G_i^k:

$$\frac{T_i^{k+1} - T_i^k}{\Delta t} = \frac{1}{2} \left[F_i^{k+1} + F_i^k \right] + G_i^k + \overline{Q}_i^{k+1/2}, \quad i = 1, \ldots, n,$$

$$\frac{S_{i,j}^{k+1} - S_{i,j}^k}{\Delta t} = \frac{1}{2} \mathrm{Pe_s}^{-1} \left[\delta_z^2 S_{i,j}^{k+1} + \delta_z^2 S_{i,j}^k \right], \quad j = 2, \ldots, n_{\mathrm{s}}, \qquad i = 1, \ldots, n,$$

where $\overline{Q}_i^{k+1/2} = (\overline{Q}_i^k + \overline{Q}_i^{k+1})/2$. We then correct this prediction by using a Runge-Kutta, order 2, method on G_i^k using the prediction $\hat{G}_i^k$:

$$\frac{T_i^{k+1} - T_i^k}{\Delta t} = \frac{1}{2} \left[F_i^{k+1} + F_i^k \right] + \frac{1}{2} \left(G_i^k + \hat{G}_i^k \right) + \overline{Q}_i^{k+1/2}, \quad i = 1, \ldots, n,$$

$$\frac{S_{i,j}^{k+1} - S_{i,j}^k}{\Delta t} = \frac{1}{2} \mathrm{Pe_s}^{-1} \left[\delta_z^2 S_{i,j}^{k+1} + \delta_z^2 S_{i,j}^k \right], \quad j = 2, \ldots, n_{\mathrm{s}}, \qquad i = 1, \ldots, n.$$

A.3.3 Numerical Solution of Model (1D)

The numerical scheme used for model (1D) is a simple Crank-Nicolson scheme:

$$\frac{T_{i,j}^{k+1} - T_{i,j}^k}{\Delta t} = \frac{1}{2} \epsilon^{-2} \mathrm{Pe_f}^{-1} \left(\delta_z^2 T_{i,j}^k + \delta_z^2 T_{i,j}^{k+1} \right) + Q_{i,j}^{k+1/2}, \qquad j = 1, \ldots, n_{\mathrm{f}}$$

$$\frac{T_{i,j}^{k+1} - T_{i,j}^k}{\Delta t} = \frac{1}{2} \mathrm{Pe_s}^{-1} \left(\delta_z^2 T_{i,j}^k + \delta_z^2 T_{i,j}^{k+1} \right), \qquad j = n_{\mathrm{f}} + 1, \ldots, n_{\mathrm{f}} + n_{\mathrm{s}},$$

where $i = 1, \ldots, n$ and n, n_{f} and n_{s} are the same as in §A.3.1.

A.3.4 Convergence Results

For what follows we define the discrete $L2$ error, $E(t)$, where

$$E^2(t) = \frac{\sum\limits_{i=1}^{n} \left(\sum\limits_{j=1}^{n_{\mathrm{f}}} \Delta z_i \left| T_{i,j}^{\mathrm{comp}} - T_{i,j}^{\mathrm{bench}} \right|^2 + \Delta z_{\mathrm{s}} \sum\limits_{j=1}^{n_{\mathrm{s}}} \left| T_{i,j}^{\mathrm{comp}} - T_{i,j}^{\mathrm{bench}} \right|^2 \right)}{\sum\limits_{i=1}^{n} \left(\sum\limits_{j=1}^{n_{\mathrm{f}}} \Delta z_i \left| T_{i,j}^{\mathrm{bench}} \right|^2 + \Delta z_{\mathrm{s}} \sum\limits_{j=1}^{n_{\mathrm{s}}} \left| T_{i,j}^{\mathrm{bench}} \right|^2 \right)},$$

and $T_{i,j}^{\mathrm{comp}}$ is the computed temperature and $T_{i,j}^{\mathrm{bench}}$ is a benchmark solution which, for the results presented next, we take to be the numerical solution on the finest grid since no exact solution is known.
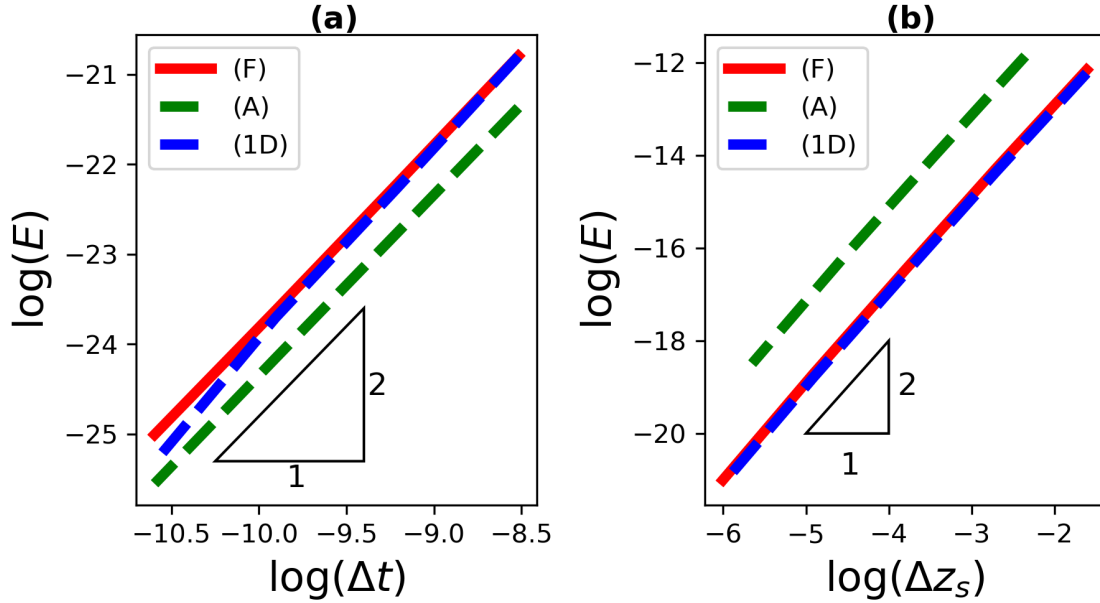
Figure A.3 **(a)** Δt convergence for (F), (A), and (1D) in the stationary curved film case. All models use $O(\Delta t^2)$ schemes. **(b)** Δz_{s} convergence for (F), (A), and (1D) in the stationary curved film case where h is given by Equation (2.52), but time-independent. All models use $O(\Delta z_{\mathrm{s}}^2)$ schemes.
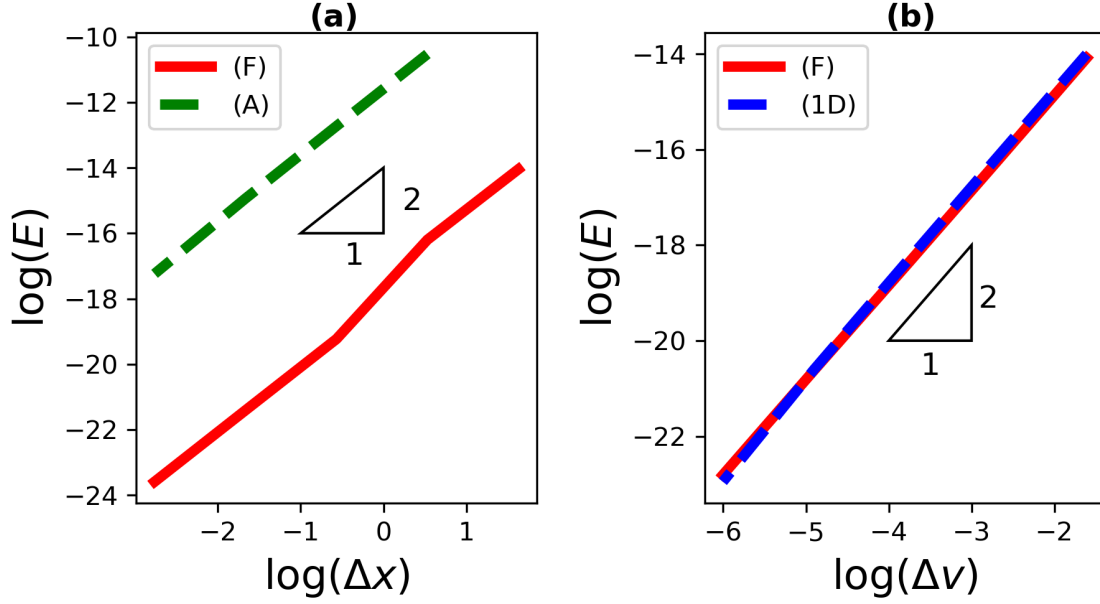
Figure A.4 **(a)** Δx convergence for (F) and (A) in the stationary curved film case (Note that (1D) has no derivatives with respect to x). Each model uses a $O(\Delta x^2)$ scheme. **(b)** Δv convergence for (F) and (1D) in the stationary curved film case (Note that T_f is independent of z for (A)). Each model uses a $O(\Delta v^2)$ scheme.

A.4 Variation of Temperature with Film Thickness

In the case when the film is flat, its temperature is independent of the in-plane variables and conservation of energy may be reduced to an expression for the average film temperature, written as a simple balance of source heating and substrate cooling:

$$\partial_t T_\mathrm{avg} = \mathrm{Pe}_\mathrm{f}^{-1} \left[\frac{-\mathcal{K}}{h} \left(\partial_z T_\mathrm{s} \right) |_{z=0} + \overline{Q} \right]. \tag{A.4}$$
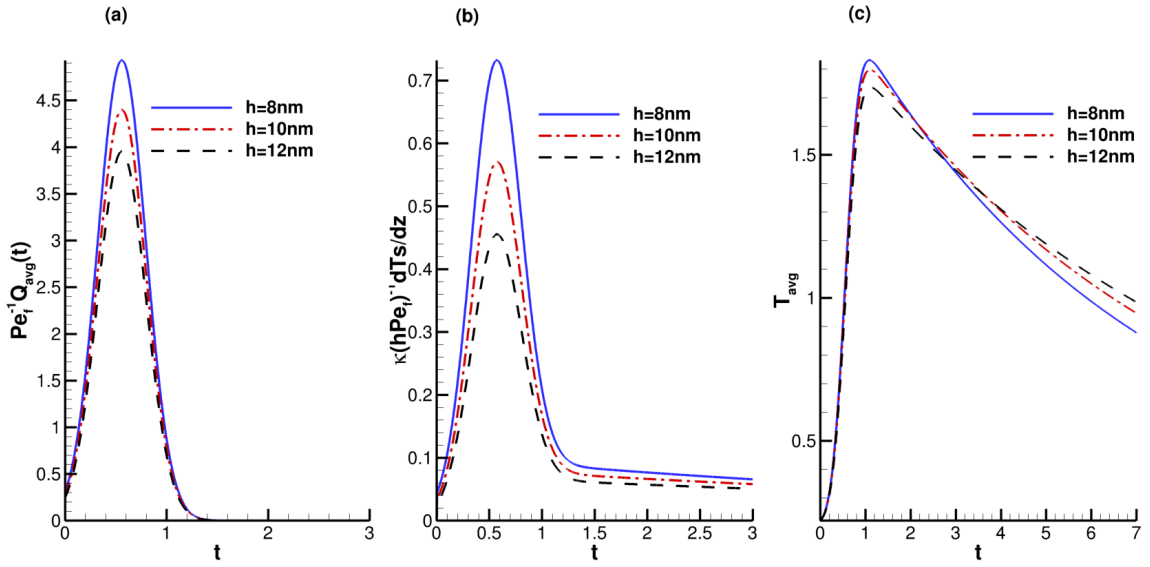
Figure A.5 (a) Average Source, $\overline{Q}$, and (b) magnitude of film heat loss through the substrate, $\mathcal{K}(hPe_\mathrm{f})^{-1}\partial_z T_\mathrm{s}|_{z=0}$ and (c) average film temperature all for flat films of $h = 8$nm (blue, solid), $h = 10$nm (red, dot-dashed), and $h = 12$nm (black, dashed).

Figure A.5 shows the variation of both (a) source heating (measured by $Pe_\mathrm{f}^{-1}\overline{Q}$) and (b) substrate cooling (measured by $(hPe_\mathrm{f})^{-1}\left(\partial_z T_\mathrm{f}\right)|_{z=0}$) for three different film thicknesses, $h = 8, 10, 12$ nm. Figure A.5(c) gives the average film temperatures for each case. As seen in Figure A.5(a), thinner films retain more energy from the source and, in the absence of cooling, should be hotter. Physically, thicker films reflect more energy and absorb less. Although (to keep the presentation simple) we use $\overline{Q}$ here rather than Q from Equation (2.18), it can be shown also that $dQ/dh < 0$ for all times. Figure A.5(b) demonstrates that thinner films also cool faster (through the substrate) than thicker ones. When these two effects are combined, we arrive at average film temperatures that are non-monotonic in film thickness h. In Figure A.5(c), thinner films are observed to be initially hotter over the early stages of evolution, primarily due the magnitude of the laser heating, which is initially larger than that of cooling. Over the later stages, the source decreases in strength sufficiently so that the trend of cooling with film thickness is dominant and thinner films are colder. Note that this

non-monotonic behavior depends on the relative strengths of the heat source and the cooling term and may change if different forms are used to describe these effects. The explanation given above is the primary reason for the behavior seen in Figure 2.2(b).

A.5 Values of Parameters

Table A.3 Parameters used for Liquid Cu Film and Thick SiO_2 Substrate

Parameter	Notation	Value	Unit
Base Viscosity	μ_f [33]	4.3×10^{-3}	$Pa \cdot s$
Base Surface tension	γ_f [33]	1.303	$J \cdot m^{-2}$
Wavelength of max. growth	λ_m	180.84	nm
Vertical length scale	H	10	nm
Horizontal length scale	$L = \lambda_m/(2\pi)$	28.78	nm
Time scale	$t_s = 3L\mu_f/(\epsilon^3\gamma_f)$	26.86	ns
Melting Temperature	T_{melt}	1358	K
Film density	ρ_f [33]	8000	$kg \cdot m^{-3}$
SiO_2 density	ρ_s [33]	2200	$kg \cdot m^{-3}$
Film specific heat capacity	c_f [33]	495	$J \cdot kg^{-1} \cdot K^{-1}$
SiO_2 specific heat capacity	c_s [33]	937	$J \cdot kg^{-1} \cdot K^{-1}$
Film heat conductivity	k_f [33]	340	$W \cdot m^{-1} \cdot K^{-1}$
SiO_2 heat conductivity	k_s [33]	1.4	$W \cdot m^{-1} \cdot K^{-1}$
Film absorption length	$\alpha_f^{-1}H$ [33]	11.09	nm
Temp. Coeff. of Surf. Tens.	γ_T [33]	-0.23×10^{-3}	$J \cdot m^{-2} \cdot K^{-1}$
Hamaker constant	A_H [52]	3.49×10^{-17}	J
Reflective coefficient	r_0 [33]	0.3655	1
Film reflective length	$\alpha_r^{-1}H$ [33]	12.0	nm
Laser energy density	E_0 [52]	1400	$J \cdot m^{-2}$
Gaussian pulse peak time	$t_p t_s$ [52]	18	ns
Equilibrium film thickness	$h_* H$	1	nm
Mean Film thickness	$h_0 H$	10	nm
SiO_2 thickness	$H_s H$	$50 - 250$	nm
Room temperature	$T_a T_{melt}$	300	K
SiO_2 Heat Transfer Coefficient	α_s	$10^5 - 10^{11}$	$W \cdot m^{-2} \cdot K^{-1}$
Characteristic Velocity	U	4.237	$m \cdot s^{-1}$
Activation Energy	E	30.5	$kJ \cdot mol^{-1}$

A.6 Model Validity: Neglecting Lateral Heat Diffusion in the Substrate

For brevity, we denote the asymptotically-reduced model described by Equations (3.6)-(3.11) as model (A). In our previous work on this system [3], it was assumed that the film is placed upon a substrate sufficiently thin that neglecting in-plane diffusion in the substrate is asymptotically justified. In Section 3.3 of the present work, we allow the underlying substrate to be thick relative to the film, so the validity of dropping terms representing in-plane diffusion in the substrate remains to be seen. For this purpose, we consider a model, denoted (FA),[1] which includes Equation (3.6) and Equations (3.8)–(3.11), but replaces Equation (3.7) with a full heat transport model in the substrate,

$$\mathrm{Pe}_\mathrm{s}\partial_t T_\mathrm{s} = \epsilon^2\partial_x^2 T_\mathrm{s} + \partial_z^2 T_\mathrm{s}. \tag{A.5}$$

---

[1]Here, "F" indicates that a "full" model is used for heat flow in the substrate, while "A" denotes the "asymptotically" reduced model that applies to heat transport in the film.
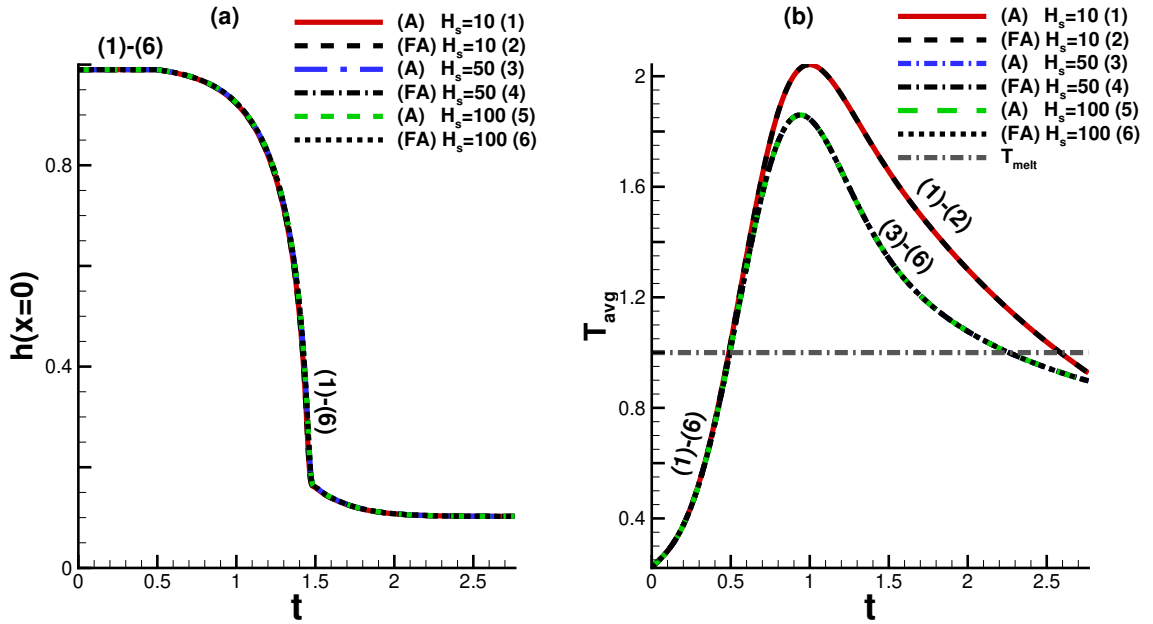
Figure A.6   (a) Film thickness at the midpoint, $x = 0$, and (b) average film temperature for model (A) (the one given by Equations (3.6)–(3.11) and model (FA) where Equation (3.7) is replaced by Equation (A.5). Models (A) and (FA) agree for substrate thicknesses $H_s = 10, 50$, and 100. For both (a) and (b) the parameters were held constant $\Gamma = \mathcal{M} = k = 1$ and $\mathrm{Bi} \approx 4.3 \times 10^{-2}$.

Figure A.6(a) shows the evolution of the film thickness at the midpoint, $x = 0$, (a) and average film temperature (b) for 2D films on substrates of thicknesses $H_s = 10, 50$, and 100. In (a), the film is initially given by Equation (3.14) and $h(x = 0)$ is determined by solving Equation (3.4) with $\Gamma = \mathcal{M} = k = 1$ and $\mathrm{Bi} \approx 4.3 \times 10^{-2}$. The heat conduction is solved using both model (A) and (FA). In particular, we find good agreement between model (A) (the thermal model used in the main text) and model (FA). This indicates that including lateral diffusion in the substrate does not influence the film (neither evolution nor heating) and can be neglected.
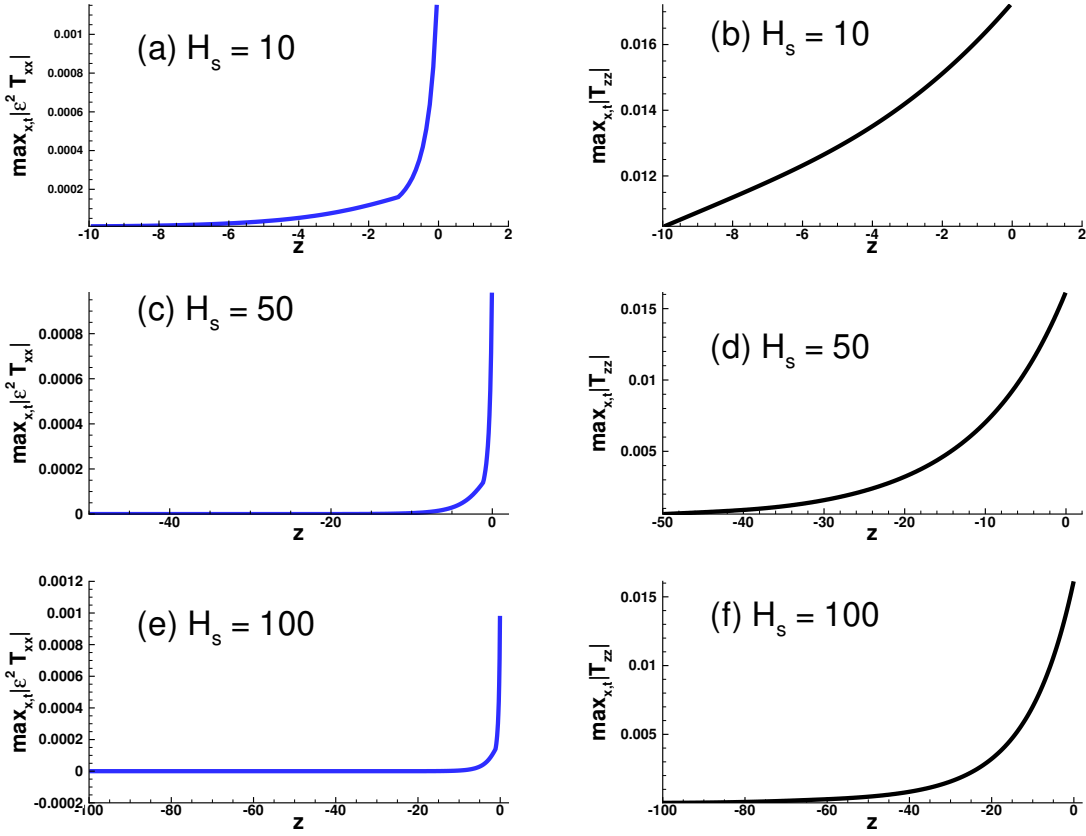
Figure A.7 Maximum magnitude of in-plane diffusion, $|\epsilon^2 T_{xx}|$ over all x and t for (a) $H_s = 10$, (b) $H_s = 50$, (c) $H_s = 100$; and maximum out-of-plane diffusion, $|T_{zz}|$ similarly for (b), (d), and (f). Out-of-plane diffusion is orders of magnitude larger than in-plane diffusion.

To further justify dropping lateral diffusion in the substrate, we simulated full heat conduction in both the film and substrate in the same case given in Figure A.6. Figure A.7 shows the largest value in magnitude of both in-plane diffusion $\max_{x,t} |\epsilon^2 T_{xx}|$ (blue) and out-of-plane diffusion $\max_{x,t} |T_{zz}|$ (black), as a function of z, for $H_s = 10$ (a, b), $H_s = 50$ (c, d), and $H_s = 100$ (e, f). In all cases the term representing in-plane diffusion is at least 10 times smaller than that representing out-of-plane diffusion, and the range of z at which in-plane diffusion might conceivably be relevant is far shorter than that of out-of-plane diffusion. The former, then, can be dropped without significant loss of accuracy.

A.7   Temperature-Varying Thermal Conductivity

The dimensionless substrate thermal conductivity, given by $k(T_s)$, depends on the local values of the substrate temperature. Limited data exists on SiO_2 thermal conductivity at high temperatures (*e.g.*, higher than film melting temperature) and the wide range of temperatures that occurs during film heating presents a modeling challenge. To determine the appropriate functional dependence for $k(T_s)$ we follow the approach of Combis *et al.* [26], which utilizes both the annealing temperature, T_{anneal}, and the softening temperature, T_{soften}. The values we use are based on changes in the thermal expansion coefficient [26], although in practice these temperatures are measured by a sudden change in various material properties (such as viscosity), which could occur in such a wide range of temperatures considered. For more general information regarding T_{anneal} and T_{soften} see, for example, the texts by Callister [21] and Petrie [106]. Based on the data provided by the manufacturer Heraeus [60] (Silica Suprasil 312 Type 2), we use $T_{anneal} = 1.03$ and $T_{soften} = 1.40$, respectively (all temperatures are normalized by the film melting temperature used in our simulations and thermal conductivity is normalized by the value at melting temperature, k_s).
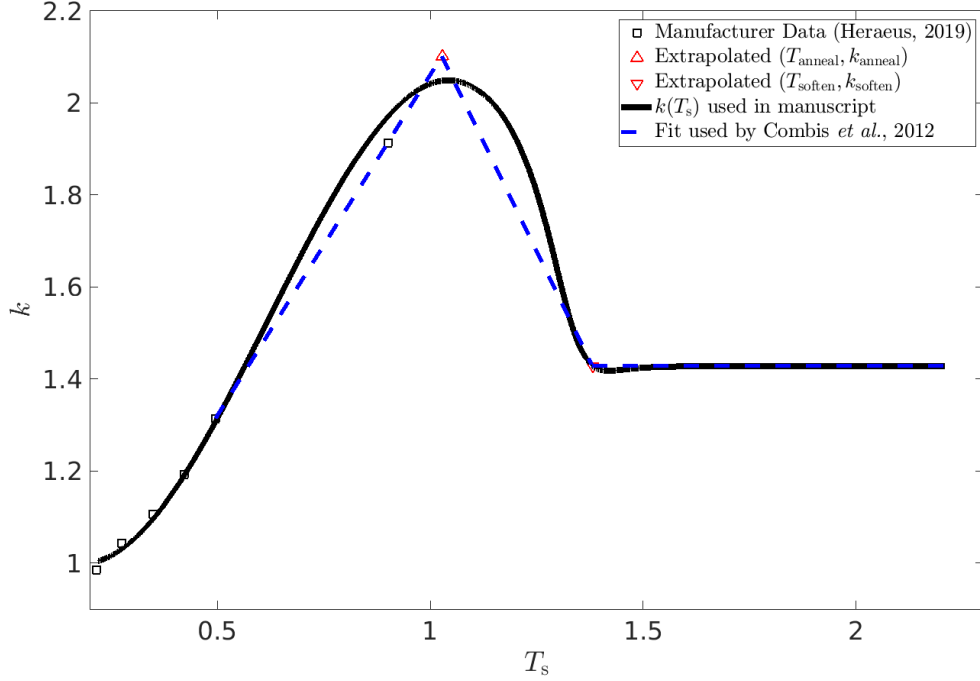
Figure A.8 Manufacturer data of thermal conductivity at various temperatures (black □), extrapolated values at annealing temperature (red △) and softening temperature (red ▽), the fit of substrate thermal conductivity to temperature T_s used in this manuscript (black solid line), and the fit used by Combis *et al.* [26] (blue dashed line).

Figure A.8 shows the piecewise functional form used for $k(T_\mathrm{s})$ (black solid line), the data provided (black squares) by the manufacturer Heraeus [60], and the fit used by Combis *et al.* [26]. Instead of using a piecewise linear profile, we use a cubic polynomial smoothed with sigmoid functions, in the following form:

$$k(T_\mathrm{s}) = \frac{1}{1 + \exp\left(\beta_1 T_\mathrm{s} - \beta_2\right)}(a + bT_\mathrm{s} + cT_\mathrm{s}^2 + dT_\mathrm{s}^3) + \frac{1}{1 + \exp\left(\beta_2 - \beta_1 T_\mathrm{s}\right)}k_\mathrm{soften},$$

(A.6)

where a, b, c, d, β_2 are fitting parameters, β_1 is a scaling factor, and k_soften is the thermal conductivity at softening temperature, which are all given in Table A.4. This form captures both the thermal conductivity at low, annealing, and softening temperatures reasonably well and provides a large range of values for use in simulations. Note

that above the softening temperature the thermal conductivity is nearly constant; a simplifying assumption due to lack of reliable data past the softening temperature.

Table A.4 Table of Parameters Used for the Fit of Temperature-Dependent Thermal Conductivity, Given by Equation (A.6)

Parameter	Notation	Value
Fitting Parameter	a	-1.23×10^{-4}
Fitting Parameter	b	2.06×10^{-1}
Fitting Parameter	c	-59.89
Fitting Parameter	d	3.22×10^{4}
Scaling Factor	β_1	30.12
Fitting Parameter	β_2	40.0
SiO$_2$ Thermal conductivity at T_{soften}	k_{soften}	1.43
SiO$_2$ Annealing Temperature	T_{anneal}	1.03
SiO$_2$ Softening temperature	T_{soften}	1.40

A.8 Relevance of Radiative Losses

Here we briefly consider the relevance of radiative losses at the film surface, $z = h$. For simplicity we consider a simple energy argument. Consider the case of a flat film $h = 1$, which is at melting temperature. The total internal thermal energy of the system is then $\rho_{\text{f}} c_{\text{f}} T_{\text{melt}} L^2 H$. The rate of energy loss at the boundary $z = h$ due to radiation is proportional to the fourth power of temperature and is given by $\sigma_{\text{SB}} \epsilon_r T_{\text{melt}}^4 \left(1 - T_{\text{a}}^4\right) L^2$, where $\sigma_{\text{SB}} = 5.67 \times 10^{-8} \text{Wm}^{-2}\text{K}^{-4}$ is the Stefan-Boltzmann constant and $\varepsilon_r \approx 0.14$ is the thermal emissitivity [49]. In time interval Δt then, the

ratio of the energy lost to free surface radiation and the internal thermal energy is,

$$r_{\text{rad}} = \frac{\Delta t \sigma_{\text{SB}} \varepsilon_r T_{\text{melt}}^4 \left(1 - T_{\text{a}}^4\right)}{H \rho_{\text{f}} c_{\text{f}} T_{\text{melt}}}. \tag{A.7}$$

For the parameter values in our problem, the timescale Δt on which these two energies become comparable, $r_{\text{rad}} = O(1)$, is found to be $\Delta t \approx 2 \times 10^{-3}$s, a millisecond time interval, which is much longer than the laser pulse and dewetting time scales of interest in this work. Therefore, radiative losses can be safely neglected.

A.9   Convergence Results

Here we show that T_{avg} from our model converges to the analytical solution given by Trice *et al.* [135], in the limit $H_{\text{s}}, \text{Bi} \to \infty$ and for a uniform flat film, $h = h_0$. Figure A.9 plots average film temperature for $H_{\text{s}} = 5, 10, 20, 30, 40, 50$ as well as the analytical solution of Trice *et al.* [135]. As substrate thickness is increased numerically, the average film temperatures converge to the analytical result, as expected.
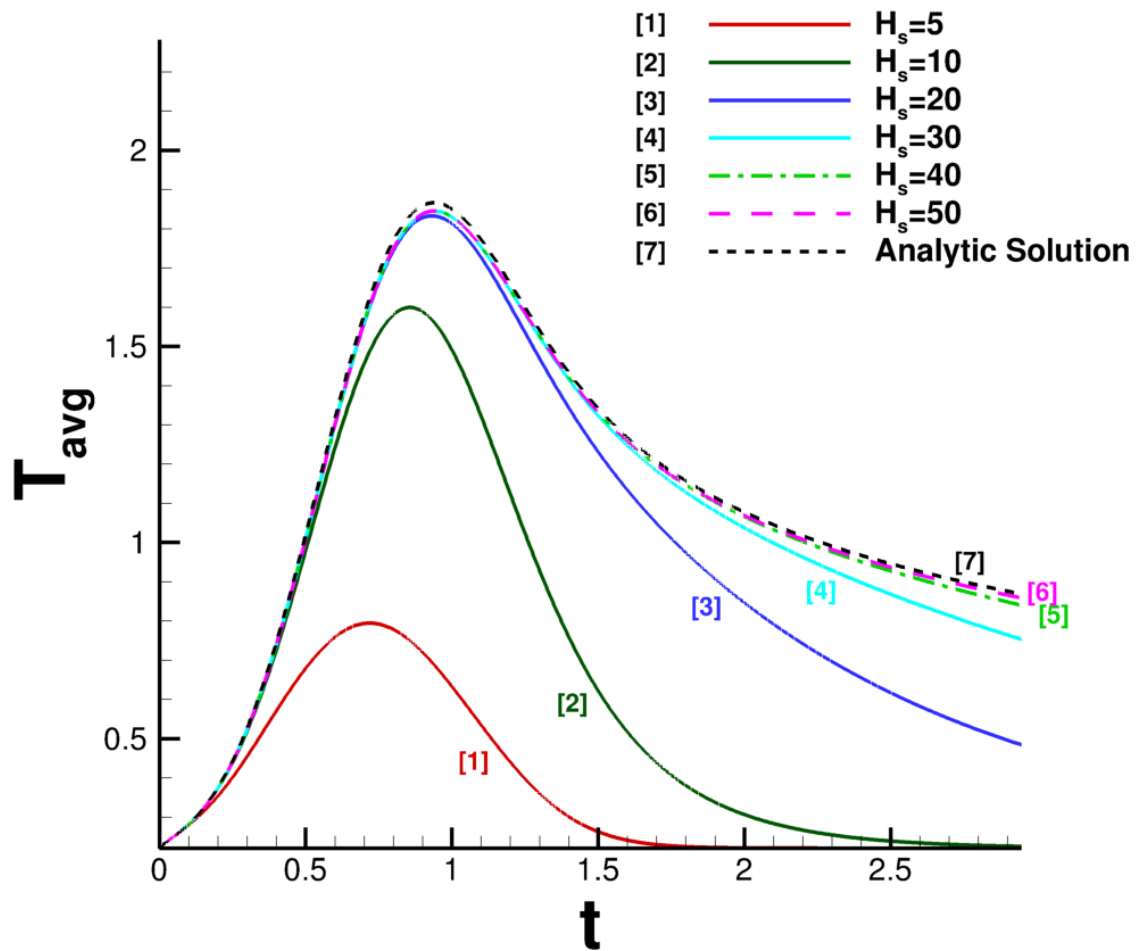
Figure A.9 Average film temperature, T_{avg}, for varying substrate thickness; and the analytical solution of Trice *et al.* [135] in the limit $H_{\mathrm{s}}, \mathrm{Bi} \to \infty$.

A.10 Influence of Substrate Thickness for $Bi = 0.2$
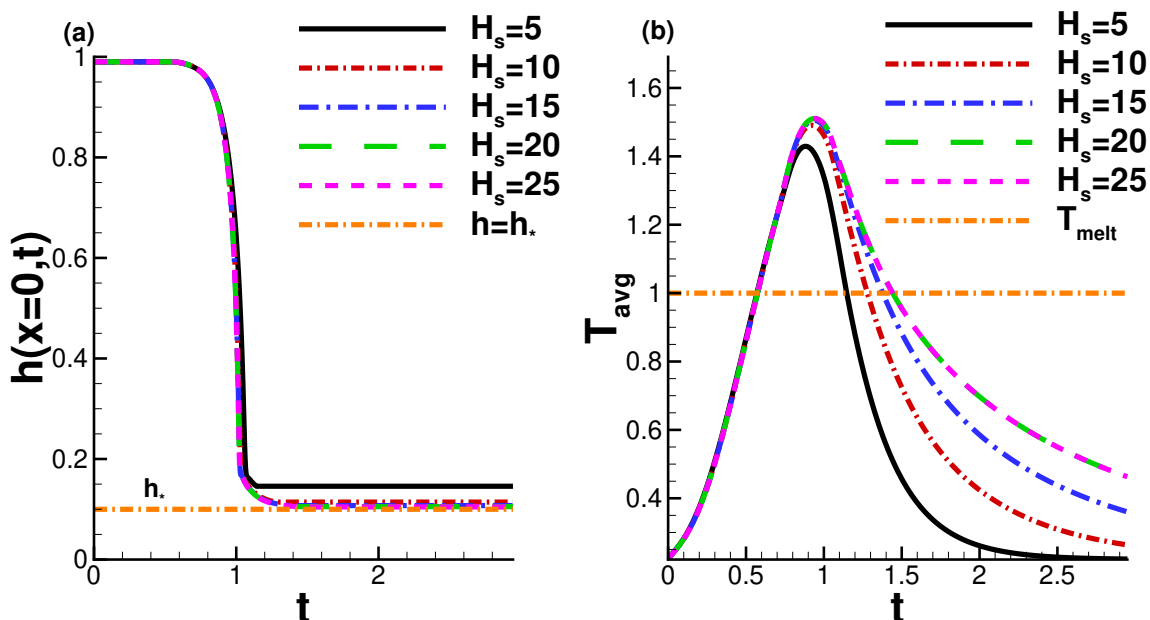
Figure A.10 (a) Evolution of film thickness at $x = 0$ for $H_s = 5$ (black), 10 (red, dash-dotted), 15 (blue dash-dotted), 20 (green dashed), 25 (magenta dashed), and the precursor thickness $h = h_*$ (orange dot-dashed). (b) Average film temperature corresponding to the H_s cases in (a) and melting temperature, T_{melt} (orange dot-dashed). The material parameters are variable, $\Gamma = \Gamma(t), \mathcal{M} = \mathcal{M}(t), k = k(T_s)$, and $Bi = 0.2$.

Figure A.10(a) and (b) show the evolution of the film midpoint and average temperatures, respectively, for five different substrate thicknesses $H_s = 5, 10, 15, 20, 25$ as in Figure 3.4, but now for $Bi = 0.2$. We see in Figure A.10(b) that the liquid lifetimes vary more significantly than for $Bi = 0.1$, but the effect of varying H_s is still small relative to that of varying Bi (compare Figure 3.3(a)). Of the H_s cases considered, the film for $H_s = 5$ shows the biggest difference (similar to Figure 3.4(a)). In contrast to the $Bi = 0.1$ case, here the film with $H_s = 5$ solidifies before full dewetting ($h(0, t)$ does not reach the equilibrium film thickness). Finally, note that despite the weak influence of H_s on film evolution, a small change in LL can cause premature solidification of the film, as we see in 3D simulations (*e.g.*, Figure 3.8).

A.11   Influence of Spatially Varying Viscosity in 3D
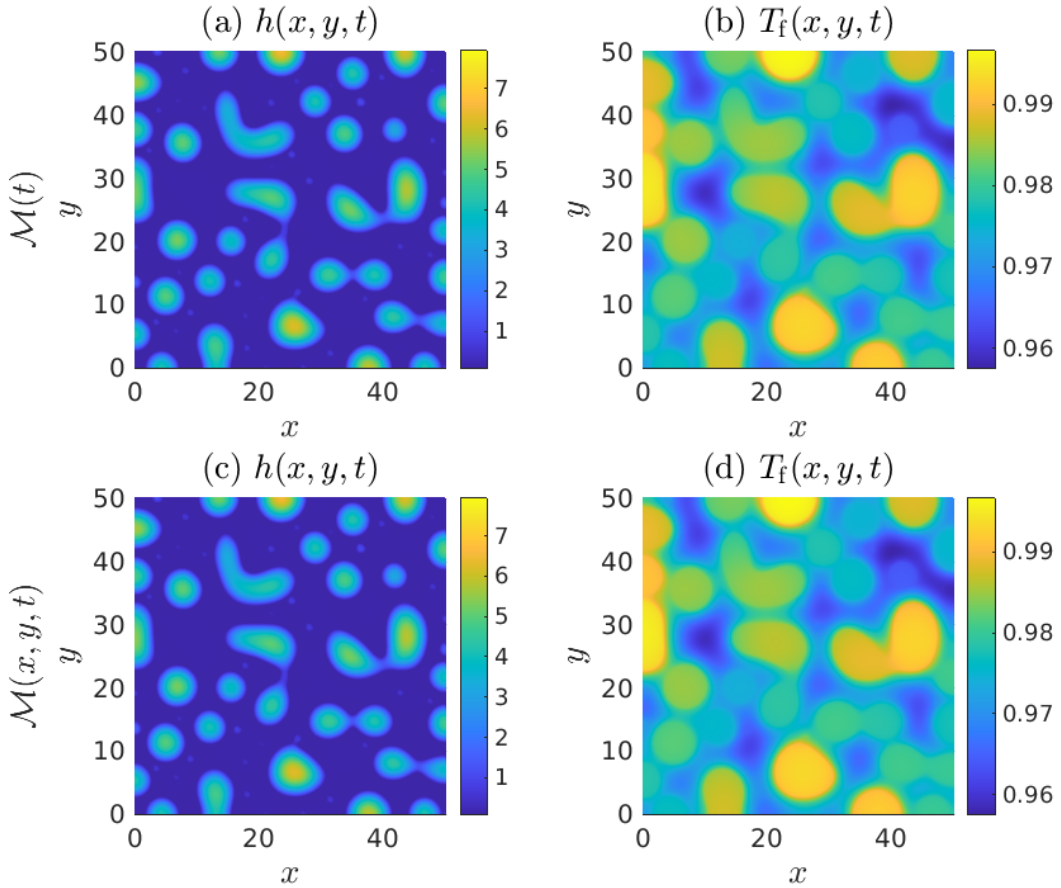
Figure A.11   Film thickness, $h(x, y, t)$ and film temperature, $T_{\mathrm{f}}(x, y, t)$ for $\mathcal{M}(t)$ (a) and (b) and $\mathcal{M}(x, y, t)$ (c) and (d).

Here we briefly consider the effect of spatially varying viscosity, where $T_{\mathrm{avg}}(t)$ is replaced by $T_{\mathrm{f}}(x, y, t)$ in the viscosity law Equation (3.5). Figure A.11(a) and (b) show film thickness $h(x, y, t)$ and film temperature $T_{\mathrm{f}}(x, y, t)$ at the final solidification time in the case where viscosity depends only on average temperature, $\mathcal{M} = \mathcal{M}(t)$ (Figure A.11(a) is identical to Figure 3.6(b)). Figure A.11(c) and (d) show the corresponding film thickness and temperature for the spatially-varying viscosity case, $\mathcal{M}(x, y, t)$. There is no noticeable difference between film thicknesses in (a) and (c), nor between temperatures in (b) and (d). Note that the spatial variation of

temperature is small in (b) and (d). Consequently, $T_{\text{avg}}(t)$ is a sufficient substitute for $T_{\text{f}}(x, y, t)$ in Equation (3.5).

A.12   2D Numerical Schemes Including Temperature-Dependent Thermal Conductivity

In this section we describe the numerical schemes used to solve for the film height, h, temperature, T_{f}, and substrate temperature, T_{s}. First, we describe the spatial discretization, and then the solution mechanism for T_{s} and T_{f}. We conclude with the numerical scheme used to compute h.

We define the cell-centered spatial grid in the x-direction, used for both film and substrate:

$$x_i = x_0 + \Delta x \left(i - 1/2 \right), \quad i = 1, \ldots, N, \qquad \Delta x = \frac{(x_{\text{max}} - x_0)}{N}, \qquad \text{(A.8)}$$

where N is the number of grid points in the x-direction, and the lateral boundaries are $x_0 = -\pi$ and $x_{\text{max}} = \pi$. An example of the spatial grid is given in Figure A.12, when $N = 7$.
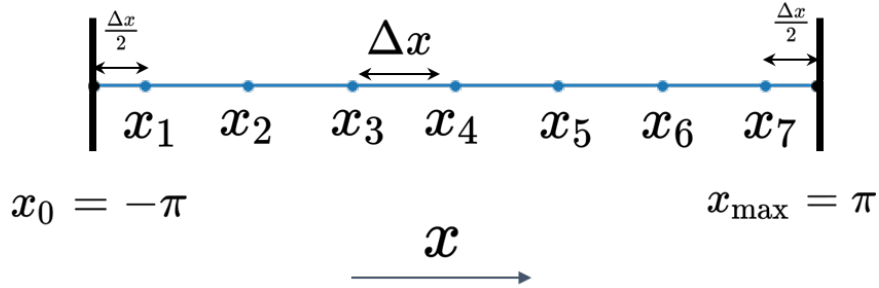
Figure A.12 Visual example of the cell-centered spatial grid in the $x-$direction for $N = 7$. The nodes are spaced by Δx, except the the first and last grid point, which are spaced $\Delta x/2$ from the boundaries x_0 and x_{max}, respectively.

Similarly, let p be the number of grid points in the z-direction (relevant only in the substrate). To reduce the computational expense, we use a nonuniform grid in the substrate, with grid points $\{z_k\}$ and variable step sizes $\{\Delta z_k\}$, $k = 0, 1, \ldots, p-1$,

where the step sizes are taken to be geometric, with ratio r,

$$\Delta z_{k+1} = r\Delta z_k, \qquad k = 1, \ldots, p - 1. \tag{A.9}$$

Figure A.13 shows an example when $p = 5$ and $r = 1.5$ (the value of r used in all results of Chapter 3). The point $z_0 = 0$ is always fixed at the liquid-solid interface, $z = 0$, and z_{p-1} is the final grid point, which lies a distance $\Delta z_p/2$ above $z = -H_s$.
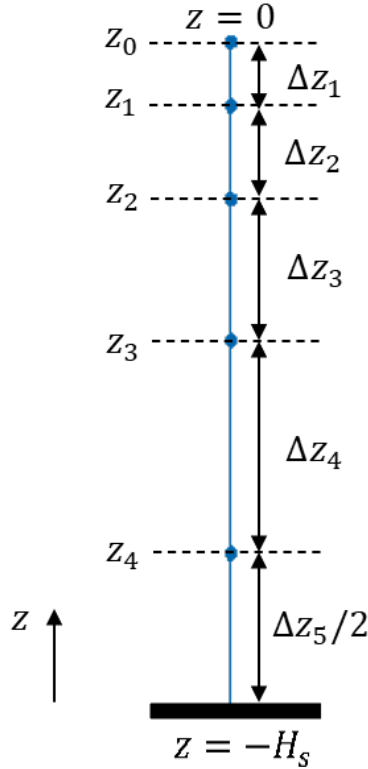
Figure A.13 Example of the nonuniform grid for $p = 5$. Here, the spacing between grid points increases by a factor of 1.5 at each increment.

We then fix the first (minimum) step size, $\Delta z_{\min} = \Delta z_1$ to ensure that $\{\Delta z_k\}$, $k = 1, 2, \ldots, p - 1$ gives the desired geometric partition of $[-H_s, 0]$,

$$\Delta z_{\min} = H_s \left(\sum_{k=1}^{p-1} r^{k-1} + \frac{1}{2}r^{p-1} \right)^{-1}. \tag{A.10}$$

With $\Delta z_{\min}$ defined, we can consistently define the sequence of step sizes and grid:

$$\Delta z_k = \Delta z_{\min} r^{k-1}, \qquad\qquad k = 1, \ldots, p \qquad\qquad \text{(A.11)}$$

$$z_k = z_{k-1} - \Delta z_k, \qquad\qquad k = 1, \ldots, p-1. \qquad\qquad \text{(A.12)}$$

We next proceed with the solution methods for the underlying equations. For simplicity, we begin with the solution scheme for Equation (3.7). We define

$$S_{i,k}^n \approx T_{\mathrm{s}}(x_i, z_k, t_n), \quad i = 1, 2, \ldots, N, \quad k = 0, 1, \ldots, p-1, \qquad \text{(A.13)}$$

to be a discrete approximation of substrate temperature, T_{s}, on the spatial grid given above. First, we apply a Crank-Nicolson time-stepping scheme, which takes the discrete form

$$\frac{S_{i,k}^{n+1} - S_{i,k}^n}{\Delta t} = \frac{1}{2} f_{i,k}^{n+1} + \frac{1}{2} f_{i,k}^n, \quad i = 1, \ldots, N, \qquad k = 1, \ldots, p-1, \qquad \text{(A.14)}$$

where $f_{i,k}(S_{i,k-1}, S_{i,k}, S_{i,k+1}) \approx \mathrm{Pe_s^{-1}} \partial_z \left(k(T_{\mathrm{s}}) \partial_z T_{\mathrm{s}} \right) \big|_{(x,z)=(x_i, z_k)}$ is a nonlinear function of $S_{i,k-1}$, $S_{i,k}$, and $S_{i,k+1}$. For the remainder of the section, we suppress the subscript i on $S_{i,k}$ and $f_{i,k}$, for simplicity. For completeness, we note that f_k can be approximated as follows

$$\partial_z \left(k(T_{\mathrm{s}}) \partial_z T_{\mathrm{s}} \right) = k(T_{\mathrm{s}}) \partial_z^2 T_{\mathrm{s}} + k'(T_{\mathrm{s}}) \left(\partial_z T_{\mathrm{s}} \right)^2, \qquad\qquad \text{(A.15)}$$

$$\partial_z \left(k(T_{\mathrm{s}}) \partial_z T_{\mathrm{s}} \right) \big|_{z=z_k} \approx A_k S_{k-1} + B_k S_k + C_k S_{k+1} + D_k \left(S_{k-1} - S_{k+1} \right)^2, \qquad \text{(A.16)}$$

$$A_k = \frac{2k(S_k)}{\Delta z_k \left(\Delta z_k + \Delta z_{k+1} \right)}, \quad B_k = \frac{-2k(S_k)}{\Delta z_k \Delta z_{k+1}}, \qquad\qquad \text{(A.17)}$$

$$C_k = \frac{2k(S_k)}{\Delta z_{k+1} \left(\Delta z_k + \Delta z_{k+1} \right)}, \quad D_k = \frac{k'(S_k)}{\left(\Delta z_k + \Delta z_{k+1} \right)^2}, \qquad\qquad \text{(A.18)}$$

where each equation is applied for a fixed i, $k'(S_k) = dk(S_k)/dS_k$, and $k = 1, 2, \ldots, p-1$.

The cases $k = 1$ and $k = p-1$ in Equation (A.16) involve unknowns S_0 and S_p, which are determined by discretizing the boundary condition at $z = 0$ (Equation (3.8))

and at $z = -H_s$ (Equation (3.9)), respectively. Since $z_0 = 0$, S_0 is simply set to the film temperature, $S_0 = T_i^n \approx T_f(x_i, t_n)$ for each i. The boundary condition given by Equation (3.9) is discretized as

$$k \left(\frac{S_{p-1} + S_p}{2} \right) \left(\frac{S_{p-1} - S_p}{\Delta z_p} \right) = \text{Bi} \left(\frac{S_{p-1} + S_p}{2} - T_a \right),$$ (A.19)

which is a nonlinear equation for the unknown S_p to be solved at each node x_i. To solve Equation (A.19), we use a Newton method, although any convergent iterative method would suffice.

Next, we assume that the substrate temperature at time t_{n+1} can be written as

$$S_k^{n+1} = S_k^* + w_k,$$ (A.20)

where S_k^* is the guess to the solution at time t_{n+1} and w_k is a correction to that guess, which we call a Newton correction in what follows to avoid confusion. Then, f is linearized around the guess:

$$f_k^{n+1} = f_k(S_k^{n+1}) = f_k(S_k^* + w_k) \approx f_k(S_k^*) + w_j \frac{\partial f_k}{\partial S_j} |_{S_j = S_j^*},$$ (A.21)

where $k = 1, \ldots, p - 1$, and $\partial f_k / \partial S_j |_{S_j = S_j^*}$ are the components of the Jacobian, denoted $F_{k,j} = \partial f_k / \partial S_j |_{S_j = S_j^*}$, evaluated at the guess for the next temperature S_j^*. Equation (A.14) is then linearized by plugging in Equations (A.20), (A.21), leading to a linear system of equations for the correction w_k, where S_k^* and S_k^n are both known (S_k^* is to be iterated):

$$\sum_{j=1}^{p-1} \left(\delta_{k,j} - \frac{1}{2} \Delta t F_{k,j} \right) w_j = R_j, \qquad k = 1, \ldots, p - 1,$$ (A.22)

where $\delta_{k,j}$ is the Kronecker delta, and the right-hand side is

$$R_j = S_j^n - S_j^* + \frac{1}{2} \Delta t f_j(S_j^*) + \frac{1}{2} \Delta t f_j(S_j^n), \qquad j = 1, \ldots, p - 1.$$ (A.23)

For simplicity, we abbreviate Equation (A.22) as $(\mathbf{A}\mathbf{w} = \mathbf{R})_i$ with the understanding that each $(p-1) \times (p-1)$ linear system is to be solved for each x_i. Solving Equation (A.22) completes one step of the iteration. Next, we check that $|w_k/S_k^*| < tol$ for all k. If yes, the iteration is finished, and $S_k^* + w_k$ becomes the substrate temperature at time t_{n+1} for each $k = 1, 2, \ldots, p-1$, namely $S_k^{n+1} = S_k^* + w_k$. If not, the iteration is completed until the specified convergence criterion is reached. We use $tol = 10^{-9}$.

Next we describe the solution mechanism for film temperature, Equation (3.6). First, we define the approximation for film temperature and thickness by

$$T_i^n \approx T_\mathrm{f}(x_i, t_n), \quad h_i^n \approx h(x_i, t_n), \quad i = 1, \ldots, N. \tag{A.24}$$

Next, for compactness, we define the following expressions

$$\Psi_i^n = \frac{1}{\mathrm{Pe_f}} \left[\delta_x^2 T_i^n + \left(\frac{\delta_x h_i^n}{h_i^n} \right) \delta_x T_i^n \right], \tag{A.25}$$

$$G_i^n = -\frac{\mathcal{K}}{\mathrm{Pe_f} h_i^n} \left[k(S_0^n) \delta_z^+(S_0^n) \right]_i, \tag{A.26}$$

where $[k(S_0^n) \delta_z^+(S_0^n)]_i \approx k(T_\mathrm{s}) \partial T_\mathrm{s}/\partial z|_{(x,z,t)=(x_i,0,t_n)}$ is an approximation of the heat flux along the liquid-solid interface, $z = 0$, at node x_i and time t_n, which we define as

$$k(S_0^n) \delta_z^+(S_0^n) = k(S_0^n) \left(a_0 S_0^n + b_0 S_1^n + c_0 S_2^n \right), \tag{A.27}$$

$$a_0 = \frac{2\Delta z_1 + \Delta z_2}{\Delta z_1 (\Delta z_1 + \Delta z_2)}, \quad b_0 = -\left(\frac{1}{\Delta z_1} + \frac{1}{\Delta z_2} \right), \quad c_0 = \frac{\Delta z_1}{\Delta z_2 (\Delta z_1 + \Delta z_2)}. \tag{A.28}$$

The second-order central difference approximations of ∂_x, ∂_x^2 are defined as δ_x and δ_x^2, respectively, and are given by

$$\delta_x T_i = \frac{T_{i+1} - T_{i-1}}{2\Delta x}, \qquad \delta_x^2 T_i = \frac{T_{i+1} - 2T_i + T_{i-1}}{\Delta x^2} \qquad i = 1, \ldots, N,$$

where T_0, T_{N+1} can be written in terms T_1 and T_N, respectively, by solving discretized versions of Equation (3.10) at the lateral boundaries, $x = \pm\pi$,

$$\partial_x (T_\mathrm{f})|_{x=-\pi} \approx \frac{T_1 - T_0}{\Delta x} = 0, \qquad \partial_x (T_\mathrm{f})|_{x=\pi} \approx \frac{T_{N+1} - T_N}{\Delta x} = 0. \tag{A.29}$$
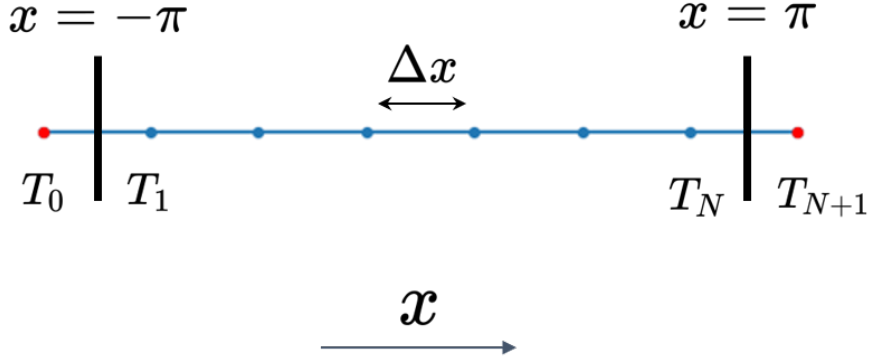
Figure A.14 Depiction of the discretized film temperature adjacent to the lateral boundaries, $x = \pm\pi$ (black, vertical bars). The blue nodes represent the grid $x_1, x_2, \ldots, x_N$ with spacing Δx. The film temperature at the first and last interior grid points, near $x = -\pi, \pi$, are T_1, T_N, and T_0, T_{N+1} represent ghost points, located at $x = \pm\left(\pi + \Delta x/2\right)$ (red nodes).

Figure A.14 shows the spatial grid in the x direction. The red nodes represent ghost points with temperatures T_0, T_{N+1}. By solving Equation (A.29), we obtain $T_1 = T_0$ and $T_{N+1} = T_N$.

Now, to solve Equations (3.6) and (3.7) for T_f and T_s, we use a predictor-corrector Runge-Kutta/Crank-Nicolson scheme combined with a Newton method as described above. In what follows, hatted quantities denote those found in the predictor phase, whereas those without hats are determined in the corrector phase. In the predictor phase, one finds intermediate "predicted" film and substrate temperatures $(\hat{T}_i^{n+1}, \hat{S}_k^{n+1})$. In the corrector phase, one uses the intermediate variables to find corrected film and substrate temperatures (T_i^{n+1}, S_k^{n+1}). In both cases, the substrate temperature is found by solving the linear systems given by Equation (A.22) for $\hat{w}$ or w. In the former case, the nonlinear system that is linearized is Equation (A.14) with $\hat{S}_k^{n+1}$ in place of S_k^{n+1} and with f_k^{n+1} replaced by $\hat{f}_k^{n+1}(\hat{S}_{k-1}^{n+1}, \hat{S}_k^{n+1}, \hat{S}_{k+1}^{n+1})$. In the predictor phase, we use a forward-Euler scheme to deal with G_i^n:

$$\frac{\hat{T}_i^{n+1} - T_i^n}{\Delta t} = \frac{1}{2}\left[\hat{\Psi}_i^{n+1} + \Psi_i^n\right] + G_i^n + \overline{Q}_i^{n+1/2}, \quad i = 1, \ldots, N, \tag{A.30}$$

$$\left(\hat{\mathbf{A}}\hat{\mathbf{w}} = \hat{\mathbf{R}}\right)_i, \quad i = 1, \ldots, N, \tag{A.31}$$

where $\overline{Q}_i^{n+1/2} = (\overline{Q}_i^n + \overline{Q}_i^{n+1})/2$, and $\hat{\Psi}_i^{n+1}$ is found by substituting $\hat{T}_i^{n+1}$ in place of T_i^{n+1} in Equation (A.25). Similarly, the components of $\hat{\mathbf{w}}$ are related to the predicted substrate temperature, $\hat{S}_k^{n+1}$, via Equation (A.20) with appropriate substitution.

Solving Equation (A.30) provides the predicted temperature $\hat{T}_i^{n+1}$. The linearized system given by Equation (A.31), where $\hat{\mathbf{A}}, \hat{\mathbf{R}}$ are found using $\hat{S}_k^*$, the guess to $\hat{S}_k^{n+1}$, and $\hat{S}_k^n$ in Equations (A.22) and (A.23), is solved iteratively for $\hat{\mathbf{w}}$ and each i. The predictor phase amounts to solving one linear system of size N for the film and N linear systems of size $p - 1$ for the substrate. More importantly, the solution to Equation (A.31) in the predictor phase gives us an approximation of substrate temperature, $\hat{S}_{i,k}^n$, so that we can calculate a prediction to the heat flux at the liquid-solid interface, $\hat{G}_i^n$. We then correct the temperature predictions by using a second-order Runge-Kutta method on G_i^n using $\hat{G}_i^n$:

$$\frac{T_i^{n+1} - T_i^n}{\Delta t} = \frac{1}{2}\left[\Psi_i^{n+1} + \Psi_i^n\right] + \frac{1}{2}\left(G_i^n + \hat{G}_i^n\right) + \overline{Q}_i^{n+1/2}, \quad i = 1, \ldots, N, \quad \text{(A.32)}$$

$$(\mathbf{A}\mathbf{w} = \mathbf{R})_i, \quad i = 1, \ldots, N, \quad \text{(A.33)}$$

Next we describe the numerical scheme for film thickness, $h(x, t)$. First, we use the Crank-Nicolson scheme to discretize Equation (3.4) in time. The resulting nonlinear system of equations is given by Equation (3.13), where $D_i(t) = D_i^n \approx D(x_i, t_n)$ is a second-order accurate spatial discretization of the derivative of flux,

$$D = -\partial_x \cdot \left[\frac{1}{\mathcal{M}}\left(h^3 \partial_x \left(\Gamma \partial_{xx} h + \Pi(h)\right)\right)\right]. \quad \text{(A.34)}$$

Following the procedure implemented for solving Equation (A.14), we apply a Newton method, first linearizing the film thickness around a guess, h_i^*, and solving a resultant linear system for the Newton correction to the guess,

$$h_i^{n+1} = h_i^* + q_i^*, \quad i = 1, \ldots, N, \quad \text{(A.35)}$$

$$\mathbf{A}_h \mathbf{q} = \mathbf{R}_h, \quad \text{(A.36)}$$

where $(\mathbf{A}_h)_{i,j} = \partial D_i / \partial h_j |_{h_j = h_j^*}$ are the components of the Jacobian, $\mathbf{q}$ is the Newton correction vector for $\mathbf{h}$, and $\mathbf{R}_h$ is the remainder, whose components, $(R_h)_i$, $i = 1, 2, \ldots, N$, are analogous to Equation (A.23):

$$(R_h)_i = h_i^n - h_i^* + \frac{1}{2}\Delta t D_i (h_i^*) + \frac{1}{2}\Delta t D_i (h_i^n).\tag{A.37}$$

For more details regarding the 2D solution mechanism for h, we refer the reader to Kondic [74].
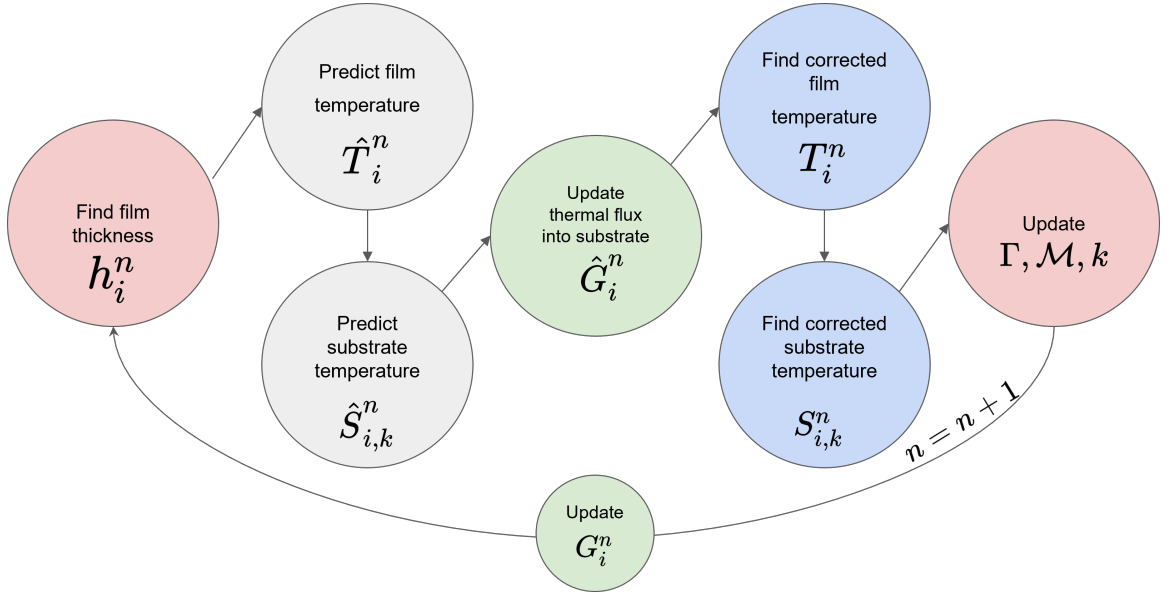
Figure A.15 Flowchart for the 2D numerical method used to solve for $h(x,t)$, $T_\mathrm{f}(x,t)$ and $T_\mathrm{s}(x,z,t)$.

Figure A.15 shows a flowchart of the solution process for finding film thickness, film temperature, and substrate temperature. Red circles indicate the beginning and end of a time-step iteration. Gray circles indicate the prediction step for heat conduction and the blue circles represent the correction step. The green circles represent intermediate stages where the thermal flux into the substrate is updated. First, h is found at time t_n by solving Equation (A.36) for every spatial node x_i. That value of h is then used to solve Equation (A.30) for a prediction of the film temperature, $\hat{T}_i^n$. That film temperature is then used to solve for the predicted

substrate temperature, $\hat{S}_{i,k}^n$ via Equation (A.31). The thermal flux at the liquid-solid interface, $\hat{G}_i^n$, is then updated using $\hat{S}_{i,k}^n$ in Equation (A.26). These temperature predictions are then corrected using Equations (A.32) and (A.33). Surface tension, Γ, viscosity, $\mathcal{M}$, and substrate thermal conductivity at $z = 0$, $k(S_{i,0}^n)$, are then updated. Finally, until the desired end time is reached, time is incremented, and G_i^n is updated using $S_{i,k}^n$ in Equation (A.26).

A.13   3D Numerical Schemes

Here, we consider the numerical scheme to solve the full 3D versions of Equations (3.4) and (3.6)–(3.7), where $h = h(x, y, t)$, $T_{\mathrm{f}} = T_{\mathrm{f}}(x, y, t)$, and $T_{\mathrm{s}} = T_{\mathrm{s}}(x, y, z, t)$. Since y-dependence is now included (see Figure 3.1), the complexity of the numerical problems are, as a minimum, increased by a factor of N for each set of equations. This creates a computational challenge, which makes serial CPU computing prohibitively slow. Parallel computing is a much more practical route. For example, the finite-difference method discretization of PDEs often leads to tri-diagonal linear systems (such as Equation (A.31)). In these cases, either the formation of the matrix/vector system, or the solution method itself, can be parallelized. Parallelization of the matrix/vector system may be done, for example, by defining the value of each element in parallel. Solving the tri-diagonal linear systems in parallel is less trivial since the Thomas Algorithm, typically used for such problems, is naturally sequential. To compensate, parallel cyclic reduction methods have been proposed that trade complexity for speed and prove superior to the traditional Thomas algorithm for many problems [148]. We use a simpler approach, however, by solving each linear system in parallel rather than parallelization of the solver (details following below).

Parallel computing with multi-node systems and multi-core processors is also used in scientific computing but is resource-limited by the number of cores available per CPU. GPUs, on the other hand, have thousands of "cores" available for computing

and allow the programmer many more degrees of freedom in parallelization [120]. Various CUDA algorithms have been developed for solving penta-diagonal systems [51, 81], for example, which often arise from 4th order PDEs such as Equation (3.4). Recently, Lam *et al.* [81] developed a GPU-based code that can be used to solve thin film problems, finding a near 4000 times speed up over similar CPU-based code for certain domain sizes. In the present work, we discuss an extension of that code, which also incorporates thermal effects with CUDA, and we briefly describe this extension next.

The remainder of the section is structured as follows. First, we define the 3D spatial grid. Then, we describe the solution methodology for computing temperatures, both in the film and in the substrate. Finally, we conclude with the solution mechanism for film thickness. We focus mainly here on the aspects of the implementation that are specific to 3D geometry.

The x-component of the spatial grid is given by Equation (A.8) and the z-component of the substrate grid by Equation (A.12). We similarly introduce the y-component of the spatial grid

$$
y_j = y_0 + \Delta y \, (j - 1/2), \quad j = 1, \dots, M, \qquad \Delta y = \frac{(y_{\max} - y_0)}{M}, \tag{A.38}
$$

where M is the number of grid points in the y-direction. Therefore, the film grid consists of $N \times M$ interior nodes $\{(x_i, y_j), \, i = 1, 2, \dots, N, \, j = 1, 2, \dots, M\}$. In the substrate there are $N \times M \times p$ nodes (x_i, y_j, z_k).

Similarly to Appendix A.12, we define

$$
T_{i,j}^n \approx T_{\mathrm{f}}(x_i, y_j, t_n), \quad S_{i,j,k}^n \approx T_{\mathrm{s}}(x_i, y_j, z_k, t_n), \quad h_{i,j}^n \approx h(x_i, y_j, t_n), \tag{A.39}
$$

as approximations to the film and substrate temperatures, and film thickness. The predictor/corrector solution methodology from Appendix A.12 is applied once more, except Equation (3.6) now requires an alternating-direction implicit (ADI) method to

achieve second-order accuracy. Similar to Appendix A.12, we begin with a predictor step to find $\hat{\mathbf{w}}$ and $(\hat{T}^{n+1}_{i,j}, \hat{S}^{n+1}_{i,j,k})$:

$$\frac{T^*_{i,j} - T^n_{i,j}}{\Delta t} = \frac{1}{2}X^*_{i,j} + \frac{1}{2}Y^n_{i,j} + \frac{1}{2}G^n_{i,j} + \frac{1}{2}\overline{Q}^{n+1/2}_{i,j}, \tag{A.40}$$

$$\frac{\hat{T}^{n+1}_{i,j} - T^*_{i,j}}{\Delta t} = \frac{1}{2}X^*_{i,j} + \frac{1}{2}\hat{Y}^{n+1}_{i,j} + \frac{1}{2}G^n_{i,j} + \frac{1}{2}\overline{Q}^{n+1/2}_{i,j}, \tag{A.41}$$

$$\left(\hat{\mathbf{A}}\hat{\mathbf{w}} = \hat{\mathbf{R}}\right)_{i,j}, \tag{A.42}$$

where

$$X_{i,j} = \mathrm{Pe}_{\mathrm{f}}^{-1}\left[\delta_x^2 T_{i,j} + \left(\frac{\delta_x h_{i,j}}{h_{i,j}}\right)\delta_x T_{i,j}\right], \tag{A.43}$$

$$Y_{i,j} = \mathrm{Pe}_{\mathrm{f}}^{-1}\left[\delta_y^2 T_{i,j} + \left(\frac{\delta_y h_{i,j}}{h_{i,j}}\right)\delta_y T_{i,j}\right], \tag{A.44}$$

$$\overline{Q}^{n+1/2}_{i,j} = \frac{\overline{Q}^n_{i,j} + \overline{Q}^{n+1}_{i,j}}{2}, \tag{A.45}$$

$$G^n_{i,j} = -\frac{\mathcal{K}}{\mathrm{Pe}_{\mathrm{f}} h^n_{i,j}}\left[k(S^n_0)\delta_z^+(S^n_0)\right]_{i,j}, \tag{A.46}$$

$h^n_{i,j} \approx h(x_i, y_j, t_n)$, $i = 1, \ldots, N$, $j = 1, \ldots, M$, and $k(S^n_0)\delta_z^+(S^n_0)$ approximates the heat flux at the interface $z = 0$ and is given in Appendix A.12. The term $T^*_{i,j}$ is the solution at an intermediate step between times t_n, t_{n+1}, and $\hat{\mathbf{A}}, \hat{\mathbf{R}}$ are defined as in Appendix A.12, but with the extra index j. The solution for h is only found at times t_n and t_{n+1}, so we approximate h at the intermediate step as

$$h^*_{i,j} = \frac{h^n_{i,j} + h^{n+1}_{i,j}}{2}. \tag{A.47}$$

Equation (A.40) yields M linear systems of equations of size N. Similarly, Equation (A.41) yields N linear systems of equation of size M. Since the ADI method treats one variable explicitly and the other implicitly, both Equations (A.40) and (A.41) are solved in parallel for each j and each i, respectively (the formation of the linear system is also parallelized; for example, $T^*_{i,j} - (\Delta t/2)X^*_{i,j}$ for j fixed and

$i = 1, \ldots, N$ are the components of the $N \times N$ matrix in Equation (A.40), which are all found simultaneously). The 3D numerical code used here is freely available [2].

Equation (A.42) is the 3D analog of Equation (A.31), but now there are $N \times M$ linear systems of equations of size $p - 1$. Since Equation (3.7) only involves z-derivatives, Equation (A.42) is trivially parallelized for each i and j. Since the solution of Equation (A.42) is iterative, careful consideration of the size of domains and the relation to memory performance is crucial. In our computations, p is relatively small in comparison to N and M so that for each i and j both the matrix and vector of the linear system (of size $p-1$) can fit on shared memory on the device (GPU), which is known to be computationally advantageous over the use of global memory [120].

Next, we correct the predictor step using the Runge-Kutta method on $G_{i,j}$,

$$\frac{T_{i,j}^* - T_{i,j}^n}{\Delta t} = \frac{1}{2} X_{i,j}^* + \frac{1}{2} Y_{i,j}^n + \frac{1}{4} \left(G_{i,j}^n + \hat{G}_{i,j}^n \right) + \frac{1}{2} \overline{Q}_{i,j}^{n+1/2}, \tag{A.48}$$

$$\frac{T_{i,j}^{n+1} - T_{i,j}^*}{\Delta t} = \frac{1}{2} X_{i,j}^* + \frac{1}{2} Y_{i,j}^{n+1} + \frac{1}{4} \left(G_{i,j}^n + \hat{G}_{i,j}^n \right) + \frac{1}{2} \overline{Q}_{i,j}^{n+1/2}, \tag{A.49}$$

$$(\mathbf{A}\mathbf{w} = \mathbf{R})_{i,j}, \tag{A.50}$$

where $i = 1, \ldots, N$, and $j = 1, \ldots, M$. We note that although the repetitive nature of the predictor-corrector scheme may appear to be a performance bottleneck, in our implementation the results from the predictor phase are stored to global memory and imported into the corrector step to speed up the computations.

Next, we briefly describe the solution mechanism for film thickness h. Now, $h = h(x_i, y_j, t_n)$ but the approach is very similar to that of Appendix A.12. First we define the divergence of the flux

$$D = -\boldsymbol{\nabla}_2 \cdot \left[\frac{1}{\mathcal{M}} \left(h^3 \boldsymbol{\nabla}_2 \left(\Gamma \boldsymbol{\nabla}_2^2 h + \Pi(h) \right) \right) \right], \tag{A.51}$$

and define $D_{i,j}^n$ to be a second-order spatial discretization of D. Equation (3.4) can then be written as

$$\frac{h_{i,j}^{n+1} - h_{i,j}^n}{\Delta t} = \frac{1}{2}D_{i,j}^{n+1} + \frac{1}{2}D_{i,j}^n, \quad i = 1, \ldots, N, \ j = 1, \ldots, M. \quad (A.52)$$

Equation (A.52) is linearized and a Newton's method is used to iterate guesses to the film thickness at time t_{n+1}. In contrast to the 2D case, D now involves derivatives with respect to y as well as x. Therefore, the Newton's method is split into two separate linear systems of equations (one where y-derivatives are treated implicitly in time and one similarly for x-derivatives), and solved iteratively. The equations in general take the form

$$\mathbf{A}_{y,(l)}\mathbf{w}_h = \mathbf{b}_{y,(l)} \quad (A.53)$$

$$\mathbf{A}_{x,(l)}\mathbf{v} = \mathbf{w}_h \quad (A.54)$$

$$\mathbf{h}_{(l+1)}^{n+1} = \mathbf{h}_{(l)}^{n+1} + \mathbf{v}, \quad (A.55)$$

where (l) represents iteration number l, $\mathbf{h}$ represents the array of values $h_{i,j}$, $\mathbf{w}_h$ is an intermediate step, and $\mathbf{v}$ is an array of corrections to the guess $\mathbf{h}_{(l)}^{n+1}$. $\mathbf{A}_{y,(l)}, \mathbf{A}_{x,(l)}$ are matrices whose components are found using pure y- and x-derivative terms, respectively, and $\mathbf{b}_{y,(l)}$ is a vector (containing flux discretizations), which we omit for brevity. For details regarding these terms we refer the reader to the work of Lam $et\ al.$ [81]. Notably, Equations (A.53) and (A.54) are penta-diagonal systems of equations, which can be solved in parallel. In the former, N linear systems of equations of size $M \times M$ are solved simultaneously, whereas in the latter, M linear systems of size $N \times N$ are solved at once.

The film thickness is again coupled to film temperature through the material parameters, film temperature is coupled to thickness via Equations (A.43) and (A.44), and substrate temperature to film temperature via the interface $z = 0$. The solution

order is identical to that of Appendix A.12, solving first for h and then T_f and T_s using a predictor-corrector method.

A.14 Random Noise in 3D

Here we describe the implementation of the initial condition given by Equation (3.16). Note that in Section 3.4.4 the domain size is $16\pi \times 16\pi$. Suppose our grid is (x_k, y_j), where $k = 1, \ldots, N$ and $j = 1, \ldots, M$ as defined in Appendix A.13. Then, to create the initial condition given in Equation (3.16), we consider wavelengths that are integral partitions of the domain length

$$\left(\lambda_{x_k}, \lambda_{y_j}\right) = \left(\frac{16\pi}{k}, \frac{16\pi}{j}\right), \quad k = 1, \ldots, N, \; j = 1, \ldots, M. \tag{A.56}$$

The possible wavenumbers are then

$$\left(q_{x_k}, q_{y_j}\right) = \left(\frac{k}{8}, \frac{j}{8}\right), \quad k = 1, \ldots, N, \; j = 1, \ldots, M. \tag{A.57}$$

Next, we generate complex numbers, $\hat{\zeta}(q_{x_k}, q_{y_j})$, with random phase shifts and amplitudes that decay for large q_{x_k} and q_{y_j}. We use

$$\hat{\zeta}(q_{x_k}, q_{y_j}) = \left(q_{x_k}^2 + q_{y_j}^2\right)^{-\alpha/2} \exp\left(2\pi i a_{k,j}\right), \tag{A.58}$$

where $a_{k,j}$ is a random number in $[0, 1]$ and α is a parameter that determines the magnitude of $\hat{\zeta}$. Here, the amplitudes of $\hat{\zeta}$ represent coefficients of the Fourier series representation of ζ and $a_{k,j}$ are random phase shifts. We set $\alpha = 25\Delta x/(2\pi)$ as used in Lam *et al.* [81] (note that this value is independent of the domain size, as discussed further below). Then, $\zeta_{k,j} = \zeta(x_k, y_j)$ is given by

$$\zeta_{k,j} = \frac{1}{MN} \sum_{m=0}^{M-1} \sum_{n=0}^{N-1} \hat{\zeta}(q_{x_n}, q_{y_m}) \exp(2\pi i k n/N) \exp(2\pi i j m/M). \tag{A.59}$$

To reduce noise at high wavenumbers, we apply a Gaussian filter to $|\zeta_{k,j}|$, [2] and denote the result by $\xi_{k,j}$. Finally, $\eta_{k,j} = \eta(x_k, y_j)$ in Equation (3.16) is defined by rescaling $\xi_{k,j}$,

$$\eta_{k,j} = 2 \frac{\xi_{k,j} - \min_{k,j} \xi_{k,j}}{\max_{k,j} \left(\xi_{k,j} - \min_{k,j} \xi_{k,j} \right)} - 1, \tag{A.60}$$

which ensures both positive and negative perturbations in the initial condition, $\eta_{k,j} \in [-1, 1]$ for all k and j.

To illustrate the Fourier spectrum of $\eta_{k,j}$, as well as the fact that α does not depend on the domain size, Figure A.16 shows $|\hat{\eta}_{k,j}|$, the amplitude of the Fourier transform of the noise, $|\eta_{k,j}|$, using the same value of α for linear domain lengths 16π (a) and 8π (b). The maximum of $|\hat{\eta}_{k,j}|$ and distribution of amplitudes for different wavenumbers q_{x_k}, q_{y_j} are similar between (a) and (b) (note that the amplitudes of individual modes are random and can therefore vary). It is easy to verify that the distribution of the mode amplitudes is random, without correlations of the x and y modes' amplitudes.

---

[2] In our implementation, the filtering is applied four times using the "imgaussfilt" tool in Matlab$^\circledR$ [90] with standard deviations $4, 3, 2$ and 1. It should be noted that one may also restrict the range of wavenumbers in Equation (A.57) or set the amplitude of the undesirable ones to 0 manually.
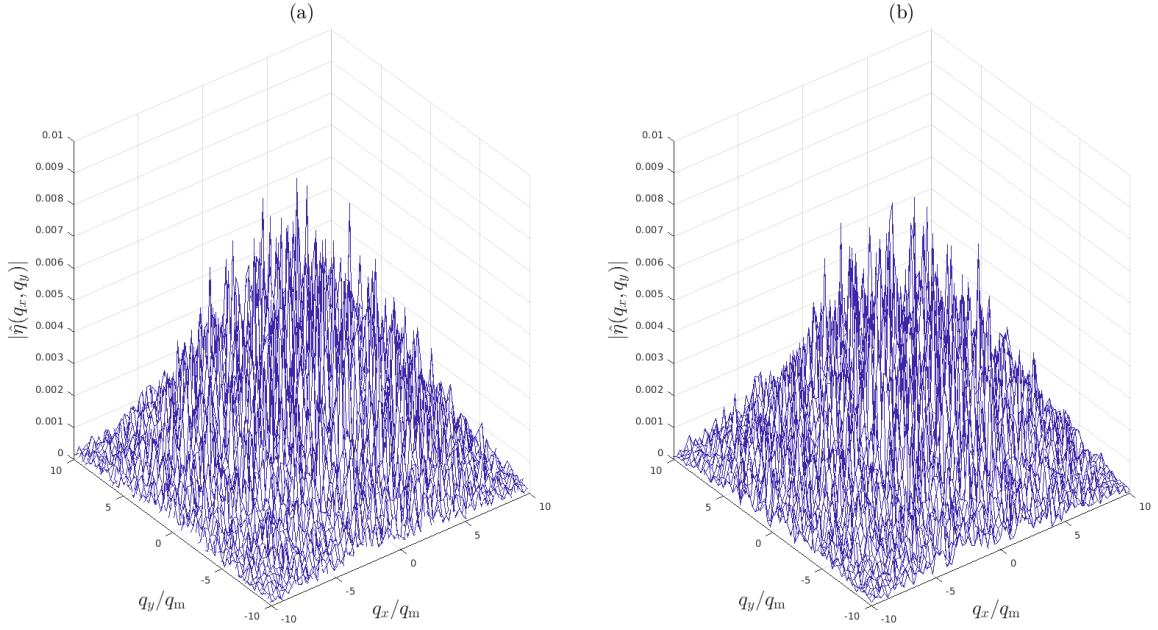
Figure A.16 Amplitude of the Fourier transform of the noise, $|\hat{\eta}|$. (a) Linear domain length, 16π with half of the $N = 1448$ modes excited. (b) Linear domain length, 8π with all $N = 724$ modes excited. The value of α is the same for both (a) and (b), and both the range and distribution of $|\hat{\eta}|$ are similar. The DC mode was removed for visualization purposes.

APPENDIX B

DETAILS AND ANALYSIS OF THE SIMULATIONS OF ALLOYS

In this appendix, we provide information regarding the molecular dynamics (MD) simulations presented in Chapters 4 and 5. Here, we provide the inter-atomic potentials used for the simulations, complementary mathematical analysis of the data, additional simulations supportive of the main conclusions, and images detailing the internal structure of the resultant nanoparticles.

B.1   Form of EAM Potential

According to Zhou *et al.*, the total energy, E, can be expressed as:

$$E = \sum_i F_i(\rho_i) + \frac{1}{2} \sum_{i,j,i \neq j} \phi_{i,j}(r_{i,j}), \qquad (B.1)$$

which is composed of an embedding energy, F_i, as a function of the atomic electron density, ρ_i, and a pairwise energy, $\phi_{i,j}$, between atoms i and j which are separated by a distance $r_{i,j}$ [149]. For alloys, it is necessary to incorporate different forms for the pairwise energy depending on if the atoms are of the same or different type. More information regarding the documentation of the parameters for the system considered here, Ni-Ag, can be found in [149].

B.2   Calibration of Lennard-Jones (LJ) Potential

To calibrate the appropriate value of ε and σ in Equation (4.1), Ni and Ag bulk structures, containing 55296 atoms, were created at 1900 K and 1750 K, respectively, by sampling from NPT, NVT, and then NVE. They were then placed upon 1 layer of graphene. The well-depth parameter, ε, was tuned so that the resultant droplets had wetting angles consistent with the ranges found in literature [19, 62, 82, 95, 112, 139]

whereas the values of σ were held fixed at 2.8 (Ni) and 3.006 (Ag) angstroms. The wetting angles of the droplets were computed using a distribution of ImageJ software, Fiji, [122] along with the Contact Angle plugin developed by Marco Brugnara, and were averaged over four images (front, back, right, left).

(a)   (b)
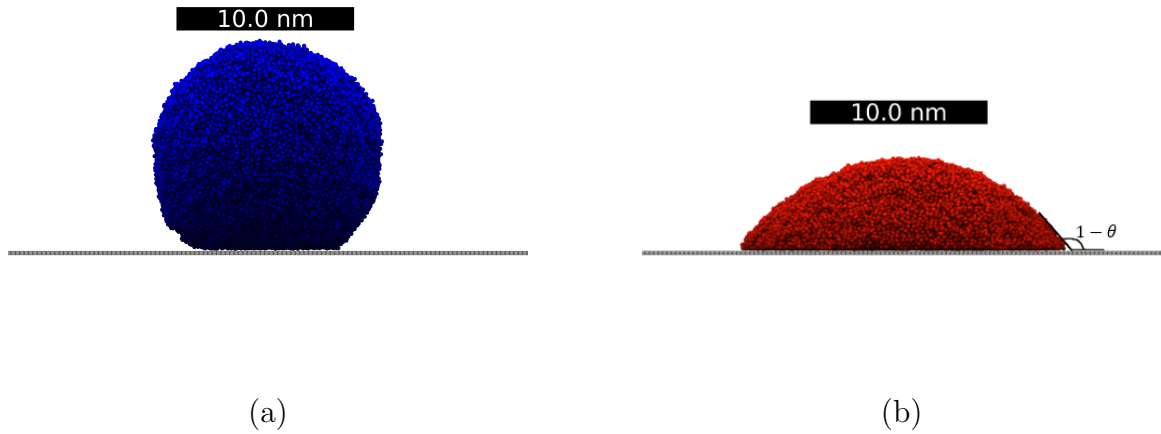
Figure B.1 Ag (a) at 1750 K and Ni (b) at 1900 K equilibrated on graphene (grey) using the NVT ensemble on the metal, while holding the graphene fixed. These pictures represent one of four pictures used to calculate the wetting angles.
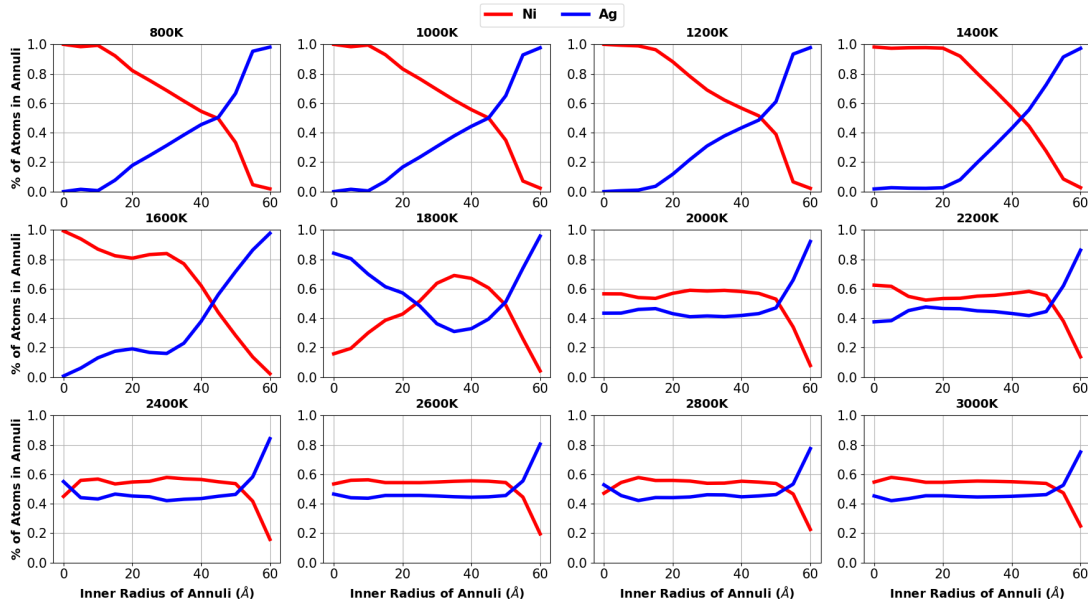
Figure B.2   Atomic concentration distribution analysis for the droplets at 200 K increments from 800 K to 3000 K. Color code: Ni, red; Ag, blue.

B.4   Bulk Construction

The process of creating these bulk structures (Figure 5.1) made the lengths, L, slightly different ((a): 1463.2 Å, (b): 1433.7 Å, (c) 1598.9 Å). The only bearing this has is on the initial prescribed stripe length, which is determined by L. The widths (y-axis in Figure 5.1) and heights (z-axis in Figure 5.1) of each of these structures were (a) $W = H = 98.3$ Å, (b) $W = H = 96.6$ Å, (c) $W = H = 96.0$ Å.
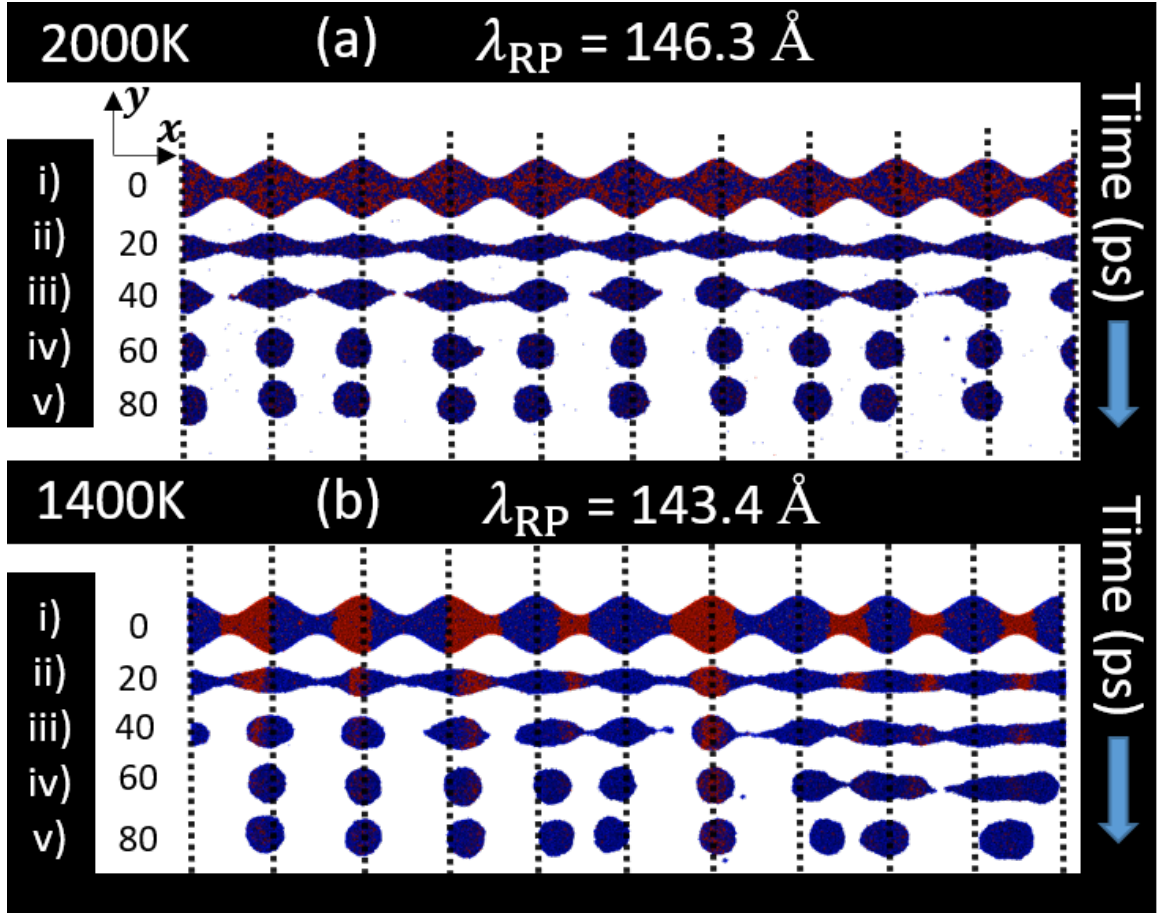
Figure B.3   Time evolution of synthetic lines patterned with amplitude $A = 16$ Å and maximum RP wavelength $\lambda_{RP} = 146.3$ Å (a) and $\lambda_{RP} = 143.4$ Å (b). Time labels (in ps) are placed next to the corresponding lines. Guides (dotted lines) are placed at the location of the original peak in i).

Figure B.3 shows an example of synthetic lines at (a) 2000 K and (b) 1400 K patterned with the maximum RP wavelength, $\lambda_{RP} = \lambda_m$. The time evolution is marked i)-v) and is shown in 20ps increments. In Figure B.3(a), at 2000 K, where the phase separation length scale is very small, the line breaks up into 10 equally-spaced nanoparticles according to the RP mechanism. In Figure B.3(b), the PS length scale is comparable in size to the prescribed maximum wavelength, ($\lambda_{PS} = 170.7$ Å). Similar to what was shown for longer λ_{RP}, when the trough is aligned with the Ag/Ni interface or in a Ag region, the soluto-capillary flow cooperates with the RP mechanism and droplets

form slightly faster and are aligned with the peak positions (see the center and left side of Figur B.3(b)). When the troughs are mostly Ni, however, the soluto-capillary flow competes with the RP mechanism as early stages of the line are observed to coarsen as Ag atoms migrate to this Ni-rich region. Ultimately, where the troughs are Ni-rich, the breakup is slower and the particle positions are not aligned with the original synthetic perturbation peak positions, consistent with the soluto-capillary effects competing with the RP.

B.6   Line Construction and Nanoparticle Slices

At the lateral ends of the lines, periodic boundary conditions are imposed. The widths of these lines are calculated so that for lines of length L, and wavelength λ, $L = N\lambda$ where N is an integer (we used $N = 5$ or $N = 3$).
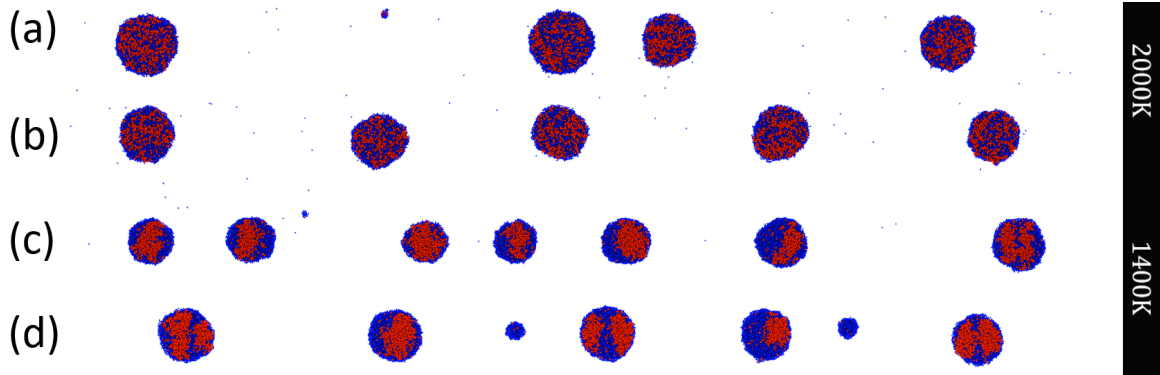
Figure B.4 Longitudinal slices of resultant nanoparticles at the final frames v) for (a) Figure 5.3 2000K, straight line (left), (b) Figure 5.3 2000 K, large amplitude (right), (c) Figure 5.3 1400 K, straight line (left), (d) Figure 5.3 1400 K, large amplitude (right). In (d) satellite droplets of pure Ag are present.
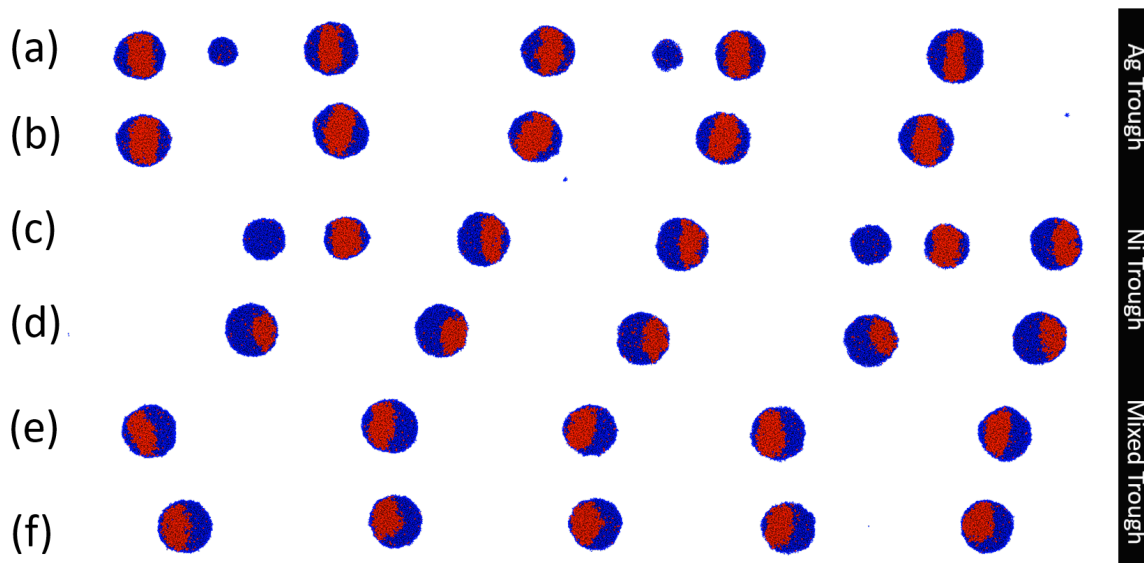
Figure B.5 Longitudinal slices of resultant nanoparticles at the final frames v) for (a) Figure 5.4 Ag trough, small amplitude (left), (b) Figure 5.4 Ag trough, large amplitude (right), (c) Figure 5.4 Ni trough, small amplitude (left), (d) Figure 5.4 Ni trough, large amplitude (right), (e) Figure 5.4 mixed trough, small amplitude (left), and (f) Figure 5.4 mixed trough, large amplitude (right). In (a) satellite droplets of nearly pure Ag are present.
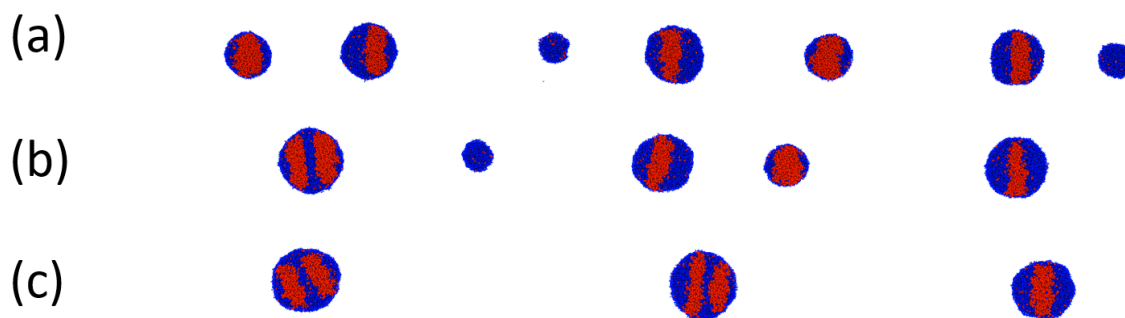
Figure B.6 Longitudinal slices of resultant nanoparticles at the final frames v) for (a) Figure 5.5 A=3.2 Å (b) Figure 5.5 A=5 Å, and (c) Figure 5.5 A=6 Å. In (a) and (b) satellite droplets of pure Ag are present.

B.7 Pure Ni and Ag simulations and Radial Distribution Functions
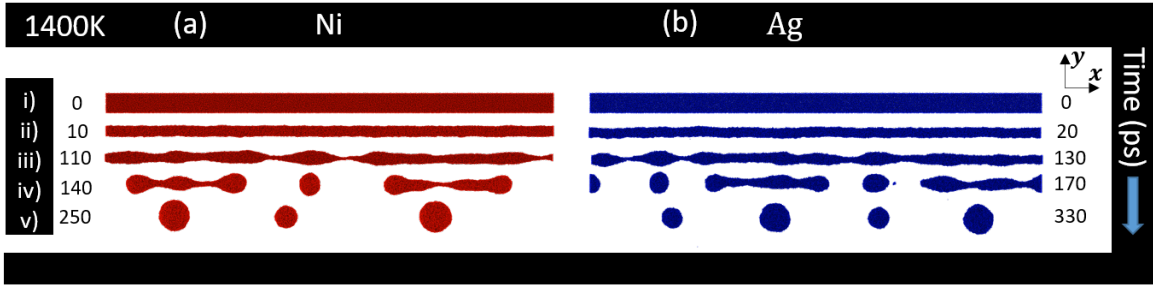
Figure B.7 Time evolution of straight lines of Ni (a) and Ag (b) at 1400 K. Time labels (in ps) are placed next to the corresponding lines. The significance of times i)-v) is similar to Figure 5.3.
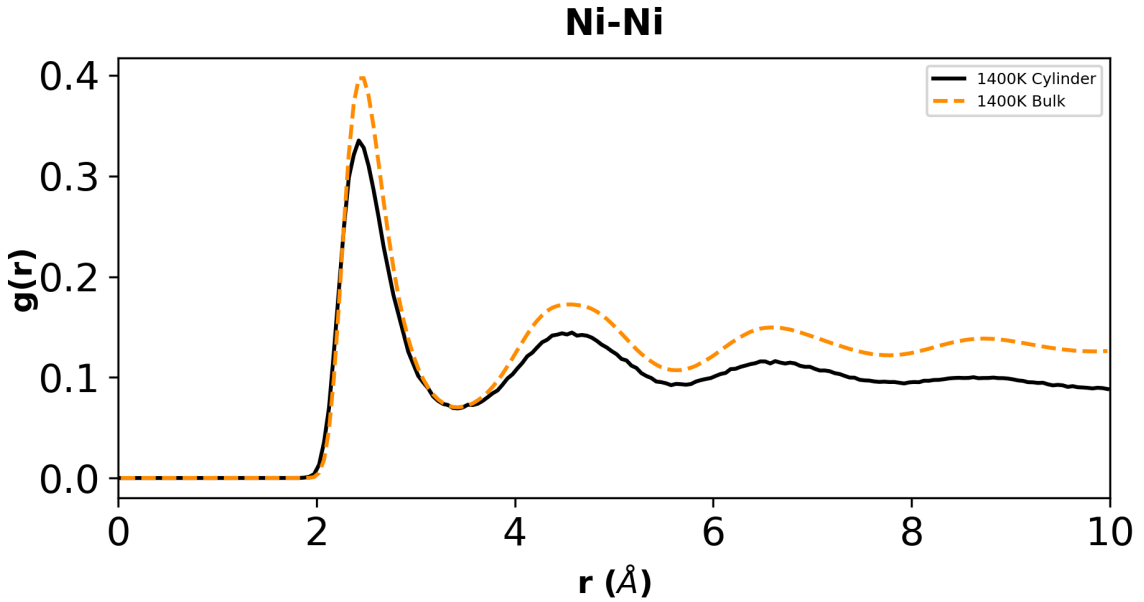
Figure B.8 Radial distribution function (rdf), g(r), for the 1400 K cylinder (black, solid) and bulk (orange, dashed) NiAg structures from ii) of Figure 5.3c and Figure 5.1b, respectively. Note the rdfs were computed with OVITO [129] and then normalized based on the number of atoms; as expected the cylinders have lower amplitude peaks consistent with some surface melting relative to the bulk structure.

APPENDIX C

SUPPLEMENTARY MATERIALS

Supplementary material related to this dissertation can be found online at https://drive.google.com/drive/folders/1zrf7h0fdBuw2sTNKqJVPn02BxK8o281E?usp=sharing, available as of May 2021.

REFERENCES

[1] H. Akbarzadeh and H. Yaghoubi. Molecular dynamics simulations of silver nanocluster supported on carbon nanotube. *J. Colloid Interface Sci.*, 418:178–184, 2014.

[2] R. H. Allaire. Gadit thermal. https://github.com/Ryallaire/GADIT_THERMAL, 2021.

[3] R. H. Allaire, L. J. Cummings, and L. Kondic. On efficient asymptotic modelling of thin films on thermally conductive substrates. *J. Fluid Mech.*, 915:A133, 2021.

[4] R. H. Allaire, A. Dhakane, R. Emery, P. Ganesh, P. D. Rack, L. Kondic, L. Cummings, and M. Fuentes-Cabrera. Surface, interface, and temperature effects on the phase separation and nanoparticle self assembly of bi-metallic Ni0.5Ag0.5: A molecular dynamics study. *Nanomaterials*, 9:1040, 2019.

[5] R. H. Allaire, L. Kondic, L. J. Cummings, P. D. Rack, and M. Fuentes-Cabrera. The role of phase separation on Rayleigh-Plateau type instabilities in alloys. *J. Phys. Chem. C*, 125:5723–5731, 2021.

[6] T. A. Arshad, C. B. Kim, N. A. Prisco, J. M. Katzenstein, D. W. Janes, R. T. Bonnecaze, and C. J. Ellison. Precision Marangoni-driven patterning. *Soft Matter*, 10:8043–8050, 2014.

[7] A. Atena and M. Khenner. Thermocapillary effects in driven dewetting and self assembly of pulsed-laser-irradiated metallic films. *Phys. Rev. B*, 80:075402, 2009.

[8] H. A. Atwater and A. Polman. Plasmonics for improved photovoltaic devices. *Nat. Mater.*, 9:205–213, 2010.

[9] S. D. Bader. Colloquium: Opportunities in Nanomagnetism. *Rev. Mod. Phys.*, 78:1, 2006.

[10] W. Batson, L. J. Cummings, D. Shirokoff, and L. Kondic. Oscillatory thermocapillary instability of a film heated by a thick substrate. *J. Fluid Mech.*, 872:928–962, 2019.

[11] M. Beerman and L. N. Brush. Oscillatory instability and rupture in a thin melt film on its crystal subject to freezing and melting. *J. Fluid Mech.*, 586:423–448, 2007.

[12] M. J. Beliatis, S. J. Henley, and S. R. P. Silva. Engineering the plasmon resonance of large area bimetallic nanoparticle films by laser nanostructuring for chemical sensors. *Opt. Lett.*, 36:1362–1364, 2011.

[13] J. G. Berryman. Random close packing of hard spheres and disks. *Phys. Rev. A*, 27:1053–1061, 1983.

[14] E. Bertrand, T. D. Blake, and J. De Coninck. Dynamics of dewetting at the nanoscale. *Eur. Phys. J. Spec. Top.*, 166:173–176, 2009.

[15] E. Bertrand, T. D. Blake, V. Ledauphin, G. Ogonowski, J. De Coninck, D. Fornasiero, and J. Ralston. Dynamics of dewetting at the nanoscale using molecular dynamics. *Langmuir*, 23:3774–3785, 2007.

[16] J. Bischof, D. Scherer, S. Herminghaus, and P. Leiderer. Dewetting modes of thin metallic films: Nucleation of holes and spinodal dewetting. *Phys. Rev. Lett.*, 77:1536, 1996.

[17] T. D. Blake, A. Clarke, J. De Coninck, and M. J. de Ruijter. Contact angle relaxation during droplet spreading: Comparison between molecular kinetic theory and molecular dynamics. *Langmuir*, 13:2164–2166, 1997.

[18] W. L. Boldman, D. A. Garfinkel, R. Collette, C. S. Jorgenson, D. K. Pradhan, D. A. Gilbert, and P. D. Rack. Exploring the composition, phase separation and structure of agfe alloys for magneto-optical applications. *Mater. Sci. Eng., B*, 266:115044, 2021.

[19] M. J. Bozack, A. E. Bell, and L. W. Swanson. Influence of surface segregation on wetting of liquid metal alloys. *J. Phys. Chem.*, 92:3925–3934, 1988.

[20] J. T. Bullerjahn, S. von Bülow, and G. Hummer. Optimal estimates of self-diffusion coefficients from molecular dynamics simulations. *J. Chem. Phys.*, 153:024116, 2020.

[21] W. D. Callister Jr. *Materials Science and Engineering: An Introduction.* New York, NY: John Wiley & Sons, Inc., 7th edition, 2007.

[22] M. Censabella, F. Ruffino, M. Zimbone, E. Bruno, and M. G. Grimaldi. Self-organization based fabrication of bimetallic PtPd nanoparticles on transparent conductive oxide substrates. *Phys. Status Solidi A*, 215:1700524, 2018.

[23] D. J. Chappell and R. D. O'Dea. Numerical-asymptotic models for the manipulation of viscous films via dielectrophoresis. *J. Fluid Mech.*, 901:A35, 2020.

[24] J. Chen. 7 - Thin film coatings and the biological interface. In Hans J Griesser, editor, *Thin Film Coatings for Biomaterials and Biomedical Applications*, pages 143–164. Cambridge, England: Woodhead Publishing, Jan. 2016.

[25] W. K. Choi, T. H. Liew, H. G. Chew, F. Zheng, C. V. Thompson, Y. Wang, M. H. Hong, X. D. Wang, L. Li, and J. Yun. A combined top-down and bottom-up approach for precise placement of metal nanoparticles on silicon. *Small*, 4:330–333, 2008.

[26] P. Combis, P. Cormont, L. Gallais, D. Hebert, L. Robin, and J. L. Rullier. Evaluation of the fused silica thermal conductivity by comparing infrared thermometry measurements with two-dimensional simulations. *Appl. Phys. Lett.*, 101:2–6, 2012.

[27] R. V. Craster and O. K. Matar. Dynamics and stability of thin liquid films. *Rev. Mod. Phys.*, 81:1131, 2009.

[28] S. H. Davis and L. M. Hocking. Spreading and imbibition of viscous liquid on a porous base. II. *Physics of Fluids*, 12:1646–1655, 2000.

[29] J. De Coninck and T. D. Blake. Wetting and molecular dynamics simulations of simple liquids. *Annu. Rev. Mater. Res.*, 38:1–22, 2008.

[30] M. J. de Ruijter, T. D. Blake, and J. De Coninck. Dynamic wetting studied by molecular modeling simulations of droplet spreading. *Langmuir*, 15:7836–7847, 1999.

[31] J. Diez and L. Kondic. Computing three-dimensional thin film flows including contact lines. *J. Comput. Phys.*, 183:274, 2002.

[32] J. A. Diez, A. G. González, D. A. Garfinkel, P. D. Rack, J. T. McKeown, and L. Kondic. Simultaneous decomposition and dewetting of nanoscale alloys: A comparison of experiment and theory. *Langmuir*, 37:2575–2585, 2021. PMID: 33587633.

[33] N. Dong and L. Kondic. Instability of nanometric fluid films on a thermally conductive substrate. *Phys. Rev. Fluids*, 1:063901, 2016.

[34] C. Favazza, R. Kalyanaraman, and R. Sureshkumar. Robust nanopatterning by laser-induced dewetting of metal nanofilms. *Nanotechnology*, 17:4229, 2006.

[35] C. Favazza, J. Trice, A. K. Gangopadhyay, H. Garcia, R. Sureshkumar, and R. Kalyanaraman. Nanoparticle ordering by dewetting of Co on SiO2. *J. Electron. Mater.*, 35:1618, 2006.

[36] C. Favazza, J. Trice, R. Kalyanaraman, and R. Sureshkumar. Self-organized metal nanostructures through laser-interference driven thermocapillary convection. *Appl. Phys. Lett.*, 91:043105, 2007.

[37] C. Favazza, J. Trice, H. Krishna, and R. Kalyanaraman. Laser-induced short- and long-range orderings of Co nanoparticles on SiO2. *Appl. Phys. Lett.*, 88:153118, 2006.

[38] G. R. Fleming and M. A. Ratner. Grand challenges in basic energy sciences. *Phys. Today*, 61:28, 2008.

[39] F. Font, S. Afkhami, and L. Kondic. Substrate melting during laser heating of nanoscale metal films. *Int. J. Heat Mass Transfer*, 113:237, 2017.

[40] J. Fowlkes, S. Horton, M. Fuentes-Cabrera, and P. D. Rack. Signatures of the Rayleigh-Plateau instability revealed by imposing synthetic perturbations on nanometer-sized liquid metals on substrates. *Angew. Chem. Int. Ed.*, 51:8768, 2012.

[41] J. D. Fowlkes, L. Kondic, J. Diez, and P. D. Rack. Self-assembly versus directed assembly of nanoparticles via pulsed laser induced dewetting of patterned metal films. *Nano Letters*, 11:2478, 2011.

[42] J. D. Fowlkes, L. Kondic, J. A. Diez, A. G. Gonzalez, Y. Wu, N. A. Roberts, C. E. McCold, and P. D. Rack. Parallel assembly of particles and wires on substrates by dictating instability evolution in liquid metal films. *Nanoscale*, 4:7376, 2012.

[43] J. D. Fowlkes, N. A. Roberts, Y. Wu, J. A. Diez, A. G. González, C. Hartnett, K. Mahady, S. Afkhami, L. Kondic, and P. D. Rack. Hierarchical nanoparticle ensembles synthesized by liquid phase directed self-assembly. *Nano Lett.*, 14:774, 2014.

[44] J. D. Fowlkes, Y. Wu, and P. D. Rack. Directed assembly of bimetallic nanoparticles by pulsed-laser-induced dewetting: A unique time and length scale regime. *ACS Appl. Mater. Interfaces*, 2:2153, 2010.

[45] D. Frenkel and B. Smit. *Chapter 6 - Molecular Dynamics in Various Ensembles*, pages 139–163. Academic Press, San Diego, CA, 2nd edition, 2002.

[46] O. A. Frolovskaya, A. A. Nepomnyashchy, A. Oron, and A. A. Golovin. Stability of a two-layer binary-fluid system with a diffuse interface. *Phys. Fluids*, 20:1–17, 2008.

[47] M. Fuentes-Cabrera, B. H. Rhodes, M. I. Baskes, H. Terrones, J. D. Fowlkes, M. L. Simpson, and P. D. Rack. Controlling the velocity of jumping nanodroplets via their initial shape and temperature. *ACS Nano*, 5:7130, 2011.

[48] M. Fuentes-Cabrera, B. H. Rhodes, J. D. Fowlkes, A. López-Benzanilla, H. Terrones, M. L. Simpson, and P. D. Rack. Molecular dynamics study of the dewetting of copper on graphite and graphene: Implications for nanoscale self-assembly. *Phys. Rev. E*, 83:041603, 2011.

[49] W. F. Gale and T. C. Totemeier. *Smithells Metals Reference Book*. Oxford, England: Butterworth-Heinemann, 8th edition, 2004.

[50] D. A. Garfinkel, G. Pakeltis, N. Tang, I. N. Ivanov, J. D. Fowlkes, D. A. Gilbert, and P. D. Rack. Optical and magnetic properties of Ag–Ni bimetallic nanoparticles assembled via pulsed laser-induced dewetting. *ACS (American Chemical Society) Omega*, 2020.

[51] A. Gloster, L. Ó. Náraigh, and K. E. Pang. cuPentBatch—A batched pentadiagonal solver for NVIDIA GPUs. *Comput. Phys. Commun*, 241:113–121, 2019.

[52] A. G. Gonzalez, J. D. Diez, Y. Wu, J.D. Fowlkes, P. D. Rack, and L. Kondic. Instability of Liquid Cu Films on a SiO$_2$ Substrate. *Langmuir*, 13:9378, 2013.

[53] D. B. Graves and P. Brault. Molecular dynamics for low temperature plasma-surface interaction studies. *J. Phys. D: Appl. Phys*, 42:194011, 2009.

[54] Y. F. Guan, R. P. Pearce, A. V. Melecho, D. K. Hensley, M. L. Simpson, and P. D. Rack. Pulsed laser dewetting of nickel catalyst for carbon nanofiber growth. *Nanotechnology*, 19:235604, 2008.

[55] N. J. Halas, S. Lal, W. Chang, S. Link, and P. Nordlander. Plasmons in strongly coupled metallic nanostructures. *Chem. Rev.*, 111:3913–3961, 2011.

[56] C. A. Hartnett, K. Mahady, J. D. Fowlkes, S. Afkhami, L. Kondic, and P. D. Rack. Instability of nano- and microscale liquid metal filaments: Transition from single droplet collapse to multidroplet breakup. *Langmuir*, 31:13609, 2015.

[57] C. A. Hartnett, I. Seric, K. Mahady, L. Kondic, S. Afkhami, J. D. Fowlkes, and P. D. Rack. Exploiting the marangoni effect to initiate instabilities and direct the assembly of liquid metal filaments. *Langmuir*, 33:8123–8128, 2017.

[58] O. S. Heavens. *Optical Properties of Thin Solid Films.* New York, NY: Dover Publications, 1955.

[59] S.J. Henley, J.D. Carey, and S.R.P. Silva. Pulsed-laser-induced nanoscale island formation in thin metal-on-oxide films. *Phys. Rev. B*, 72:195408, 11 2005.

[60] Heraeus. *Quartz Glass for Optics Data and Properties*, Dec. 2019. HQS190014.

[61] S. Herminghaus, K. Jacobs, K. Mecke, J. Bischof, A. Fery, M. Ibn-Elhaj, and S. Schlagowski. Spinodal Dewetting in Liquid Crystal and Liquid Metal Films. *Science*, 282:916, 1998.

[62] J. Hlinka and Z. Weltsch. Relation between the wetting property and electrical conduction of silver-gold (Ag-Au) alloys. *Period. Polytech. Transp. Eng.*, 41:95–98, 2013.

[63] J. R. Howell, R. Siegel, and M. Pinar Menguc. *Thermal Radiation Heat Transfer.* New York, NY: CRC Press, 2010.

[64] R. A. Hughes, E. Menumerov, and S. Neretina. When lithography meets self-assembly: a review of recent advances in the directed assembly of complex metal nanostructures on planar and textured surfaces. *Nanotechnology*, 28:282002, 2017.

[65] W. Humphrey, A. Dalke, and K. Schulten. VMD - visual molecular dynamics. *J. Molec. Graphics*, 14:33–38, 1996.

[66] J. N. Israelachvili. *Intermolecular and surface forces.* New York, NY: Academic Press, 2nd edition, 1992.

[67] J. Mckeown, Y. Wu, J. D. Fowlkes, P. D. Rack, and G. H. Campbell. Simultaneous in-situ synthesis and characterization of Co-Cu core-shell nanoparticle arrays. *Adv. Mater.*, 27:1060–1065, 2015.

[68] J. Jeong, K. Choi, and J. Ye. Investigation of a Rayleigh-like instability during the solid-state dewetting of single-crystal nickel and palladium films. *Journal of the Korean Physical Society*, 73:90–94, 2018.

[69] G. Kaptay. A unified equation for the viscosity of pure liquid metals. *Zeitschrift für Metallkunde*, 96:24–31, 2005.

[70] J. M. Katzenstein, D. W. Janes, J. D. Cushen, N. B. Hira, D. L. McGuffin, N. A. Prisco, and C. J. Ellison. Patterning by photochemically directing the Marangoni Effect. *ACS Macro Lett.*, 1:1150–1154, 2012.

[71] S. Kawano. Molecular dynamics of rupture phenomena in a liquid thread. *Phys. Rev. E*, 58:4468–4472, 1998.

[72] M. H. Kim, B. Lee, S. Lee, C. Larson, J. M. Baik, C. T. Yavuz, S. Seifert, S. Vajda, R. E. Winans, M. Moskovits, G. D. Stucky, and A. M. Wodtke. Growth of metal oxide nanowires from supercooled liquid nanodroplets. *Nano Lett.*, 9:4138–4146, 2009.

[73] W. D. Kingery. Thermal conductivity: Xii, temperature dependence of conductivity for single-phase ceramics. *J. Am. Ceram. Soc*, 38:251–255, 1955.

[74] L. Kondic. Instability in the gravity driven flow of thin liquid films. *SIAM Review*, 45:95, 2003.

[75] L. Kondic, J. Diez, P. D. Rack, Y. Guan, and J. Fowlkes. Nanoparticle assembly via the dewetting of patterned thin metal lines: Understanding the instability mechanism. *Phys. Rev. E*, 79:026302, 2009.

[76] L. Kondic, A. G. Gonzalez, J. A. Diez, J. D. Fowlkes, and P. Rack. Liquid-state dewetting of pulsed-laser-heated nanoscale metal films and other geometries. *Annu. Rev. Fluid Mech.*, 52:235–262, 2020.

[77] H. Krishna, A. K. Gangopadhyay, J. Strader, and R. Kalyanaraman. Nanosecond laser-induced synthesis of nanoparticles with tailorable magneticanisotropy. *J. Magn. Magn. Mater.*, 323:356–362, 2011.

[78] H. Krishna, R. Sachan, J. Strader, C. Favazza, M. Khenner, and R. Kalyanaraman. Thickness-dependent spontaneous dewetting morphology of ultrathin Ag films. *Nanotechnology*, 21:155601, 2010.

[79] H. Krishna, N. Shirato, C. Favazza, and R. Kalyanaraman. Energy driven self-organization in nanoscale metallic liquid films. *Phys. Chem. Chem. Phys.*, 11:8136, 2009.

[80] S. Kumar. Spreading and orientation of silver nano-drops over a flat graphene substrate: An atomistic investigation. *Carbon*, 138:26–41, 2018.

[81] M.-A. Y.-H. Lam, L. J. Cummings, and L. Kondic. Computing dynamics of thin films via large scale GPU-based simulations. *J. Comput. Phys.: X*, 2:100001, 2019.

[82] J. Lee, K. Seo, N. Hirai, N. Takahira, and T. Tanaka. Intrinsic contact angle and contact interaction between liquid silver and solid graphite. *Met. Mater. Int.*, 13:83–86, 2007.

[83] P. H. Li and P. K. Chu. 1 - thin film deposition technologies and processing of biomaterials. In Hans J Griesser, editor, *Thin Film Coatings for Biomaterials and Biomedical Applications*, pages 3–28. Cambridge, England: Woodhead Publishing, 2016.

[84] T. Li, Z. Wang, Y. Duan, J. Li, and H. Li. Molecular dynamics study on the formation of self-organized core/shell structures in the Pb alloy at the nanoscale. *RSC Advances*, 7:53509–53515, 2017.

[85] D. Lipkin, J. Israelachvili, and D. Clarke. Estimating the metal-ceramic van der Waals adhesion energy. *Phil. Mag. A*, 76:715–728, 1997.

[86] S. N. Luo, T. J. Ahrens, T. Çağın, A. Strachan, W. A. Goddard, and D. C. Swift. Maximum superheating and undercooling: Systematics, molecular dynamics simulations, and dynamic experiments. *Phys. Rev. B*, 68:134206, 2003.

[87] S. A. Maier. *Plasmonics: Fundamentals and Applications*. Springer-Verlag, New York, NY, 2007.

[88] S. A. Maier, P. G. Kik, H. A. Atwater, S. Meltzer, E. Harel, B. E. Koel, and A. A. Requicha. Local detection of electromagnetic energy transport below the diffraction limit in metal nanoparticle plasmon waveguide. *Nat. Mat.*, 2:229, 2003.

[89] S. V. Makarov, V. A. Milichko, I. S. Mukhin, I. I. Shishkin, D. A. Zuev, A. M. Mozharov, A. E. Krasnok, and P. A. Belov. Controllable femtosecond laser-induced dewetting for plasmonic applications. *Laser Photonics Rev.*, 10:91, 2016.

[90] The Mathworks, Inc., Natick, Massachusetts. *MATLAB version 9.8.0.1451342 (R2020a)*.

[91] M. Mayer, L. Scarabelli, K. March, T. Altantzis, M. Tebbe, M. Kociak, S. Bals, F. J. García de Abajo, A. Fery, and L. M. Liz-Marzán. Controlled living nanowire growth: Precise control over the morphology and optical properties of AgAuAg bimetallic nanowires. *Nano Lett.*, 15:5427–5437, 2015.

[92] J. T. McKeown, N. A. Roberts, J. D. Fowlkes, Y. Wu, T. LaGrange, B. W. Reed, G. H. Campbell, and P. D. Rack. Real-time observation of nanosecond liquid-phase assembly of nickel nanoparticles via pulsed-laser heating. *Langmuir*, 28:17168, 2012.

[93] E. Mema, L. Kondic, and L. J. Cummings. Dielectrowetting of a thin nematic liquid crystal layer. *Phys. Rev. E*, 103:032702, 2020.

[94] Y. Min, M. Akbulut, K. Kristiansen, Y. Golan, and J. Israelachvili. The role of interparticle and external forces in nanoparticle assembly. *Nat. Materials*, 7:527, 2008.

[95] Yu. V. Naidich, V. M. Perevertailo, and G. M. Nevodnik. Wetting of graphite by nickel as affected by the liquid-phase dissolution process of carbon. *Powder Metall. Met. Ceram.*, 10:45–47, 1971.

[96] L. Ó Náraigh and J.-L. Thiffeault. Nonlinear dynamics of phase separation in thin films. *Nonlinearity*, 23:1559–1583, 2010.

[97] T. D. Nguyen, M. Fuentes-Cabrera, J. D. Fowlkes, J. A. Diez, A. G. González, L. Kondic, and P.D. Rack. Competition between collapse and breakup in nanometer-sized thin rings using molecular dynamics and continuum modeling. *Langmuir*, 28:13960, 2012.

[98] T. D. Nguyen, M. Fuentes-Cabrera, J. D. Fowlkes, and P. D. Rack. Coexistence of spinodal instability and thermal nucleation in thin-film rupture: Insights from molecular levels. *Phys. Rev. E*, 89:032403, 2014.

[99] NVIDIA, Péter Vingelmann, and Frank H.P. Fitzek. CUDA, release: 10.2.89, 2020.

[100] Y. Oh, J. Lee, and M. Lee. Fabrication of Ag-Au bimetallic nanoparticles by laser-induced dewetting of bilayer films. *Appl. Surf. Sci.*, 434:1293–1299, 2018.

[101] A. Oron. Nonlinear dynamics of irradiated thin volatile liquid films. *Phys. Fluids*, 12:29–41, 2000.

[102] A. Oron. Three dimensional nonlinear dynamics of thin liquid films. *Phys. Rev. Lett.*, 85:2108, 2000.

[103] A. Oron, S. H. Davis, and S. G. Bankoff. Long-scale evolution of thin liquid films. *Rev. Mod. Phys.*, 69:931, 1997.

[104] A. Oron and Y. Peles. Stabilization of thin liquid films by internal heat generation. *Phys. Fluids*, 10:537–539, 1998.

[105] Z. Pan, V. Borovikov, M. I. Mendelev, and F. Sansoz. Development of a semi-empirical potential for simulation of Ni solute segregation into grain boundaries in Ag. *Model. Simul. Mat. Sci. Eng.*, 26:075004, 2018.

[106] E. M. Petrie. *Handbook of Adhesives and Sealants.* McGraw-Hill Education, New York, NY, 2nd edition, 2007.

[107] S. Plimpton. Fast Parallel Algorithms for Short-Range Molecular-Dynamics. *J. Comp. Phys.*, 117:1, 1995.

[108] R. W. Powell, C. Y. Ho, P. E. Liley, United States National Bureau of Standards, and United States Department of Commerce. *Thermal conductivity of selected materials.* U.S. Dept. of Commerce, National Bureau of Standards; for sale by the Superintendent of Documents, U.S. Govt. Print. Off., Washington, 1966.

[109] G. Prado, Y. Amarouchene, and H. Kellay. Experimental evidence of a Rayleigh-Plateau instability in free falling granular jets. *Phys. Rev. Lett.*, 106:198001, 2011.

[110] P. D. Rack, Y. F. Guan, J. D. Fowlkes, A. V. Melechko, and M. L. Simpson. Pulsed laser dewetting of patterned thin metal films: A means of directed assembly. *Appl. Phys. Lett.*, 92:223108, 2008.

[111] H. Reinhardt, H. C. Kim, C. Pietzonka, J. Kruempelmann, B. Harbrecht, B. Roling, and N. Hampp. Self-organization of multifunctional surfaces - The fingerprints of light on a complex system. *Adv. Mater.*, 25:3313–3318, 2013.

[112] E. Ricci and R. Novakovic. Wetting and surface tension measurements on gold alloys. *Gold Bull.*, 34:41–49, 2001.

[113] K. M. Ridings, T. S. Aldershof, and S. C. Hendy. Surface melting and breakup of metal nanowires: Theory and molecular dynamics simulation. *J. Chem. Phys.*, 150:094705, 2019.

[114] F. M. Ross. Controlling nanowire structures through real time growth studies. *Rep. Prog. Phys.*, 73:114501, 2010.

[115] F. Ruffino and M. G. Grimaldi. Nanostructuration of thin metal films by pulsed laser irradiations: A review. *Nanomaterials*, 9:1133, 2019.

[116] F. Ruffino, A. Pugliara, E. Carria, C. Bongiorno, C. Spinella, and M.G. Grimaldi. Formation of nanoparticles from laser irradiated Au thin film on SiO_2/Si: Elucidating the Rayleigh-instability role. *Mater. Lett.*, 84:27–30, 2012.

[117] R. Sachan, S. Yadavali, N. Shirato, H. Krishna, V. Ramos, G. Duscher, S. J. Pennycook, A. K. Gangopadhyay, H. Garcia, and R. Kalyanaraman. Self-organized bimetallic Ag–Co nanoparticles with tunable localized surface plasmons showing high environmental stability and sensitivity. *Nanotechnology*, 23:275604, 2012.

[118] F. Saeki, S. Fukui, and H. Matsuoka. Optical interference effect on pattern formation in thin liquid films on solid substrates induced by irradiative heating. *Phys. Fluids*, 23:112102, 2011.

[119] F. Saeki, S. Fukui, and H. Matsuoka. Thermocapillary instability of irradiated transparent liquid films on absorbing solid substrates. *Phys. Fluids*, 25:062107, 2013.

[120] J. Sanders and E. Kandrot. *CUDA by example*. Addison-Wesley, Upper Saddle River, NJ, 2011.

[121] D. Schebarchov and S. C. Hendy. Effects of epitaxial strain on the melting of supported nickel nanoparticles. *Phys. Rev. B*, 84:085407, 2011.

[122] J. Schindelin, I. Arganda-Carreras, E. Frise, V. Kaynig, M. Longair, T. Pietzsch, S. Preibisch, C. Rueden, S. Saalfeld, B. Schmid, J. Y. Tinevez, D. J. White, V. Hartenstein, K. Eliceiri, P. Tomancak, and A. Cardona. Fiji: an open-source platform for biological-image analysis. *Nat. Methods*, 9:676–682, 2012.

[123] L. E. Scriven and C. V. Sternling. On cellular convection driven by surface-tension gradients: effects of mean surface tension and surface viscosity. *J. Fluid Mech.*, 19:321–340, 1964.

[124] I. Seric, S. Afkhami, and L. Kondic. Influence of thermal effects on stability of nanoscale films and filaments on thermally conductive substrates. *Phys. Fluids*, 30:012109, 2018.

[125] N. Shirato, J. Strader, A. Kumar, A. Vincent, P. Zhang, A. Karakoti, P. Nacchimuthu, H. J. Cho, S. Seal, and R. Kalyanaraman. Thickness dependent self limiting 1-D tin oxide nanowire arrays by nanosecond pulsed laser irradiation. *Nanoscale*, 3:1090–1101, 2011.

[126] S. Shklyaev, A. A. Alabuzhev, and M. Khenner. Long-wave Marangoni convection in a thin film heated from below. *Phys. Rev. E*, 85:016328, Jan 2012.

[127] S. Shklyaev, M. Khenner, and A. A. Alabuzhev. Oscillatory and monotonic modes of long-wave Marangoni convection in a thin film. *Phys. Rev. E*, 82:025302, Aug 2010.

[128] A. V. Sosunov and L. V. Spivak. Magnetic properties of bimetallic Au/Co nanoparticles prepared by thermal laser treatment. *Phys. Solid State*, 58:1371–1374, 2016.

[129] A. Stukowski. Visualization and analysis of atomistic simulation data with OVITO - the open visualization tool. *Modelling Simul. Mater. Sci. Eng.*, 18:015012, 2009.

[130] S. Sun, C. Murray, D. Weller, L. Folks, and A. Moser. Monodisperse FePt nanoparticles and ferromagnetic FePt nanocrystal superlattices. *Science*, 287:1989, 2000.

[131] Y. Tang, X. D. Wang, Q. P. Cao, S. Y. Liu, D. X. Zhang, J. Zhang, Z. H. Wu, T. D. Hu, H. L. Xie, T. Q. Xiao, and J. Z. Jiang. Nanometer-scale phase separation in $Al_{60}Ge_{30}Mn_{10}$ amorphous alloy. *J. Alloy. Compd.*, 802:166–172, 2019.

[132] F. Tavazza, T. P. Senftle, C. Zou, C. A. Becker, and A. C. T van Duin. Molecular dynamics investigation of the effects of tip-substrate interactions during nanoindentation. *J. Phys. Chem.*, 119:13580–13589, 2015.

[133] U. Thiele, D. V. Todorova, and H. Lopez. Gradient dynamics description for films of mixtures and suspensions: Dewetting triggered by coupled film height and concentration fluctuations. *Phys. Rev. Lett.*, 111:1–5, 2013.

[134] C. V. Thompson. Solid-state dewetting of thin films. *Annu. Rev. Mater. Res.*, 42:399–434, 2012.

[135] J. Trice, D. Thomas, C. Favazza, R. Sureshkumar, and R. Kalyanaraman. Pulsed-laser-induced dewetting in nanoscopic metal films: Theory and experiments. *Phys. Rev. B*, 75:235439, 2007.

[136] J. Trice, D. Thomas, C. Favazza, R. Sureshkumar, and R. Kalyanaraman. Novel Self-Organization Mechanism in Ultrathin Liquid Films: Theory and Experiment. *Phys. Rev. Lett.*, 101:017802, 2008.

[137] D. Tseluiko and D. T. Papageorgiou. Nonlinear dynamics of electrified thin liquid films. *SIAM J. Appl. Math*, 67:1310–1329, 2007.

[138] S. Ulrich and A. Zippelius. Stability of freely falling granular streams. *Phys. Rev. Lett.*, 109:166001, 2012.

[139] Z. Weltsch, A. Lovas, J. Takács, Á. Cziráki, A. Toth, and G. Kaptay. Measurement and modelling of the wettability of graphite by a silver-tin (Ag-Sn) liquid alloy. *Appl. Surf. Sci.*, 268:52–60, 2013.

[140] Y. Wu, J. D. Fowlkes, P. D. Rack, J. A. Diez, and L. Kondic. On the Breakup of Patterned Nanoscale Copper Rings into Droplets via Pulsed-Laser-Induced Dewetting: Competing Liquid-Phase Instability and Transport Mechanisms. *Langmuir*, 26:11972, 2010.

[141] Y. Wu, J. D. Fowlkes, N. A. Roberts, J. A. Diez, L. Kondic, A. G. González, and P. D. Rack. Competing liquid phase instabilities during pulsed laser induced self-assembly of copper rings into ordered nanoparticle arrays on SiO_2. *Langmuir*, 27:13314, 2011.

[142] Y. Wu, G. Li, C. Cherqui, N. W. Bigelow, N. Thakkar, D. J. Masiello, J. P. Camden, and P. D. Rack. Electron energy loss spectroscopy study of the full plasmonic spectrum of self-assembled Au–Ag alloy nanoparticles: Unraveling size, composition, and substrate effects. *ACS Photonics*, 3:130–138, 2016.

[143] Y. Y. Wu, J. D Fowlkes, and P. D. Rack. The Optical Properties of Cu-Ni Nanoparticles Produced via Pulsed Laser Dewetting of Ultrathin Films: The Effect of Nanoparticle Size and Composition on the Plasmon Response. *J Mater Res*, 26:277, 2011.

[144] S. Yadavali, M. Khenner, and R. Kalyanaraman. Pulsed laser dewetting of Au films: Experiments and modeling of nanoscale behavior. *Mater. Res.*, 28:1715–1723, 2013.

[145] P. Yang, H. Yan, S. Mao, R. Russo, J. Johnson, R. Saykally, N. Morris, J. Pham, R. He, and H. J. Choi. Controlled growth of ZnO nanowires and their optical properties. *Adv. Funct. Mater.*, 12:323–331, 2002.

[146] A. Zadražil, F. Stepanek, and O. K. Matar. Droplet spreading, imbibition and solidification on porous media. *J. Fluid Mech.*, 562:1–33, 2006.

[147] S. Zhang. *Nanostructured thin films and coatings : functional properties.* CRC Press, New York, NY, 2010.

[148] Y. Zhang, J. Cohen, and J. D. Owens. Fast tridiagonal solvers on the GPU. *ACM SIGPLAN Notices*, 45:127–136, 2010.

[149] X. W. Zhou, R. A. Johnson, and H. N. G. Wadley. Misfit-energy-increasing dislocations in vapor-deposited CoFe/NiFe multilayers. *Phys. Rev. B*, 69:144113, 2004.